eman ta zabal zazu

Universidad del País Vasco

Euskal Herriko Unibertsitatea

Biodegradable Polyesters with Potential Applications in 3D Printing: Structure, Morphology and Crystallization

Maria Rosaria Caputo

Ph.D. Thesis

Department of Polymers and Advanced Materials: Physics, Chemistry and Technology, University of the Basque Country UPV/EHU

Donostia-San Sebastian, October 2023

eman ta zabal zazu

Universidad del País Vasco
Euskal Herriko Unibertsitatea

Biodegradable Polyesters with Potential Applications in 3D Printing: Structure, Morphology and Crystallization

Maria Rosaria Caputo

Ph.D. Thesis

Advisors
Prof. Alejandro Jesús Müller Sánchez
Prof. Haritz Sardón Muguruza

Department of Polymers and Advanced Materials: Physics, Chemistry and Technology, University of the Basque Country UPV/EHU

Donostia-San Sebastian, October 2023

Acknowledgements **Agradecimientos** **Ringraziamenti**

The end of my four-year journey has now come and I feel like thanking a few people who have been fundamental and indispensable in reaching this stage.

La fine di questo mio viaggio durato quattro anni è ormai arrivata e mi sento di ringraziare alcune persone, che sono state fondamentali ed indispensabili per il raggiungimento di questa tappa.

I thank my supervisors, Prof. Alejandro J. Müller and Prof. Haritz Sardón, for welcoming me into their research groups and for everything they taught me. Their teachings made me grow personally and professionally. Thanks also to all the POLYMAT Professors, who have always been available and professional and who have contributed to the achievement of many results contained in this work.

Thanks to all members of both the Advanced Multiphasic Polymer Group and Catalysis and Sustainable Polymer Group for always helping me.

Muchas gracias a Jorge, mi gran amigo mexicano, quien me apoyó desde el primer día que llegué a la Universidad como solo un AMIGO puede y sabe hacer. Sabes lo importante que eres para mí y espero corresponder todo lo que has hecho por mí.

Muchas gracias a Valentina, la catalana de mi corazón, a la que he sentido amiga desde el momento en que la conocí. Gracias por todas nuestras risas, nuestras noches en el sincrotrón, nuestras salidas y todas las experiencias que siempre recordaré.

Gracias Elena, por cada momento que vivimos juntas y por todas las veces que me ayudaste. Gracias porque, gracias a ti, entendí que las cosas más difíciles pueden volverse simples.

Ringrazio in particolare Andromeda, così simile a me da comprendere ogni aspetto di questo delicato percorso, di vita soprattutto. Grazie per tutte le nostre infinite chiacchierate. Spero di poter continuare ad averti nella mia vita anche dopo questa esperienza.

Ringrazio Alessandra, divenuta parte integrante di questo gruppo di Ricerca. Grazie per l'allegria che hai portato con te da Napoli, grazie per avermi ricordato le

origini del mio amore per la ricerca e grazie, soprattutto, per i momenti di spensieratezza che, spero, rimarranno anche oltre tutto questo.

Muchas gracias a Marta, a quien conocí quizás demasiado tarde para dejarme absorber por su alegría. Segura que si te hubiera conocido al principio de este camino, me lo hubiera tomado todo con más filosofía. Gracias por todas tus enseñanzas y ayuda imprescindible.

Grazie mille a Federica, che si è dimostrata, in così poco tempo, un'amica sincera, di quelle che incontri poche volte nella vita, vera e leale.

Agradezco a Eider, Nico, Juan, Mario y al resto de mis compañeros porque, cada uno de ellos, me ha aportado algo que siempre llevaré conmigo. Lo mejor de tenerlos a todos a mi lado es guardar algo de cada lugar del mundo, aunque nunca hayan estado allí.

Grazie mille ai miei amici di vita. Grazie a Roberta e Alessandro, per tutte le nostre cene, per tutte le nostre esperienze di questi anni che mi hanno aiutata a rilassarmi e a divertirmi in ogni momento, soprattutto quelli più complicati. Grazie ad Angelo, che si è preso cura della mia alimentazione da lontano e che, soprattutto, ha ascoltato ogni mio sfogo, confortandomi sempre, senza mai giudicare. Grazie Antonella, la mia amica di sempre, per esserci e per rimanere accanto a me nonostante la lontananza, nonostante i cambiamenti, nonostante la vita. Grazie ad Alessandra, la mia compagna di studi di sempre, grazie per avermi supportata alla fine di ogni giornata. Grazie ad Anna e Alessia, amiche con cui ho condiviso questo percorso da lontano, grazie perchè, nonostante tutto, so che ci sarete sempre per me.

Voglio ringraziare i miei genitori che mi sono stati accanto come meglio hanno potuto. Spero di rendervi fieri di me, sempre.

Grazie Francesca, la sorella migliore del mondo. Grazie per avermi insegnato ancora tanto in questi anni. Separarmi da te è stata forse la cosa più difficile da affrontare durante questi lunghi quattro anni. Grazie per aver fatto in modo che ogni giorno fosse meno duro.

Grazie Nut, dolce cagnolino, per avermi fatto esplodere il cuore e per esserti seduto accanto a me durante ogni giorno della stesura di questa tesi, aspettando che terminassi per poter giocare e passeggiare insieme.

Grazie Antonio per il tuo bene e per la tua saggezza. Sei, come già ti dissi, il fratello che non ho mai avuto e spero possa essere sempre così.

Grazie Antonella per tutti i tuoi consigli e per la tua allegria, soprattutto, che ha reso più lieti questi anni.

Ringrazio poi ogni altra persona della mia famiglia per tutto ciò che hanno fatto per me in questi anni di lontananza, per farmi sentire meno sola e per avermi dato tanta forza.

Grazie infinite a Rino, la famiglia che ho scelto e che continuerò a scegliere ogni giorno. Tu sei l'unico che sa quanto questo percorso sia stato difficile per me, quanto mi abbia cambiata e quanto mi sia costato. Sai a quante cose mi ha fatto rinunciare e sai a quante cose ho rinunciato io per paura. Grazie per essere stato letterarlmente al mio fianco, dandomi la mano e asciugando le mie lacrime, quando volevo mollare tutto, quando mi sono sentita piccola in confronto a tutto questo, grazie per la forza che mi hai dato. Grazie per avermi assecondata sempre e grazie per tutte le esperienze vissute in questi ultimi anni, so che sarebbero potute essere molte di più, tu scusami se puoi. Grazie per accendere quella famosa luce nella mia testolina incasinata. Grazie per avermi scelta, spero tu possa continuare a farlo ogni giorno. Spero di poterti regalare tanta felicità e di poterti rimanere accanto per percorrere la strada della vita insieme, mano nella mano, sostenendoci a vicenda.

Index

Abstract 1
Chapter I 5
1. Introduction 5
1.1 General Introduction 6
1.2 Objectives 9
1.3 Structure of the Thesis 9
1.4 Principles of Characterization of Polymers 11
1.4.1 Crystallization in Polymers 11
1.4.2 Crystal Structure and Morphology 12
1.4.3 Crystal Growth 15
1.4.4 Polymer Crystallization theories 18
1.4.4.1 Avrami Theory 19
1.4.4.2 Lauritzen and Hoffman Theory 21
1.5 References 24
Chapter II 35
2. Experimental Part 35
2.1 Characterization Methods 36
2.1.1 Differential Scanning Calorimetry (DSC) 36
2.1.1.1 Non-isothermal DSC experiments 37
2.1.1.2 Isothermal DSC experiments 38
2.1.1.3 Successive Self-nucleation and Annealing (SSA) 39
2.1.2 Polarized light optical microscopy (PLOM) 40
2.1.2.1 Non-isothermal crystallization and Spherulitic growth rate (G) 41
2.1.3 Thermogravimetric analysis (TGA) 42
2.1.4 Wide-angle X-ray Scattering (WAXS) 42
2.1.5 Nuclear Magnetic Resonance (NMR) 43
2.1.6 Rheological Characterization 44
2.1.7 3D Printing of the samples 45
2.1.8 Printing Conditions 45
2.1.9 Pressure–Volume–Temperature (PVT) measurements 47
2.1.10 Compression Molding 49
2.1.11 Tensile Tests 49
2.1.12 Cross-section morphology 50
2.1.13 Heat Transfer Simulation 50

2.1.14 Size exclusion chromatography (SEC) 51
2.1.15 Preparation and characterization of single crystals 52
2.1.16 Transmission Electron Microscopy (TEM) 52
2.1.17 Optical Property Measurements 53
2.1.18 Barrier Property Measurements 53
2.2 Materials and Methodologies 53
2.2.1 Materials studied in Chapter III 53
2.2.2 Materials studied in Chapter IV 54
2.2.3 Materials studied in Chapter V 54
2.2.3.1 Standard CopolymerizationMethodology 54
2.2.3.2 Materials for comparison purposes 56
2.2.4 Materials studied in Chapter VI 56
2.2.4.1 Synthesis of η-Heptalactone 57
2.2.4.2 Synthesis of poly(η-heptalactone) 57
2.3 References 59
Chapter III 61
3. Effect of chain stereoconfiguration on poly(3-hydroxybutyrate) crystallization kinetics 61
3.1 Abstract 62
3.2 Introduction 63
3.3 Results and Discussion 66
3.3.1 NMR and TGA Results 66
3.3.2 Non-isothermal DSC 68
3.3.3 Powder diffraction and *In Situ* WAXS Real-Time Synchrotron Results 72
3.3.4 Morphology and Spherulite Growth 80
3.3.5 Study of the Overall Crystallization Kinetics by DSC 89
3.3.5.1 Equilibrium melting point determination 100
3.4 Study of a controlled stereo-defects semicrystalline and biodegradable poly(3-hydroxybutyrate), *sr*-P3HB. 103
3.5 Conclusions 109
3.6 References 111
Chapter IV 117
4. Influence of FFF Process Conditions on the Thermal, Mechanical, and Rheological Properties of Poly(hydroxybutyrate-co-hydroxy Hexanoate) 117
4.1 Abstract 118
4.2 Introduction 119
4.3 Results and Discussion 122
4.3.1 Thermal Analysis 122

4.3.1.1 Differential Scanning Calorimetry (DSC) 122
4.3.1.2 Rheological Characterization....126
4.3.1.3 Evaluation of the Effect of Pressure and Temperature on Specific Volume/Density....135
4.3.2 Mechanical Properties....138
4.3.2.1 Effect of the Bed and Nozzle Temperatures....139
4.3.2.1 Effect of the Printing Velocity....140
4.3.2.2 Effect of the Raster Angle 142
4.3.2.3 FFF vs. Compression Molding 143
4.3.3 SEM Analysis: Cross-Sectional Morphology 144
4.4 Conclusions....145
4.5 References....147
Chapter V 157
5. **Tailoring the nucleation and crystallization of Polyhydroxybutyrate by copolymerization**....157
5.1 Abstract....158
5.2 Introduction....159
5.3 Results and Discussion....162
5.3.1 Melt-segregation by in Situ SAXS Real-Time Synchrotron 162
5.3.2 TGA and Non-isothermal DSC Results 164
5.3.3 Non-isothermal PLOM Results 169
5.3.4 Isothermal PLOM Results 173
5.3.5.1 PHB block crystallization within PHB_{39}-b-PCL_{61} and crystallization of the PHB component within P(HB_{72}-ran-CL_{28}) 179
5.3.5.2 PCL block crystallization in PHB_{39}-b-PCL_{61} from crystalline and amorphous PHB.....188
5.4 Conclusion 194
5.5 References....196
Chapter VI....203
6. Experimental Part Synthesis, morphology and crystallization kinetics of Polyheptalactone (PHL) 203
6.1 Abstract 204
6.2 Introduction 205
6.3 Results and Discussion 207
6.3.2 Synthesis of poly(η-heptalactone)....207
6.3.3 X-ray powder diffraction 212
6.3.4 TGA Results 213
6.3.5 Non-isothermal DSC....214

6.3.6 Morphology and Spherulitic Growth 217
6.3.7 Overall crystallization kinetics obtained by DSC 222
6.3.8 Transmission Electron Microscopy (TEM) 231
6.4 Conclusions 234
6.5 References 235
Chapter VII 241
7. Conclusions 241
7.1 General Conclusions 241
7.2 List of Publications 245
7.3 Conference Presentations 246
7.4 Collaborations 247
Resumen y Conclusiones 249

Abstract

In this work, various systems based on polyesters have been studied to understand their structure-properties relationship and design strategies to improve them.

The family of polyesters most investigated in this thesis is that of polyhydroxyalkanoates (PHAs). These materials are biodegradable polyesters of bacterial origin with excellent thermal and barrier properties, ideal for applications in packaging and the biomedical industry, but with two major defects that have limited their use: high crystallinity leading to poor mechanical properties and melting points that are very close to their degradation temperatures, thus limiting their processing windows. The most studied homopolymer, belonging to this family, is polyhydroxybutyrate (PHB), with properties similar to polypropylene but with the shortcomings mentioned before, i.e., PHB is fragile and easy to degrade during processing. To limit these problems, copolymers with other PHAs that have slightly better properties have been produced by bacteria. However, these copolymers are challenging to obtain with controlled molecular weights and specific properties.

This work explores the replacement of classic bacterial PHB by novel synthetic PHB-based systems whose structure, morphology, and properties are studied with several techniques: differential scanning calorimetry (DSC), polarized optical light microscope (PLOM), mechanical properties, wide and small angle x-ray diffraction (WAXS and SAXS), electron scanning and transmission (SEM and TEM) microscopy and 3D printing.

The first part of this thesis presents, for the first time, a complete thermal and morphological study of novel synthetic PHB samples with different molecular weights compared with a bacterial PHB. Samples of synthetic PHB are a racemic mixture of

macromolecules with 50% R and 50% S configuration, whereas bacterial PHB is enantiomerically pure with 100% R chains. Non-isothermal and isothermal crystallization experiments were carried out, from which it was revealed that R and S chains in PHB can co-crystallize in the same unit cell as the R-PHB. Most notably, the presence of S chains has a retarding effect on the overall crystallization rate, potentially offering benefits regarding the material's manufacturability and industrial applications. Furthermore, a preliminary investigation is carried out on a sample of PHB in which imperfections in the stereochemistry are introduced in a controlled manner to evaluate potential alterations in its thermal, mechanical, optical, and barrier properties. Despite what usually happens, in this case, the presence of stereodefects improves the mechanical and optical properties. Furthermore, the barrier properties remain similar to those of the materials normally used in packaging.

This research continues reporting an innovative study for the family of PHAs as, before this, it had never been tried to 3D print a PHA without using additives to aid the printing. This research examines the influence of the specific printing parameters used in fuse filament fabrication (FFF) on the characteristics of poly(hydroxybutyrate-co-hydroxyhexanoate) or PHBH. A preliminary rheological study was conducted to verify the printability of PHBH. Furthermore, it has been observed that unlike what happens typically in FFF, the crystallization of PHBH occurs isothermally, in accordance with calorimetric measurements and with a computational study performed to simulate the temperature profile during the printing process. In addition, the mechanical properties have been shown to improve with higher nozzle and print bed temperatures.

To increase the available palette of PHAs-based materials, a part of this research is dedicated to studying two new copolymers of synthetic origin based on PHB and polycaprolactone (PCL). The work reports the thermal and morphological structural study

of a block copolymer and a random copolymer, and various results have been obtained: the presence of the comonomer influences the non-isothermal crystallization, decreasing the crystallization and melting temperatures. SAXS analysis reveals a significant structural difference between block and random copolymer: block copolymer exhibits weak phase segregation in the melt, which is absent in random copolymer.

In both copolymers, there is a reduction in the size of the spherulites, thereby improving the transparency of the copolymeric materials compared to the neat PHBs. Furthermore, the growth of spherulites is also slowed down, reducing the overall crystallization kinetics of PHB in the copolymers. These results are promising as they show how the properties of PHB-based products can be tailored by copolymerization to improve their processability and end-use properties.

Finally, the synthesis of a novel biobased polyester that has one more carbon atom than PCL, polyheptalactone (PHL) is reported. This work also investigates the influence of molecular weight on the primary nucleation rate, spherulitic growth, and overall crystallization rate of PHL. It has been observed that high molecular weights increase these rate values until they reach a plateau. Furthermore, single crystals of PHL were obtained from solution, and their hexagonally-shaped flat morphology was observed by TEM. This study reveals great similarities between PHL and PCL, which is important for the diffusion of sustainable materials.

Chapter I

1. Introduction

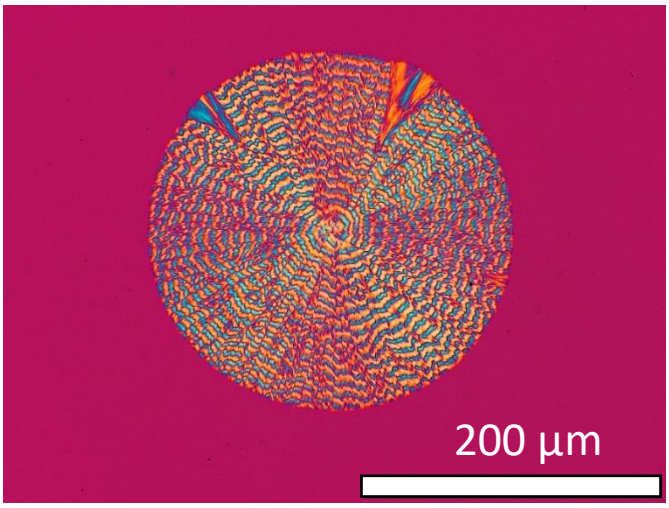

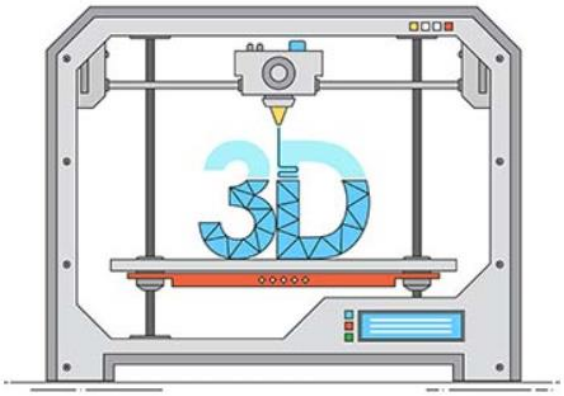

1.1General Introduction

Polymeric materials have been present in society since the time of the ancient Egyptians, who used gum arabic, a polysaccharide with adhesive properties.[1,2] Following the vulcanization process patented by Goodyear in 1844, it was discovered that natural rubber could also assume elastic properties.[3] The use of polymers was implemented during the 20th century: in those years, the first synthetic polymer was discovered, the bakelite, a thermosetting polymer with thermoelectric insulating properties.[4]

During the 20th century, other polymeric materials were also discovered and produced, the use of which is extremely widespread even today, such as, for example, polyethylene[5,6], polyvinyl chloride[7], polystyrene [8] and nylon [9]. Therefore, a world without polymers is unimaginable as they are present in every area, from packaging[10] to medicine [11].

Since many of these polymeric materials are petroleum-based, a problem that has arisen over the years has been that of recycling these materials or converting them into products with a higher added value.[12–17] These limitations have driven research toward new polymeric materials and technologies based on renewable, biobased, and biodegradable sources.[18–20]

According to the ASTM D6866 standard, a polymer is defined as "biobased" when at least a part of the polymer consists of material produced from renewable sources; on the other hand, according to the ASTM D6400 standard, a polymer is defined as biodegradable when it can undergo a degradation process by microorganisms existing in nature. An important aspect to define is that there are some polymers which are biobased but which are not biodegradable (bio-PE and bio-PP, [21]), some which are biodegradable

and biobased (PLA [22,23] and PHB [24]) and others which are not biobased but biodegradable. (PCL [25])

An extremely popular and attractive group of polymers is that of polyesters due to their biodegradability.[26,27] Polyesters contain the ester functional group in their main chain, and furthermore, they can be classified into thermoplastics and thermosets.[28,29] Among the thermoplastics, we find linear aromatic polyesters, thermoplastic elastomers, liquid crystals, polyhydroxyalkanoates, and aliphatic polyesters.[30] Some of them also have natural origin and are biocompatible, and this makes them particularly suitable for biomedical applications. [31,32].

In this work, aliphatic polyesters and, in particular, polyhydroxyalkanoates have been mainly used and studied. Polyhydroxyalkanoates (PHA) are materials of natural origin, more specifically of bacterial origin: in fact, some bacteria can produce these polyesters in particular conditions as an energy reserve.[33,34] This class of materials has many similarities to polypropylene in terms of barrier properties and moisture resistance. However, unlike polyolefins, PHAs do not enjoy the same diffusion due to their poor mechanical properties; in fact, they are brittle and stiff as they have very high degrees of crystallinity and large spherulitic superstructures.[35]

This aspect depends on the ability of PHAs to re-crystallize at room temperature through aging, and, in fact, the mechanical properties of these materials also change according to storage times. Furthermore, another limit to the diffusion of PHA is their high melting temperature, very close to the degradation temperature, and this makes it difficult to spread on an industrial level. Therefore, the investigation moved to creating PHA-based blends, copolymers, and composites to improve their flexibility and reduce their crystallization. [35,36]

Furthermore, as anticipated, one aspect to be improved is certainly the processability of this type of material, hopefully to increase its diffusion. Given their biocompatibility[37,38], the ideal application, in addition to packaging, would be in the biomedical field. In this field, extreme precision is required in the final products and, therefore, a valid process method would be that of additive manufacturing (also known as 3D Printing).

Additive manufacturing (AM) is a technique that emerged many years ago and allows you to obtain products on-demand. In fact, it is possible to produce models using virtual software and then create them by depositing material.[39] In this context, depending on the material available, there are different techniques to use. [40]

Material extrusion printing, better known as fused deposition modeling or fused filament fabrication (FDM or FFF), in which a filament of material is extruded from a nozzle at a temperature such as to melt the material and deposit it, layer by layer and according to a predefined path, on a plate until the desired shape is obtained. The important factor for this technique is that the material is thermoplastic in such a way as to make it a filament that can be extruded.

Another technique is Vat polymerization: in this case, a previously designated 3D model is transferred to a printer, consisting of a vat where an acrylate or methacrylate resin is inserted. Subsequently, a UV light is used to activate the radical polymerization and crosslink the resin to obtain the predefined shape. [41] In this technique, the requirements that a resin must have in order to have a successful printing process are two: an adequate viscosity and an appropriate curing speed at the moment of exposure to the light source. The viscosity of the resins suitable for this type of process is between 0.2 and 10 Pa·s. [41–43]

1.2 Objectives

Considering the background exposed above, the main objective of this thesis is to investigate and study different new polymeric systems based on polyesters and polyhydroxyalkanoates that can be used for various applications due to their biodegradability and biocompatibility.

As crystallization and morphology determine, in many cases, mechanical and optical properties, as well as biodegradation rates, the structure, morphology, and crystallization kinetics have been studied in detail for all the polyesters and co-polyesters employed in this thesis.

1.3 Structure of the Thesis

This thesis is divided into seven chapters, each presenting the basic concepts, the experimental methods and techniques used, and the various systems studied.

More details of each chapter are given below:

- **Chapter I**. This chapter provides a general introduction to the topic related to this thesis and a brief overview of the world of AM. Also, the basic concepts, which are necessary to understand the content of this thesis, are presented in this Chapter, such as crystallization theories and their mathematical models are described;
- **Chapter II.** In this section, an overall description of all the materials, methods, and experimental techniques used in each project involved in this thesis is reported in detail;
- **Chapter III.** This chapter is entirely dedicated to the study of the progenitor of the PHAs family: polyhydroxybutyrate (PHB). Indeed, in this section, the study of the structure, morphology and thermal properties of synthetic PHBs with different molecular weights is reported for the first time. The effect of the stereoconfiguration of the chains on the crystallization kinetics is evaluated. In

addition, an initial investigation is carried out on a sample of PHB deliberately modified with stereodefects under controlled conditions. The purpose of this study is to assess potential changes in the thermal, mechanical, optical, and barrier characteristics of the material, which normally change when stereodefects are introduced;

- **Chapter IV.** This chapter studies the effect of various printing conditions (FFF) on the mechanical and morphological properties of a copolymer of PHB, poly(hydroxybutyrate-co-hydroxy hexanoate), or PHBH. Preliminarily, a rheological study was carried out to confirm the printability of this material, and a computational simulation to study the temperature profile during the printing process;
- **Chapter V.** In this chapter, the effect on nucleation and crystallization of PHB when it is copolymerized with another polyester, PCL, was evaluated. Specifically, a random copolymer and a block copolymer were used, and the morphology, structure, and isothermal crystallization kinetics were studied in comparison with the respective neat polymers.
- **Chapter VI.** Given the various promising aspects of polyesters, this chapter reports the synthesis, morphology, and crystallization kinetics of a new polyester, polyheptalactone (PHL). Furthermore, the effect of the molecular weight on the crystallization kinetics of PHL is reported, and the results obtained from the preparation of the first single crystal of this polymer are reported.
- **Chapter VII.** Finally, this chapter presents the general conclusions of the thesis.

1.4 Principles of Characterization of Polymers

1.4.1 Crystallization in Polymers

In polymeric materials, crystallization is a process that depends on two factors: nucleation and growth.

The crystallization of a polymeric material can occur in a specific temperature range between the glass transition temperature (T_g) and the melting temperature at equilibrium (T_m^0). This is because at temperatures lower than the glass transition, the long range movements of the polymeric chains are impeded, and at temperatures higher than the equilibrium melting temperature, nucleation is impossible.

As it is known, the nucleation ($\dot{N}$) and growth (G) rates are dependent in a different way with respect to supercooling, as it appears evident in Figure 1.1. Generally, the maximum $\dot{N}$ value is recorded for higher supercooling values since, at these low temperatures, the movements of small chain segments are reduced, implying the formation of a large number of small crystals. Instead, on the contrary, for higher temperatures, crystalline growth is favored, with the formation of a lower number of larger crystals [44–47].

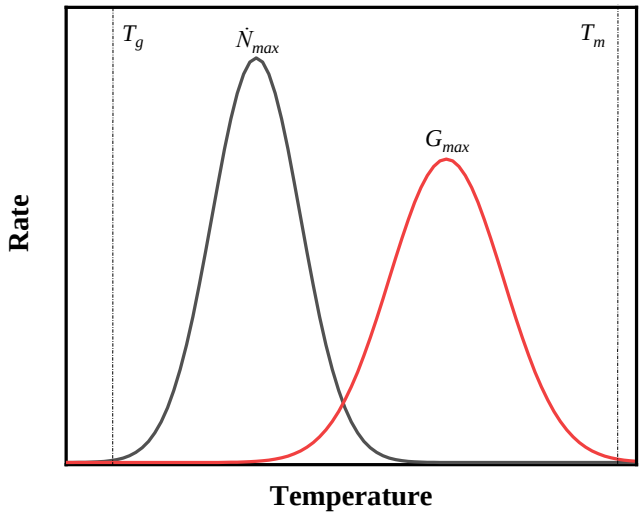

Figure 1.1. Schematic representation of nucleation rate ($\dot{N}$) and growth rate (G) as a function of temperature.

1.4.2 Crystal Structure and Morphology

Crystallizable polymeric materials are also defined as semi-crystalline as they are never 100% crystalline since kinetics controls the crystallization of long macromolecules. Hence, they are partially crystalline and partially amorphous, and their degree of crystallinity tends to be between 10 and 80%.

The crystallization of a material can occur either from the melt (cooling from the melt), or by mechanical stretching or solvent evaporation. On the other hand, the crystallization kinetics and the final degree of crystallinity depend on various factors: molecular structure, growth conditions, presence of impurities and/or additives, crystallization temperatures, cooling rate, tacticity, molecular weight, and its distribution, etc.[48,49].

There is a correlation between the morphology of the crystals and the final properties of a polymer, which implies certain applications and, therefore, one way to manage the properties of the polymers is the control of the morphology. The morphology of polymers is determined by crystallization kinetics and depends on the chemical structure of the materials and crystallization conditions. This is the reason why different types of morphologies can be obtained, such as lamellae[50–53], cylinders[54–58], ribbons[59], capsules[60], although the lamellar morphology is the most common for homopolymers.

During the thermal process of crystallization from the melt, the macromolecular chains that are entangled in the melt disentangle from each other and arrange themselves to form an ordered structure called lamella, represented in Figure 1.2. The lamellar thickness is approximately 10 nm as the chains are aligned and folded together [48]. Individual lamellae or single crystals are typically obtained from solution. From the melt,

the lamellae organize in superstructural aggregates, such as axialites (2D) or spherulites (3D).

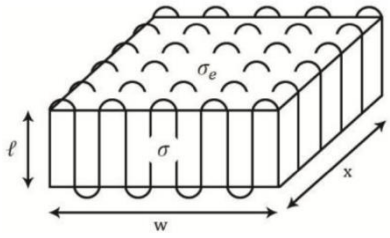

Figure 1.2. Schematic representation of a lamellar crystal with chain folds (*l*, *w*, *x*: lamellar thickness, length and width; σ and σ_e : lateral and fold surface free energies of the lamellae, respectively) [61].

In the case of block copolymers in which one component is semi-crystalline and one is amorphous, the crystallizable component forms lamellar crystals, leaving the amorphous component outside the crystal. Different morphologies can be obtained based on the composition of the AB-type diblock copolymer, such as spheres, cylinders or lamellae, due to micro-phase segregation even in the amorphous block copolymers (Figure 1.3)[62–67].

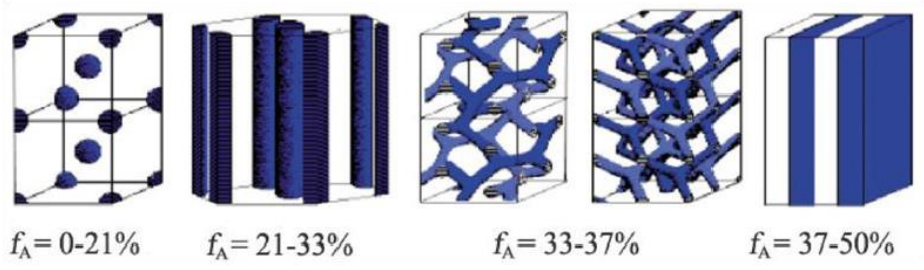

Figure 1.3. Possible morphogies in strongly segregated AB-type diblock copolymers. The blue component represents the minority phases A, and f_A determines the block volume fraction of block A [62].

The morphology of diblock copolymers is a function of the segregation strength (i.e., the product of χN, where χ is the Flory-Huggins parameter and N the degree of polymerization). When one of both blocks can crystallize, they will do so within the phase-segregated microdomains, if the phase segregation is strong. When the phase segregation is intermediate or weak, crystallization can break-out, and crystalline lamellae can be obtained organized within spherulites or axialites.

In the case in which the two blocks crystallize at different temperatures, it is possible to find oneself in two different situations: the crystallization of the first block determines the final morphology of the polymer because the second block must crystallize in the previously formed structure or the subsequent crystallization of the second block can modify or redefine the previous structure formed. [62,68–75] Even if the two blocks are miscible in the melt, due to the confined crystallization of one block in the lamellar crystals of the other, lower melting and crystallization temperatures can be obtained. [68,76,77]. Consequently, many morphologies can be obtained by changing the sequence in which the components of a copolymer crystallize. [62,78,79]

Furthermore, by adding a potentially crystallizable third or fourth component to obtain triblock terpolymers or tetrablock quaterpolymers, the crystalline structure analysis is made much more difficult, and other morphologies can be obtained.

Some possible morphologies for strongly segregated ABC-type triblock terpolymers are shown in Figure 1.4. The morphologies represented in Figure 1.4 (a-c) are the most common, while the rest are predictions not yet experimentally discovered.[80–84]

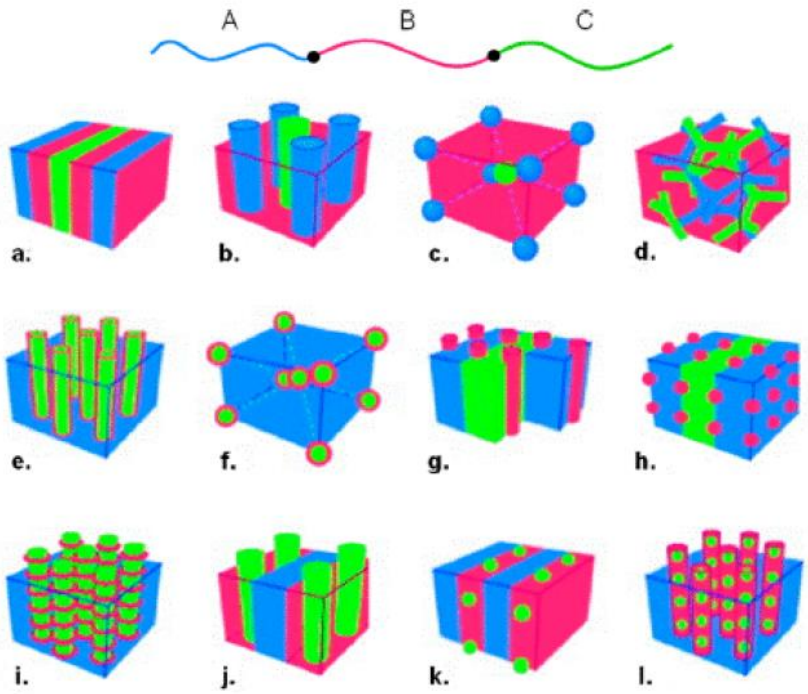

Figure 1.4. Possible morphologies of ABC type triblock terpolymers.[80]

1.4.3 Crystal Growth

As anticipated above, during the crystallization process, the polymer chains arrange themselves to form folded-chain lamellae. Folded-chain lamellae are fundamental units of lamellar clusters, which grow to form supramolecular structures such as spherulites, axialites, and hedrites. [85,86]

As part of the crystallization process, the spherulite growth rate is governed by supercooling. Figure 1.5 shows a general representation of the crystal growth rate as a function of the crystallization temperature, which has a bell-shaped curve with a maximum.

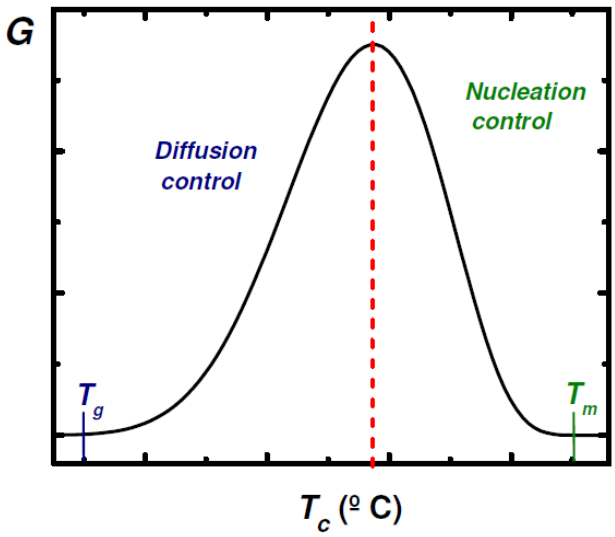

Figure 1.5. Crystal growth range (G) as a function of the isothermal crystallization temperature.

The left side of the bell-shape curve is dominated by diffusion (higher supercooling); at these temperatures, the diffusion of the chains is more difficult because melt viscosity increases exponentially as temperature decreases and reaches very high values near the glass transition temperatures, where all long-range chain mobility stops. On the other hand, the right-hand side of the bell-shape curve is controlled by secondary nucleation; as the supercooling increases, *G* increases as the thermodynamic driving force for crystallization also increases until diffusion becomes important and the maximum of the curve is reached [87,88].

The spherulitic structures that form during the crystallization process appear as birefringent structures when observed under a polarized light optical microscope (PLOM) and generally show a typical extinction pattern called the Maltese cross, well observable in Figure 1.6. The second extinction pattern type, common in polyesters, is banding. Figure 1.6 shows ring-banded spherulites.

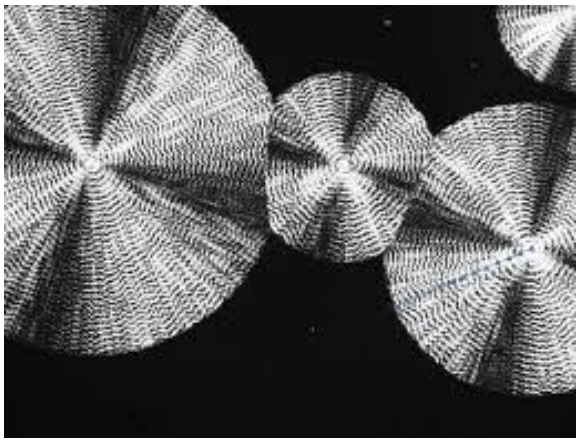

Figure 1.6. Maltese cross observed in ring-banded spherulites by means of PLOM [86].

Through transmission electron microscopy (TEM), it was observed that the internal zones of the spherulites consist of lamellae that grow radially separated by amorphous interlamellar zones. The chains are arranged perpendicular to the flat horizontal surface of the lamella and thus tangential to the spherulite and growth direction (Figure 1.7).

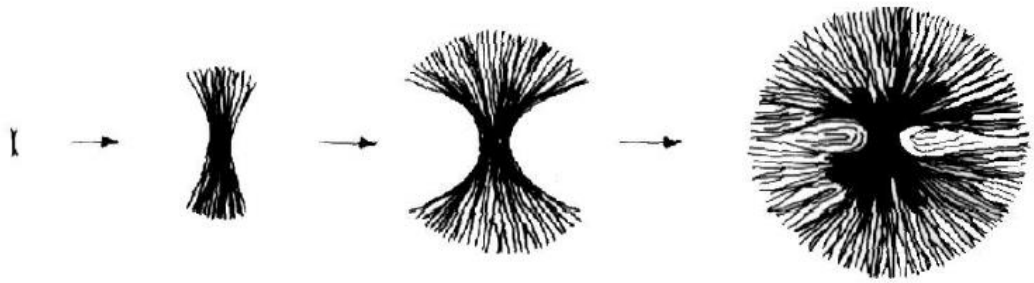

Figure 1.7. Diagram of the development of a spherulite from a homogeneous nucleus. [46]

The primary lamellae extend from the center to the end of the spherulite and further along the growth axis, branches are formed by secondary lamellae. To identify the regions present in the spherulite, at present, the model presented by Mandelkern in 1964 [45] is accepted. The first is the crystalline region formed by lamellae, the second is the

amorphous region of disordered conformation, and the third is the interfacial region of intermediate nature, created by chain segments that form part of the lamellae, entering and leaving the interfacial region (Figure 1.8).

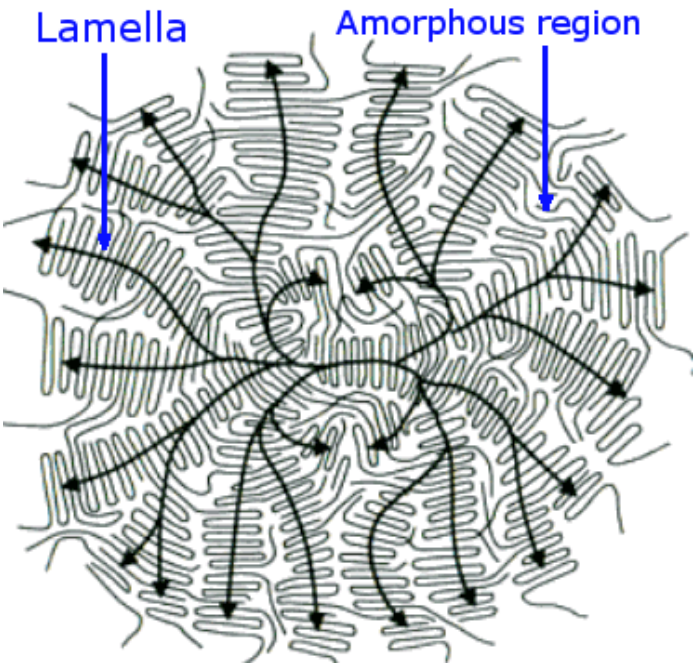

Figure 1.8. Amorphous and crystalline regions in spherulite.

The difference in size and morphology between spherulites of different polymers depends on the chemical nature, molecular weight and distribution, crystallization conditions, and mainly on the density of heterogeneities capable of inducing nucleation (i.e., catalytic debris or other impurities) present in the material.

1.4.4 Polymer Crystallization theories

This work employs two classic crystallization theories to fit the experimental data related to crystallization kinetics: Avrami's theory and Lauritzen and Hoffman's theory. These two theories have been applied to the experimental data obtained in isothermal crystallization experiments, and a brief description of them is given below.

1.4.4.1 Avrami Theory

The general Avrami equation describes well the primary crystallization of polymeric materials (i.e., before any spherulite impingement occurs). It describes the time evolution of the relative overall crystallization at constant temperature. Avrami's equation was developed to quantify the transition between liquid and solid state and can be expressed as follows[89,90]:

$$1 - V_c(t - t_0) = \exp(-K(t - t_0)^n) \quad (1.1)$$

where, t is the experimental time, t_0 is the induction time, V_c is the relative volumetric transformed fraction, n is the Avrami index, and K is the overall crystallization rate constant. $(1 - V_c)$ is the amorphous fraction.

The Avrami index (n) is composed of two terms[91]

$$n = n_d + n_n \quad (1.2)$$

where, n_d is the dimensionallity of the growing crystals, and this number can be 1, 2 or 3, for one, two or three-dimensional entities. n_n is the time dependence of the nucleation, this parameter can be 0 or 1, 0 corresponds to purely instantaneous (I) nucleation and 1 to purely sporadic nucleation (S). Table 1.1 shows the different combinations that can be obtained and the morphology that represents the Avrami index. The Avrami index (n) increases with increasing "dimensionality" of the growing crystal.

Table 1.1. Description of the different values of Avrami index (n).

Avrami Index	n_d	n_n	Description
1	1	0	Rod (I)
2	1	1	Rod (S)
2	2	0	Axialite (I)
3	2	1	Axialite (S)
3	3	0	Spherulite (I)
4	3	1	Spherulite (S)

The volume fraction (V_c) can be calculated as follows:

$$V_c = \frac{W_c}{W_c + \frac{\rho_c}{\rho_a}(1 - W_c)} \tag{1.3}$$

where, W_c is the crystalline mass fraction in the sample, ρ_c and ρ_a are the polymer densities of the crystalline and amorphous phases, respectively. W_c is calculated from the following equation:

$$W_c = \frac{\Delta H(t)}{\Delta H_{total}} \tag{1.4}$$

where, $\Delta H(t)$ is the enthalpy as a function of time at a given crystallization temperature, and ΔH_{total} is the maximum enthalpy value reached at the end of the isothermal crystallization process.

The crystallization half-time, $t_{50\%}$, is the time required to achieve 50% of the relative crystallinity of the polymer ($1 - V_c = 0.5$). It can be predicted by the Avrami theory as follows:

$$t_{50\%} = \left(\frac{-ln(1 - V_c)}{k}\right)^{1/n} = \left(\frac{-ln0.5}{k}\right)^{1/n} \tag{1.5}$$

To obtain the Avrami parameters, the linearization of the Avrami equation is represented as follows:

$$log\left[-ln\left(1 - V_c(t - t_0)\right)\right] = log(K) + n\ log(t - t_0) \tag{1.6}$$

With this linearization it is possible to plot $ln[-ln(1-V_c)]$ vs $ln\ (t - t_0)$. If the crystallization kinetics follows the Avrami equation, then a straight line is obtained.

Figure 1.9 shows the plots that can be obtained from the Avrami equation and its linearization. These plots were obtained from the Origin® plug-in developed by Lorenzo, *et al.* [92].

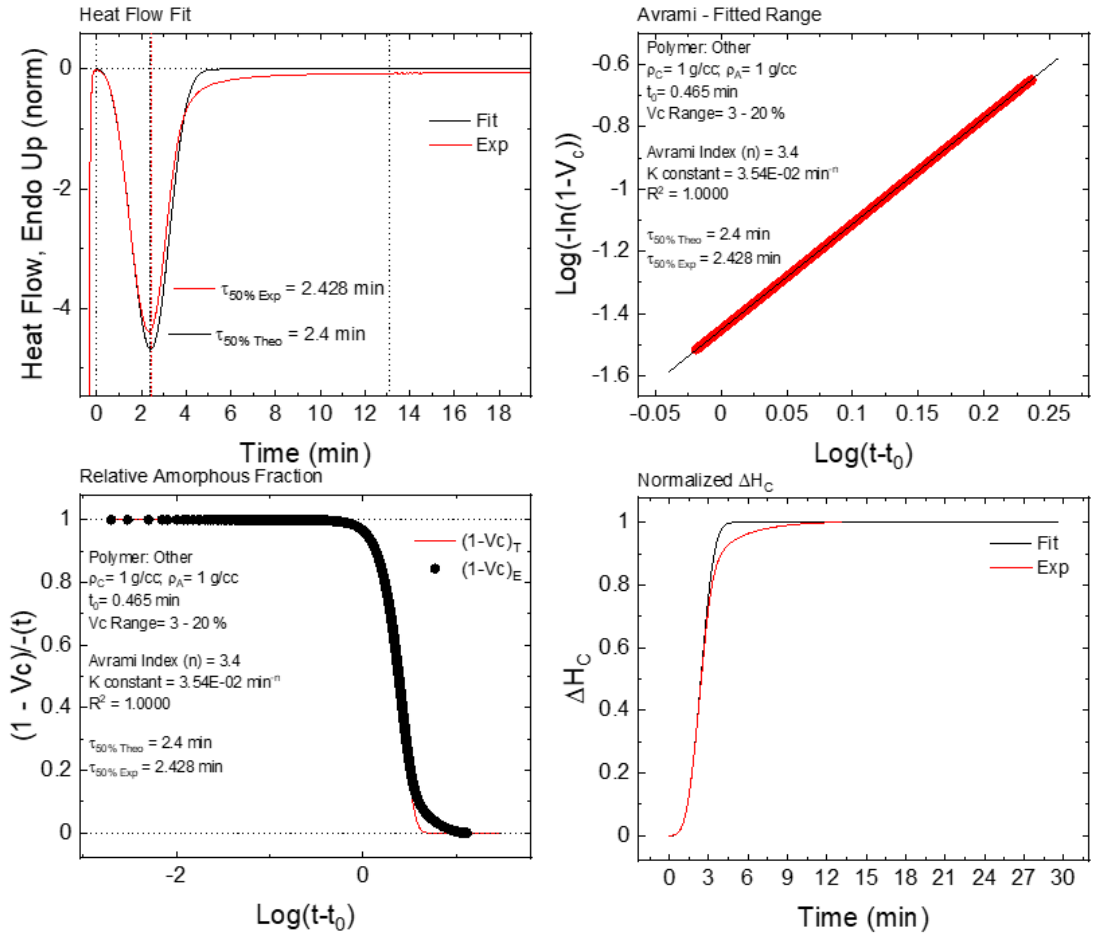

Figure 1.9. Avrami plots obtained through the Origin ® plug

1.4.4.2 Lauritzen and Hoffman Theory

This theory (LH) has been the dominant secondary nucleation theory for polymer crystallization, as it provides analytical expressions that can be used to fit experimental data. One of the advantages of the LH is that it provides a simple form to connect microscopic parameters with macroscopic quantities.

The LF theory provides expressions for linear growth rate (G), i.e., spherulitic growth rate as a function of supercooling ($\Delta T = T_m^0 - T_c$), where T_m^0 is the equilibrium melting temperature, and T_c is the crystallization temperature. The linear growth rate is determined by polarized light optical microscopy (PLOM). The LH theory can be expressed as:

$$G(T) = G_0 \exp\left(\frac{-U^*}{R(T_c - T_\alpha)}\right) \exp\left(\frac{-K_g^G}{T_c \Delta T_f}\right) \quad (1.7)$$

where, G_0 is a pre-exponential growth rate constant. The first term is related with molecular diffusion, U* is the activation energy for the transport of the polymer chains to the growth front (a value of 1500 cal/mol is usually employed), R is the gas constant, T_c is the crystallization temperature, T_α is the temperature at wich chain mobility ceases (normally is T_g – 30 K). The second term is the secondary nucleation term, ΔT is the supercooling (T_m^0 - T_c), and T_m^0 is the equilibrium melting temperature. The factor f is a temperature correction equal to $2T_c/(T_c+T_m^0)$, and K_g^G is a secondary nucleation constant that is proportional to the energy barrier for spherulitic growth.

The value K_g^G can be represented as:

$$K_g^G = \frac{j b_0 \sigma \sigma_e T_m^0}{k \Delta h_f} \quad (1.8)$$

where, j is determined by the crystallization regime and is equal to 4 for regime I and III, and is taken as 2 for regime II; b_0 is the width of the polymer chain, σ is the lateral surface free energy, σ_e is the fold surface free energy, k is the Boltzman constant, and Δh_f is the heat of fusion of a perfect crystal.

The LH theory analyzes the growth data according to the competition between the rate of deposition of secondary nuclei (i) and the rate of lateral surface spreading (g), resulting in three different regimes:

- Regime I: when $i << g$ and may be found at very low ΔT.
- Regime II: i is of the same order as g and occurs at moderate ΔT.
- Regime III: $i > g$ and is found at very high ΔT.

The overall crystallization kinetics is determined by the contributions of both nucleation and growth. The LH theory can be applied to the isothermal crystallization kinetics data collected by DSC. Following the equation:

$$\frac{1}{\tau_{50\%}}(T) = G_0^\tau \exp\left(\frac{-U^*}{R(T_C - T_\alpha)}\right) \exp\left(\frac{-K_g^\tau}{T \Delta T_f}\right) \quad (1.9)$$

The superscript τ is used to indicate that the parameters depend on the experimental data obtained by DSC, the superscript *G* indicates that the parameters were obtained by PLOM experimental data.

To apply the Lauritzen-Hoffman theory to the experimental data, the Origin ® plug-in developed by Lorenzo, *et al*. [92] was used. Figure 1.9 shows the plots obtained with this software.

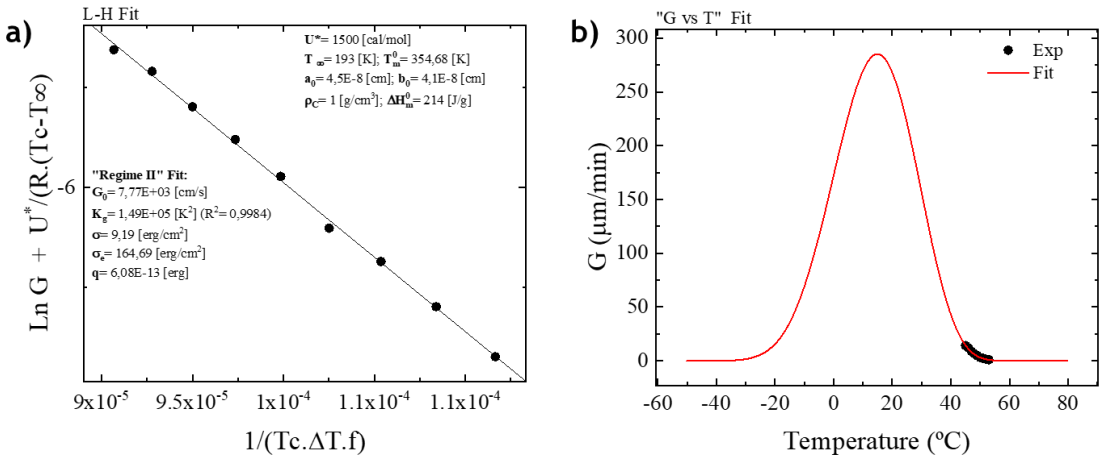

Figure 1.10. Lauritzen-Hoffman plots obtained through the Origin ® plug

1.5 References

1. Glicksman, M. Gum Arabic (Gum Acacia). In *Food hydrocolloids*; CRC Press, 2019; pp. 7–29 ISBN 0429290373.
2. Musa, H.H.; Ahmed, A.A.; Musa, T.H. Chemistry, Biological, and Pharmacological Properties of Gum Arabic. *Bioact. Mol. Food; Springer Int. Publ. AG Cham, Switz.* **2018**, 1–18.
3. Fisher, H.L. Vulcanization of Rubber Vulcanization of Rubber. *Ind. Eng. Chem.* **1939**, *31*, 1381–1389.
4. Baekeland, L.H. The Synthesis, Constitution, and Uses of Bakelite. *Ind. Eng. Chem.* **1909**, *1*, 149–161.
5. Demirors, M. The History of Polyethylene. In *100+ Years of Plastics. Leo Baekeland and Beyond*; ACS Publications, 2011; pp. 115–145 ISBN 1947-5918.
6. Trossarelli, L.; Brunella, V. Polyethylene: Discovery and Growth. In Proceedings of the UHMWPE meeting; 2003.
7. Mulder, K.; Knot, M. PVC Plastic: A History of Systems Development and Entrenchment. *Technol. Soc.* **2001**, *23*, 265–286.
8. Amos, J.L. The SPE International Award Address—1973 the Development of Impact Polystyrene–a Review. *Polym. Eng. Sci.* **1974**, *14*, 1–11.
9. Kohan, M.I. The History and Development of Nylon-66. In Proceedings of the High Performance Polymers: Their Origin and Development: Proceedings of the Symposium on the History of High Performance Polymers at the American Chemical Society Meeting held in New York, April 15–18, 1986; Springer, 1986; pp. 19–37.
10. Laorenza, Y.; Chonhenchob, V.; Bumbudsanpharoke, N.; Jittanit, W.; Sae-Tan, S.; Rachtanapun, C.; Chanput, W.P.; Charoensiddhi, S.; Srisa, A.; Promhuad, K.

Polymeric Packaging Applications for Seafood Products: Packaging-Deterioration Relevance, Technology and Trends. *Polymers (Basel)*. **2022**, *14*, 3706.

11. Modjarrad, K.; Ebnesajjad, S. *Handbook of Polymer Applications in Medicine and Medical Devices*; Elsevier, 2013; ISBN 0323221696.
12. Rorrer, N.A.; Nicholson, S.; Carpenter, A.; Biddy, M.J.; Grundl, N.J.; Beckham, G.T. Combining Reclaimed PET with Bio-Based Monomers Enables Plastics Upcycling. *Joule* **2019**, *3*, 1006–1027, doi:10.1016/j.joule.2019.01.018.
13. Ávila, A.F.; Duarte, M. V. A Mechanical Analysis on Recycled PET/HDPE Composites. *Polym. Degrad. Stab.* **2003**, *80*, 373–382, doi:10.1016/S0141-3910(03)00025-9.
14. Frounchi, M. Studies on Degradation of PET in Mechanical Recycling. *Macromol. Symp.* **1999**, *144*, 465–469, doi:10.1002/masy.19991440142.
15. Achilias, D.S.; Roupakias, C.; Megalokonomos, P.; Lappas, A.A.; Antonakou, V. Chemical Recycling of Plastic Wastes Made from Polyethylene (LDPE and HDPE) and Polypropylene (PP). *J. Hazard. Mater.* **2007**, *149*, 536–542, doi:10.1016/j.jhazmat.2007.06.076.
16. Jehanno, C.; Alty, J.W.; Roosen, M.; De Meester, S.; Dove, A.P.; Chen, E.Y.-X.; Leibfarth, F.A.; Sardon, H. Critical Advances and Future Opportunities in Upcycling Commodity Polymers. *Nature* **2022**, *603*, 803–814.
17. Vollmer, I.; Jenks, M.J.F.; Roelands, M.C.P.; White, R.J.; van Harmelen, T.; de Wild, P.; van Der Laan, G.P.; Meirer, F.; Keurentjes, J.T.F.; Weckhuysen, B.M. Beyond Mechanical Recycling: Giving New Life to Plastic Waste. *Angew. Chemie Int. Ed.* **2020**, *59*, 15402–15423.
18. Gross, R.A.; Kalra, B. Biodegradable Polymers for the Environment. *Science (80-.).* **2002**, *297*, 803–807.

19. Nair, L.S.; Laurencin, C.T. Biodegradable Polymers as Biomaterials. *Prog. Polym. Sci*. **2007**, *32*, 762–798.

20. Vroman, I.; Tighzert, L.; Vroman, I.; Tighzert, L. Biodegradable Polymers. Materials (Basel) 2: 307–344 2009.

21. Siracusa, V.; Blanco, I. Bio-Polyethylene (Bio-PE), Bio-Polypropylene (Bio-PP) and Bio-Poly (Ethylene Terephthalate)(Bio-PET): Recent Developments in Bio-Based Polymers Analogous to Petroleum-Derived Ones for Packaging and Engineering Applications. *Polymers (Basel)*. **2020**, *12*, 1641.

22. Shin, B.Y.; Jang, S.H.; Kim, B.S. Thermal, Morphological, and Mechanical Properties of Biobased and Biodegradable Blends of Poly (Lactic Acid) and Chemically Modified Thermoplastic Starch. *Polym. Eng. Sci*. **2011**, *51*, 826–834.

23. Sudesh, K.; Iwata, T. Sustainability of Biobased and Biodegradable Plastics. *CLEAN–Soil, Air, Water* **2008**, *36*, 433–442.

24. Markl, E.; Grünbichler, H.; Lackner, M. PHB-Bio Based and Biodegradable Replacement for PP: A Review. *Nov. Tech. Nutr. Food Sci* **2018**, *2*, 206–209.

25. Abedalwafa, M.; Wang, F.; Wang, L.; Li, C. Biodegradable Poly-Epsilon-Caprolactone (PCL) for Tissue Engineering Applications: A Review. *Rev. Adv. Mater. Sci* **2013**, *34*, 123–140.

26. Vert, M.; Li, S.M.; Spenlehauer, G.; Guérin, P. Bioresorbability and Biocompatibility of Aliphatic Polyesters. *J. Mater. Sci. Mater. Med.* **1992**, *3*, 432–446.

27. Vert, M. Aliphatic Polyesters: Great Degradable Polymers That Cannot Do Everything. *Biomacromolecules* **2005**, *6*, 538–546.

28. Deopura, B.L.; Alagirusamy, R.; Joshi, M.; Gupta, B. *Polyesters and Polyamides*; Elsevier, 2008; ISBN 1845694600.

29. Yamashita, H.; Nakano, Y. *Polyester: Properties, Preparation and Applications*; Nova Science Publishers, Incorporated, 2008; ISBN 1604567538.

30. Rosato, D. V; Rosato, D. V; v Rosato, M. *Plastic Product Material and Process Selection Handbook*; Elsevier, 2004; ISBN 0080514057.

31. Manavitehrani, I.; Fathi, A.; Badr, H.; Daly, S.; Negahi Shirazi, A.; Dehghani, F. Biomedical Applications of Biodegradable Polyesters. *Polymers (Basel).* **2016**, *8*, 20.

32. Brannigan, R.P.; Dove, A.P. Synthesis, Properties and Biomedical Applications of Hydrolytically Degradable Materials Based on Aliphatic Polyesters and Polycarbonates. *Biomater. Sci.* **2017**, *5*, 9–21.

33. Poli, A.; Di Donato, P.; Abbamondi, G.R.; Nicolaus, B. Synthesis, Production, and Biotechnological Applications of Exopolysaccharides and Polyhydroxyalkanoates by Archaea. *Archaea* **2011**, *2011*.

34. Raza, Z.A.; Abid, S.; Banat, I.M. Polyhydroxyalkanoates: Characteristics, Production, Recent Developments and Applications. *Int. Biodeterior. Biodegrad.* 2018, *126*, 45–56.

35. Bugnicourt, E.; Cinelli, P.; Lazzeri, A.; Alvarez, V.A. Polyhydroxyalkanoate (PHA): Review of Synthesis, Characteristics, Processing and Potential Applications in Packaging. **2014**.

36. Gigante, V.; Cinelli, P.; Seggiani, M.; Alavarez, V.A.; Lazzeri, A. Processing and Thermomechanical Properties of PHA. *Handb. Polyhydroxyalkanoates* **2020**, 91–118.

37. Zhao, K.; Deng, Y.; Chen, J.C.; Chen, G.-Q. Polyhydroxyalkanoate (PHA) Scaffolds with Good Mechanical Properties and Biocompatibility. *Biomaterials* **2003**, *24*, 1041–1045.

38. Dwivedi, R.; Pandey, R.; Kumar, S.; Mehrotra, D. Poly Hydroxyalkanoates (PHA): Role in Bone Scaffolds. *J. oral Biol. craniofacial Res.* **2020**, *10*, 389–392.

39. Chiulan, I.; Frone, A.N.; Brandabur, C.; Panaitescu, D.M. Recent Advances in 3D Printing of Aliphatic Polyesters. *Bioengineering* **2017**, *5*, 2.

40. Sanchez-Rexach, E.; Johnston, T.G.; Jehanno, C.; Sardon, H.; Nelson, A. Sustainable Materials and Chemical Processes for Additive Manufacturing. *Chem. Mater.* 2020, *32*, 7105–7119.

41. Appuhamillage, G.A.; Chartrain, N.; Meenakshisundaram, V.; Feller, K.D.; Williams, C.B.; Long, T.E. 110th Anniversary: Vat Photopolymerization-Based Additive Manufacturing: Current Trends and Future Directions in Materials Design. *Ind. Eng. Chem. Res.* **2019**, *58*, 15109–15118.

42. Smith, P.T.; Narupai, B.; Tsui, J.H.; Millik, S.C.; Shafranek, R.T.; Kim, D.-H.; Nelson, A. Additive Manufacturing of Bovine Serum Albumin-Based Hydrogels and Bioplastics. *Biomacromolecules* **2019**, *21*, 484–492.

43. Le Fer, G.; Becker, M.L. 4D Printing of Resorbable Complex Shape-Memory Poly (Propylene Fumarate) Star Scaffolds. *ACS Appl. Mater. Interfaces* **2020**, *12*, 22444–22452.

44. Gedde, U.W.; Hedenqvist, M.S. *Fundamental Polymer Science*; Springer, 2019; Vol. 2;.

45. Mandelkern, L. *Crystallization of Polymers: Volume 2, Kinetics and Mechanisms*; Cambridge University Press, 2004; ISBN 1139453505.

46. Reiter, G.; Strobl, G.R. *Progress in Understanding of Polymer Crystallization*; Springer, 2007; Vol. 714; ISBN 3540473076.

47. Schultz, J.M. The Development of Crystalline Order in Thermoplastic Polymers 2001.

48. Arif P., M.; Kalarikkal, N.; Thomas, S. Introduction on Crystallization in Multiphase Polymer Systems. *Cryst. Multiph. Polym. Syst.* **2018**, 1–13.

49. Liang, G.; Bao, S.; Zhu, F. Theoretical Aspects of Polymer Crystallization in Multiphase Systems. *Cryst. Multiph. Polym. Syst.* **2018**, 17–48.

50. Zhang, B.; Chen, J.; Baier, M.C.; Mecking, S.; Reiter, R.; Mülhaupt, R.; Reiter, G. Molecular-Weight-Dependent Changes in Morphology of Solution-Grown Polyethylene Single Crystals. *Macromol. Rapid Commun.* **2015**, *36*, 181–189.

51. Scheinhardt, B.; Trzaskowski, J.; Baier, M.C.; Stempfle, B.; Oppermann, A.; Wöll, D.; Mecking, S. Anisotropic Polyethylene Nanocrystals Labeled with a Single Fluorescent Dye Molecule: Toward Monitoring of Nanoparticle Orientation. *Macromolecules* **2013**, *46*, 7902–7910.

52. Bärenwald, R.; Goerlitz, S.; Godehardt, R.; Osichow, A.; Tong, Q.; Krumova, M.; Mecking, S.; Saalwächter, K. Local Flips and Chain Motion in Polyethylene Crystallites: A Comparison of Melt-Crystallized Samples, Reactor Powders, and Nanocrystals. *Macromolecules* **2014**, *47*, 5163–5173.

53. Ortmann, P.; Trzaskowski, J.; Krumova, M.; Mecking, S. Precise Microstructure Self-Stabilized Polymer Nanocrystals. *ACS Macro Lett.* **2013**, *2*, 125–127.

54. Zhou, H.; Lu, Y.; Zhang, M.; Guerin, G.; Manners, I.; Winnik, M.A. PFS-b-PNIPAM: A First Step toward Polymeric Nanofibrillar Hydrogels Based on Uniform Fiber-like Micelles. *Macromolecules* **2016**, *49*, 4265–4276.

55. Nazemi, A.; Boott, C.E.; Lunn, D.J.; Gwyther, J.; Hayward, D.W.; Richardson, R.M.; Winnik, M.A.; Manners, I. Monodisperse Cylindrical Micelles and Block Comicelles of Controlled Length in Aqueous Media. *J. Am. Chem. Soc.* **2016**, *138*, 4484–4493.

56. Li, X.; Jin, B.; Gao, Y.; Hayward, D.W.; Winnik, M.A.; Luo, Y.; Manners, I.

Monodisperse Cylindrical Micelles of Controlled Length with a Liquid-Crystalline Perfluorinated Core by 1D "Self-Seeding." *Angew. Chemie Int. Ed.* **2016**, *55*, 11392–11396.

57. Zhang, J.; Li, C.; Zhang, R.; Zhang, F.; Liu, W.; Liu, X.; Lee, S.M.-Y.; Zhang, H. A Phosphinate-Based near-Infrared Fluorescence Probe for Imaging the Superoxide Radical Anion in Vitro and in Vivo. *Chem. Commun.* **2016**, *52*, 2679–2682.

58. Guerin, G.; Rupar, P.; Molev, G.; Manners, I.; Jinnai, H.; Winnik, M.A. Lateral Growth of 1D Core-Crystalline Micelles upon Annealing in Solution. *Macromolecules* **2016**, *49*, 7004–7014.

59. Wu, J.; Weng, L.-T.; Qin, W.; Liang, G.; Tang, B.Z. Crystallization-Induced Redox-Active Nanoribbons of Organometallic Polymers. *ACS Macro Lett.* **2015**, *4*, 593–597.

60. Wang, W.; Qi, H.; Zhou, T.; Mei, S.; Han, L.; Higuchi, T.; Jinnai, H.; Li, C.Y. Highly Robust Crystalsome via Directed Polymer Crystallization at Curved Liquid/Liquid Interface. *Nat. Commun.* **2016**, *7*, 10599.

61. Mohammadi, H. On the Melting and Crystallization of Linear Polyethylene, Poly (Ethylene Oxide) and Metallocene Linear Low-Density Polyethylene 2018.

62. De Rosa, C.; Di Girolamo, R.; Malafronte, A.; Scoti, M.; Talarico, G.; Auriemma, F.; de Ballesteros, O.R. Polyolefins Based Crystalline Block Copolymers: Ordered Nanostructures from Control of Crystallization. *Polymer (Guildf).* **2020**, *196*, 122423.

63. Kalloudis, M.; Glynos, E.; Pispas, S.; Walker, J.; Koutsos, V. Thin Films of Poly (Isoprene-b-Ethylene Oxide) Diblock Copolymers on Mica: An Atomic Force Microscopy Study. *Langmuir* **2013**, *29*, 2339–2349.

64. Liang, G.; Xu, J.; Fan, Z. Structure of Crystalline Domains in Semicrystalline Block Copolymer Thin Films. *Chinese J. Polym. Sci.* **2006**, *24*, 341–344.

65. Liang, G.-D.; Xu, J.-T.; Fan, Z.-Q.; Mai, S.-M.; Ryan, A.J. Effect of Substrate Surface on Dewetting Behavior and Chain Orientation of Semicrystalline Block Copolymer Thin Films. *J. Phys. Chem. B* **2006**, *110*, 24384–24389.

66. Liang, G.-D.; Xu, J.-T.; Fan, Z.-Q.; Mai, S.-M.; Ryan, A.J. Thin Film Morphology of Symmetric Semicrystalline Oxyethylene/Oxybutylene Diblock Copolymers on Silicon. *Macromolecules* **2006**, *39*, 5471–5478.

67. Liang, G.-D.; Xu, J.-T.; Fan, Z.-Q. Lamellar Orientation in Thin Films of Symmetric Semicrytalline Polystyrene-b-Poly (Ethylene-Co-Butene) Block Copolymers: Effects of Molar Mass, Temperature of Solvent Evaporation, and Annealing. *J. Phys. Chem. B* **2007**, *111*, 11921–11928.

68. Castillo, R. V; Müller, A.J. Crystallization and Morphology of Biodegradable or Biostable Single and Double Crystalline Block Copolymers. *Prog. Polym. Sci.* **2009**, *34*, 516–560.

69. Müller, A.J.; Arnal, M.L.; Balsamo, V. Crystallization in Block Copolymers with More than One Crystallizable Block. *Prog. Underst. Polym. Cryst.* **2007**, 229–259.

70. Myers, S.B.; Register, R.A. Crystalline− Crystalline Diblock Copolymers of Linear Polyethylene and Hydrogenated Polynorbornene. *Macromolecules* **2008**, *41*, 6773–6779.

71. Nojima, S.; Ono, M.; Ashida, T. Crystallization of Block Copolymers II. Morphological Study of Poly (Ethylene Glycol)-Poly (ε-Caprolactone) Block Copolymers. *Polym. J.* **1992**, *24*, 1271–1280.

72. Castillo, R.V.; Muller, A.J.; Lin, M.-C.; Chen, H.-L.; Jeng, U.-S.; Hillmyer, M.A. Confined Crystallization and Morphology of Melt Segregated PLLA-b-PE and

PLDA-b-PE Diblock Copolymers. *Macromolecules* **2008**, *41*, 6154–6164.

73. Loo, Y.-L.; Register, R.A.; Ryan, A.J. Modes of Crystallization in Block Copolymer Microdomains: Breakout, Templated, and Confined. *Macromolecules* **2002**, *35*, 2365–2374.

74. Sun, L.; Liu, Y.; Zhu, L.; Hsiao, B.S.; Avila-Orta, C.A. Self-Assembly and Crystallization Behavior of a Double-Crystalline Polyethylene-Block-Poly (Ethylene Oxide) Diblock Copolymer. *Polymer (Guildf).* **2004**, *45*, 8181–8193.

75. Sakurai, T.; Nojima, S. Significant Increase in the Melting Temperature of Poly (ε-Caprolactone) Blocks Confined in the Crystallized Lamellar Morphology of Poly (ε-Caprolactone)-Block-Polyethylene Copolymers. *Polym. J.* **2011**, *43*, 370–377.

76. He, W.-N.; Xu, J.-T. Crystallization Assisted Self-Assembly of Semicrystalline Block Copolymers. *Prog. Polym. Sci.* **2012**, *37*, 1350–1400.

77. Hamley, I.W. Crystallization in Block Copolymers. *Interfaces Cryst. Viscoelasticity* **1999**, 113–137.

78. Van Horn, R.M.; Zheng, J.X.; Sun, H.-J.; Hsiao, M.-S.; Zhang, W.-B.; Dong, X.-H.; Xu, J.; Thomas, E.L.; Lotz, B.; Cheng, S.Z.D. Solution Crystallization Behavior of Crystalline− Crystalline Diblock Copolymers of Poly (Ethylene Oxide)-Block-Poly (ε-Caprolactone). *Macromolecules* **2010**, *43*, 6113–6119.

79. Liang, G.; Weng, L.-T.; Lam, J.W.Y.; Qin, W.; Tang, B.Z. Crystallization-Induced Hybrid Nano-Sheets of Fluorescent Polymers with Aggregation-Induced Emission Characteristics for Sensitive Explosive Detection. *ACS Macro Lett.* **2014**, *3*, 21–25.

80. Chang, A.B.; Bates, F.S. The ABCs of Block Polymers. *Macromolecules* 2020, *53*, 2765–2768.

81. Zheng, W.; Wang, Z.-G. Morphology of ABC Triblock Copolymers. *Macromolecules* **1995**, *28*, 7215–7223.

82. Mogi, Y.; Nomura, M.; Kotsuji, H.; Ohnishi, K.; Matsushita, Y.; Noda, I. Superlattice Structures in Morphologies of the ABC Triblock Copolymers. *Macromolecules* **1994**, *27*, 6755–6760.

83. Stadler, R.; Auschra, C.; Beckmann, J.; Krappe, U.; Voight-Martin, I.; Leibler, L. Morphology and Thermodynamics of Symmetric Poly (A-Block-B-Block-C) Triblock Copolymers. *Macromolecules* **1995**, *28*, 3080–3097.

84. Park, C.; Yoon, J.; Thomas, E.L. Enabling Nanotechnology with Self Assembled Block Copolymer Patterns. *Polymer (Guildf).* **2003**, *44*, 6725–6760.

85. Schultz, J.M. *Polymer Crystallization: The Development of Crystalline Order in Thermoplastic Polymers*; Amer Chemical Society, 2001; ISBN 0841236690.

86. Enrique-Jiménez, P.; Vega, J.F.; Martínez-Salazar, J.; Ania, F.; Flores, A. Estudio Del Bandeado En Esferulitas Poliméricas Mediante Nanoindentación. **2017**.

87. Müller, A.J.; Michell, R.M.; Lorenzo, A.T. Isothermal Crystallization Kinetics of Polymers. *Polym. Morphol. Princ. Charact. Process.* **2016**, *714*, 181–203.

88. Lorenzo, A.T.; Müller, A.J. Estimation of the Nucleation and Crystal Growth Contributions to the Overall Crystallization Energy Barrier. *J. Polym. Sci. Part B Polym. Phys.* **2008**, *46*, 1478–1487, doi:10.1002/POLB.21483.

89. Lorenzo, A.T.; Arnal, M.L.; Albuerne, J.; Müller, A.J. DSC Isothermal Polymer Crystallization Kinetics Measurements and the Use of the Avrami Equation to Fit the Data: Guidelines to Avoid Common Problems. *Polym. Test.* **2007**, *26*, 222–231.

90. Gedde, U.L.F. *Polymer Physics*; Springer Science & Business Media, 1995; ISBN 0412626403.

91. Müller, A.J.; Balsamo, V.; Arnal, M.L. Nucleation and Crystallization in Diblock and Triblock Copolymers. *Block Copolym. II* **2005**, 1–63.

92. Lorenzo, A.T.; Arnal, M.L.; Albuerne, J.; Müller, A.J. DSC Isothermal Polymer Crystallization Kinetics Measurements and the Use of the Avrami Equation to Fit the Data: Guidelines to Avoid Common Problems. *Polym. Test.* **2007**, *26*, 222–231, doi:10.1016/j.polymertesting.2006.10.005.

Chapter II

2. Experimental Part

This chapter describes the characterization methods and materials for each system presented in the thesis.

2.1 Characterization Methods

2.1.1 Differential Scanning Calorimetry (DSC)

The thermal behavior of the polymeric materials was analyzed using the differential scanning calorimetry technique. This technique is very effective in determining the enthalpy changes, melting, crystallization and glass transition temperatures of a substance. A DSC equipment consists of two cells: in one cell an empty pan is placed as a reference, and in the other cell, a pan with the sample to be analyzed is placed. Most of the DSC experiments performed in this thesis work used a compensating power calorimeter; this type of tool consists of two electronic heating circuits, the first is responsible for changing the temperature in the two furnaces at the speed rate indicated in the program, the second circuit keeps the temperature difference between the two furnaces equal to zero, since, when an exothermic or endothermic process occurs in the sample, this circuit compensates the temperature imbalance (by applying or substracting power to the sample cell) so that the temperatures in the furnaces remain constant. This technique, applied to polymers, makes it possible to determine temperature changes associated with changes in the physical state of the polymers or in the chemical composition. This analysis determines the melting temperature (T_m), the crystallization temperature (T_c), the cold crystallization temperature (T_{cc}) and the glass transition (T_g) and the related enthalpies. Furthermore, from the enthalpy of melting, the degree of crystallinity of a polymer can be calculated using the following equation:

$$x_c = \frac{\Delta H_m - \Delta H_{cc}}{\Delta H_m^0 x\, f} \times 100 \qquad (2.1)$$

where ΔH_m is the melting enthalpy, ΔH_{cc} is the cold crystallization enthalpy (if this phenomenon is present , ΔH_m^0 is the enthalpy of fusion at equilibrium and f is the percentage of polymer present in each sample.

Three types of DSC have been used in this thesis work and are described below:

In the case of Chapter III, for the study of racemic PHB with distinct molecular weight, a Perkin Elmer Pyris I DSC equipped with an Intracooler 2P was employed to characterize thermal properties. All the experiments were performed under ultrapure nitrogen flow, and the instrument was calibrated with indium and tin standards. Samples of 2 mg for each type of PHB were used. Measurements were performed by placing the samples in sealed aluminum pans.

In Chapter IV, to determine the thermal properties of the PHBH filament, a TA Instruments Q2000 DSC (this is a heat-flow calorimeter) calibrated with Indium and Tin under 50 mL/min of nitrogen flow was used to carry out these experiments.

In Chapters V and VI the materials were studied through a Perkin Elmer DSC 8500 equipped with an Intracooler III as a cooling system.

The sample placed for the experiments was always around 5 mg. The different experiments performed in the DSC are explained below.

2.1.1.1 Non-isothermal DSC experiments

The non-isothermal study of the samples involved in this thesis work was performed according to the following steps:

1. First Heating from T_0 (25 ºC) to a T_f (between 20 - 30 ºC above the polymer melting peak), at a heating rate of 20 ºC min^{-1}.
2. Wait 3 min at T_f to erase the thermal history of the material.
3. Cooling from T_f down to 0 ºC at 20 ºC min^{-1}.

4. Isothermal step for 3 min at -70 ºC.

5. Second Heating from -20 ºC to T_f at 20 ºC min^{-1}.

2.1.1.2 Isothermal DSC experiments

In this thesis work, the following method was used to perform isothermal crystallization experiments at DSC, suggested by Lorenzo *et al*., [1]:

1. Wait 3 min at T_f to erase the thermal history of the material.

2. Cooling from T_f to T_c at 60 ºC min^{-1}.

3. Isothermal step at T_c for sufficient time to complete the crystallization process.

4. Heating from T_c to T_f at 20 ºC min^{-1}.

This procedure is repeated at least for 10 different T_c, starting from $T_{c,min}$, which is the minimum temperature at which no crystallization of the polymer occurs during cooling.

In the case of the Chapter V in which a copolymer in which both blocks are crystallizable was investigated, a slightly modified procedure was performed: since in PHB_{39}-*b*-PCL_{61} both blocks are crystallizable, a separate study of the kinetics of each block was performed. At first, the overall crystallization kinetics of the PHB block was investigated (keeping the PCL block molten), and subsequently, that of the PCL block. The overall crystallization kinetics of the PCL block was studied for two cases: keeping the PHB block amorphous or semi-crystalline. In the first case, rapid cooling from the melt was performed (at 60 ºC/min) to the T_c chosen for PCL, a condition under which the PHB block could not crystallize. In the second case, both PHB and PCL blocks were allowed to crystallize during the crystallization process from the melt at 20 ºC/min, and then the sample was heated to 100 ºC to melt the PCL block only, as the melting point of

PHB is greater than 100 ºC. Then the cooling from 100 ºC to T_c was performed at 60 ºC/min. In this way, the PHB block crystals remained unmolten while the PCL isothermal crystallization was determined. In the case of the P(HB_{72}-*ran*-CL_{28}) sample, since it exhibits only one melting and crystallization, this separate study was not conducted.

2.1.1.3 Successive Self-nucleation and Annealing (SSA)

In chapter III, a study of Successive Self-Nucleation and Annealing was performed for the sample sr-PHB. SSA is a thermal fractionation technique designed by Prof. A.J. Müller that is performed using a Differential Scanning Calorimetry (DSC) to study the different molecular segregation capacity that, normally, the semicrystalline polymeric systems exhibit during isothermal crystallization and annealing processes [2] . The many different purposes of the SSA technique are amply shown and described by Perez-Camargo *et al*. [3]. The SSA experiments were carried out following the protocol defined by Müller *et al*. [2,4] and summarized in the graph in Figure 2.1. The first heating scan is the one in which the thermal history of the sample is erased (heating the sample 20 ºC above the melting point and keeping at that temperature for 1 minutes). For this work, during the second step the samples were cooled down to -20 ºC. After 1 min at this temperature, the sample is heated to a temperature of 7.5 °C lower than the end-temperature melting (as a proxy of the ideal self-nucleation temperature) and kept for 1 min at that temperature. Subsequently, the sample was cooled again to -20 ºC and held at this temperature for 1 min. This cyclic process was repeated by varying the T_{si} 10 times, decreasing it at each cycle by 7.5 ºC. Finally, the sample was heated to the molten state (200 ºC in this case) to observe the results of the thermal fractionation.

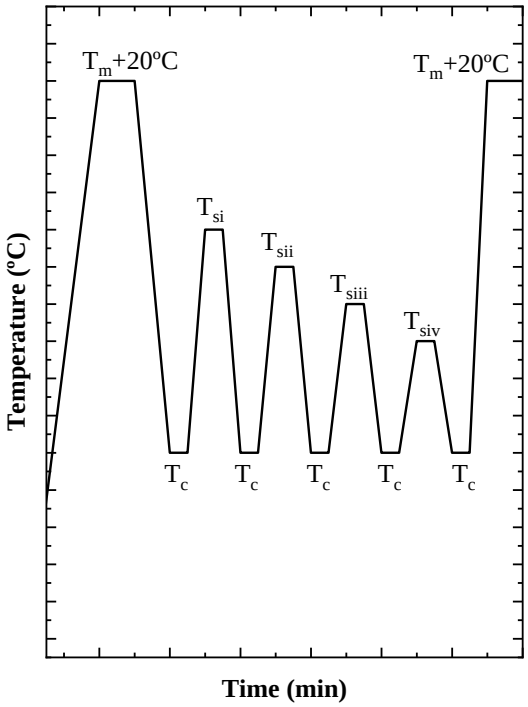

Figure 2.1. Scheme of all the steps necessary to perform the SSA thermal fraction.

2.1.2 Polarized light optical microscopy (PLOM)

This technique uses an optical microscope equipped with two polarizing filters, placed below and above the sample to be analyzed. When the polarizers are crossed, light is allowed to pass only in the orthogonal direction. This means that the light is not transmitted through the polarizers when there is no sample or when the sample has an isotropic disordered structure, as in the case of amorphous polymers or semi-crystalline polymers in the melt. In the case where the polarizers are crossed and a semicrystalline polymer, a birefrigent sample, is to be observed, an interference phenomenon occurs (i.e., the crystals have the ability to reorient the polarization of the light), causing the light beam to pass through the polarizer. In this way, there are areas of the sample, the ordered anisotropic regions, which appear bright on a smooth or dark background, which corresponds to the fraction of amorphous or molten material. Polarized optical

microscopy is, therefore, a suitable technique in the study of ordered regions of semicrystalline polymers.

In this thesis an OLYMPUS BX51 microscope was employed, this microscope has a programmable heating chamber Metter Toledo FP82 HT.

In this equipment two types of experiments were performed, the first one the preliminary morphology of the sample through non-isothermal crystallization experimentsand the second one to obtain the spherulitic growth rate as a function of time. To perform these tests, a thin film of the mixture to be studied was placed on a glass slide.

2.1.2.1 Non-isothermal crystallization and Spherulitic growth rate (G)

To observe the preliminary morphology of the samples, non-isothermal crystallization experiments were carried out by inserting a small amount of sample between two glass slides and applying the same thermal treatment described in paragraph 2.1.1.1.

To calculate the spherulite growth rate (G) as a function of the isothermal crystallization temperature (T_c), the radius of a spherulite as it grew was measured by the following steps:

1. The thermal history of the material is erased by holding at T_f for 3 min.
2. Cooling from T_f to a selected crystallization temperature at 50 ºC min^{-1}.
3. An isolated small spherulite is located. The growth of the spherulite is recorded as a function of time, taking pictures at different times by means of a digital camera.
4. Afterwards, the radius is plotted as a function of time, a straight line is obtained, from the slope of which the growth rate of the spherulite is calculated.
5. These steps are repeated for 10 different T_c.

2.1.3 Thermogravimetric analysis (TGA)

Thermogravymetry is a technique in wich the mass sample is measured as a function of temperature or time. TGA is the most commonly used method to investigate the thermal decomposition processes of polymers. In TGA experiments, at heating rates around 10 ^{o}C min^{-1}, a sample of around 5-15 mg is enough to ensure that it is in thermal equilibrium with the equipment used [5], In the development of this thesis, this technique was used to determine the temperature at which the materials studied begin to decompose, the conditions for this study were the same in all cases, at 10^{o}C min^{-1} from 40^{o}C to 800^{o}C.

2.1.4 Wide and Smallangle X-ray Scattering (WAXS and SAXS)

X-ray diffraction is a physical phenomenon that occurs when an x-ray beam of a certain wavelength interacts with a crystalline material. When the beam is incident on a solid material, part of the beam is scattered in all directions because of the electrons associated with the atoms or ions in the path, but the rest of the beam gives rise to the phenomenon of x-ray diffraction, provided that there is an orderly arrangement of atoms, and Bragg's Law is satisfied. This law relates the wavelength and the interatomic distance to the angle of incidence of the diffracted beam.

In this thesis work, several diffractomers have been used.

X-ray powder diffraction patterns at room temperature were collected by using a Philips X'pert PRO automatic diffractometer operating at 40 kV and 40 mA, in theta-theta configuration, secondary monochromator with Cu-$K\alpha$ radiation (λ = 1.5418 Å) and a PIXcel solid-state detector (active length in 2θ 3.347^{o}). Data were collected from 5^{o} to 50° 2θ (step size = 0.026 and time per step = 60 s) at room temperature.

Furthermore, the X-ray diffraction profiles during the crystallization and melting process were collected following the procedure and conditions of non-isothermal experiments conducted in the DSC equipment. Wide-angle X-ray scattering (WAXS)

experiments were measured at beamline BL11-NCD in the ALBA Synchrotron (Barcelona, Spain). Aluminum pans were employed to place samples in the beam path. A THMS600 Linkam hot stage and a liquid nitrogen cooling device were employed for temperature control and to heat and cool the samples. The X-ray energy source amounted to 12.4 keV. For WAXS, the sample-detector distance was 132.6 mm with a 21.2° tilt angle, and chromium(III) oxide was employed to do the calibration (Rayonix LX255-HS detector, Evanston, IL, USA, with a resolution of 1920 × 5760 pixels and pixel size of 44 μm^2). SAXS experiments were performed during the crystallization and melting of the samples. These experiments were performed at the BL11-NCD beamline in the ALBA Synchrotron in Barcelona (Cerdanyola del Vallés, Spain).

To carry out the heat treatment, the samples were placed in aluminum pans (the same ones used in the DSC), and a Linkam THMS600 hot-stage was used for the controlled crystallization and melting of the materials.

The energy of the X-ray source is 12.4 KeV, corresponding to a wavelength of 1A, and the exposure time is 2s. For the acquisition of the SAXS spectrum, the sample-detector distancewas 6640 mm with a tilt angle of 0º, and a Pilatus 1M as detector, supplied by Dectris with an active area of 981 x 1043 pixels and a pixel size of 172 μm^2. Silver behenate was used for the calibration. The SAXS profiles are plotted as a function of the scattering vector q ($=4\pi \sin(\theta) \lambda^{-1}$, where λ is the X-ray wavelength and 2θ is the scattering vector).

2.1.5 Nuclear Magnetic Resonance (NMR)

Nuclear magnetic resonance is the technique that provides structural information. It is able to observe the nuclei of the atoms and to deduce the influence in each molecular

environment on each of the atoms. In this way it is possible to know the general structure of the molecule to be studied.

The most abundant atoms in polymeric compounds, hydrogen (H) and carbon (C) can be easily observed with relatively small amounts of sample. Therefore, with this technique, it is possible to deduce the chemical structure of the polymeric compounds.

For the characterization of the single-ion conduction polymer, proton and carbon nuclear magnetic resonance (H^1-NMR and C^{13}-NMR) experiments were performed at room temperature in chloroform (CDCl3) using a Bruker AMX spectrometer (400 MHz). In all cases, 5 mg of sample was dosed in 700 µL of solvent.

2.1.6 Rheological Characterization (Performed by Mercedes Fernández, Researcher of Rheology at the University of the Basque Country)

The rheological properties were determined using a strain-controlled ARES-G2 rotational rheometer (TA Instruments). Samples of 1 mm thickness and 25 mm diameter were analyzed in parallel plate geometry. To minimize degradation effects, residual moisture was removed by drying the PHBH pellets overnight under vacuum at T=60 ºC, and rheometer experiments were performed under a nitrogen atmosphere.

Characterization included small amplitude oscillatory shear (SAOS) and continuous flow experiments. Viscoelastic functions such as elastic modulus, G', viscous modulus, G'', and complex viscosity, η*, were measured in the linear viscoelastic regime (strain amplitude below 5 %) in a frequency range from 628 to 0.628 rad/s, at varying temperatures from 130 to 180 ºC. Two consecutive tests were performed at each temperature to check reproducibility, with each test lasting 3 minutes; the error between measurements was less than 4%. The Time-Temperature superposition (TTS) principle was used to shift frequency data into a single master curve at T=190 ºC. Continuous flow

measurements at T=190 ºC were also carried out to test the validity of the Cox-Merz rule[6].

$$\eta^*(\omega) \equiv \eta(\dot{\gamma})\big|_{\omega=\dot{\gamma}} \tag{2.2}$$

where $\eta^*(\omega)$ is the complex viscosity as a function of frequency and $\eta(\dot{\gamma})$ is the viscosity obtained in continuous flow at the corresponding shear rates ($\dot{\gamma}$).

2.1.7 3D Printing of the samples

The PHBH X131A pellets, in the Chapter IV, were dried at 80 °C at least 6 hours. Filaments were prepared by extrusion of dried PHBH pellets at 150 °C at 20 rpm using a FilaFab PRO 350 extruder (FD3D Innovations Limited, UK). The average diameter of the filaments was 1.75 ± 0.03 mm (measured with a digital caliper at several places).[7]

A model of the parts was designed and converted to STL file format for FFF. Then, the PHBH filament was printed using the TUMAKER Voladora V1 FFF machine, provided by Tumaker (Spain), and controlled with the Simplify3D Software (Creative Tools AB). The software was used to generate a G-code and then to set up the different processing conditions used in this study. The maximum printing size of the 3d printer was 22 × 22 × 30 cm (length, width, and height, respectively) with a nozzle diameter of 0.4 mm. In addition, a representative model of the logo of the University of the Basque Country has also been printed to verify the printability of the material.

2.1.8 Printing Conditions

In the Chapter IV, before manufacturing the samples, the filament was placed in an oven at 60 ºC for 12h to eliminate any trace of moisture. To find the most adequate printing conditions, different combinations of variables were used. Nine printing conditions were employed, which are shown in Table 2.1. Three factor levels (low (L), medium (M), and high (H)) and three process conditions (nozzle temperature (ºC), bed

temperature (ºC), and printing velocity (mm/s)) were used in this the study, employing the Taguchi experimental design method. The selected response variables to optimize were the Young modulus, tensile strength, and strain at break.

Table 2.1 Printing conditions explored in this work

Name	Nozzle Temperature (ºC)	Bed Temperature (ºC)	Printing Velocity (mm/s)
L12	180	30	30
L22	180	50	30
M12	190	30	30
M22	190	50	30
M21	190	50	20
M23	190	50	40
H12	200	30	30
H22	200	50	30
M12 [90, 90]	190	30	30

There are few works in the literature that report attempts at additive manufacturing by FFF for neat PHBH, so the levels of each printing parameter were specified based on the processing temperatures values for the materials used by Giubilini *et al*. [8] and Kovalcik *et al*.[7] for the PHBH scaffold preparation. These variables were modified to obtain adequate printing conditions to improve the mechanical properties.

Samples were printed using the eight conditions of Table 2.1 in a rectilinear form 45º/-45º. Once the most adequate condition was determined (M12), specimens were printed in which the layers were all oriented in the same direction (that of the longest axis of the specimen) to mimic patterns obtained by compression molding, as reported by Candal *et al*. [9]. They molded PBS-based materials in this direction, obtaining mechanical parameters similar to those of injection molding. In all the conditions, the layer height and the fill density were 0.3 mm and 100%, respectively. Five specimens for each condition were printed.

In this work, two different types of shapes were printed. The first ones were dog bone specimens (Type IV) with a flat-on configuration which were subsequently used to perform tensile tests (see Figure 2.2, left). The second type of specimen was a kind of tower in upright orientation (0.9x0.6x0.3 mm) to study the thermal properties of the different layers (Figure 2.2, right).

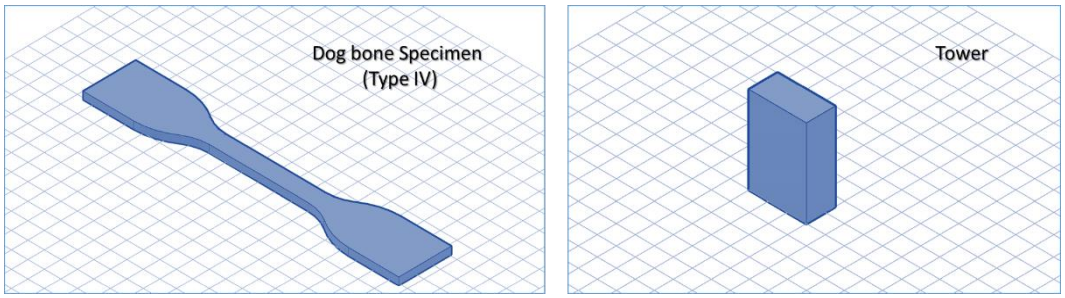

Figure 2.2. Parts/orientation printed in this work.

2.1.9 Pressure–Volume–Temperature (PVT) measurements (Performed by Mercedes Fernández, Researcher of Rheology at the University of the Basque Country)

PVT measurements were carried out in the Chapter IV using a PVT apparatus of the piston die type, PVT100, made by Haake. The sample was contained in a floating measurement cylinder (8 mm diameter), and pressure was applied hydraulically to a

piston at the top of the cell with a PTFE disc seal. An identical piston and sealing system were located at the bottom of the cell. The data were obtained using an isobaric cooling mode procedure in a pressure range from 200 to 1000 bar with a cooling rate of 5 ºC min^{-1}, and the temperature range from 200 ºC to 0 ºC was controlled by using liquid nitrogen. The results at a pressure of 1 bar were obtained by extrapolation to the Tait model included in the software[10].

The following equations give the 2-domain Tait PVT equation

$$v(T,P) = v_0\left[1 - C\ln\left(1 + \frac{P}{B(t)}\right)\right] + v_t(T,P) \quad (2.3)$$

where for polymers in the molten state, above the liquid-solid transition temperature:

$$v_0 = b_{1m} + b_{2m}(T - b_5) \quad (2.4)$$

$$B(T) = b_{3m}exp[-b_{4m}(T - b_5)] \quad (2.5)$$

$$v_t(T,P) = 0 \quad (2.6)$$

and for polymers in the solid state, below the liquid-solid transition temperature:

$$v_0 = b_{1s} + b_{2s}(T - b_5) \quad (2.7)$$

$$B(T) = b_{3s}exp[-b_{4s}(T - b_5)] \quad (2.8)$$

$$v_t(T,P) = b_7\ exp\{[b_8(T - b_5)] - (b_9P)\} \quad (2.9)$$

The liquid-solid transition temperature, which is the glass transition temperature for amorphous polymers and the melting or crystallization temperature for semicrystalline polymers, is calculated by:

$$T_t(P) = b_5 + b_6P \quad (2.10)$$

In these equations, v is the specific volume, the coefficient C is a constant equal to 0.0894, B is the sensitivity to pressure of the material, b_{1m} and $b_{1s}$to b_{4s} describe the dependence on pressure and temperature in the molten and solid state, respectively. b_5 and b_6 are parameters that describe the change of transition temperature with pressure, b_7 to b_9 are particular parameters of semicrystalline polymers that describe the form of the state transition.

2.1.10 Compression Molding

In the Chapter IV, PHBH Specimens of the same size as those of Type IV (dogbone specimens for tensile tests) obtained by 3D printing were produced by compression molding. The equipment used for the hot-pressing process was a Collin P200E hydraulic press (Ebersberg, Baviera, Germany). A certain amount of material was placed in a mold and between the plates of a press at 170 ºC and 200 bar. Preheating without pressure (2 min), compression under pression (3 min) and cooling under pressure (6 min) were carried out to produce the specimens.

2.1.11 Tensile Tests

To perform tensile tests in the Chapters III and IV, an INSTRON 5569 testing machine was used. This test was performed for all the 3D printed patterns and for the specimens obtained by compression molding in che Chapter IV and for *sr*-PHB and *R*-PHB in the Chapter III . The tests were performed according to ASTM D638 guidelines[11]. Young's modulus, tensile strength, and tensile strain at break were measured using 20 mm/min as cross-head speed and 65 mm as the distance between grips. This analysis compares the mechanical properties of the 3D printed samples with those obtained by compression molding.

2.1.12 Cross-section morphology

To observe the cross-section of the samples obtained by 3D printing in the Chapter X, SEM analysis was conducted with a HITACHI TM3030Plus Tabletop Scanning Electron Microscope (SEM) at 15 kV. Before the observation, all the samples were cryogenically fractured in liquid nitrogen and gold-coated in an SC7620 Mini Sputter Coater (Quorum). The images of the specimens were captured with a digital camera with a resolution of 25 nm. For comparative purposes, the samples obtained by compression molding were also observed.

2.1.13 Heat Transfer Simulation (Performed by Robert Hernandez, Researcher at the University of the Basque Country)

In the Chapter IV, temperature profiles were simulated in two dimensions, solving the heat transfer equation described in (2.11) using the heat transfer module of COMSOL Multiphysics 5.6 software.

$$\rho c_p \frac{\partial T}{\partial t} - \nabla \cdot (k\nabla T) = Q \qquad (2.11)$$

where ρ is the material density, c_p is the heat capacity, and k is the thermal conductivity, respectively. The calculations were conducted for PHBH using experimentally determined parameters summarized in Table 2.2.

Density. Density measurements were performed using an electronic densitometer (Mirage SD-120 L), and n-butanol was used as the immersion liquid. Six impact specimens were weighed for each reported value, and the immersion liquid temperature was determined (with 0.1ºC precision). The measured value is 1.21648 g/cm^3.

Thermal conductivity: The measurement of thermal conductivity was carried out with the aid of the Gottfert Rheograph 25 instrument, following the ASTM D5930 standard, in a cooling and heating process in the temperature range between 30 ºC and

190 ºC. This value is 0.170 W/m*K for low temperatures and 0.198 W/m*K for high temperatures.

Thermal capacity: The measurement of the thermal capacity was carried out with a DSC Q2000, supplied by TA instruments, calibrated with sapphire and indium. The thermal capacity was measured during cooling in the temperature range between 50 / 30 ºC and 200 / 180 ºC.

The following boundary conditions were established: room temperature: 25 ºC, platform temperature: 30 ºC, printing temperature: 190 ºC. Extra layers were added manually to analyze the effect of the number of deposited layers.

Table 2.2: List of parameters of PHBH used in the simulation

Parameter	**Description**
Density (□□□in kg/m^3	1216
Heat capacity (c_p) in J/(kg·°C)	$c_p(T)=-0.033T^2 + 14.277T + 912.36$
Thermal conductivity (k) in W/(m·°C)	$k(T) = 0.0002T + 0.1294$ (30 °C <T< 95 °C)
	$k(T)= 0.0013T + 0.0262$ (95 °C <T< 105 °C)
	$k(T) = 0.000Tx + 0.132$ (105 °C<T< 105 °C)

2.1.14 Size exclusion chromatography (SEC) (Performed by Bo Li, in the research group of Prof. Andrew Dove at the University of Birmingham)

Columns in series with refractive index (RI) detection (Agilent 390-MDS on PLgel Mixed-D type) were used to perform size exclusion chromatography (SEC). To

calculate the weights, a calibration curve was used. The standard used to create the calibration curve was poly(styrene) with chloroform (0.5% NEt3) as eluent flowing at 1.0 $mL.min^{-1}$ and sample concentration 3 mg mL^{-1}.

2.1.15 Preparation and characterization of single crystals (Performed by Anna Malafronte in the research group of Prof. Claudio De Rosa at the University of Naples, Federico II)

In the Chapter VI, a 0.012 wt% solution of the sample PHL 66 in 1-hexanol was prepared by dissolving the polymer (0.3 mg) into 3 mL of solvent. The solution was placed at 85 °C and maintained at this temperature for 1 h to completely dissolve the polymer. The solution was then slowly cooled to 50 °C (estimated cooling rate ≈ 1.2 °C min^{-1}) and left at this temperature for 21 h to allow crystallization. Afterward, the solution was slowly cooled down to room temperature (estimated cooling rate lower than 1 °C min^{-1}). Drops of crystal suspension were placed on carbon-coated grids and left to dry before transmission electron microscopy (TEM) analysis.

2.1.16 Transmission Electron Microscopy (TEM)

TEM analysis was conducted to observe the morphology at the lamellar level. A RuO_4 solution was used for staining PHL films of roughly 1 mm thickness fo 16 h. After, ultra-thin sections were cut at -90ºC with a diamond knife with a Leica EMFC6 ultra-cryo-microtome device. The ultra-thin thick sections have been placed on 200 mesh copper grids and examined with the aid of a TECNAI G2 20 TWIN TEM (LaB_6 as operating filament and 120 kV as accelerating voltage).

2.1.17 Optical Property Measurements (Performed in the research group of Prof. Eugene Chen at the University of Colorado State)

A Cary 5000 UV-vis NIR spectrophotometer from Agilent was used to measure the optical properties of thin films in Chapter III that were acquired by solvent casting from a suitable solvent. The films were cast in circular polypropylene petri dishes with a diameter of 4 in. Film thickness was measured to be 0.02 +/- 0.01 mm. Films were acquired by solvent casting from an appropriate solvent which was allowed to evaporate overnight, covered by a crystallization dish to allow for slow evaporation, before testing.

2.1.18 Barrier Property Measurements (Performed in the research group of Prof. Eugene Chen at the University of Colorado State)

Water vapor transmission rate was determined employing the gravimetric method according to ASTM E96-95 at 25 °C. The permeation cell employed is made of polytetrafluoroethylene and is partially filled with water. The membrane is placed in the top and it is fixed with the other part of the cell. The weight change is measured with a Sartorius BP 210 D balance with 10^{-5} g readability and the data is recorded for further data treatment. The values shown are, at least, the average value of three films.

Oxygen permeability was measured in a Mocon OX-TRAN 2/21 MH instrument at 1 atm, 23 °C and 0 % relative humidity (RH). The surface area exposed to oxygen is 5 cm^2. At least two films were measured for each reported value.

2.2 Materials and Methodologies

2.2.1 Materials studied in Chapter III

Five different PHBs were used in this study: a bacterial PHB (denoted herein as *R*-PHB) obtained commercially in white powder form (without any additives), supplied by Sigma-Aldrich, and four laboratory synthesized PHBs (denoted as *R/S*-PHB in view

of their 50/50 racemic mixture characteristics) prepared following the recently reported ROP eight-membered cyclic dimer of 3-hydroxybutyrate, or eight-membered dimethyl diolide,[12,13]. The values of molecular weight and the dispersity for all the samples used in this work are reported in Table 1. The different synthetic PHBs are named based on their closest M_n value.

2.2.2 Materials studied in Chapter IV

A commercial thermoplastic biodegradable grade of poly(hydroxybutyrate-co-hydoxyhexanoate) with 6% hexanoate, PHBH, in pellets was employed. The PHBH denoted Green Planet™ X131A with a density of 1.2 g cm^{-1} and purchased from Kaneka Corporation (KITA-KU Osaka, Japan) was used. In a previous study by our group[14], properties such as molecular weight (M_n number-average and M_w weight-average), polydispersity (Đ), and melt volume rates were determined, and they are reported in Table 2.3.

Table 2.3. Molecular weight (number-average and weight-average, polydispersity, melt volume rate, and melt flow index of PHBH (data taken from ref. [14]).

M_n (kDa)	M_w (kDa)	Đ	MVR (cm^3 10 min^{-1})	MFI (g 10 min^{-1})
121	163	1.35	18.3	2 (at 165 ºC, 5 kg)

2.2.3 Materials studied in Chapter V

2.2.3.1 Standard Copolymerization Methodology

Polymerizations to produce the two copolymer samples were performed in our previous work,[37] and in 100 mL glass reactors inside an inert glovebox at room temperature (~ 23 °C). The reactor was filled with a predetermined quantity of monomers (mixture of racemic eight-membered dimethyldiolide, *rac*-8DL^{Me}, with ε-caprolactone,

ε-CL) and dichloromethane (DCM) in a glovebox, and the mixture of catalyst and initiator in DCM was stirred at room temperature for 10 min in another 5.5 mL reactor. The polymerization was initiated by rapidly adding the catalyst solution to the monomer solution. Once the desired duration elapsed, the polymerization process was promptly quenched by introducing 5 mL of benzoic acid/ chloroform (10 mg/mL). Subsequently, 0.02 mL sample was extracted from the reaction mixture and processed for ^{1}H NMR analysis to determine the percentage of monomer conversion. After the quench, the mixture was poured into 300 mL of cold methanol under constant stirring. The precipitate was then filtered, washed with cold methanol to eliminate any remaining unreacted monomers, and finally, in tas dried at room temperture in a vacuum oven until a constant weight was achieved.. More details and the scheme of reactions are given in Figure 2.3.

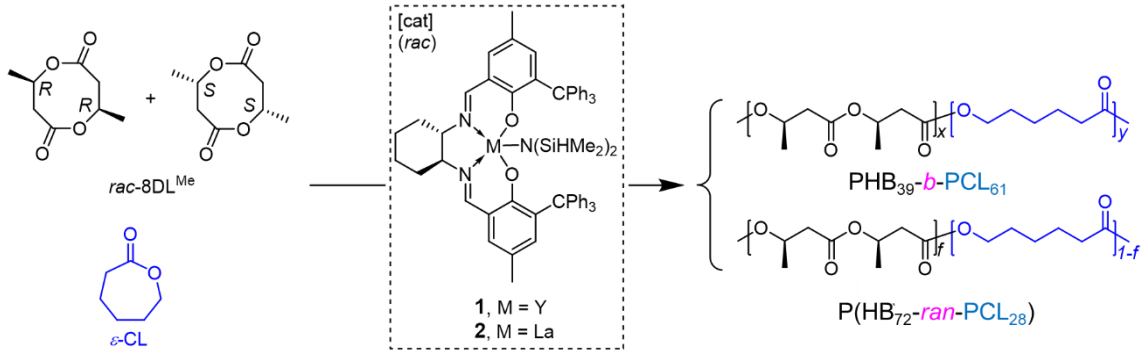

Figure 2.3. Scheme of reactions.

1. Block copolymer PHB_{39}-*b*-PCL_{61}

rac-DL^{Me} = 4.132 g (24 mmol), ε-CL = 1.370 g (12 mmol), Cat **2** (La-trityl) = 51 mg (45 µmol), BnOH = 4.87 mg (45 µmol), DCM = 36 mL, time = 24 h

(Conditions: *rac*-DL^{Me}/ ε-CL = 2/1, [*rac*-DL^{Me} + ε-CL]/[**2**]/[BnOH] = 800/1/1, 24 h)

2. Random copolymer $P(HB_{72}$-*ran*-$CL_{28})$

rac-DL^{Me} = 5.165 g (30 mmol), ε-CL = 34.242 g (300 mmol), Cat **1** (Y-trityl) = 162 mg (150 µmol), BnOH = 16.2 mg (150 µmol), DCM = 30 mL, time = 25 min

(Conditions: *rac*-DL^{Me}/ ε-CL = 1/10, [*rac*-DL^{Me}]/[**1**]/[BnOH] = 200/1/1, 25 min)

2.2.3.2 Materials for comparison purposes

For comparison purposes, homopolymer PCL and PHB samples with similar molecular weights to the prepared copolymers were used. The PCL sample was synthesized according to the procedure reported by Fernández *et al.*,[48] and PHB was obtained according to Tang *et al*.[28,49] Data for these two comparative samples were obtained by Fernández *et al.*[48] for the PCL and by Caputo *et al*.[29] for the PHB (one of those used in Chapter 3).

Table 2.4. Molecular weight and dispersity values of the reference homopolymers and the two copolymers studied in this chapter

Sample	M_n **(g/mol)***	$Đ$
R/S-PHB 38K	38000*	1.07
PCL-22K	22100[#]	1.60
PHB_{39}-*b*-PCL_{61}	36000*	1.01
$P(HB_{72}$-*ran*-$CL_{28})$	75000*	1.05

*measured by size-exclusion chromatography (SEC), as described by Tang *et al*.[49]

[#] measured by SEC, as described by Fernández *et al.*[48]

2.2.4 Materials studied in Chapter VI

Solvents and reagents used in this chapter have been provided by Sigma Aldrich, Acros, Fluka, Fisher Chemical, Alfa Aesar, or VWR. Dry solvents were purified using

the MBRAUN SPS solvent purification system. Before proceeding with the vacuum distillation, the η-Heptalactone monomer was dried for 24 hours over calcium hydride.

2.2.4.1 Synthesis of η-Heptalactone

Since η-heptalactone is not available in the market, it was synthesized through the Baeyer-Villiger oxidation method according to previously reported literature[15]. Briefly, the cycloheptanone and *m*-chloroperbenzoic acid (1.2 eq.) were mixed in CH_2Cl_2. The as obtained suspension was heated for three days under reflux. An ice bath was used to cool the reaction, and Celite was used to filtrer the solids. The filtrate was washed twice with CH_2Cl_2 and twice with 10% $Na_2S_2O_3$ solution, twice saturated with Na_2CO_3 solution, and once with brine solution. The organic layers were recollected, dried over $MgSO_4$, filtered, and evaporated under reduced pressure. To reach the 70% yield of the final product, the resulting liquid was distilled over CaH_2.

^{1}H NMR (400 MHz, 298 K, $CDCl_3$): δ = 4.28 (t, 2H, C*H*$_2$O), 2.48 (t, 2H, C*H*$_2$C=OO), 1.75 (m, 4H, C*H*$_2$), 1.52 (m, 4H, C*H*$_2$) ppm. ^{13}C NMR (125 MHz, 298 K, $CDCl_3$): δ = 176.4 (O*C*OCH$_2$), 64.3 (OCO*C*H$_2$), 31.0 (*C*H$_2$COO), 30.5 (OCH$_2$*C*H$_2$), 28.0 (*C*H$_2$CH$_2$COO), 25.4 (*C*H$_2$CH$_2$ CH$_2$COO) and 23.5 (OCH$_2$CH$_3$*C*H$_2$) ppm.

2.2.4.2 Synthesis of poly(η-heptalactone)

Four different homopolymers of polyheptalactone (PHL) with different molecular weights were prepared in this study. Briefly, in a glove box, solutions of diphenylphosphate (1 eq) in dry toluene and dual-head CTA (1 eq.) in dry toluene were added to η-heptalactone (100 eq). The solution was stirred at room temperature and removed from the glove box, precipitated three times into ice-cold methanol, and collected by centrifugation. It should be noted that the polymers must have no evidence of high or low molecular weight shoulders by SEC before proceeding with RAFT polymerizations and self-assembly. ^{1}H NMR (400 MHz, $CDCl_3$) δ/ppm: 4.04-4.11 (t,

C*H*$_2$OH), 3.63 (m, C(CN)C*H*$_2$CH$_2$), 3.33 (q, SC*H*$_2$CH$_3$), 2.28 (t, OCOC*H*$_2$), 1.61-1.35 (m, OCOCH$_2$(C*H*$_2$)$_3$CH$_2$OH).

2.3 References

1. Lorenzo, A.T.; Arnal, M.L.; Albuerne, J.; Müller, A.J. DSC Isothermal Polymer Crystallization Kinetics Measurements and the Use of the Avrami Equation to Fit the Data: Guidelines to Avoid Common Problems. *Polym. Test.* **2007**, *26*, 222–231, doi:10.1016/j.polymertesting.2006.10.005.
2. Müller, A.J.; Michell, R.M.; Pérez, R.A.; Lorenzo, A.T. Successive Self-Nucleation and Annealing (SSA): Correct Design of Thermal Protocol and Applications. *Eur. Polym. J.* **2015**, *65*, 132–154, doi:10.1016/J.EURPOLYMJ.2015.01.015.
3. Pérez-Camargo, R.A.; Cavallo, D.; Müller, A.J. Recent Applications of the Successive Self-Nucleation and Annealing Thermal Fractionation Technique. *Front. Soft Matter* **2022**, *2*, doi:10.3389/FRSFM.2022.1003500.
4. Müller, A.J.; Arnal, M.L. Thermal Fractionation of Polymers. *Prog. Polym. Sci.* **2005**, *30*, 559–603, doi:10.1016/J.PROGPOLYMSCI.2005.03.001.
5. Witkowski, A.; Stec, A.A.; Hull, T.R. Thermal Decomposition of Polymeric Materials. *SFPE Handb. fire Prot. Eng.* **2016**, 167–254.
6. Cox, W, Mertz, E. Correlation of Dynamic and Steady Flow Viscosities. *J. Polym. Sci., 28*, 619–622, doi:http://dx.doi.org/10.1002/pol.1958.120281181253.
7. Kovalcik, A.; Smilek, J.; Machovsky, M.; Kalina, M.; Enev, V.; Dugova, H.; Cernekova, N.; Kovacova, M.; Spitalsky, Z. Properties and Structure of Poly (3-Hydroxybutyrate-Co-4-Hydroxybutyrate) Filaments for Fused Deposition Modelling. *Int. J. Biol. Macromol.* **2021**, *183*, 880–889, doi:https://doi.org/10.1016/j.ijbiomac.2021.04.183.
8. Giubilini, A.; Siqueira, G.; Clemens, F.J.; Sciancalepore, C.; Messori, M.; Nyström, G.; Bondioli, F. 3D-Printing Nanocellulose-Poly(3-Hydroxybutyrate-Co-3-Hydroxyhexanoate) Biodegradable Composites by Fused Deposition Modeling. *ACS Sustain. Chem. Eng.* **2020**, *8*, 10292–10302, doi:10.1021/acssuschemeng.0c03385.
9. Candal, M.V.; Calafel, I.; Aranburu, N.; Fernández, M.; Gerrica-Echevarria, G.; Santamaría, A.; Müller, A.J. Thermo-Rheological Effects on Successful 3D Printing of Biodegradable Polyesters. *Addit. Manuf.* **2020**, *36*, 101408, doi:10.1016/j.addma.2020.101408.

10. Wang, J.; Hopmann, C.; Schmitz, M.; Hohlweck, T.; Wipperfürth, J. Modeling of PvT Behavior of Semi-Crystalline Polymer Based on the Two-Domain Tait Equation of State for Injection Molding. *Mater. Des.* **2019**, *183*, 108149, doi:https://doi.org/10.1016/j.matdes.2019.108149.
11. ASTM Standard Test Method for Tensile Properties of Plastics (ASTM D638-14) 2014.
12. Tang, X.; Chen, E.Y.X. Chemical Synthesis of Perfectly Isotactic and High Melting Bacterial Poly(3-Hydroxybutyrate) from Bio-Sourced Racemic Cyclic Diolide. *Nat. Commun. 2018 91* **2018**, *9*, 1–11, doi:10.1038/s41467-018-04734-3.
13. Tang, X.; Westlie, A.H.; Watson, E.M.; Y-X Chen, E. *Stereosequenced Crystalline Polyhydroxyalkanoates from Diastereomeric Monomer Mixtures*;
14. Kovalcik, A.; Sangroniz, L.; Kalina, M.; Skopalova, K.; Humpolíček, P.; Omastova, M.; Mundigler, N.; Müller, A.J. Properties of Scaffolds Prepared by Fused Deposition Modeling of Poly(Hydroxyalkanoates). *Int. J. Biol. Macromol.* **2020**, *161*, 364–376, doi:10.1016/j.ijbiomac.2020.06.022.
15. Van Der Mee, L.; Helmich, F.; De Bruijn, R.; Vekemans, J.A.J.M.; Palmans, A.R.A.; Meijer, E.W. Investigation of Lipase-Catalyzed Ring-Opening Polymerizations of Lactones with Various Ring Sizes: Kinetic Evaluation. *Macromolecules* **2006**, *39*, 5021–5027, doi:10.1021/ma060668j.

Chapter III

3. Effect of chain stereoconfiguration on poly(3-hydroxybutyrate) crystallization kinetics

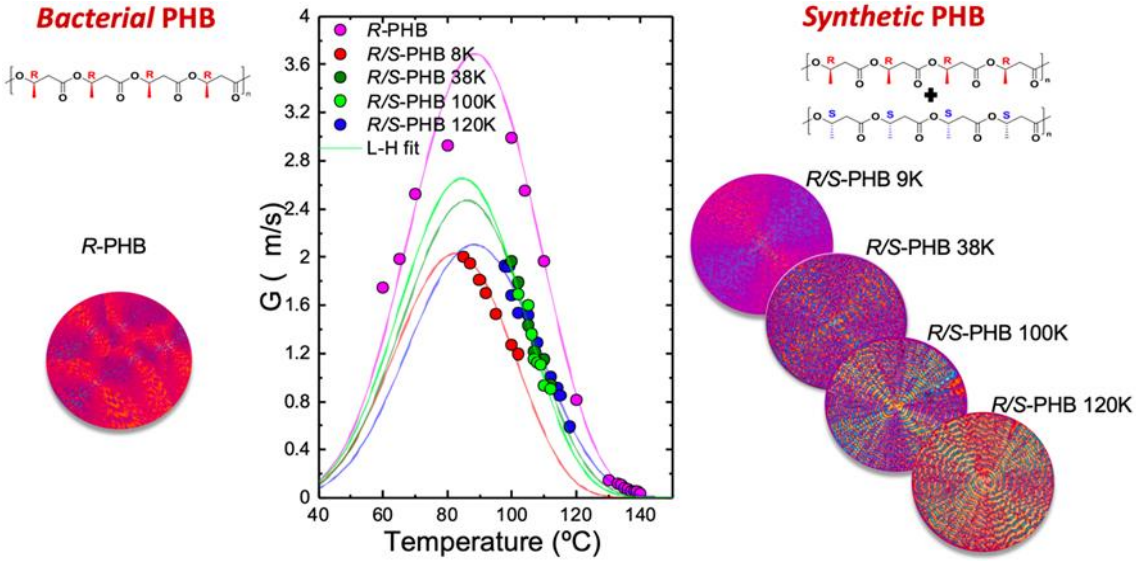

3.1 Abstract

Poly(3-hydroxybutyrate) (PHB) is naturally accumulated by bacteria but can also be synthesized chemically. Its processability is limited as it tends to degrade at temperatures above its melting temperature; hence, investigation into crystallization kinetics and morphology of PHB materials of both natural and synthetic origins is of great need and interest to get a better understanding of structure-property relationship. Accordingly, this contribution reports a first study of the crystallization and morphology of synthetic PHB materials of different molecular weights. These synthetic PHBs are racemic mixtures (50/50 mol%) of *R* and *S* chain configurations and are compared with an enantiopure bacterial *R*-PHB. Non-isothermal and isothermal crystallization studies show that *R* and *S* chains of PHB can co-crystallize in the same unit cell as the *R*-PHB. Most significantly, the results show that the presence of *S* chains decreases the overall crystallization rate, which could enhance the processability and industrialization of PHB-based materials. Furthermore, a preliminary study on a PHB sample in which stereodefects have been introduced in a controlled manner is conducted to evaluate possible variations in the thermal, mechanical, optical and barrier properties.

Caputo, M. R., Tang, X., Westlie, A. H., Sardon, H., Chen, E. Y. X., & Müller, A. J. (2022). Effect of chain stereoconfiguration on poly (3-hydroxybutyrate) crystallization kinetics. *Biomacromolecules*, *23*(9), 3847-3859.

3.2 Introduction

Over the past few decades, the massive use of petroleum-based plastics, polyolefins, in particular, has led to an increase in problems related to their disposal. Recycling these materials to obtain value-added products [1–6] has been one of the main solutions implemented to manage the environmental problem associated with plastic disposal. Additionally, major R&D efforts are directed at developing biobased and biodegradable polymers that are characterized by an intrinsically lower environmental impact. [7],[8]

In this context, biobased polyesters, particularly polyhydroxyalkanoates (PHAs), are more environmentally benign, sustainable plastics. PHAs were discovered by Leimogne in 1925, in the form of poly(3-hydroxybutyrate) (PHB) in a bacterium called *Bacillus megaterium*, [9]. Natural PHAs are produced by various microorganisms that can store them in their cytoplasm as a source of energy. [10],[11] Bacteria can store PHAs as granules in large amounts: the amount of polyesters reaches up to 90% by weight of the dry cells. The most important aspect of this class of materials is that PHAs are 100% of biological origin and can degrade under different environmental conditions. [12] These features make PHAs fall into the group of materials that can be defined as both ‘‘biobased’’ *and* ‘‘biodegradable’’, according to the ASTM D6866 and ASTM D6400.

From a chemical point of view, bacterial PHAs are optically active polyesters [12],[13] due to their absolute (*R*) main-chain chirality, and their general structure is given in Scheme 1.1

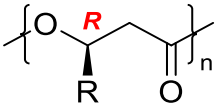

Scheme 3.1 General structure of PHAs.

The pendant group R can have different configurations with respect to the main-chain backbone, leading to different stereochemically defined PHAs with different properties. The most studied is PHB, the simplest yet most important member of the large PHA family; the purely isotactic PHB is a polymer whose thermal properties are comparable to those of isotactic polypropylene. As other PHAs, the bacterial PHB is enantiomerically pure, with stereocenters being *R* configuration only, and its structure is represented in Scheme 3.2.

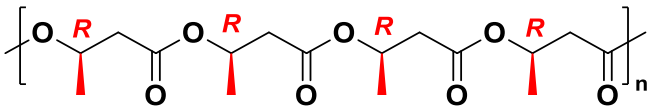

Scheme 3.2 Structure of poly[(*R*)-3-hydroxybutyrate] (*R*-PHB).

PHB has good resistance to moisture, excellent barrier to gas, insolubility in water, and also some resistance to hydrolytic degradation and ultra-violet rays, [12],[14],[15]. However, it also has several drawbacks: it is brittle and suffers from thermal decomposition at temperatures just above its melting temperature (T_m). These problems can be solved, in part, by producing blends with other polyesters or by copolymerizing it with suitable comonomers, [16]. Owing to these drawbacks, PHB has not been widely employed industrially, as it is difficult to process and mechanically brittle. Additionally, its biosynthesis (by bacteria) is slow, as it is the process of extracting it from bacteria. As a result, its cost is high in comparison with commodity plastics. Furthermore, as biosynthesis is a polycondensation process in nature, it is difficult to control the resulting PHB molecular weight and dispersity. For these reasons, developing the chemical synthesis of PHA homopolymers and copolymers with controlled molecular weight and low dispersity values as well as diverse stereomicrostructures is highly desirable.

Two main synthetic routes have been developed, both based on the ring-opening polymerization (ROP) of cyclic esters. The four-membered ring *rac*-β-butyrolactone (β-BL) can be polymerized to iso-enriched, syndiotactic, or atactic P3HB, depending on the catalyst employed,[17]. Early organometallic catalyzed ROP of *rac*-β-BL by alkylaluminum species yielded mixtures of P3HB that could be fractionated into soluble atactic and insoluble isotactic fractions.[18–25] These catalysts were often sluggish, and the low activity did not yield high molecular weight P3HB. Employment of discrete chromium salophen species in ROP of *rac*-β-BL showed much higher activity and allowed for the production of higher molecular weight P3HB but with broad dispersity ($Đ \geq 5.2$) and reasonable isoselectivity (P_m up to 0.66).[26] A discrete diiminate zinc alkoxide initiator was found to have very high activity resulting in controlled and high molecular weight with narrow dispersity, but atactic P3HB. [27] The ROP of *rac*-β-BL with discrete yttrium complexes supported by tetradentate, dianionic alkyoxy-amino-bis(phenolate) ligands results in high activity, controlled reactivity, and high syndioselectivity.[28–30] Recently, a new route based on the ROP eight-membered cyclic dimer of 3-hydroxybutyrate, or eight-membered dimethyl diolide ($8DL^{Me}$) with two stereogenic centers, has been developed for the living synthesis of perfectly isotactic, syndiotactic, or stereodiblock P3HB materials [31],[32]. The use of discrete yttrium amido complexes supported by salcy ligands results was found to be highly stereoselective and highly active – 100% conv. in < 10 min to high molecular weight and narrow dispersity (M_n = 154 kg mol^{-1}, $Đ$ =1.01) polymer.[32] The isotactic polymer produced by the ROP of *rac*-$8DL^{Me}$ was different than the biological PHB as the resulting PHB is a racemic mixture of chains with 50% *R* configuration and 50% *S* configuration represented in Scheme 3.3 below.

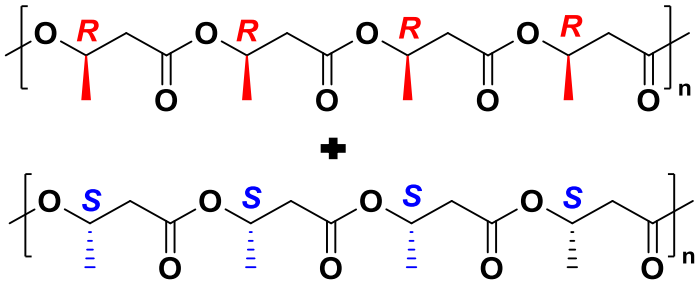

Scheme 3.3 Schematic structure of synthetic racemic, isotactic PHB consisting of *R* and *S* chains in a 50/50 composition.

The crystallization kinetics of these novel 50/50 *R/S*-PHB materials have never been investigated and compared to the microbially-derived *R*-PHB. To study the crystallization, morphology, and thermal properties of the synthetic *R/S*-PHBs (with different molecular weights), a comparative study with a commercial bacterial *R*-PHB has been performed for the first time. Although the crystalline structures of *R/S*-PHB and *R*-PHB are shown to be the same, the racemic mixture with both enantiomeric chain configurations is found to slow down the primary nucleation and the growth of the chain ensemble during crystallization in comparison with *R*-PHB chains.

3.3 Results and Discussion

The five PHBs samples involved in this work were investigated by ^{1}H nuclear magnetic resonance spectroscopy (NMR), thermal gravimetric analysis (TGA), differential scanning calorimetry (DSC), polarized light optical microscope (PLOM), and wide-angle X-ray scattering (WAXS).

3.3.1 NMR and TGA Results

Comparing the ^{1}H NMR spectra of the bacterial and synthetic PHBs (Fig. 3.1) showed no detectable differences in stereochemistry, as expected due to the high

stereoregularity of these PHBs. Likewise, degradation profiles of these five PHBs revealed by TGA (Fig. 3.2) were similar, showing no weight loss below 200 °C. To avoid problems of possible sample degradation, temperatures higher than 190 ºC were never used in all the analyses carried out in this study.

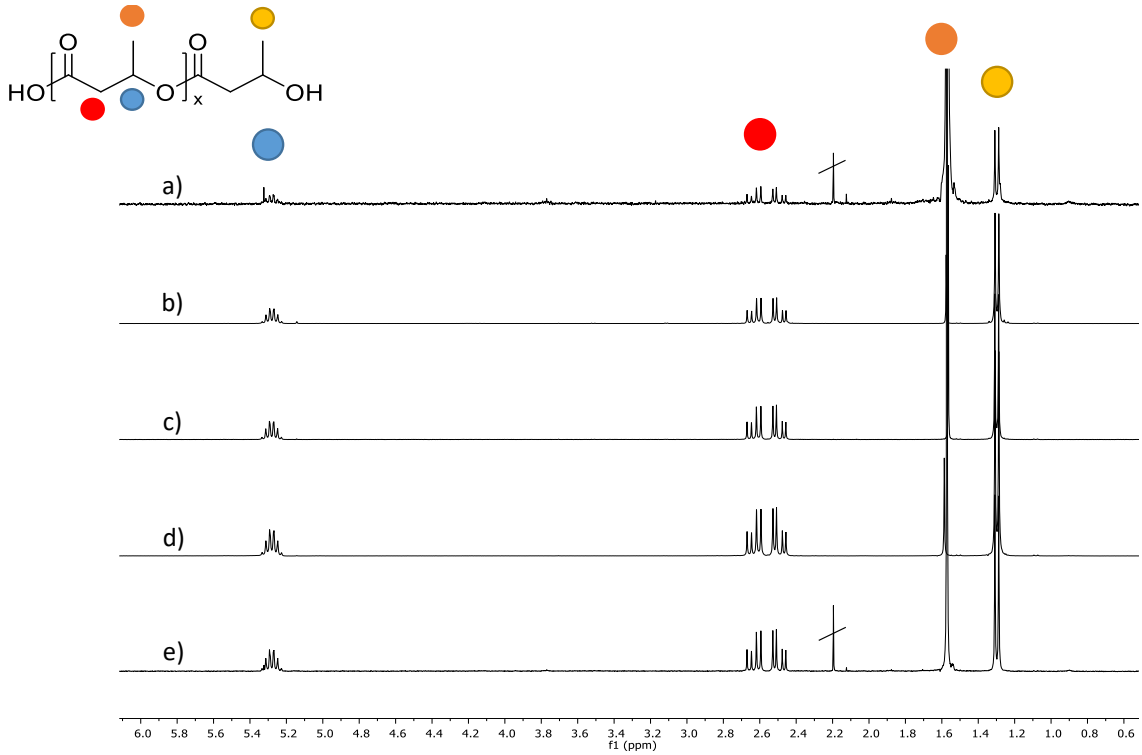

Figure 3.1 ^{1}H NMR spectroscopy in $CDCl_3$ of Bacterial *R* (a) and Synthetic *R/S*-PHBs, 8K (b) 38K (c), 100K (d), 120K (e).

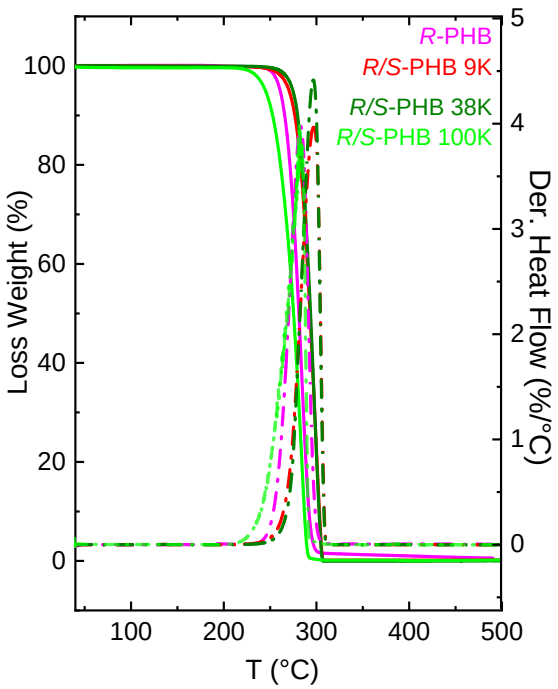

Figure 3.2. Loss Weight (%) and Derivate of Heat Flow (%/°C) as function of the temperature (°C) for Bacterial *R* and Synthetic *R/S* PHBs.

3.3.2 Non-isothermal DSC

The results of the non-isothermal characterization are shown in Figure 3.3. The samples belonging to *R/S*-PHBs (denoted as a function of their molecular weight as 9K, 38K, 100K, and 120K) showed no substantial differences during cooling compared to bacterial *R*-PHB 240K, with the exception of *R/S*-PHB 120K, which had a lower peak crystallization temperature (T_c) and a smaller and broader crystallization exotherm. In fact, during the cooling scan in Figure 3.3a, the *R/S*-PHB 120K sample did not crystallize to saturation, and during the second heating scan, cold crystallization was observed (See Figure 3.3b).

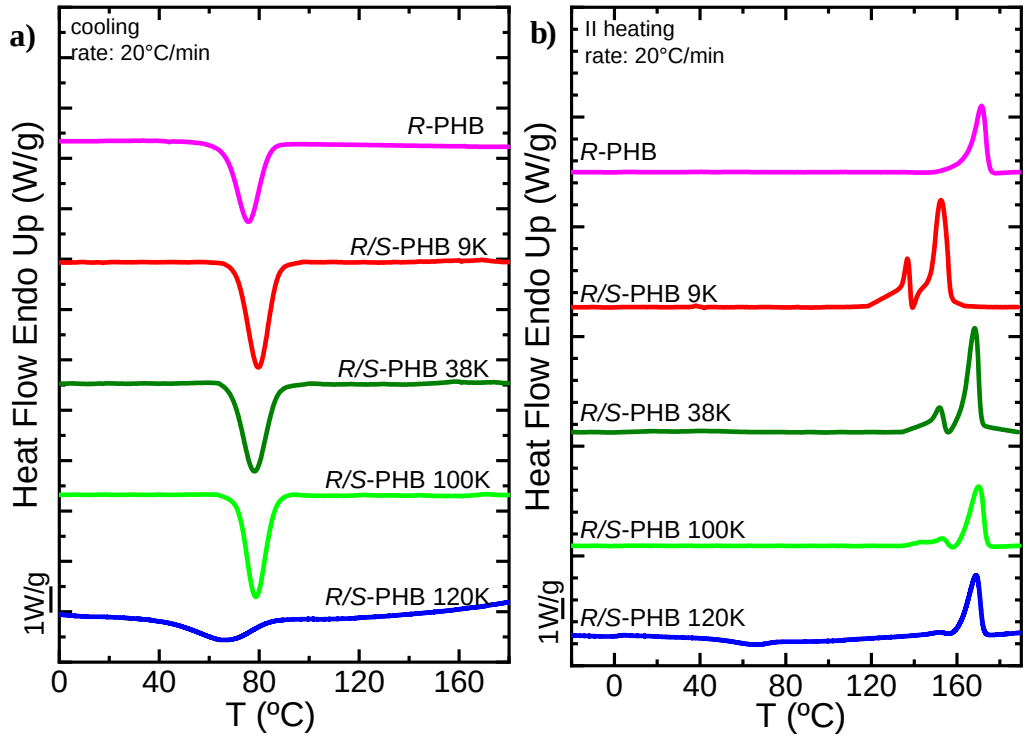

Figure 3.3. a) DSC cooling scans at 20 ºC/min and b) subsequent DSC heating scans at 20 ºC/min for bacterial *R* and synthetic *R/S*-PHBs.

Figure 3.4a represents the T_c and the x_c values extracted from the non-isothermal DSC scan and plotted as a function of molecular weight. The degree of crystallinity was calculated from the DSC cooling scan as reported in the equation 2.1.

The T_c values during cooling from the melt are influenced by the non-isothermal crystallization kinetics and by the nucleating influence of heterogeneities. As the same synthetic methods and reagents were employed, we assumed the nucleating influence of heterogeneities is constant, at least within the *R/S*-PHB synthetic samples. The trend is similar for both parameters in the case of the *R/S*-PHBs as both the degree of crystallinity and the T_c decreases as a function of molecular weight. Therefore, the lowest values of both the T_c and degree of crystallinity were found in the *R/S*-PHB with the highest molecular weight prepared (i.e., 120 kg/mol). The highest molecular weight *R/S*-PHB chains require more time to crystallize during cooling from the melt at 20 ºC/min (as their

diffusion may be limited due to a higher entanglement density and thus higher melt viscosity).

On the other hand, the bacterial *R*-PHB 240K, even though it has a higher molecular weight than the *R/S*-PHB 120K sample, showed relatively high T_c and x_c values (Figure 3.4a) and no significant cold crystallization during the second heating scan (Figure 3.3b). This strikingly different behavior is attributed to the sample's enantiomeric purity, which has an all *R* chain configuration that can crystallize faster under non-isothermal conditions than the *R/S*-PBH 120K sample when cooling from the melt, despite its higher molecular weight. The 50% content of *S* chains in the *R/S*-PHB racemic mixture must be slowing down the non-isothermal crystallization from the melt.

Figure 3.4b shows a plot of the peak T_m values obtained during the second DSC heating scans shown in Figure 1.3b (the highest melting peaks were employed for the plot). As all the *R/S*-PHB samples exhibited a complex fusion behavior (Figure 3.3b) where a small, lower T_m peak can be seen, followed by a second, more pronounced peak at higher temperatures, we performed in-situ WAXS to demonstrate that this small peak is due to a reorganization process where thinner lamellae melt, recrystallize, and finally melt at higher temperatures (see also Figure 3.5 and its discussion below). As expected, the T_m value is a function of molecular weight that saturates beyond a critical molecular weight. The results were fitted with Flory's equation [34,35], written as:

$$\frac{1}{T_m} - \frac{1}{T_m^{sat}} = \frac{2RM_o}{\Delta H_m^0 M_n} \tag{3.1}$$

where T_m^{sat} is the T_m when the saturation is reached (170.5 °C), *R* is the gas constant, ΔH_m^0 is the enthalpy of fusion at equilibrium, [33] and M_o is the molecular weight of the repeating unit. See Table 3.1 for the values employed for the fitting of Flory´s equation.

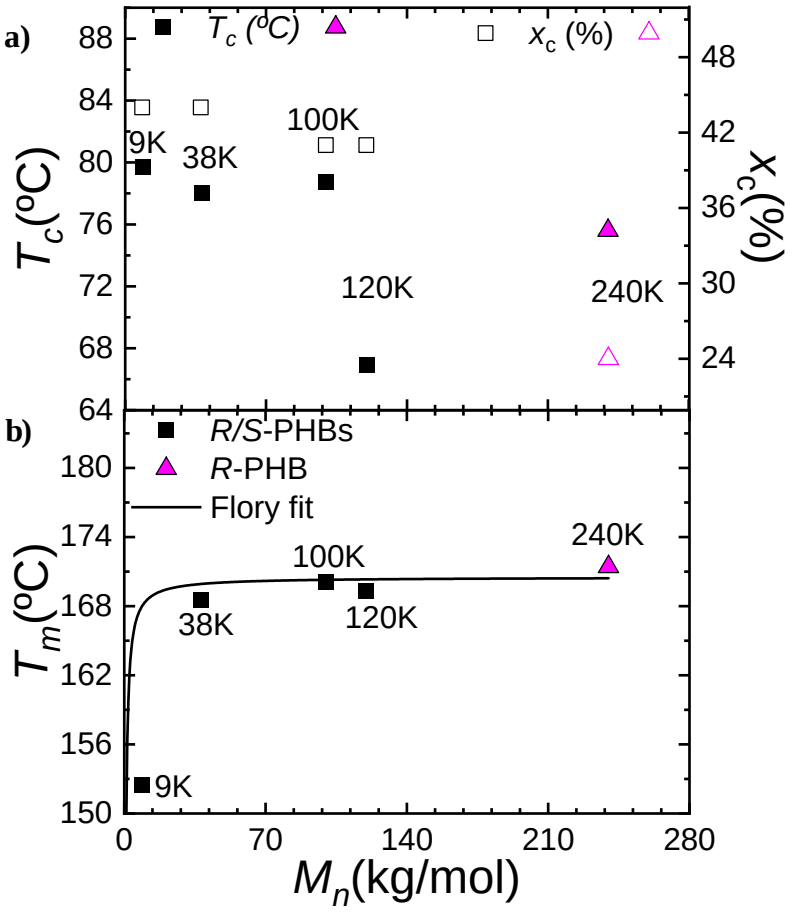

Figure 3.4. Crystallinity degree, crystallization (a), and melting (b) temperatures as a function of molecular weight of the synthetic *R/S* (black squares) and bacterial *R* (pink triangle) PHBs; the solid black line in the bottom plot is a fit to Flory´s equation for the experimental T_m values.

Table 3.1. Thermal DSC cooling and heating properties of Bacterial *R* PHB and Synthetic *R/S* PHB 8K, 38K, 100K and 120K.

***R*-PHB**	***R/S*-PHB 9K**	***R/S*-PHB 38K**	***R/S*-PHB 100K**	***R/S*-PHB 120K**
T_c=75.6°C	T_c=79.7°C	T_c=78.0°C	T_c=78.7°C	T_c=66.9°C
ΔH_c=65 J/g	ΔH_c=64 J/g	ΔH_c=60 J/g	ΔH_c=60 J/g	ΔH_c=35 J/g
				T_{cc}=65.2°C
				ΔH_{cc}=-11 J/g
T_m=171.4°C	T_{mI}=136.8°C,	T_{mI}=151.8°C,	T_{mI}=153.1.°C,	T_m=169.3°C
ΔH_m=67 J/g	T_{mII}=152.5°C	T_{mII}=168.5°C	T_{mII}=170.1°C	ΔH_m=60 J/g
	ΔH_{mI}=19 J/g	ΔH_{mI}=14 J/g	ΔH_{mI}=5 J/g	
	ΔH_{mII}=100 J/g	ΔH_{mII}=87 J/g	ΔH_{mII}=51 J/g	
T_g=4°C				T_g=1.4°C
x_c=44%	x_c=44%	x_c=41%	x_c=41%	x_c=24%

3.3.3 Powder diffraction and *In Situ* WAXS Real-Time Synchrotron Results

WAXS data at room temperature were collected for all the PHB as prepared samples, and the profiles obtained are shown in Figure 3.5, where the scattering intensity is reported as a function of *2θ*, the diffraction angle. The diffraction profiles are very similar for all the samples, which indicates no differences in the crystalline structure between *R*-PHB and *R/S*-PHBs. Through Bragg's law, it was possible to assign a Miller index to each peak, the relative data are reported in Tables 3.2-3.6. These results indicate that, despite the different absolute stereoconfigurations, all the PHB samples employed

here crystallize in an identical way to *R*-PHB, [36] with an orthorhombic unit cell with the following dimensions:

a = 5.76 Å,

b = 13.30 Å,

c = 5.96 Å.

Overall, these results indicate that the racemic mixtures synthesized here with 50/50 *R/S* chains form a single phase in the crystalline state, which is identical to that of *R*-PHB.

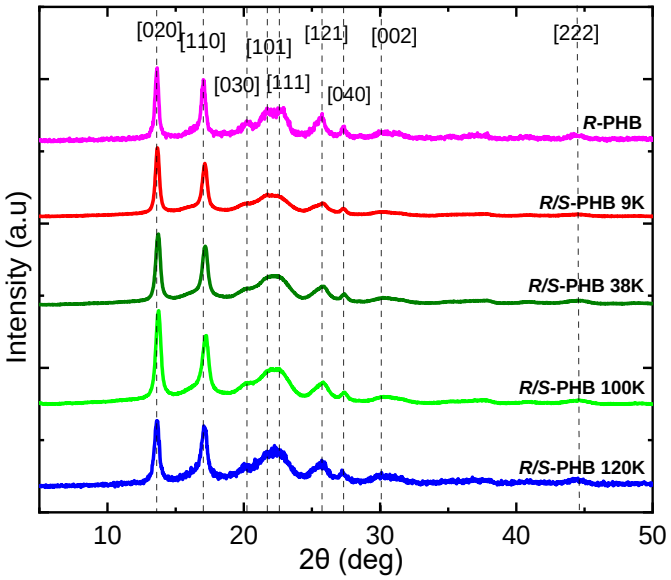

Figure 3.5. WAXS patterns taken at room temperature for the bacterial *R*-PHB and synthetic racemic *R/S*-PHBs as prepared. The planes that give origin to the reflections are indicated in the figure.

Table 3.2.Diffraction Angle (2θ), interplanar experimental (d exp) and calculated (d calc) distance and Miller index for Bacterial *R* PHB.

2θ exp (deg)	**d exp (Å)**	**d calc (Å)**	**Miller index**
13.64	6.492	6.600	020
17.03	5.206	5.760	110
20.24	4.387	4.400	030

21.73	4.089	4.141	101
22.89	3.885	3.951	111
25.75	3.459	3.508	121
27.28	3.269	3.300	040
29.90	2.988	2.980	002
44.03	2.056	1.975	222

Table 3.3.Diffraction Angle (2θ), interplanar experimental (d exp) and calculated (d calc) distance and Miller index for Synthetic *R/S*-PHB 9K.

2θ exp (deg)	**d exp (Å)**	**d calc (Å)**	**Miller index**
13.68	6.472	6.600	020
17.09	5.188	5.760	110
20.03	4.433	4.400	030
21.80	4.076	4.141	101
22.77	3.905	3.951	111
25.72	3.463	3.508	121
30.07	3.255	2.980	002
44.70	2.027	1.975	222

Table 3.4.Diffraction Angle (2θ), interplanar experimental (d exp) and calculated (d calc) distance and Miller index for Synthetic *R/S*-PHB 38K.

2θ exp (deg)	**d exp (Å)**	**d calc (Å)**	**Miller index**
13.73	6.449	6.600	020
17.17	5.164	5.760	110
19.96	4.448	4.400	030

21.74	4.087	4.141	101
22.45	3.960	3.951	111
25.92	3.437	3.508	121
29.88	3.255	2.980	002
44.70	2.027	1.975	222

Table 3.5.Diffraction Angle (2θ), interplanar experimental (d exp) and calculated (d calc) distance and Miller index for Synthetic *R/S*-PHB 100K.

2θ exp (deg)	**d exp (Å)**	**d calc (Å)**	**Miller index**
13.73	6.449	6.600	020
17.17	5.164	5.760	110
20.11	4.415	4.400	030
21.64	4.106	4.141	101
22.40	3.969	3.951	111
25.66	3.471	3.508	121
27.40	3.278	3.300	040
29.99	2.979	2.980	002
44.60	2.0315	1.975	222

Table 3.6.Diffraction Angle (2θ), interplanar experimental (d exp) and calculated (d calc) distance and Miller index for Synthetic *R/S*-PHB 120K.

2θ exp (deg)	**d exp (Å)**	**d calc (Å)**	**Miller index**
13.62	6.501	6.600	020
17.06	5.197	5.760	110
20.02	4.435	4.400	030

22.05	4.031	4.141	101
25.72	3.463	3.508	121
27.40	3.278	3.300	040
30.11	2.979	3.300	002
44.16	2.051	1.975	222

As described above, the *R/S*-PHB samples exhibited two melting peaks and cold crystallization events (Figure 3.3). Therefore, we performed in situ WAXS studies by cooling the samples from the melt and then performed subsequent heating at the same rate used in the DSC studies at the Alba synchrotron for three representative samples: *R*-PHB and *R/S* PHBs (9K and 120K) to ensure that the preceding small T_m peak, appeared before the considerably larger, higher T_m peak, was due to a reorganization process.

The WAXS diffraction spectra for cooling and heating scans are reported in Figure 3.6-3.8, in which the intensity is reported as a function of the scattering vector *q*. The diffraction patterns are similar to those shown and described in Figure 3.5, and in them, the change in intensity of the peaks following crystallization and melting of the samples is clearly observed.

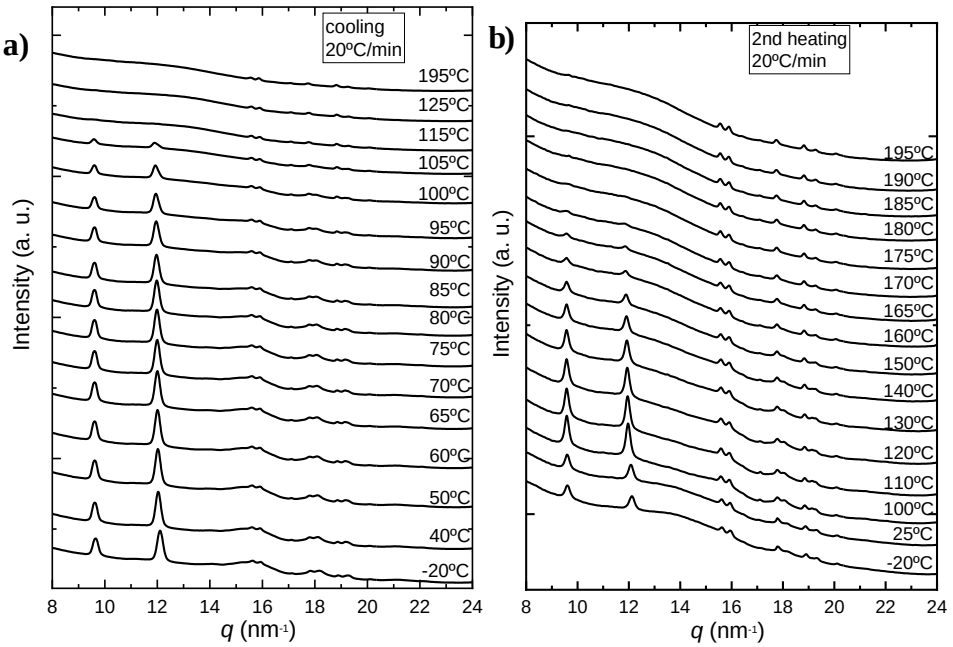

Figure 3.6. WAXS diffractograms, at different temperatures, acquired during the cooling (a) and heating scan (b) for Bacterial *R*-PHB.

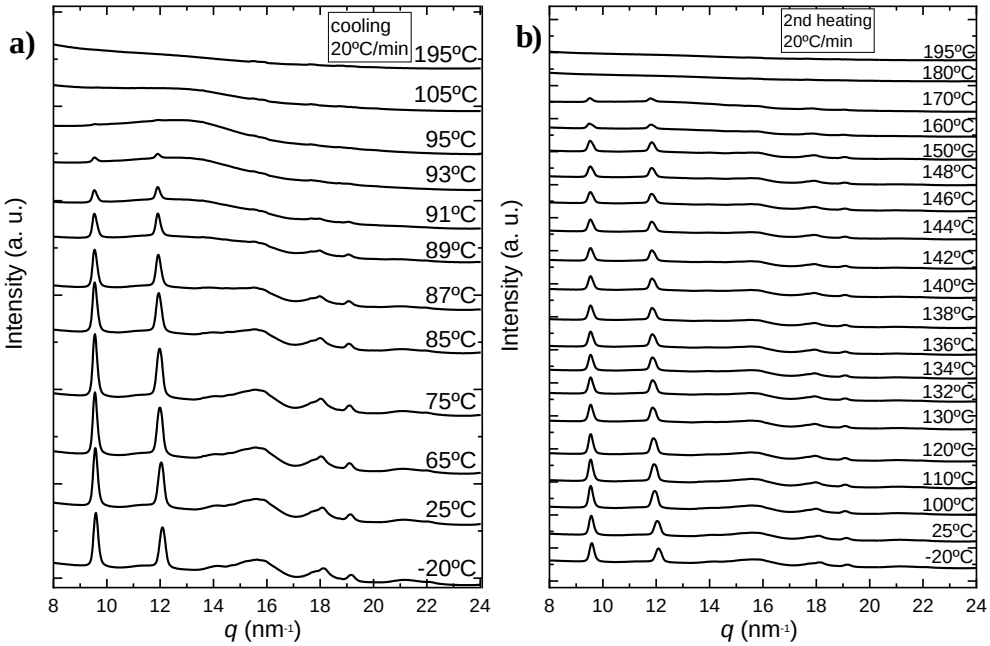

Figure 3.7. WAXS diffractograms, at different temperatures, acquired during the cooling (a) and heating scan (b) for *R/S*-PHB 9K.

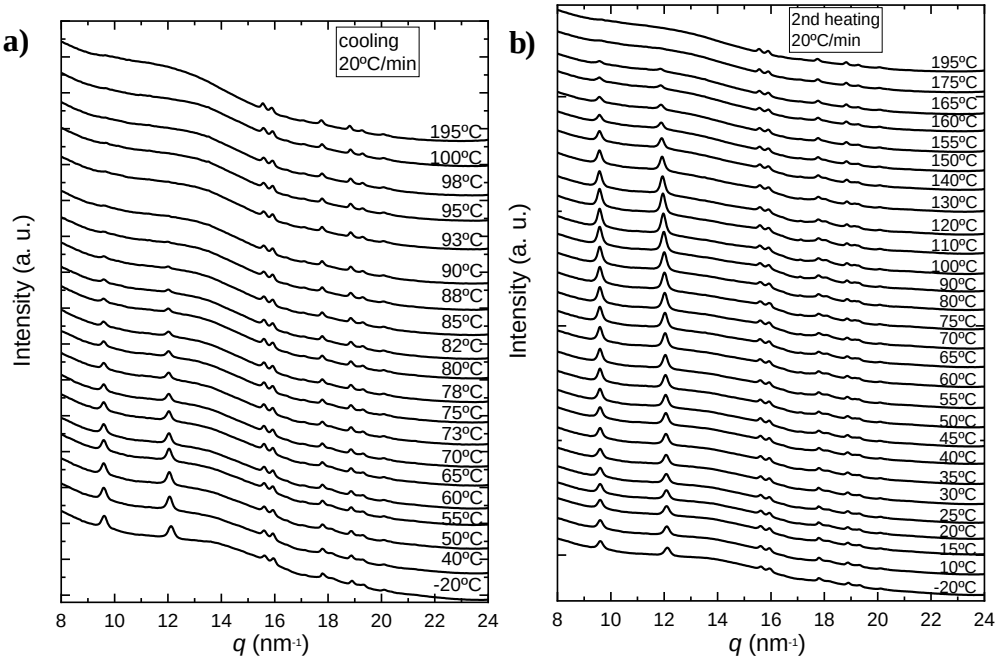

Figure 3.8. WAXS diffractograms, at different temperatures, acquired during the cooling (a) and heating scan (b) for *R/S*-PHB 120K.

To better analyze the nature of the double peak present in the DSC fusion scan, the intensity of the highest intensity diffraction peak was measured for the three samples mentioned earlier. The normalized intensity value acquired during the second heating scan is shown in Figure 3.9 as a function of temperature, for racemic *R/S*-PHB 9K (a), *R/S*-PHB 120K (b), and bacterial *R*-PHB (c) samples.

Based on the DSC heating scan analysis, the phenomenon of cold crystallization can be observed clearly only for the racemic *R/S*-PHB 120K sample. However, Figure 3.9 shows that the three samples examined, *R/S*-PHB 9K, *R/S*-PHB 120K, and *R*-PHB all undergo cold-crystallization during heating as the relative intensity of the chosen reflection increase with temperature during heating. The *R/S*-PHB 9K only undergoes an approximate 20% relative increase in intensity during heating in the temperature range of approximately 50-100 ºC, while the *R/S*-PHB 120K sample (which shows a clear cold crystallization exotherm in this temperature range, as shown in Figure 3.9) exhibits a 60%

relative increase in intensity. The peak intensity of the crystalline reflection chosen is proportional to the crystallinity degree.

For the *R/S*-PHB samples in Figure 3.9, the differences in cold crystallization behavior are due to their different molecular weights (9 kg/mol vs 120 kg/mol). The lower molecular weight sample crystallizes much faster during the previous cooling process, hence it exhibits far less cold crystallization during heating.

In the case of bacterial PHB, despite having a higher molecular weight (240 kg/mol), it has an increase in relative intensity of only 20%, much lower than the *R/S*-PHB 120K. We hypothesized that the reason behind this phenomenon is due to the enantiomeric purity of the bacterial PHB sample. Thus, as the pure *R* crystallizes faster during the previous cooling from the melt, no significant cold crystallization was observed during the second heating scan.

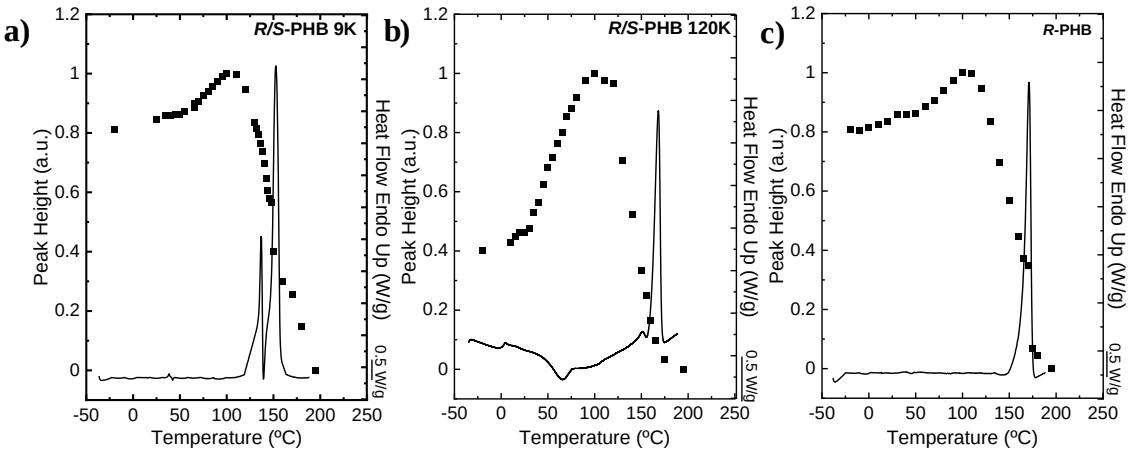

Figure 3.9. Normalized WAXS heating peak height intensities as a function of temperature for synthetic *R/S*-9K (a), *R/S*-120K (b), and bacterial *R*-PHB (c), overlapped on the second heating curves from DSC.

3.3.4 Morphology and Spherulite Growth

Besides DSC and WAXS experiments, the morphology and spherulite growth of different samples were analyzed by PLOM to get a better understanding of the effect of molecular weight and stereochemistry on the crystallization behaviour.

A thermal stability study is presented in Figure 3.10, where the T_m and T_c values are plotted as a function of the number of measuring cycles in the DSC. A decrease of 1 to 1.5 ºC is always observed when passing from the first to the third step; therefore, the sample degrades during the repeated scans. For this reason, we always employed a fresh sample for each measurement to try to minimize the effects of degradation in our measurements.

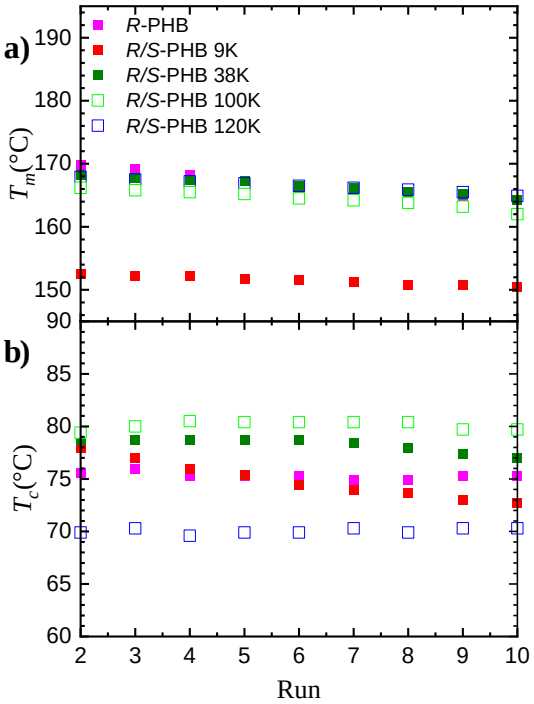

Figure 3.10. a) Melting point (T_m) and and b) crystallization point (T_c) versus the number of run (stability test) for Bacterial *R* and Synthetic *R/S* PHB.

Figure 3.11 shows the PLOM micrographs of all PHB samples using the same magnification scale (200 µm). These micrographs were collected at 25 ºC after non-isothermal crystallization from the melt at 20 ºC/min. All samples crystallize to form

spherulites, but with differences in the Maltese Cross extinction patterns. The bacterial *R*-PHB forms banded positive spherulites that agree with previous literature reports for the enantiomerically pure *R*-PHB [33],[37]. On the other hand, the racemic mixtures *R/S*-PHB samples form non-banded spherulites, at least after non-isothermal crystallization at 20 ºC/min. In addition, their spherulites reveal a mixed character where extinction patterns point towards a mixture of positive and negative spherulites, with a higher percentage of positive spherulites. Furthermore, spherulitic density (after non-isothermal crystallization) appears to moderately increase with molecular weight, especially from *R/S*- PHB 9K to *R/S*-PHB 100K, and then remains similar. These results imply a slight increase in non-isothermal nucleation density with molecular weight.

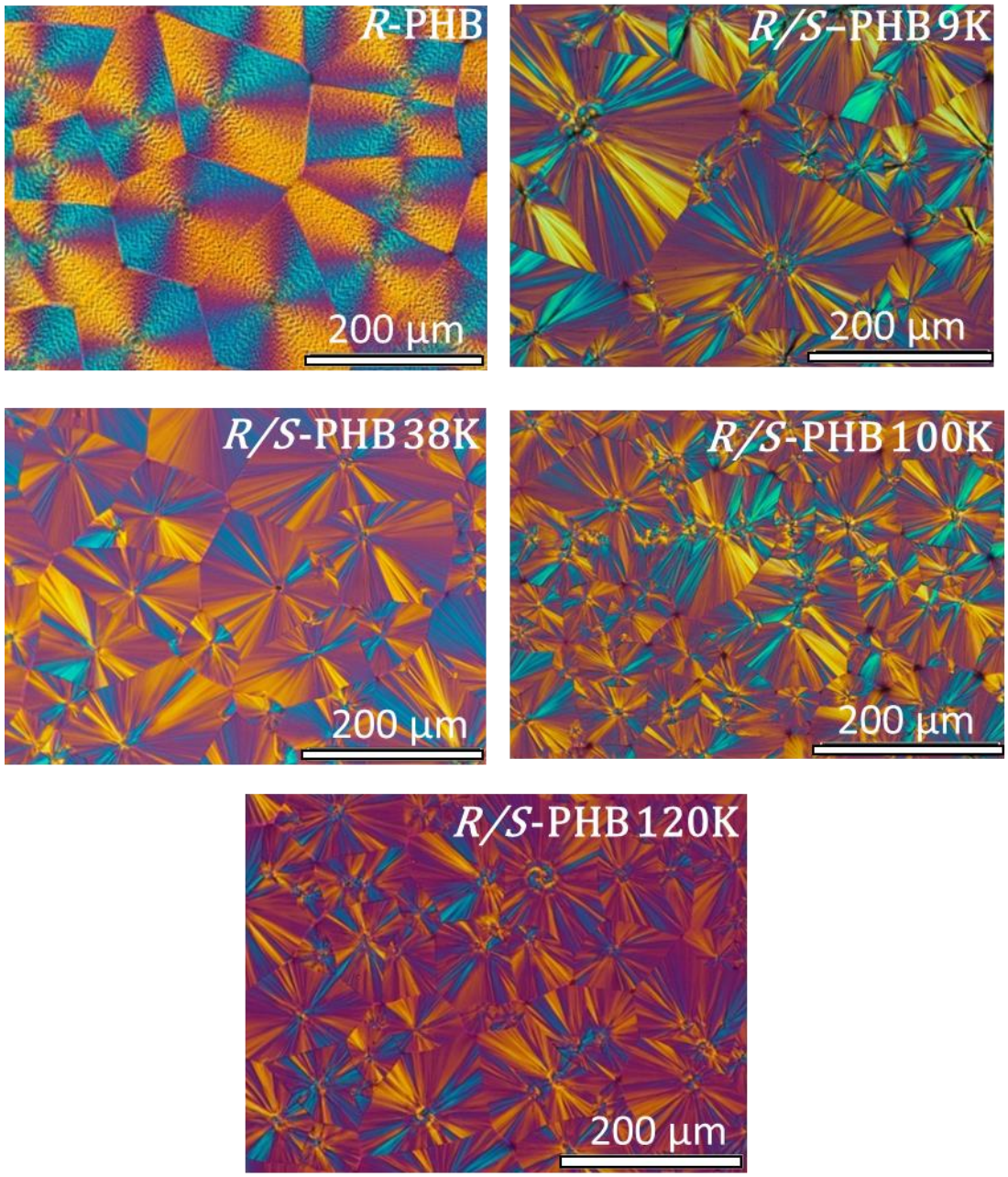

Figure 3.11. PLOM micrographs for bacterial and synthetic PHB samples. Micrographs were taken at 25 ºC after melting for 1 minute and cooling at 20 ºC/min.

The isothermal growth of spherulites was determined by PLOM measurements. The samples were cooled from the melt (at 50 ºC/min) to a chosen crystallization temperature in the range of 60 to 140 °C. Spherulitic growth rates for each sample, *G* (µm/s), were determined at different crystallization temperatures from the slope of radius versus time plots (which were always linear).

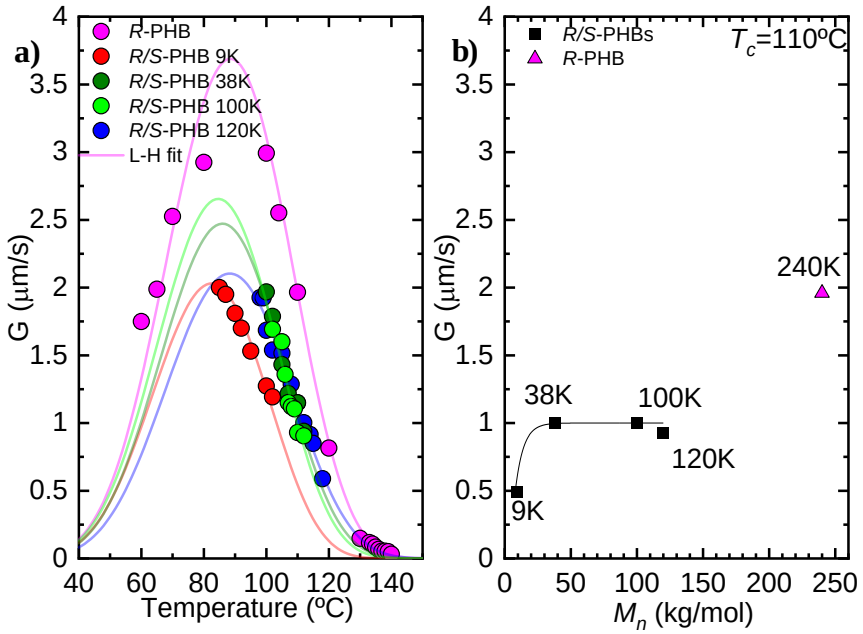

Figure 3.12. Spherulitic growth rate (G) as a function of: (a) crystallization temperature and (b) molecular weight at T_c =110 ºC, for bacterial *R*-PHB, *R/S*-PHB 9K, 38K, 100K, and 120K. The solid lines in the left graph are fits to the Lauritzen and Hoffman equation. The solid line in the right plot is a line to guide the eye.

Figure 3.12a shows the spherulitic growth rates as a function of T_c. The typical bell shape curve was obtained for *R*-PHB, which arises from the competition of two opposing trends, [38,39]. The growth rate increases as T_c decreases on the right-hand side of the plot as secondary nucleation increases with supercooling until a maximum is reached when the viscosity of the melt is so high that the growth of the crystals becomes dominated by the slow diffusion of the chains to the crystallizing front. Therefore, the growth rate decreases with supercooling and becomes zero at T_g. On the other hand, in the case of the racemic synthetic *R/S*-PHB samples, it was not possible to measure growth rates in the left part of the curve because during the cooling process from the melt to T_c (at 50 ºC/min), the samples crystallized until saturation in the observation area.

In Figure 3.12a, it is apparent that the growth rate value is higher in the enantiomerically pure bacterial *R*-PHB case. This aspect is peculiar because, given the higher molecular weight (240 kg/mol) of the sample compared to all synthetic others, one could have anticipated a lower growth rate. However, it appears that the enantiomeric purity is the dominating factor here and causing a faster growth rate despite the higher molecular weight of the sample. Therefore, it is apparent that the 50% content of *S*-PHB chains is slowing down the spherulitic growth rate of the *R/S* racemic mixture.

In the case of the racemic *R/S*-PHB synthetic samples, the growth rate is always lower than that of the enantiomerically pure *R*-PHB bacterial sample. Figure 3.12b shows how the growth rate depends on molar mass at the same T_c value (i.e., 110 ºC). It can be seen that, within the family of racemic PHBs, the growth rate increases with the molecular mass and saturates at a value of approximately 1 μm/s (the slight decrease for the sample with 120 kg/mol in molecular weight is insignificant). However, the *R*-PHB sample has a growth rate of around 2 μm/s, so it grows twice as fast at this T_c, presumably because of its enantiomerically pure *R* nature, even though its molecular weight is much higher (i.e., 240 kg/mol).

The solid lines in Figure 3.12a are fits to the Lauritzen and Hoffman theory. The detailed analysis of the fittings and the parameters obtained can be found in the Table 7.

Table 3.7. Isothermal kinetics data parameters derived from experimental results obtained by PLOM. The last row shows the data present in the literature[33].

Sample	G^0(cm/s)	K^G_g (K^2)	σ (erg/cm^2)	σ_e (erg/cm^2)	q (erg)	R^2
R-PHB	70	3.0x10^5	8.39	256.4	9.46x10^{-13}	0.997
R/S-PHB 9K	27.6	2.47x10^5	8.39	218.7	8.07x10^{-13}	0.999
R/S-PHB 38K	136	3.33x10^5	8.39	284.2	1.05x10^{-12}	0.986
R/S-PHB 100K	154	3.42x10^5	8.39	285.4	1.15x10^{-12}	0.996
R/S-PHB 120K	230	3.8x10^5	8.43	320.9	1.18x10^{-12}	0.995
Barham *et al*. PHB[33]	121	4.9x10^5	8.35	359.7	1.32x10^{-12}	0.989

Small differences are noted for K_g^G (constant proportional to the energy barrier for the spherulitic growth or secondary nucleation) and σ_e (fold surface energy) values in the family of *R/S* PHBs, in which these values increase slightly with molecular weight, probably due to the lower chain diffusion. The value of q (work that the macromolecule does to fold) also increases, and this could indicate that the chains require more energy to fold on the surface of the lamellae, [40]. For the sake of completeness, the values obtained by Barham *et al*. are also reported, [33]. The bacterial PHB used in the work of Barham *et al*. was a pure *R* sample but had a different molecular weight (133 kg/mol) than the *R*-PHB used in the present work. Although there are slight differences in the reported values, these are not significantly important as there are no differences in the growth rate G trend as a function of the T_c, as observed in Figure 3.13.

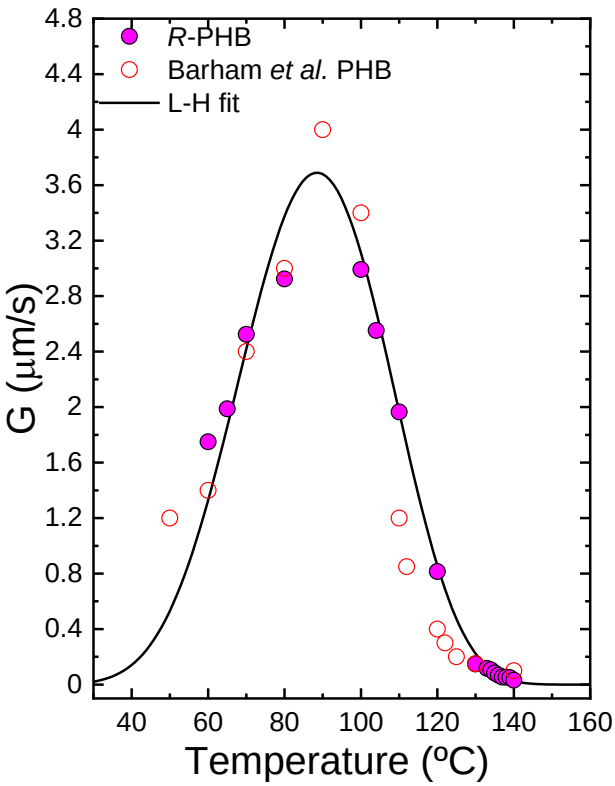

Figure 3.13. Spherulitic growth rate (*G*) as a function: of crystallization temperature for R-PHB studied in this work (filled pink circles) and for R-PHB reported in literature [33] (red empty circles).

From the isothermal spherulitic growth experiments, it was possible to observe banded spherulites for all the racemic synthetic PHB samples, even though in non-isothermal crystallization they did not form banded spherulites, presumably because of the relatively fast cooling rate (20 °C/min). It is well known that banding periodicity in *R*-PHB is sensitive to T_c, and its periodicity increases with T_c. In Figure 3.14a, PLOM micrographs at different T_c are reported; they are collected at the indicated T_c values, and the bands in the spherulites are clearly visible in the case of the *R/S*-PHB samples. Through the Image J software, the band periodicity for different T_c values was calculated. Figure 14b shows how the band periodicity increases as T_c increases. This trend is similar to that reported for *R*-PHB in the literature, [33]

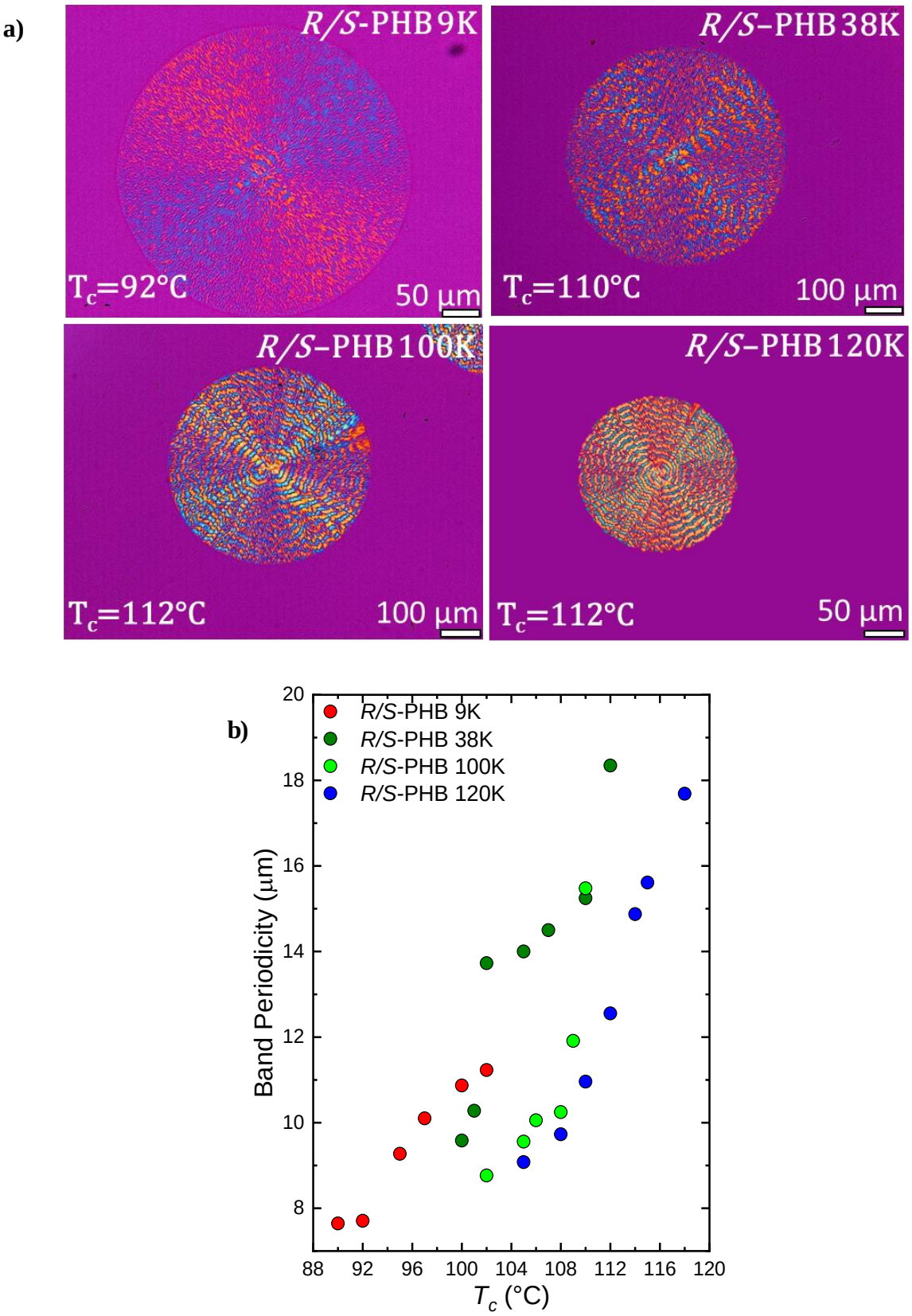

Figure 3.14. (a) PLOM micrographs taken at the indicated T_c and (b) band periodicity as a function of T_c for *R*-PHB, *R/S*-PHB 9K, 38K, 100K, and 120K

3.3.5 Study of the Overall Crystallization Kinetics by DSC

To study the overall crystallization kinetics (which includes both nucleation and growth contributions), isothermal crystallization experiments were performed by DSC. The obtained experimental data were analyzed with the Avrami theory and the Lauritzen and Hoffman theory, [41,42].

Figure 3.15 shows the inverse of the induction time (t_0) as a function of T_c for the bacterial *R*-PHB and the synthetic racemic *R/S*-PHBs. The induction time is the primary nucleation time, which elapses before the DSC detects any crystallization process. Therefore, its inverse is proportional to the primary nucleation rate before crystallization starts. It can be seen that the bacterial *R*-PHB under isothermal conditions has a higher primary nucleation rate than the racemic *R/S*-PHBs if the trends of the plots are extrapolated as a function of T_c, so that they can be compared at similar T_c values (for instance at 125 ºC). Furthermore, the fact that *R*-PHB needs much lower supercooling to nucleate than all the *R/S*-PHB samples is also proof that enantiomerically pure *R*-PHB can nucleate faster than the former racemically mixed *R/S*-PHBs under isothermal conditions, even when its molecular weight is higher. This enhanced nucleation in the bacterial *R*-PHB is presumably due to the easier nucleation ability of *R*-PHB chains.

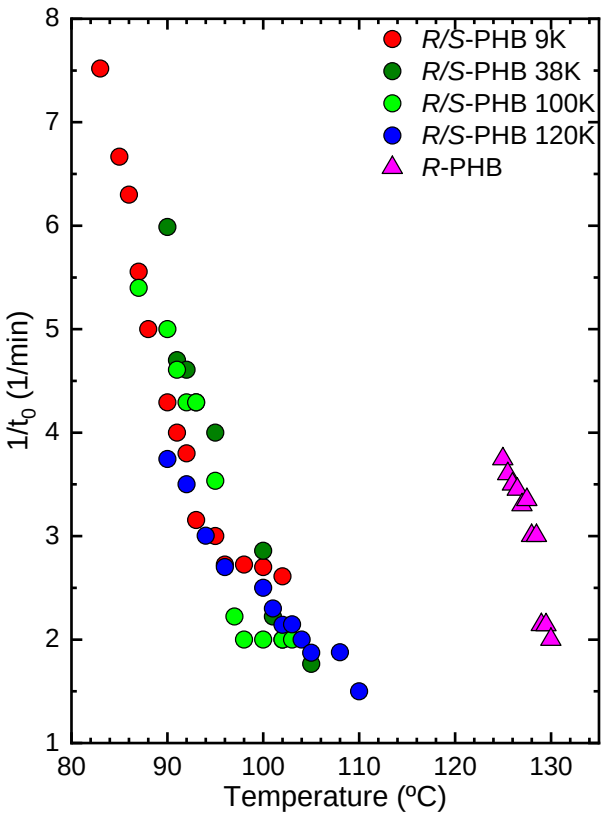

Figure 3.15. Inverse of induction time ($1/t_0$) as a function of T_c

The inverse of the half crystallization rate ($1/\tau_{50\%}$) is plotted, in Figure 3.16, as a function of T_c (a), of the supercooling, ΔT (b), and molecular weight with the same ΔT = 77 ºC (c). This value is the inverse of the time that, during an isothermal process, polymers need to achieve the 50% of their relative crystallinity. Moreover, this parameter represents the experimental overall crystallization rate, which considers both nucleation and growth contributions. The trend is similar to that seen in Figure 3.15 for the inverse of the induction time: bacterial *R*-PHB with a higher molecular weight (240 kg/mol), crystallizes faster and at lower supercooling than any of the *R/S*-PHB samples with lower molecular weights. Within the family of racemic *R/S*-PHB mixtures, slight differences are noted due to the molecular weight, even if the involved crystallization rates are lower, as shown in Figures 3.16a and 3.16b.

An important trend can be appreciated in Figure 3.16c, where $1/\tau_{50\%}$ is plotted as a function of molecular weight at a constant supercooling value of ΔT = 77 ºC. It is observed that for the racemic synthetic *R/S*-PHB samples, the overall crystallization rate values are similar, within the limits of the experimental error compared to the bacterial *R*-PHB sample, which exhibits an overall crystallization rate (obtained by extrapolating the fit of the LH theory) that is remarkably five times faster than the lowest molecular weight *R/S*-PHB sample (i.e., 9 kg/mol). In the case of the growth rates determined above by PLOM, the increase in growth rates for the *R*-PHB with respect to *R/S*-PHBs went up to two times at specific T_c values (Figure 3.12b). This much higher overall isothermal crystallization rate (which measures both nucleation and growth) is an indication that not only is crystal growth faster, but also isothermal nucleation is faster at specific T_c values in enantiomerically pure *R*-PHB, something in line with the estimations of nucleation rate. Although we couldn't rule out the potential effects of trace nuclearting impurities possibly present in the commercial bacterial sample (the synthetic samples were

repeatedly purified until constant thermal property values were reached), the experimental evidence pointed to the conclusion that the stereochemistry is the decisive factor for the differences observed in the bacterial and synthetic PHB samples.

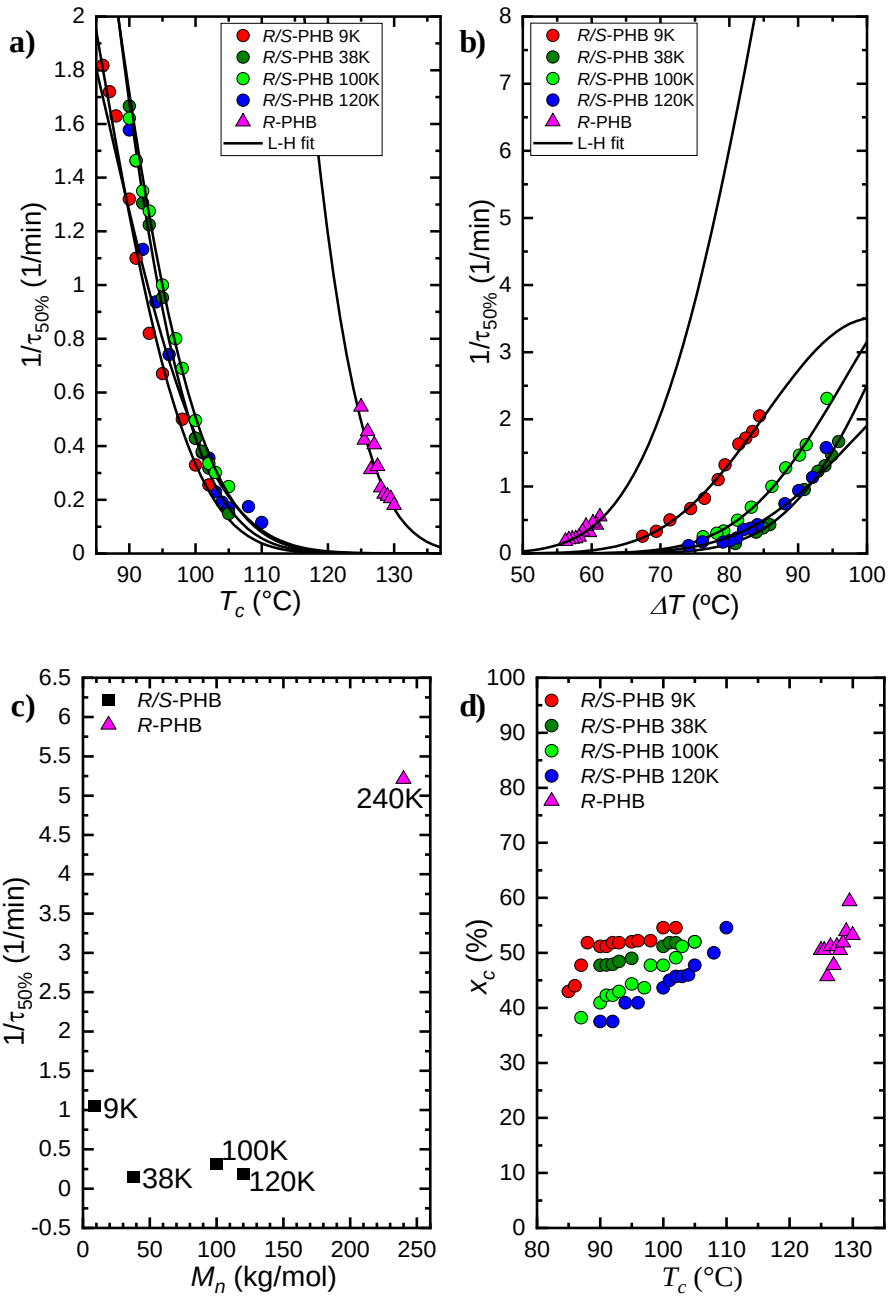

Figure 3.16. Inverse of half-crystallization time ($1/\tau_{50\%}$) as a function of T_c (a), supercooling, ΔT (b) and M_n (c) at ΔT = 77 ºC. Degree of crystallinity (x_c) calculated during isothermal crystallization as a function of T_c (d). The solid lines in Figure a and b represent the fits to the Lauritzen and Hoffman theory.

Figure 3.16d shows the degree of crystallinity (x_c) obtained at the end of the isothermal crystallization process for all samples.

As can be seen from Figure 3.16d, the degree of crystallinity increases as T_c increases. Interestingly, in the T_c range of 90 to 105 ºC, the crystallinity degree for the *R/S*-PHB samples increases as the molecular weight decreases. This trend is consistent with the slower diffusion ability of the higher molecular weight chains in the racemic mixtures. However, the enantiomerically pure *R*-PHB sample with a higher molecular weight (compare *R/S*-PHB 120K with *R*-PHB 240K) reaches similar degrees of crystallinity or slightly higher at lower supercooling dictated by the stereochemistry.

To fit the DSC overall crystallization rate experimental data, the Avrami theory[43,44] was employed. The Avrami equation can be expressed as:

$$1 - V_c(t - t_0) = \exp(-k(t - t_0)^n) \quad (3.2)$$

where V_c is the relative volumetric transformed fraction, t is the time of the experiment, t_0 is the induction time already described above, k is the overall crystallization rate constant, and n is the Avrami index, related to the nucleation rate and the growth dimensionality of the crystals. In the case of bulk polymers, the values of n fluctuate between 2 and 4. If instantaneously nucleated axialites are obtained during primary crystallization, the corresponding n values would be 2 (which experimentally could fluctuate between 1.5-2.4). In the case of spherulites, the n values are close to 3 for instantaneous nucleation (i.e., 2.5-3.4) and 4 for sporadic nucleation (i.e., 3.5-4).

The Avrami theory usually fits the crystallization data in the primary crystallization regime, where the free growth of superstructural crystals (i.e., axialites or spherulites) is seen. After they start impinging one another, secondary crystallization sets in, and the Avrami equation cannot perfectly describe this complex process. In the case

of *R*-PHB very few works are reported in the literature in which the overall crystallization kinetics have been studied.

Dubini *et al* [45] use the same conditions employed in this work, but the bacterial PHB used had a different molecular weight. An *et al*. [46] and Gunaratne *et al*.[47] studied the same *R*-PHB employed here but using different conditions, such as higher temperatures and times to erase the thermal history in the melt. Furthermore, none of the reported works performed isothermal crystallization experiments using fresh samples for each T_c. This procedure could not prevent possible degradation of the sample during the experiments, as we demonstrated in Figure 3.10, in which a decrease in T_m and T_c was observed for successive cycles of crystallization and melting.

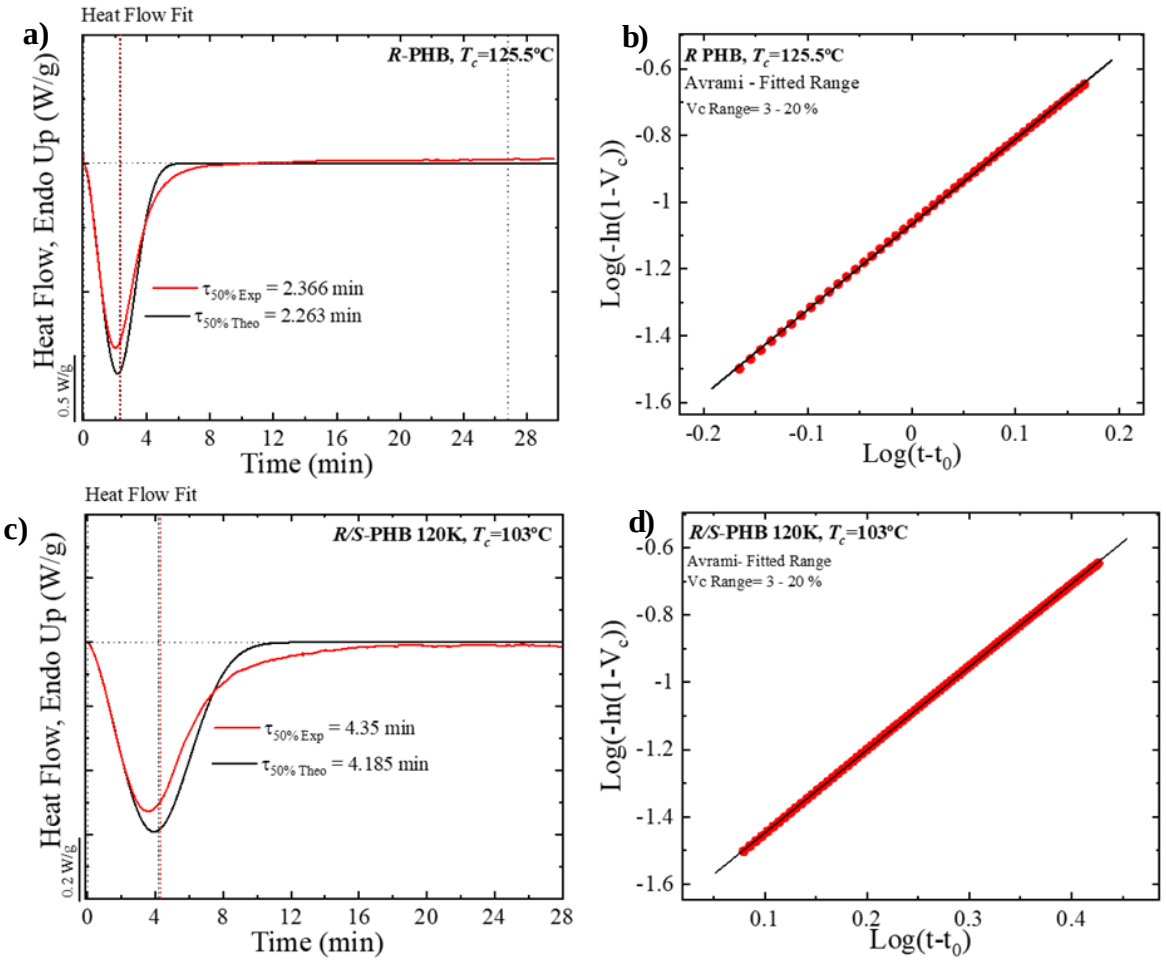

Figure 3.17. The Avrami fit equation using the free Origin plug in developed by Pérez-Camargo *et al*. [48] for bacterial *R*-PHB (a, b) and synthetic *R/S*-PHB 120K (c, d) at the indicated T_c.

Figures 3.17a and 3.17c present two examples where the experimental DSC isotherms are plotted for *R*-PHB and for *R/S*-PHB 120K together with the superposition of their respective Avrami fits. Figures 3.17c and 3.17d show the typical Avrami plots in the conversion range (i.e., the relative crystallinity range) employed to perform the fit (3-20%) obtained by the free App developed by Pérez-Camargo et al.[48] , which was used to perform the fittings. In the primary crystallization range, the fittings obtained are excellent, with correlation coefficients that are always larger than 0.999. Tables 3.8-3.12 list the fitting parameters for all the samples employed here. Comparing the experimental values of $\tau_{50\%}$ with those predicted by the Avrami theory, one can have an idea of whether the theory holds until 50% relative conversion to the semi-crystalline state, and in this case, the agreement is very good.

Table 3.8. Avrami fitting parameters obtained from by the free App [48] for *R*-PHB.

T_c(°C)	t_0(s)	$\tau_{50\%\ Exp}$ (min)	$\tau_{50\%\ Theo}$ (min)	n	$K^{\frac{1}{n}}(min^{-1})$	$K\ (min^{-n})$	R^2
125	0.267	1.833	1.754	2.5	0.492	$1.70x10^{-1}$	0.999
125.5	0.263	2.366	2.263	2.56	0.383	$8.58x10^{-2}$	0.999
126	0.285	2.199	2.034	2.54	0.301	1.14E-02	0.999
126.5	0.289	3.200	3.102	2.52	0.279	$1.36x10^{-1}$	0.999
127	0.303	2.467	2.327	2.50	0.358	$7.70x10^{-2}$	0.999
127.5	0.298	3.084	2.898	2.67	0.300	$4.04x10^{-2}$	0.999
128	0.333	4.083	3.729	2.69	0.233	$2.00x10^{-2}$	0.999

128.5	0.333	4.516	4.149	2.68	0.210	$1.53x10^{-2}$	0.999
129	0.467	4.682	4.525	2.89	0.202	$2.47x10^{-2}$	0.999
129.5	0.467	4.883	4.683	3.03	0.196	$7.17x10^{-3}$	0.999
130	0.501	5.566	5.236	2.99	0.168	$4.91x10^{-3}$	0.999

Table 3.9. Avrami fitting parameters obtained from by the free App [48] for *R/S*-PHB 9K.

T_c (°C)	t_0(s)	$\tau_{50\%}$ Exp (min)	$\tau_{50\%}$ Theo (min)	n	$K^{\frac{1}{n}}(min^{-1})$	$K\ (min^{-n})$	R^2
83	0.133	0.465	0.450	2.20	1.780	8.13	0.999
85	0.150	0.487	0.477	2.16	1.766	3.42	0.999
86	0.158	0.550	0.555	2.4	1.544	2.84	0.999
87	0.180	0.581	0.579	2.37	1.479	2.53	0.999
88	0.20	0.613	0.604	2.57	1.437	2.54	0.999
90	0.233	0.757	0.743	2.49	1.160	1.45	0.999
91	0.250	0.909	0.934	2.52	1.162	$8.81x10^{-1}$	0.999
92	0.263	0.987	0.972	2.89	1.189	1.65	0.999
93	0.317	1.219	1.215	2.57	0.698	$3.97x10^{-1}$	0.999
95	0.333	1.492	1.585	2.79	0.552	$1.91x10^{-1}$	0.999
96	0.367	1.666	1.650	2.82	0.525	$2.21x10^{-1}$	0.999
98	0.367	2.021	1.985	2.89	0.508	$7.70x10^{-2}$	0.999
100	0.370	3.032	3.103	2.57	0.285	$2.28x10^{-2}$	0.999
102	0.383	3.916	3.788	2.79	0.237	$7.28x10^{-3}$	0.999

Table 3.10. Avrami fitting parameters obtained from by the free App [48] for *R/S*-PHB 38K.

T_c (°C)	t_0(s)	$\tau_{50\%}$ Exp (min)	$\tau_{50\%}$ Theo (min)	n	$K^{\frac{1}{n}}(min^{-1})$	$K\ (min^{-n})$	R^2
90	0.167	0.599	0.602	2.61	1.366	2.26	0.999
91	0.212	0.683	0.702	2.63	1.239	1.76	0.999
92	0.217	0.766	0.771	3.07	1.151	1.54	0.999

93	0.233	0.817	0.830	2.7	1.053	1.15	0.999
95	0.250	1.050	1.032	3.23	0.864	$6.25x10^{-1}$	0.999
100	0.350	2.330	2.255	3.78	0.40195	$3.19x10^{-2}$	0.999
101	0.450	2.631	2.526	2.71	0.40769	$8.79x10^{-2}$	0.999
102	0.501	3.150	3.086	3.28	0.28925	$1.71x10^{-2}$	0.999
105	0.567	6.749	6.330	2.98	0.13927	$2.81x10^{-3}$	0.999

Table 3.11. Avrami fitting parameters obtained from by the free App [48] for *R/S*-PHB 100K.

T_c (°C)	t_0(s)	$\tau_{50\%\ Exp}$ (min)	$\tau_{50\%\ Theo}$ (min)	n	$K^{\frac{1}{n}}(min^{-1})$	$K\ (min^{-n})$	R^2
87	0.18519	0.432	0.468	2.17	1.804	3.60	0.999
90	0.200	0.616	0.659	2.48	1.309	1.95	0.999
91	0.217	0.682	0.691	2.68	1.224	1.72	0.999
92	0.233	0.740	0.760	2.89	1.342	2.37	0.999
93	0.233	0.784	0.792	2.88	1.112	1.36	0.999
95	0.283	1.000	1.015	3.22	0.879	$5.88x10^{-1}$	0.999
97	0.450	1.250	1.105	2.95	0.835	$1.96x10^{-1}$	0.999
98	0.500	1.449	1.508	3.07	0.588	$6.93x10^{-2}$	0.999
100	0.500	2.016	2.151	3.01	0.411	$3.11x10^{-2}$	0.999
102	0.500	2.984	3.007	2.82	0.292	$2.48x10^{-2}$	0.999
103	0.500	3.316	3.242	2.83	0.270	$5.68x10^{-3}$	0.999

Table 3.12. Avrami fitting parameters obtained from by the free App [48] for *R/S*-PHB 120K.

T_c (°C)	t_0(s)	$\tau_{50\%\ Exp}$ (min)	$\tau_{50\%\ Theo}$ (min)	n	$K^{\frac{1}{n}}(min^{-1})$	$K\ (min^{-n})$	R^2
90	0.267	0.633	0.615	2.20	1.276	1.74	0.999
92	0.285	0.883	0.825	2.35	0.958	0.906	0.999
94	0.333	1.066	1.123	2.20	0.797	0.591	0.999
96	0.370	1.350	1.317	2.52	0.545	1.267	0.999
100	0.400	2.333	2.160	2.6	0.401	0.0933	0.999
101	0.434	2.667	2.459	2.68	0.354	0.0622	0.999

102	0.467	2.816	2.752	2.62	0.314	0.0484	0.999
103	0.418	4.349	4.185	2.47	0.206	0.466	0.999
104	0.500	5.249	4.987	2.84	0.185	0.333	0.999
105	0.534	5.900	5.710	2.19	0.166	0.534	0.999
108	0.533	5.733	5.225	2.55	0.166	0.533	0.999
110	0.667	8.682	7.845	2.43	0.116	0.667	0.999

In Figure 3.18, the values of $k^{1/n}$ (a) and n (b) are plotted as a function of T_c, where $k^{1/n}$ is directly proportional to the overall crystallization rate. The trend in Figure 3.18a is very similar to the one obtained experimentally by measuring $1/\tau_{50\%}$ (Figure 16a), attesting for the good fit of the Avrami theory.

Regarding the Avrami index values shown in Figure 3.18b, it can be seen that they fluctuate from 2.1 to 4 for the *R/S*-PHB racemic synthetic samples and this indicates the presence of axialites for low crystallization temperatures and spherulites for high crystallization temperatures. For the bacterial *R*-PHB sample, n values between 2.5 and 4 were obtained, indicative of the presence of spherulites for the whole range of crystallization temperatures. These results are in good agreement with the observations performed by PLOM. Figure 3.18b shows that the Avrami index generally tends to increase with T_c for most samples. This trend can be explained when the morphology is fixed (i.e., for spherulites only or in the present case, when the Avrami index changes from 2.5 to 4) by the fact that the nucleation tends to change from instantaneous to sporadic as temperature increases, [49].

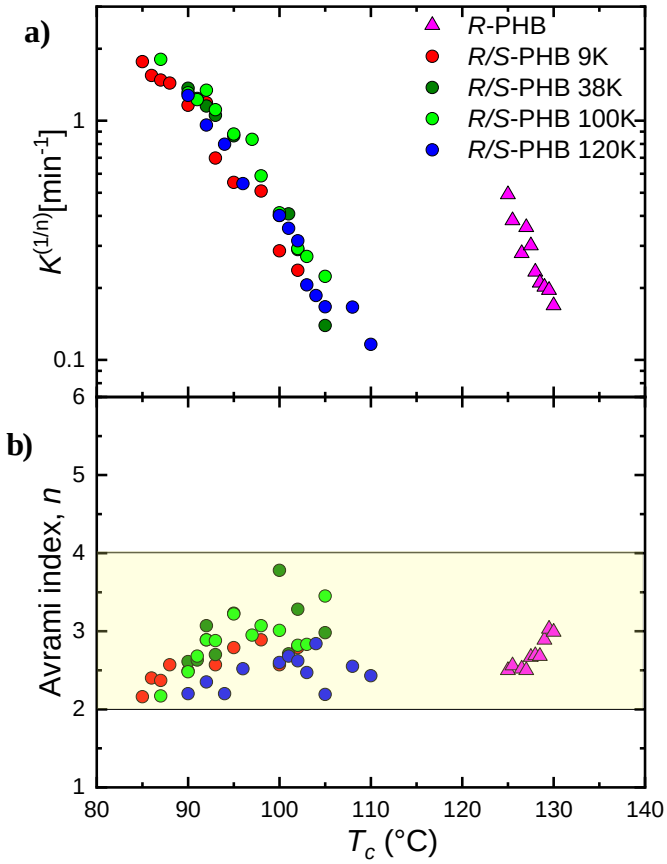

Figure 3.18. (a) Isothermal crystallization rate constant obtained by Avrami model ($k^{1/n}$) and (b) Avrami index (n) as function of T_c for bacterial *R*-PHB, *R/S*-PHB 9K, 38K, 100K, and 120K.

3.3.5.1 Equilibrium melting point determination

In the present work, during the isothermal crystallization process, the equilibrium melting temperatures (T_m^0) were calculated for the five PHB samples involved in the study. For this purpose, the Hoffman-Weeks extrapolation was used. In Figure 3.19, the extrapolations performed for all the PHB samples are shown.

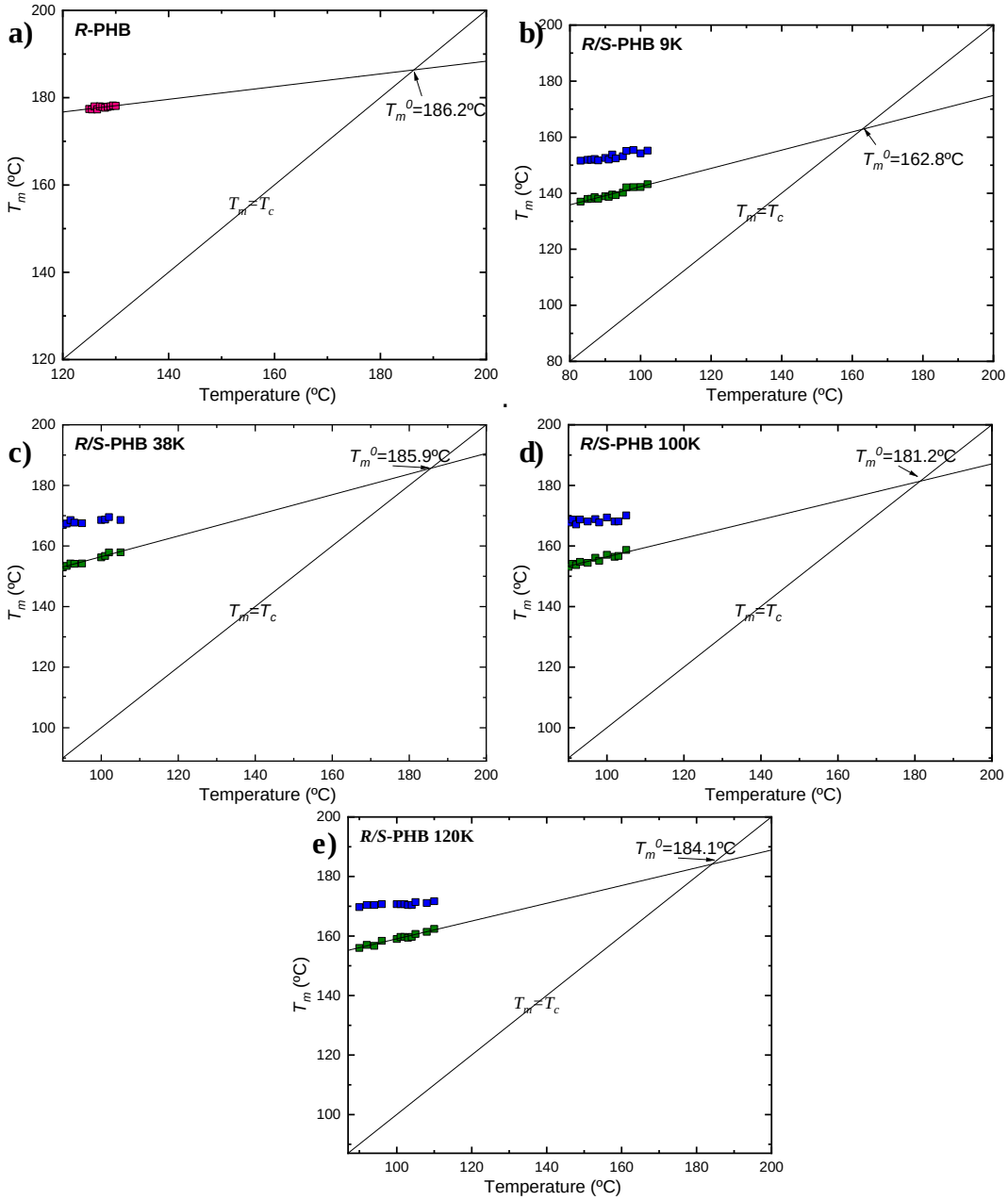

Figure 3.19. Hoffman-Weeks plots for *R* PHB (a), *R/S* PHB 8K (b), 38K (c), 100K (d), and 120K (e).

Two endothermic peaks were recorded for the synthetic *R/S*-PHB racemic samples in the heating curves following the isothermal crystallization process. However, the temperatures chosen to extrapolate the T_m^0 were the ones derived from the first melting peaks, since they increase as T_c increases, and therefore they represent the melting of the isothermally crystallized crystals. The second melting peak, obtained at high temperatures, is due to the melting of crystals reorganized during the heating scan and did not exhibit a significant variation of T_m with T_c.

Figure 3.20 shows the T_m^0 values obtained as a function of the molecular weight of the samples. They are compared in the same plot with the apparent T_m measured by non-isothermal DSC experiments (reported in Figure 3b). The T_m^0 values were also fitted with the Flory equation [34,35], and it is possible to note an increase of T_m^0 with the increase of molecular weight up to a saturation point. As expected, the T_m^0 values are larger than the apparent experimentally determined T_m. The difference in this case is nearly 15 ºC for most samples. No significant difference was found in the T_m^0 between the *R*-PHB sample and the *R/S* samples of higher molecular weights, i.e., after a saturation value (185 °C) is obtained. The T_m^0 for the *R*-PHB of bacterial origin was previously measured in different works [33],[50],[35] [40], and the values obtained are reported in Table 3.13, where a good agreement with the value obtained in the present work is noted.

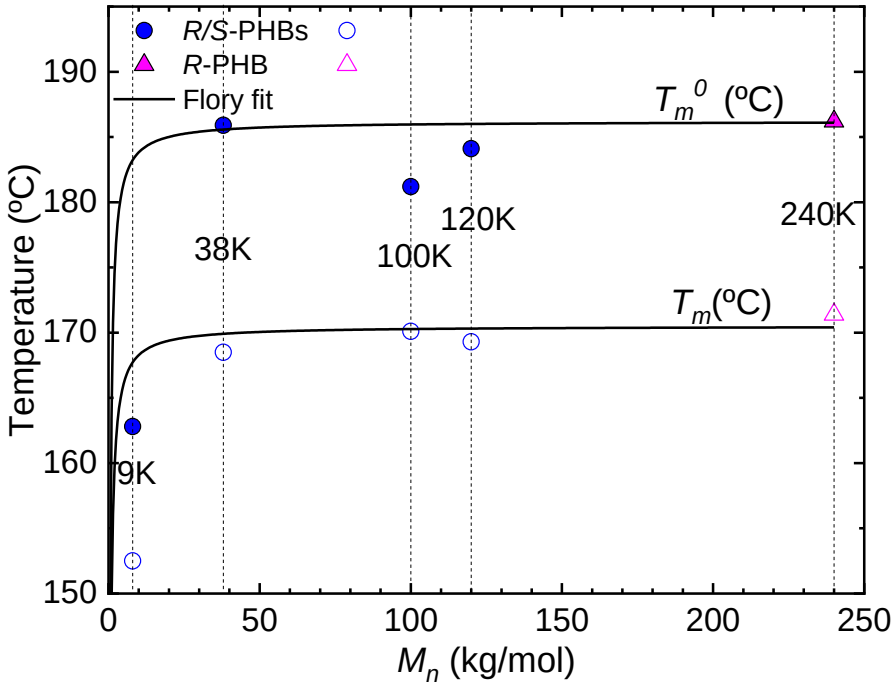

Figure 3.20. Melting Temperature (T_m) and Equilibrium Melting Temperature (T_m^0) as function of molecular weight for bacterial *R*-PHB, *R/S*-PHB 9K, 38K, 100K, and 120K; the solid black lines are Flory's fit for the experimental points.

Table 3.13. Equilibrium melting temperature values reported in the literature.

	T_m^0 (ºC)
Barham et al. PHB[33]	195.0
Greco et al. PHB [50]	196.0
Avella et al.[51]	194.0
Paglia et al. PHB [45]	187.9

3.4 Study of a controlled stereo-defects semicrystalline and biodegradable poly(3-hydroxybutyrate), *sr*-P3HB.

Stereo-defects present in stereoregular polymers often diminish thermal and mechanical properties, and thus suppressing or eliminating them is a major aspirational goal of achieving polymers with optimal or enhanced properties. Here, we accomplish the opposite: by introducing controlled stereo-defects to semicrystalline biodegradable poly(3-hydroxybutyrate), which offers an attractive biodegradable alternative to semicrystalline isotactic polypropylene but is brittle and opaque, we enhance specific properties and mechanical performance of P3HB by drastically toughening it and also rendering it with the desired optical clarity, while maintaining its biodegradability and crystallinity. More specifically, syndio-rich P3HB (*sr*-P3HB), readily synthesized from the eight-membered *meso*-dimethyl diolide, has a unique set of stereomicrostructures comprising enriched syndiotactic [*rr*] and no isotactic [*mm*] triads but abundant stereo-defects randomly distributed along the chain. The highly stereoregular *R/S*-PHB 120K and *st*-P3HB have a high T_m of ~175 °C but a relatively low degradation temperature (T_d, defined as the temperature at 5% weight loss) of ~250 °C, which gives a narrow processing window and makes melt-processing challenging[29,32]. In comparison, *sr*-P3HB, designed as such herein, exhibits a lower T_m of 114 °C (heat of fusion, ΔH_f = 26.7 J/g), while the T_d is maintained at 255 °C (Figure 3.21A,B), thus giving *sr*-P3HB a much wider processing window. It is apparent that *sr*-P3HB shows a much broader melting transition than *R/S*-PHB 120K and *st*-P3HB with higher crystallinity[31,52].

To better understand this difference, successive self-nucleation and annealing (SSA) thermal fractionation studies were performed on *sr*-P3HB and on *R/S*-PHB 120K for comparison purposes[53–55]. We found that *sr*-P3HB can be successfully fractionated by SSA, producing a number of clear and well-resolved thermal fractions

(Figure 3.21C) with a monomodal distribution. In contrast, *R/S*-PHB 120K has a different SSA thermal fractionation profile: there is only one main thermal fraction and a minor secondary one, attesting to its highly regular isotactic structure. This behavior occurs because the thermal fractionation ability of any material increases as the number of defects that can interrupt the linear and stereoregular crystallizable sequences increases. The tacticity defects present in *sr*-P3HB *are randomly distributed along the chain* (hence their monomodal distribution of melting peaks after SSA fractionation[54,55]) and they frequently interrupt crystallizable sequences. This frequent interruption reduces its degree of crystallinity (73% for *R/S*-PHB 120K vs. 15% for *sr*-P3HB after the SSA treatment) and its melting temperature. Figure 3.21D shows a polarized light optical microscopy (PLOM) image of *R/S*-PHB 120K, (already shown above) and it is compared with a micrograph obtained for the *sr*-P3HB sample (Figure 3.21E), under the same cooling conditions from the melt (20 °C/min). The *R/S*-PHB 120K sample is characterized by large spherulites (> 150 μm).[56,57] Instead, *sr*-P3HB has a morphology characterized by a sub-micron spherulitic texture, which will induce optical transparency as the characteristic crystalline aggregates are smaller than the typical wavelength of visible light (i.e., 400 nm) and will not produce any light scattering. This morphology is a consequence of the much higher nucleation density of *sr*-P3HB induced smaller than the typical wavelength of visible light (i.e., 400 nm) and will not produce any light scattering. This morphology is a consequence of the much higher nucleation density of *sr*-P3HB induced by the tacticity defects along the chains. To obtain a larger microspherulitic texture, a heat treatment was performed to *sr*-P3HB followed by isothermal crystallization at 65 °C (Figure 3.21F). Even so, the microspherulites obtained are still

orders of magnitude smaller than those in *R/S*-PHB 120K.

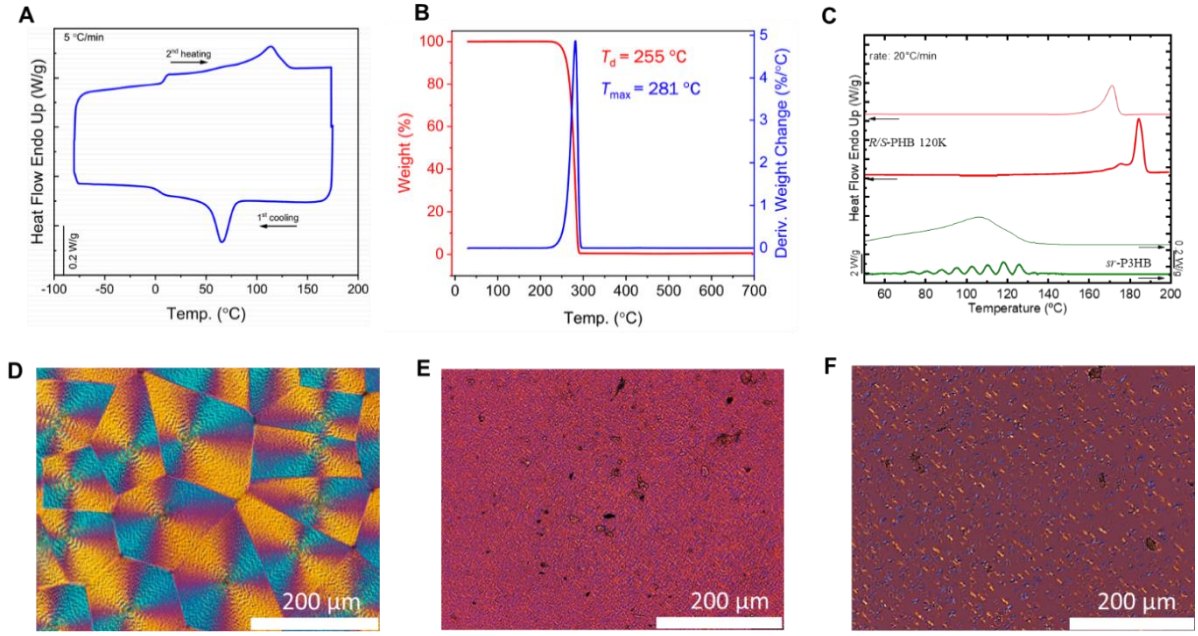

Figure 3.21. (A) Differential scanning calorimetry (DSC) curves of *sr*-P3HB (M_n = 171 kDa, $Đ$ = 1.07). (B) Thermogravimetric analysis (TGA) and derivative thermogravimetry (DTG) curves of *sr*-P3HB. (C) SSA curves of thin lines: DSC second heating curve at 20 °C/min of *sr*-P3HB (green) and *R/S*-PHB 120K (red); thick lines: final DSC heating scans after the SSA protocol for sr-P3HB (green) and *R/S*-PHB 120K (red). (D) PLOM micrographs for *R/S*-PHB 120K. (E) PLOM micrographs for sr-P3HB. Micrographs were taken at 25 °C after melting for 1 min at 190 °C and cooling at 20 °C. (F) PLOM micrographs for sr-P3HB at 65 °C after holding for 1 min at 230 °C and cooling at 20 °C/min.

Tensile testing of the *sr*-P3HB with M_n = 171 kDa ($Đ$ = 1.07) was performed on dog-bone specimens (ASTM D638 standard; Type V), showing a high σ_B of 33.8 ± 1.4 MPa and elastic modulus (E) of 217 ± 12 MPa (Figure 22). More impressively, this *sr*-P3HB material exhibits an excellent ε_B of 419 ± 25% and overall high toughness (U_T) of

96 ± 6 MJ/m^3, making it over 100 times tougher than *it*-P3HB (σ_B = ~35 MPa, ε_B ~3-5%, U_T ~0.6-0.9 MJ/m^3). This large difference in toughness is because *sr*-P3HB has a much lower degree of crystallinity and, at the same time, a refined microspherulitic texture that is expected to lead to a higher ductility.

To ascertain the commercial relevance of *sr*-P3HB, the tensile properties were compared to high-density polyethylene (HDPE), low-density polyethylene (LDPE), polybutylene adipate terephthalate (PBAT), and isotactic polypropylene (*it*-PP) (Figure 3.22). Relative to the high-performance *it*-PP (M_n = 97 kDa), the *sr*-P3HB exhibits comparable σ_B and ε_B values. When compared to HDPE (melt flow index, MFI = 7.6) and LDPE (MFI = 7.5), the *sr*-P3HB shows a similar ε_B but a considerably higher σ_B. It also outperforms PBAT (M_n = 88.5 kDa, σ_B = 21.4 MPa, ε_B = 400%),[59] a commercialized biodegradable alternative to LDPE. These comparative studies demonstrate that the mechanical properties of *sr*-P3HB are competitive with both commodity plastics and their established biodegradable alternatives.

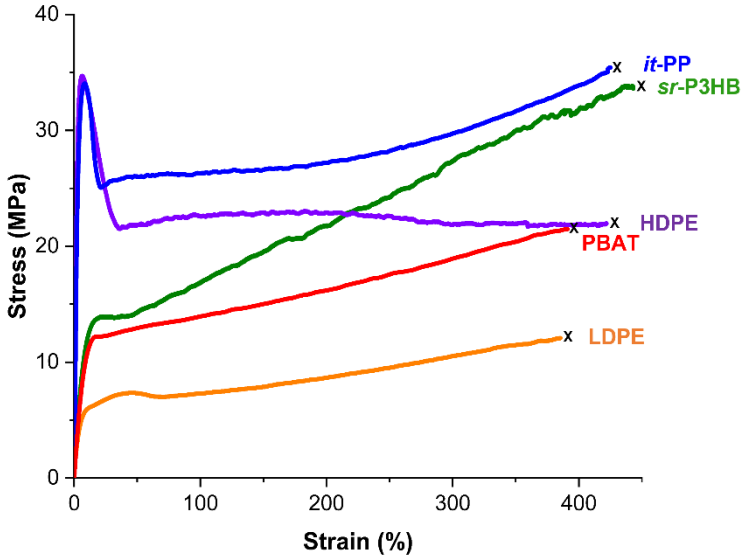

Figure 3.22. Stress-strain curve overlays of *sr*-P3HB (green) with commercialized commodity plastics including *it*-PP (blue), HDPE (purple), PBAT (red), and LDPE (orange). Strain rate: 5.0 mm/min, ambient temperature.

In Figure 3.23 the results of the optical properties are reported and it can be observed that the semicrystalline *sr*-PHB is optically clear by analysis of its transmittance and reflectance properties. Comparing to the transmittance values of commercial materials well-known for their excellent optical properties, *sr*-PHB is as good as poly(methyl methacrylate) (PMMA; *T*% = 92%) and a 40-gallon Ziploc® Bag (LDPE, *T*% = 89%), and far superior to *R*-PHB (*T*% = 19%). This high value of the transmittance registered for *sr*-PHB is due to its particular morphology constituted by very small superstructural aggregates,

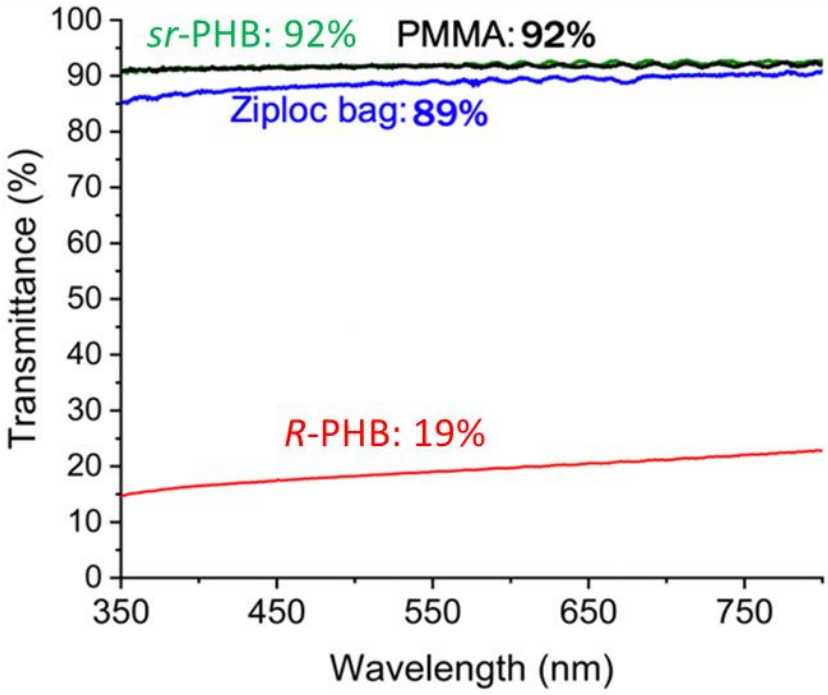

Figure 3.23 Transmittance overlays of *sr*-P3HB (green), PMMA (black), Ziploc Bag® (blue), *it*-P3HB (red).

Figure 3.24 shows the results of the barrier properties. *R*-PHB is known to have outstanding barrier properties with a low water vapor transmission rate (WVTR) and low oxygen permeability (PO_2). These barrier properties are attributed to the high degree of crystallinity of *R*-PHB, as the penetrants cannot be solubilized in the crystallites that

create a tortuous pathway decreasing the diffusion coefficient and thus the permeability. Because *sr*-PHB has a lower degree of crystallinity compared to *it*-P3HB, it is expected that the barrier properties would be inferior. Nonetheless, the *sr*-PHB exhibits barrier properties that outcompete LDPE and commercialized biodegradable alternatives (PBAT and PLLA) in PO_2 and are comparable with PLLA and superior to PBAT in WVTR.

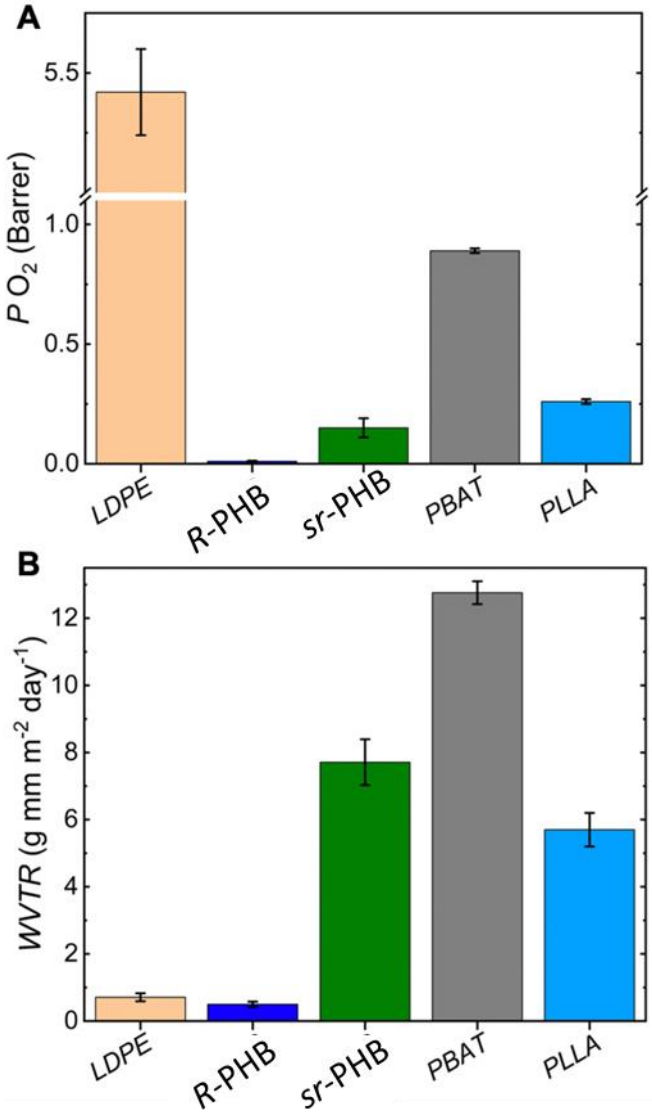

Figure 3.24 (A) Oxygen barriers of *sr*-P3HB compared to commercial plastics: 1 atm, 23 °C, 0% relative humidity. (B) water vaper barriers of *sr*-P3HB compared to commercial plastics, 25 °C.

3.5 Conclusions

In this study, we aimed to uncover the potential effect of the PHB stereochemistry on the crystallization behavior. To do so we performed an in-depth analysis of *R*-PHB with pure *R* stereoconfigurational structure and the analogous racemic mixture when blended with 50% of *S* chains. While we observed no effect of the stereochemistry in the equilibrium melting temperature, given the fact that the crystalline structure of both *R* and 50/50 *R/S*-PHB samples are also identical, we observed an important effect in the crystallization behaviour. Indeed, a higher spherulitic growth rate and an even higher overall crystallization rate were found for the *R*-PHB sample, despite possessing a much higher molecular weight than all the 50/50 *R/S*-PHB racemic mixture samples employed here. Such enhancement in nucleation and growth can only be explained by the differences in enantiomeric character between the samples. The mixture of chains with both *R* and *S* chain configurations can slow down the primary nucleation and the growth of the chain ensemble during crystallization, relative to *R*-PHB chains with only *R* chain configuration. An implication of these results is that the use of the synthetic, racemic PHB could spread the use of PHB-based materials because its employment in the preparation of copolymers and blends with other polyesters could lead to new materials with a slower crystallization kinetics and a wider processability window. Regarding the sample of PHB with stereodefects, a particularly interesting and broader insight obtained from this work is that the randomly distributed, abundant stereo-defects along the *sr*-P3HB chain frequently interrupt crystallizable sequences and thus create a refined sub-microspherulitic morphology that leads to the observed ductility despite being semicrystalline with high tensile strength. In a nutshell, the stereo-defects present in *sr*-P3HB render its superior materials properties in comparison to those of stereo-perfect or highly stereoregular *R/S*-PHB 120K and *st*-P3HB. More broadly, these results further the

more sustainable, mono-material design approach that creates a diverse range of materials properties of polymers via stereomicrostructural engineering without changing their chemical composition.

3.6 References

1. Rorrer, N.A.; Nicholson, S.; Carpenter, A.; Biddy, M.J.; Grundl, N.J.; Beckham, G.T. Combining Reclaimed PET with Bio-Based Monomers Enables Plastics Upcycling. *Joule* **2019**, *3*, 1006–1027, doi:10.1016/j.joule.2019.01.018.
2. Ávila, A.F.; Duarte, M. V. A Mechanical Analysis on Recycled PET/HDPE Composites. *Polym. Degrad. Stab.* **2003**, *80*, 373–382, doi:10.1016/S0141-3910(03)00025-9.
3. Frounchi, M. Studies on Degradation of PET in Mechanical Recycling. *Macromol. Symp.* **1999**, *144*, 465–469, doi:10.1002/masy.19991440142.
4. Achilias, D.S.; Roupakias, C.; Megalokonomos, P.; Lappas, A.A.; Antonakou, V. Chemical Recycling of Plastic Wastes Made from Polyethylene (LDPE and HDPE) and Polypropylene (PP). *J. Hazard. Mater.* **2007**, *149*, 536–542, doi:10.1016/j.jhazmat.2007.06.076.
5. Jehanno, C.; Alty, J.W.; Roosen, M.; De Meester, S.; Dove, A.P.; Chen, E.Y.-X.; Leibfarth, F.A.; Sardon, H. Critical Advances and Future Opportunities in Upcycling Commodity Polymers. *Nature* **2022**, *603*, 803–814.
6. Vollmer, I.; Jenks, M.J.F.; Roelands, M.C.P.; White, R.J.; van Harmelen, T.; de Wild, P.; van Der Laan, G.P.; Meirer, F.; Keurentjes, J.T.F.; Weckhuysen, B.M. Beyond Mechanical Recycling: Giving New Life to Plastic Waste. *Angew. Chemie Int. Ed.* **2020**, *59*, 15402–15423.
7. Ganewatta, M.S.; Wang, Z.; Tang, C. Chemical Syntheses of Bioinspired and Biomimetic Polymers toward Biobased Materials. *Nat. Rev. Chem.* **2021**, *5*, 753–772.
8. Rosenboom, J.G.; Langer, R.; Traverso, G. Bioplastics for a Circular Economy. *Nat. Rev. Mater. 2022 72* **2022**, *7*, 117–137, doi:10.1038/s41578-021-00407-8.
9. LEMOIGNE; M. Produits de Deshydration et de Polymerisation de L'acide B=Oxybutyrique. *Bull. Soc. Chim. Biol.* **1926**, *8*, 770–782.
10. Raza, Z.A.; Abid, S.; Banat, I.M. Polyhydroxyalkanoates: Characteristics, Production, Recent Developments and Applications. *Int. Biodeterior. Biodegrad.* 2018, *126*, 45–56.
11. Sharma, V.; Sehgal, R.; Gupta, R. Polyhydroxyalkanoate (PHA): Properties and Modifications. *Polymer (Guildf).* **2021**, *212*, 123161,

doi:10.1016/J.POLYMER.2020.123161.

12. Khanna, S.; Srivastava, A.K. Recent Advances in Microbial Polyhydroxyalkanoates. *Process Biochem.* **2005**, *40*, 607–619, doi:10.1016/j.procbio.2004.01.053.
13. Le Borgne, A.; Spassky, N. Stereoelective Polymerization of β-Butyrolactone. *Polymer (Guildf).* **1989**, *30*, 2312–2319, doi:https://doi.org/10.1016/0032-3861(89)90267-X.
14. Bonartsev, A.P.; Boskhomodgiev, A.P.; Iordanskii, A.L.; Bonartseva, G.A.; Rebrov, A. V; Makhina, T.K.; Myshkina, V.L.; Yakovlev, S.A.; Filatova, E.A.; Ivanov, E.A. Hydrolytic Degradation of Poly (3-Hydroxybutyrate), Polylactide and Their Derivatives: Kinetics, Crystallinity, and Surface Morphology. *Mol. Cryst. Liq. Cryst.* **2012**, *556*, 288–300, doi:https://doi.org/10.1080/15421406.2012.635982.
15. Lin, X.; Fan, X.; Li, R.; Li, Z.; Ren, T.; Ren, X.; Huang, T. Preparation and Characterization of PHB/PBAT–Based Biodegradable Antibacterial Hydrophobic Nanofibrous Membranes. *Polym. Adv. Technol.* **2018**, *29*, 481–489, doi:https://doi.org/10.1002/pat.4137.
16. Sudesh, K.; Abe, H.; Doi, Y. Synthesis, Structure and Properties of Polyhydroxyalkanoates: Biological Polyesters. *Prog. Polym. Sci.* 2000, *25*, 1503–1555.
17. Li, H.; Shakaroun, R.M.; Guillaume, S.M.; Carpentier, J.F. Recent Advances in Metal-Mediated Stereoselective Ring-Opening Polymerization of Functional Cyclic Esters towards Well-Defined Poly(Hydroxy Acid)s: From Stereoselectivity to Sequence-Control. *Chem. – A Eur. J.* **2020**, *26*, 128–138, doi:10.1002/CHEM.201904108.
18. Wu, B.; Lenz, R.W. Stereoregular Polymerization of [R, S]-3-Butyrolactone Catalyzed by Alumoxane− Monomer Adducts. *Macromolecules* **1998**, *31*, 3473–3477.
19. Jaimes, C.; Arcana, M.; Brethon, A.; Mathieu, A.; Schue, F.; Desimone, J.M. Structure and Morphology of Poly ((RS)-b-Butyrolactone) Synthesized from Aluminoxane Catalyst. *Eur. Polym. Journal-Paper Ed.* **1998**, *34*, 175–186.
20. Bloembergen, S.; Holden, D.A.; Bluhm, T.L.; Hamer, G.K.; Marchessault, R.H. Stereoregularity in Synthetic β-Hydroxybutyrate and β-Hydroxyvalerate

Homopolyesters. *Macromolecules* **1989**, *22*, 1656–1663.

21. Tani, H.; Yamashita, S.; Teranishi, K. Stereospecific Polymerization of β-Methyl-β-Propiolactone1. *Polym. J.* **1972**, *3*, 417–418.
22. Teranishi, K.; Iida, M.; Araki, T.; Yamashita, S.; Tani, H. Stereospecific Polymerization of β-Alkyl-β-Propiolactone. *Macromolecules* **1974**, *7*, 421–427.
23. Lida, S. Directed Integration of an F'plasmid by Integative Suppression. Isolation of Plaque Forming Lamb-Da Transducing Phage for DnaC Gene. *Mol. Gen. Genet. S* **1977**, *15*, 153–162.
24. Agostini, D.E.; Lando, J.B.; Shelton, J.R. Synthesis and Characterization of Poly-β-hydroxybutyrate. I. Synthesis of Crystalline DL-poly-β-hydroxybutyrate from DL-β-butyrolactone. *J. Polym. Sci. Part A-1 Polym. Chem.* **1971**, *9*, 2775–2787.
25. Yasuda, T.; Aida, T.; Inoue, S. Living Polymerization of B-butyrolactone Catalysed by Tetraphenylporphinatoaluminum Chloride. *Die Makromol. Chemie, Rapid Commun.* **1982**, *3*, 585–588.
26. Zintl, M.; Molnar, F.; Urban, T.; Bernhart, V.; Preishuber-Pflügl, P.; Rieger, B. Variably Isotactic Poly (Hydroxybutyrate) from Racemic B-Butyrolactone: Microstructure Control by Achiral Chromium (III) Salophen Complexes. *Angew. Chemie Int. Ed.* **2008**, *47*, 3458–3460.
27. Rieth, L.R.; Moore, D.R.; Lobkovsky, E.B.; Coates, G.W. Single-Site β-Diiminate Zinc Catalysts for the Ring-Opening Polymerization of β-Butyrolactone and β-Valerolactone to Poly (3-Hydroxyalkanoates). *J. Am. Chem. Soc.* **2002**, *124*, 15239–15248.
28. Amgoune, A.; Thomas, C.M.; Roisnel, T.; Carpentier, J. Ring-opening Polymerization of Lactide with Group 3 Metal Complexes Supported by Dianionic Alkoxy-amino-bisphenolate Ligands: Combining High Activity, Productivity, and Selectivity. *Chem. Eur. J.* **2006**, *12*, 169–179.
29. Ajellal, N.; Bouyahyi, M.; Amgoune, A.; Thomas, C.M.; Bondon, A.; Pillin, I.; Grohens, Y.; Carpentier, J.-F. Syndiotactic-Enriched Poly (3-Hydroxybutyrate) s via Stereoselective Ring-Opening Polymerization of Racemic β-Butyrolactone with Discrete Yttrium Catalysts. *Macromolecules* **2009**, *42*, 987–993.
30. Bouyahyi, M.; Ajellal, N.; Kirillov, E.; Thomas, C.M.; Carpentier, J. Exploring Electronic versus Steric Effects in Stereoselective Ring-Opening Polymerization of Lactide and B-Butyrolactone with Amino-alkoxy-bis (Phenolate)–Yttrium

Complexes. *Chem. Eur. J.* **2011**, *17*, 1872–1883.

31. Tang, X.; Westlie, A.H.; Watson, E.M.; Chen, E.Y.X. Stereosequenced Crystalline Polyhydroxyalkanoates from Diastereomeric Monomer Mixtures. *Science (80-.).* **2019**, *366*, 754–758, doi:10.1126/science.aax8466.
32. Tang, X.; Chen, E.Y.X. Chemical Synthesis of Perfectly Isotactic and High Melting Bacterial Poly(3-Hydroxybutyrate) from Bio-Sourced Racemic Cyclic Diolide. *Nat. Commun. 2018 91* **2018**, *9*, 1–11, doi:10.1038/s41467-018-04734-3.
33. Barham, P.J.; Keller, A.; Otun, E.L.; Holmes, P.A. Crystallization and Morphology of a Bacterial Thermoplastic: Poly-3-Hydroxybutyrate. *J. Mater. Sci. 1984 199* **1984**, *19*, 2781–2794, doi:10.1007/BF01026954.
34. Müller, A.J.; Avila, M.; Saenz, G.; Salazar, J. Crystallization of PLA-Based Materials. In *Poly (lactic acid) science and technology: processing, properties, additives and applications*; The Royal Society of Chemistry London, UK, 2015; Vol. 2015, pp. 66–98.
35. Garlotta, D. A Literature Review of Poly (Lactic Acid). *J. Polym. Environ.* **2001**, *9*, 63–84, doi:https://doi.org/10.1023/A:1020200822435.
36. Okamura, K.; Marchessault, R.H. X-Ray Structure of Poly-β-Hydroxybutyrate. In *Conformation of Biopolymers*; G.N. Ramachandran, Ed.; Elsevier, 1967; pp. 709–720.
37. Crist, B.; Schultz, J.M. Polymer Spherulites: A Critical Review. *Prog. Polym. Sci.* 2016, *56*, 1–63.
38. Müller, A.J.; Michell, R.M.; Lorenzo, A.T. Isothermal Crystallization Kinetics of Polymers. *Polym. Morphol. Princ. Charact. Process.* **2016**, *714*, 181–203.
39. Michell, R.M.; Mueller, A.J. Confined Crystallization of Polymeric Materials. *Prog. Polym. Sci.* **2016**, *54*, 183–213, doi:https://doi.org/10.1016/j.progpolymsci.2015.10.007.
40. Wang, Q.; Xie, S.; Hua, Z.; Niu, H. Influence of Isotactic Polypropylene Grafted with Styryl-Group on the Polymer Crystallization Behavior. *Polym. Test.* **2022**, *108*, 107508, doi:https://doi.org/10.1016/j.polymertesting.2022.107508.
41. Lorenzo, A.T.; Müller, A.J. Estimation of the Nucleation and Crystal Growth Contributions to the Overall Crystallization Energy Barrier. *J. Polym. Sci. Part B Polym. Phys.* **2008**, *46*, 1478–1487, doi:10.1002/POLB.21483.
42. Hoffman, J.D.; Lauritzen, J.I.; Jr. Crystallization of Bulk Polymers With Chain

Folding: Theory of Growth of Lamellar Spherulites. *J. Res. Natl. Bur. Stand. Sect. A, Phys. Chem.* **1961**, *65A*, 297, doi:10.6028/JRES.065A.035.

43. Avrami, M. Granulation, Phase Change, and Microstructure Kinetics of Phase Change. III. *J. Chem. Phys.* **1941**, *9*, 177–184, doi:https://doi.org/10.1063/1.1750872.
44. Avrami, M. Kinetics of Phase Change. II Transformation-time Relations for Random Distribution of Nuclei. *J. Chem. Phys.* **1940**, *8*, 212–224, doi:https://doi.org/10.1063/1.1750631.
45. Paglia, E.D.; Beltrame, P.L.; Canetti, M.; Seves, A.; Marcandalli, B.; Martuscelli, E. Crystallization and Thermal Behaviour of Poly (D (−) 3-Hydroxybutyrate)/Poly (Epichlorohydrin) Blends. *Polymer (Guildf).* **1993**, *34*, 996–1001, doi:https://doi.org/10.1016/0032-3861(93)90220-5.
46. An, Y.; Dong, L.; Xing, P.; Zhuang, Y.; Mo, Z.; Feng, Z. Crystallization Kinetics and Morphology of Poly(β-Hydroxybutyrate) and Poly(Vinyl Acetate) Blends. *Eur. Polym. J.* **1997**, *33*, 1449–1452, doi:10.1016/S0014-3057(97)00015-3.
47. Gunaratne, L.; Shanks, R.A. Isothermal Crystallisation Kinetics of Poly (3-Hydroxybutyrate) Using Step-Scan DSC. *J. Therm. Anal. Calorim.* **2006**, *83*, 313–319, doi:https://doi.org/10.1007/s10973-005-6872-8.
48. Pérez-Camargo, R.A.; Liu, G.; Wang, D.; Müller, A.J. Experimental and Data Fitting Guidelines for the Determination of Polymer Crystallization Kinetics. *Chinese J. Polym. Sci* **2022**, *40*, 1–34, doi:https://doi.org/10.1007/s10118-022-2724-2.
49. Gedde, U.L.F. *Polymer Physics*; Springer Science & Business Media, 1995; ISBN 0412626403.
50. Greco, P.; Martuscelli, E. Crystallization and Thermal Behaviour of Poly(d(—)-3-Hydroxybutyrate)-Based Blends. *Polymer (Guildf).* **1989**, *30*, 1475–1483, doi:10.1016/0032-3861(89)90219-X.
51. Avella, M.; Martuscelli, E.; Greco, P. Crystallization Behaviour of Poly(Ethylene Oxide) from Poly(3-Hydroxybutyrate)/Poly(Ethylene Oxide) Blends: Phase Structuring, Morphology and Thermal Behaviour. *Polymer (Guildf).* **1991**, *32*, 1647–1653, doi:10.1016/0032-3861(91)90401-4.
52. Amgoune, A.; Thomas, C.M.; Ilinca, S.; Roisnel, T.; Carpentier, J.F. Highly Active, Productive, and Syndiospecific Yttrium Initiators for the Polymerization

of Racemic β-Butyrolactone. *Angew. Chemie - Int. Ed.* **2006**, *45*, 2782–2784, doi:10.1002/anie.200600058.

53. Bruckmoser, J.; Henschel, D.; Vagin, S.; Rieger, B. Combining High Activity with Broad Monomer Scope: Indium Salan Catalysts in the Ring-Opening Polymerization of Various Cyclic Esters. *Catal. Sci. Technol.* **2022**, 3295–3302, doi:10.1039/d2cy00436d.
54. Müller, A.J.; Michell, R.M.; Pérez, R.A.; Lorenzo, A.T. Successive Self-Nucleation and Annealing (SSA): Correct Design of Thermal Protocol and Applications. *Eur. Polym. J.* **2015**, *65*, 132–154, doi:10.1016/J.EURPOLYMJ.2015.01.015.
55. Pérez-Camargo, R.A.; Cavallo, D.; Müller, A.J. Recent Applications of the Successive Self-Nucleation and Annealing Thermal Fractionation Technique. *Front. Soft Matter* **2022**, *2*, doi:10.3389/FRSFM.2022.1003500.
56. Connor, E.F.; Nyce, G.W.; Myers, M.; Möck, A.; Hedrick, J.L. First Example of N-Heterocyclic Carbenes as Catalysts for Living Polymerization: Organocatalytic Ring-Opening Polymerization of Cyclic Esters. *J. Am. Chem. Soc.* **2002**, *124*, 914–915, doi:10.1021/ja0173324.
57. Yang, J. C.; Yang, J.; Li, W. B.; Lu, X. B.; Liu, Y. Carbonylative Polymerization of Epoxides Mediated by Tri-Metallic Complexes: A Dual Catalysis Strategy for Synthesis of Biodegradable Polyhydroxyalkanoates. *Angew. Chem. Int. Ed* **2022**, *61*, doi:10.1002/anie.202116208.
58. Quinn, E.C.; Westlie, A.H.; Sangroniz, A.; Caputo, M.R.; Xu, S.; Zhang, Z.; Urgun-Demirtas, M.; Müller, A.J.; Chen, E.Y.-X. Installing Controlled Stereo-Defects Yields Semicrystalline and Biodegradable Poly (3-Hydroxybutyrate) with High Toughness and Optical Clarity. *J. Am. Chem. Soc.* **2023**.
59. Sangroniz, A.; Sangroniz, L.; Aranburu, N.; Fernández, M.; Santamaria, A.; Iriarte, M.; Etxeberria, A. Blends of Biodegradable Poly(Butylene Adipate-Co-Terephthalate) with Poly(Hydroxi Amino Ether) for Packaging Applications: Miscibility, Rheology and Transport Properties. *Eur. Polym. J.* **2018**, *105*, 348–358, doi:10.1016/j.eurpolymj.2018.06.016.

Chapter IV

4. Influence of FFF Process Conditions on the Thermal, Mechanical, and Rheological Properties of Poly(hydroxybutyrate-co-hydroxy Hexanoate)

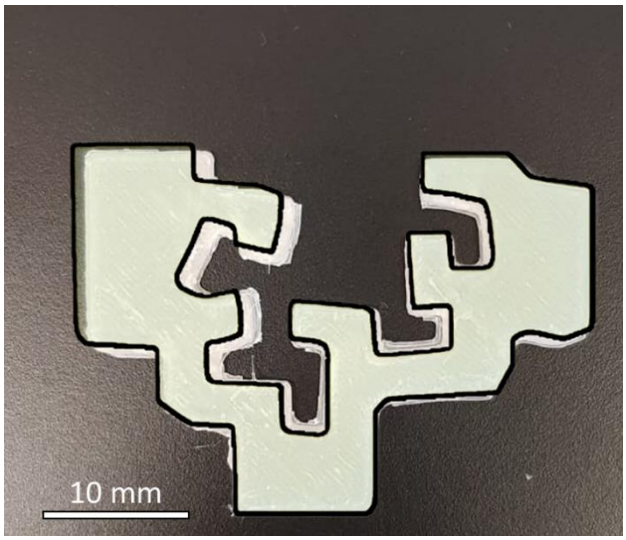

4.1 Abstract

Polyhydroxyalkanoates are natural polyesters synthesized by microorganisms and bacteria. Due to their properties, they have been proposed as substitutes for petroleum derivatives. This work studies how the printing conditions employed in fuse filament fabrication (FFF) affect the properties of poly(hydroxybutyrate-co-hydroxy hexanoate) or PHBH. Firstly, rheological results predicted the printability of PHBH, which was successfully realized. Unlike what usually happens in FFF manufacturing or several semi-crystalline polymers, it was observed that the crystallization of PHBH occurs isothermally after deposition on the bed and not during the non-isothermal cooling stage, according to calorimetric measurements. A computational simulation of the temperature profile during the printing process was conducted to confirm this behavior, and the results support this hypothesis. Through the analysis of mechanical properties, it was shown that the nozzle and bed temperature increase improved the mechanical properties, reducing the void formation and improving interlayer adhesion, as shown by SEM. Intermediate printing velocities produced the best mechanical properties.

Caputo, M. R., Fernández, M., Aguirresarobe, R., Kovalcik, A., Sardon, H., Candal, M. V., & Müller, A. J. (2023). Influence of FFF Process Conditions on the Thermal, Mechanical, and Rheological Properties of Poly (hydroxybutyrate-co-hydroxy Hexanoate). *Polymers*, *15*(8), 1817.

4.2 Introduction

Plastics are the most important materials for producing useful objects and molded parts in modern life. They are lightweight, have good mechanical properties, low corrosion properties, relatively low cost, and are versatile. However, many parts made of plastic materials are manufactured for single use. These materials take many years to degrade and contribute to the high volume of waste generated in the world (the so-called islands of plastic in the ocean, made up of microplastics of different origins), which is a severe environmental problem that exists today and needs to be solved.

Many solutions to plastic pollution could be applied: (a) reduce the use of single-use plastics, (b) participate in a beach cleanup, (c) fulfill support legislation related to plastic waste, (d) recycle/reuse, and (e) make the public aware of this problem. Another solution is the development and use of more environmentally friendly materials. Many researchers are studying the use of biopolymers to be scaled in industry, such as poly(lactic acid) (PLA), poly(ε-caprolactone), poly(butylene succinate), poly(hydroxy alkanoates) (PHA), thermoplastic starch, among others. The production of these materials has been experiencing continuous growth in recent years, although it still represents less than 1% of the production of conventional plastics [1].

Polyhydroxyalkanoates (PHA) are linear thermoplastic polyesters of hydroxy alkanoic acids synthesized by various microorganisms and bacteria [2–6]. They have been proposed to replace some petrochemical-derived plastics [2–4], References [7–10] such as polyethylene, polypropylene, and polyethylene terephthalate. They are biocompatible, biodegradable, and non-toxic polymers that can be produced from renewable resources. They are highly crystalline, piezoelectric, and non-soluble in water.

PHA is considered one of the most important candidates to decrease the problem of plastic contamination [11], thus reducing the carbon footprint and contributing to a

circular economy. However, PHAs have some disadvantages, including poor thermal-mechanical properties, susceptibility to thermal degradation, difficulty processing using conventional plastic processing techniques, and high production cost [12,13].

PHAs have a wide range of properties depending on the monomeric composition of polymers or copolymers, which are likely responsible for their different applications in various industries such as: (a) Biomedical sector: stents and artificial heart valves [14,15], pericardial patches, tissue engineering [16,17], nerve repair and regeneration [18–20], articular cartilage and tendon repair devices, bio-implant patches [21], sutures, tacks, staples, surgery [22], wound dressing [23], adhesion barriers, ocular cell implants, skin substitutes, prosthetics [24], meniscus repair devices, bone plates and bone plating systems, orthopedic pins, spinal fusion cages, bone graft substitutes, bone dowels, bone marrow scaffolds [25–29]; (b) pharmaceutical industries: biosurfactants and drug delivery systems [30–38]; (c) packaging sector (films, bags, containers, paper coatings) [39,40]; (d) disposable products (razors, cosmetic containers (shampoo bottles and cups utensils), diapers, feminine hygiene products [41]; (e) water treatment; (f) paper modification (sizing of paper); (g) cosmetic industries and (h) agricultural sector [42].

There are different PHAs produced at an industrial scale. These include poly(3-hydroxybutyrate) (PHB), poly(3-hydroxybutyrate-co-3-hydroxyvalerate) (PHBV), poly(3-hydroxybutyrate-co-4-hydroxybutyrate) (P3HB4HB), and poly(3-hydroxybutyrate-co-3-hydroxyhexanoate) (PHBH) [41,43,44].

The random copolymer PHBH shows a broader processing window than PHB and PHBV. Moreover, PHBH has good thermo-mechanical and physicochemical properties due to its tailorable composition of elastomeric (3-HH) and highly crystalline (3-HB) units [45].

Nowadays, there is a great interest in using this eco-friendly material (PHBH) for two applications: packaging (disposable bags, food packaging, and agricultural mulch films) [46] and tissue engineering (scaffolds) due to its flexibility and room temperature compostability, biocompatibility, and biodegradation properties. Specifically, the manufacture of scaffolds used in tissue engineering with PHBH is recommended through additive manufacturing (AM) (3D printing), more specifically, fused filament fabrication (FFF). Various PHA-based materials have already been processed with this technique: for example, Wu et al. studied the printability of esterified PHBV containing different fillers [47–49]. Furthermore, Tian et al. [50] have studied how the presence of wood flour improves the stiffness of PHAs and reduces the costs associated with their production. The use of the PHBH for biomedical applications is promising because it exhibits excellent mechanical properties, does not have cytotoxicity, and has a significant proliferation of mouse embryonic fibroblast cells. Additionally, its hydrolytic degradation is faster than PLA [51,52], and some blends with PHBH are used by FFF to improve specific properties.

Stanzani et al. [53] and Giubilini et al. [54] used PHBH reinforced with cellulose nanocrystals (CNCs) to make scaffolds for eco-sustainable regenerative medicine because of the increase in the degree of disintegration of the polymers under simulated composting conditions. Furthermore, FFF allows complex structures to be produced as scaffolds. Valentini et al. [55] studied the properties of the composite of fibrillated nano cellulose (NCF)/PHBH in 3D printing by FFF. The stress at break and elongation at break showed a maximum at 0.5 wt% NCF, but the presence of NCF did not affect the thermal degradation behavior of the polymer.

Kovalcik et al. [51] studied the properties of 3D printing gelatin-coated and non-coated scaffolds of PHBH. The gelatin-coated in the PHBH scaffold does not significantly

affect the adhesion and proliferation of cells compared with the pure PHBH, which promotes cell growth due to its hydrophilicity.

However, no publications are reported in the literature on measuring the tensile properties of parts manufactured by FFF with PHBH and their relationship with thermal and rheological properties. This work studies the relationship between the FFF processing conditions and the thermal, mechanical, and rheological properties, complemented by numerical simulation, to understand the process of deposition and cooling of the layers during PHBH additive manufacturing. The correlation between crystallinity degree, melt viscosity, and tensile test properties on printing conditions are presented. The mechanical properties of manufactured parts have been compared with compression-molded specimens.

4.3 Results and Discussion

4.3.1 Thermal Analysis

4.3.1.1 Differential Scanning Calorimetry (DSC)

a. Virgin material (filament)

Figure 4.1 compares the cooling and second heating DSC scans of the PHBH filament. In the second heating, a cold crystallization phenomenon is observed in the sample, which then melts with a bimodal profile. Cold crystallization is a typical phenomenon of polyhydroxyalkanoates already reported by Caputo et al. [56] in the case of high molecular weight PHB. During cooling at 20 °C/min, the PHBH cannot complete crystallization until saturation; hence, it exhibits cold crystallization in the subsequent heating scan. The double melting peak observed is most probably due to melting and reorganization during the scan, as also reported for other thermoplastic materials [57,58]. However, a more detailed study (outside the scope of the present work) would be needed to confirm this fact.

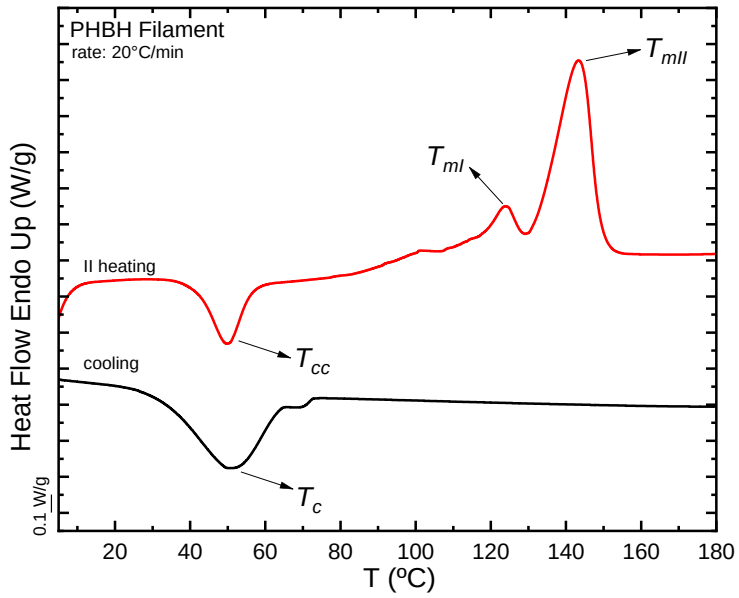

Figure 4.1 DSC scans of cooling and second heating for the filament of PHBH.

Table 4.1 reports the thermal parameters obtained through these experiments. As expected, the crystallization and melting temperatures of PHBH and the related enthalpies, regardless of whether in the form of a filament or a 3D printed specimen, are lower than those reported for PHB [56], as the PHB is randomly copolymerized with the hydroxyhexanoate to obtain PHBH. The comonomeric units interrupt the crystallizable PHB sequences; therefore, the lamellar thickness is reduced and, concomitantly, the melting point. Analyzing these values made it possible to determine the minimum temperature for printing. Having to use a temperature at least 30 °C higher than the melting point to melt the polymer and erase its crystalline thermal history fully [59], the minimum temperature that could be used would be 170 °C. Despite this, at this temperature, the polymer does not reach such a fluidity to be extruded with the supplied printer used in this work. Therefore, the minimum printing temperature was set at 180 °C.

Table 4.1 Thermal DSC cooling and heating properties of the PHBH filament.

Sample	**Cooling**		**Second Heating**				
	T_c **(°C)**	ΔH_c **(J/g)**	T_{cc} **(°C)**	ΔH_{cc} **(J/g)**	T_m **(°C)**	ΔH_m **(J/g)**	x_c **(%)**
Filament	50.2	43	51.2	17	124.1/143.5	60	49

Furthermore, since the thermogravimetric analysis performed by Kovalcik et al. [51] showed that the degradation temperature of PHBH is 220 °C, the maximum printing temperature used in this work was 200 °C.

b. Printed part (Tower)

A study of the melting temperature of the different layers of a 3D-printed tower was carried out to observe any variations in this value and clarify whether the crystallization process occurs in an isothermal manner or not. A small sample was taken from five different layers in the tower, and a heating DSC ramp was performed. Figure 4.2a shows the DSC first heating scans for the five layers analyzed compared to the first heating scan of the filament. In Figure 4.2b, the melting temperatures and enthalpies are shown as a function of the layer number. As already found in the case of the filament, the scans of the various layers also show a bimodal melting peak; furthermore, only minor differences are observed in the melting temperatures and enthalpies values, as seen in Figure 3b. This result was unexpected as FFF is usually a non-isothermal process.

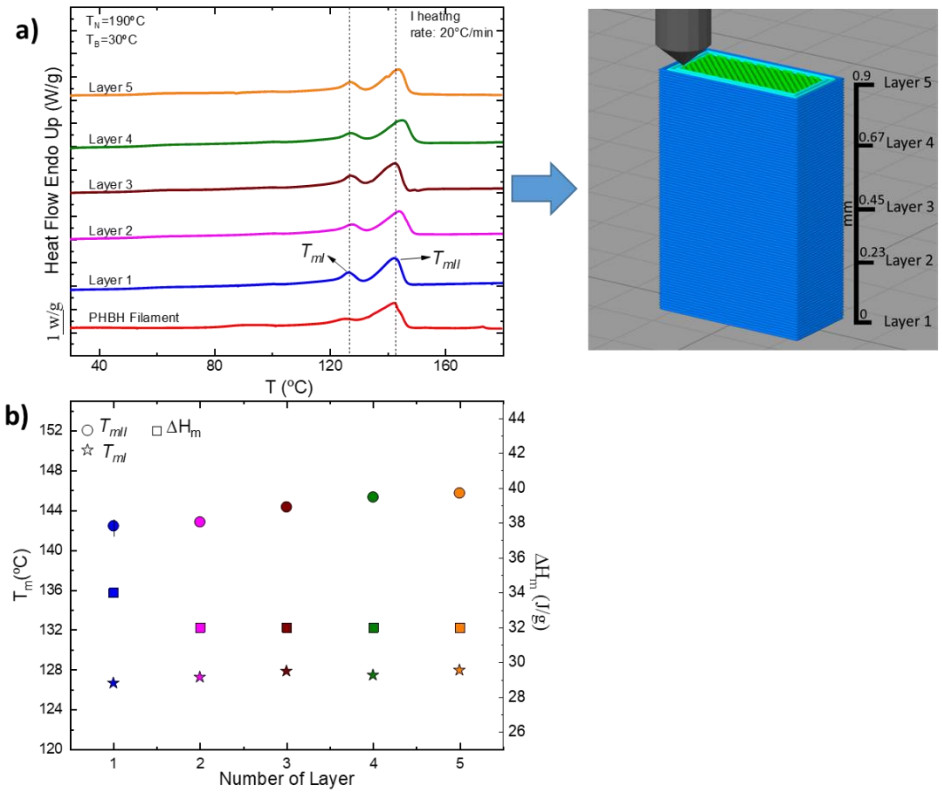

Figure 4.2 (**a**) First heating DSC scans of different layers of the PHBH tower and (**b**) melting temperatures as a function of the number of layers.

Because of the similar T_m and ΔH_m results, heat transfer simulations were carried out to better understand the thermal properties (crystallization conditions) during the 3D-printing process, specifically, why intrinsically non-isothermal manufacturing (FFF) leads to no differences in the crystallinity of the material.

Figure 4.3a shows the temperature evolution for a printing system of different layers (layers 1 to 5). In that case, "n" represents the deposited layer, and "n − 1" represents the layer below the printed layer. According to the results, except for the first layer, the deposited polymer reached a constant temperature of 25 °C (T_{amb}) in 5 seconds. This time is very short and, therefore, could prevent the crystallization of PHBH during the cooling from the melt. In addition, the temperature reached for the "n − 1" layer was around 40 °C, much below the cold crystallization temperature of the material. Although polymers are not good thermal conductors, the surface area in contact with air is

sufficiently high to produce such a fast temperature decrease. In addition, the results are in good agreement with previously reported data for ABS [60]. More interestingly, the thermal profile that the material suffers during manufacturing is similar, regardless of the layer number, and therefore, no differences in crystallization should be expected among layers.

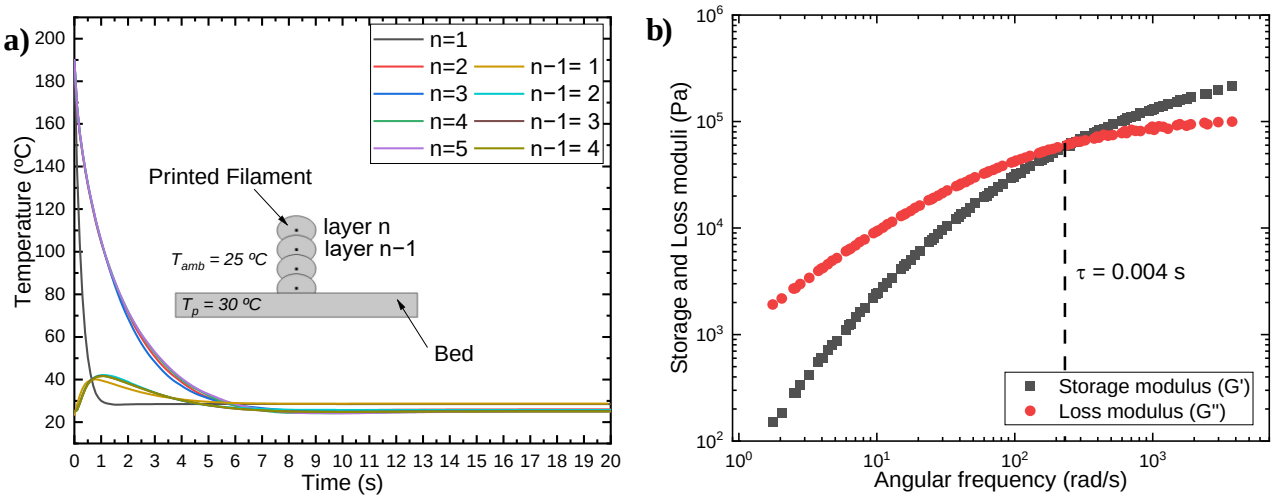

Figure 4.3 (**a**) Temperature profile during the cooling of the filament as a function of layer and (**b**) frequency sweep experiments at 190 °C. Relaxation time was calculated as the reciprocal of the cross-over frequency.

It is noteworthy that such a high cooling printing velocity might affect the interlayer adhesion of the printed specimens. However, as can be seen from the rheological frequency sweep experiments (Figure 4.3b), the relaxation time of the polymer chains at the nozzle temperature is below 10^{-2} seconds, which ensures interlayer adhesion [61].

4.3.1.2 Rheological Characterization

The properties of biodegradable polymers are highly dependent on processing conditions such as humidity, temperature, shear rates, and processing time, so rheological characterization can provide valuable information for optimizing the 3D printing process of these materials.

Many efforts have been made to identify the relevant physical parameters that govern 3D printing. The application of rheological knowledge to understand the critical physics and implications in all aspects of the process, involving nozzle flow, the nozzle-bed standoff region, and finally, the deposition on the print bed, is considered of great importance to determine and identify the correlation between material properties, processing variables, and the resulting mechanical properties. Most recent reviews, gathering numerous studies and detailed discussions on the subject, highlight the following key aspects to deep in this understanding [62–65]: (a) temperature-dependent shear and extensional viscosity correlate with the extrusion quality through the print nozzle and in the region between the nozzle and the bed; (b) chain dynamics as the melt cools once deposited, governs the degree of interlayer welding and controls mechanical performance; (c) the evaluation of the flow-induced crystallization under complex flow and thermal fields developed within the nozzle is relevant in the predictions of the mechanical properties. Therefore, evaluating the polymer relaxation dynamics under the combined effect of shear rate and temperature profile, from the perspective of the disentanglement and orientation state of the chains during extrusion and post-extrusion entanglement recovery, is contemplated as essential for the improvement of the simulation and optimization of the 3D printing process.

The viscoelastic behavior of the polymer determines two essential aspects of the 3D printing process: the extrusion of the melt through the nozzle and the welding of layers during the subsequent deposition stage [66]. Thus, the analysis of the dynamics and time scales of the polymer and how they are affected by the printing temperature and velocity will be fundamental aspects of the rheological characterization performed in this work.

The melt viscosity and its dependence on temperature and shear rate determine the ability of polymers to flow. Figure 4.4 shows the melt viscosity curves of PHBH at T

= 190 °C. The aforementioned Cox–Merz rule is fulfilled as a good correlation of continuous values, $\eta(\dot{\gamma})$, and dynamic, $\eta^*(\omega)$, viscosities are observed as a function of frequency. Considering that the rule does not hold for phase-separated (e.g., block copolymers) or complex polymer systems, this result suggests the random nature of the PHBH copolymer [67].

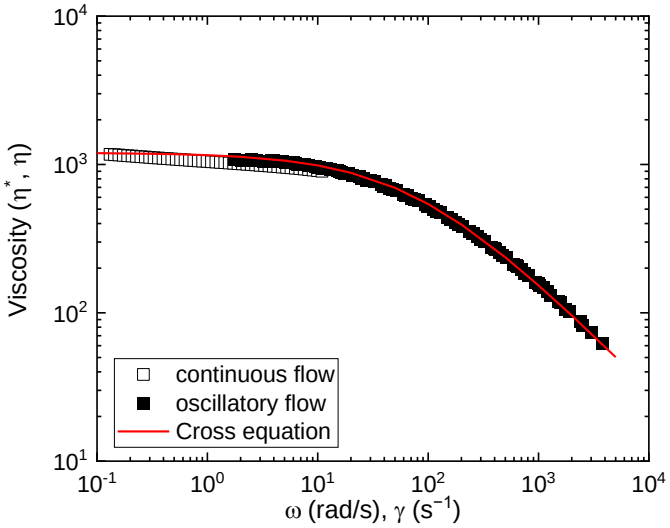

Figure 4.4 PHBH viscosity curves at T = 190 °C from continuous flow and oscillatory flow (TTS superposition master curve). A fitting to the Cross equation is included [η_0 = 1200 Pa s, λ_0 = 0.013 s, and α = 0.75].

As can be seen in Figure 4.4, PHBH flow is quite sensitive to shear, the pseudoplastic behavior well characterized by the Cross equation [68]:

$$\eta = \frac{\eta_0}{1+(\dot{\gamma}\lambda_0)^{\alpha}} \tag{4.1}$$

where η_0 is the Newtonian viscosity, λ_0 is the relaxation time, and α a non-linearity index. The values of the fit of experimental data to the equation for the polymer PHBH are included in Figure 5. The viscosity curve is comparable to commercial materials widely used in filament-based 3D printing. As an example, at typical extrusion shear rates of $\dot{\gamma}$ = 200 s^{-1}, the viscosity of PHBH, η = 400 Pa s, lies between the viscosities of ABS acrylonitrile-styrene (ABS), η = 1000 Pa s, and that of polylactic acid

(PLA), η = 200 Pa s, as observed in Figure 9 of [57] (Candal et al., 2020). Therefore, as a first result, the flow behavior of this biodegradable polymer would meet the requirements to be processed by extrusion during 3D printing.

However, the complete evaluation of this polymer requires special attention to its welding response, which is one of the critical parameters of 3D technology. Poor adhesion between deposited filaments often results in poor mechanical properties of the printed samples. Polymer-polymer welding, necessary to ensure the strength of the final printed part, implies a satisfactory interdiffusion and reentanglement of the molten polymer across the filament-filament interfaces [69]. Thus, this property, which is highly dependent on the viscoelastic response, will also be addressed in our study.

The entanglement due to the hypothetical tubular region that restricts the diffusive motion of a polymer chain can be modeled to obtain the characteristics time scales that account for the molecular dynamics: reptation time, τ_d, which governs chain orientation and alignment to relax, and the Rouse time τ_R, which is the time for the polymer chain to relax within the tube region and governs stretch relaxation [70]. Under typical printing conditions, the residence time is similar to the reptation time, τ_d (related to the time that has been determined with the Cross Equation, λ_0) and which allows assuming that a stationary flow develops at the printer nozzle. The relevant parameter that gathers information about the diffusion of the entanglement in the weld zone is considered to be the entanglement density, Z_e, which is defined as $Z = M_e/M_w$, where M_e is the molecular weight of the entanglement and M_w is the molecular weight of the polymer. M_e is related to the entanglement modulus, G_N^0 through the generally accepted equation:

$$G_N^0 = \rho RT/M_e \tag{4.2}$$

where ρ is the density, and R is the gas constant.

The experimental viscoelastic functions, storage modulus, G', and loss modulus, G'', measured at different frequencies and temperatures, were analyzed using the time-temperature superposition method. The nice superposition is shown in Figure 4.4 (complex viscosity) and Figure 4.5 (storage and loss moduli). Shift factors, a_T, follow a temperature Arrhenius-like dependence, which is given by:

$$a_T = Ae^{-\frac{E_a}{RT}} \tag{4.3}$$

where A is a pre-exponential factor, R is the gas constant and E_a = 51 KJ/mol is the flow activation energy. The master curve obtained at T = 190 °C, as the reference temperature, contains information about the terminal and the rubbery zones, from which it is possible to calculate the entanglement density in the absence of shear, Ze. To determine this parameter, the experimental master curve was fitted to the Likhtman–McLeish theory [71] using RepTate software [72].

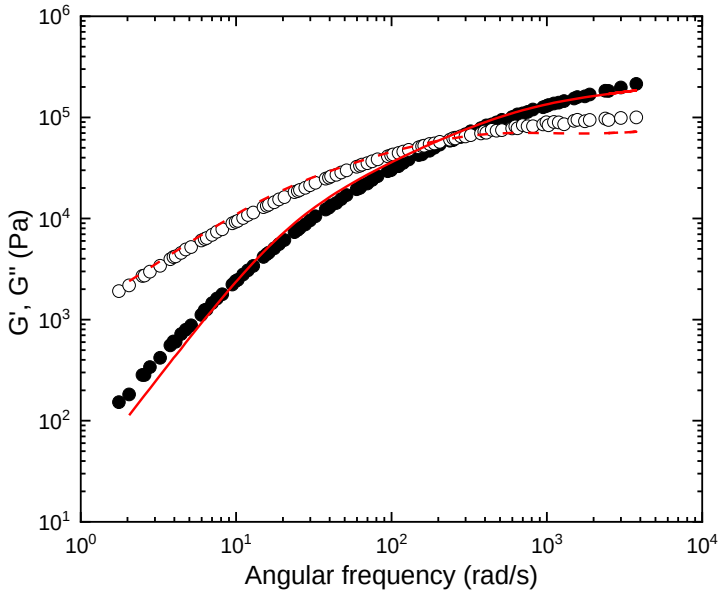

Figure 4.5 Master curve at the reference temperature T = 190 °C for PHBH fitted to the Likhtman–McLeish theory. [G_N^0 = 400,000 Pa, M_e = 8960 g/mol and τe = $3.5 \cdot 10^{-6}$ s, τ_d = 0.026 s, τ_R = 0.001s].

The entanglement molecular weight, M_e, is then used to characterize the entanglement density, Z_e. Considering the molecular weight of M_w=163,000 g/mol (Table 1), a value Z = 18 is obtained for PHBH.

According to the model of McIlroy and Olmsted [69], the entanglement number Z_e should be in the range Z = 20–30 to obtain a good welding response. The lower limit is very close to the result estimated here for PHBH and similar to those found in the literature for printable PLA polymers with good interlayer adhesion, such as the value of Z = 17 for polylactic acid (PLA) where the mass M_w = 156,000 g/mol and M_e = 9000 g/mol [73], and the value of Z = 19 for the PLA polymer of M_w = 173,000g/mol and M_e = 9000 g/mol [70]. Notwithstanding, an acceptable strength across the interface, with considerably lower Z values, was observed for some polymers, as in the case of PBS and PBSA [66]. In particular, a value of Z = 8 was reported for PBS with M_e = 8750 and M_w = 79,250, and a value of Z = 9 for PBSA with M_e = 9000 and M_w = 78,600. This leads us to consider that molecular chain diffusion might not be the only controlling factor during weld formation for these polymers.

In fact, the high speed of cooling inherent to the 3D printing process could also affect interlayer welding. The polymer chains have to diffuse across the layer interface at a distance equivalent to the radius of gyration (Rg) to ensure interlayer adhesion [69]. The extent of interdiffusion will depend on the time available before the chain loses mobility due to crystallization [74]. At the temperatures selected in this study [Section 3.1.1.b], the PHBH chains are expected to have sufficient time for good interlayer adhesion to be acquired. The interdiffusion time of PHBH, in terms of the reptation time, τ_d = 0.026 s (shown in Figure 4.5, T = 190 °C), is close to the value reported by Das et al. [77] for PLA, τ_d = 0.048 s (T = 190 °C) subjected to a printing process characterized by bond strength increasing with printing temperature and crystallization that did not impede

interdiffusion dynamics. Moreover, the time for welding could be even lower if models based on reptation adapted to non-isothermal conditions are considered. Yang et al. (2002) [75] studied PEEK-based polymers during 3D printing. They suggested that experimental welding times shorter than the reptation time could be explained if the interpenetration length at the weld is redefined. Indeed, minor chains (end chains) would not need to diffuse across a distance equal to Rg to reach bulk properties.

The effects of molecular orientation during polymer extrusion must also be considered. Typical shear rates in 3D printing vary between 100 s^{-1} and 1000 s^{-1} in the non-Newtonian flow regime of polymers, where chains can be oriented and aligned in the direction of flow if the deformation is faster than molecular relaxation times. In case the macromolecular chain orientation can be retained after deposition, the resulting anisotropy could lead to improved mechanical properties such as elastic modulus and tensile strength, as reported by Gonzalez Ausejo et al. (2018) [76] for a PLA/PHA blend. A more ordered chain configuration can facilitate and enhance crystallization, as observed for PCL (Liu et al. (2018)) [77] and polyamide (PA) 12 (De Jager et al. (2020)) [78].

On the other hand, interlayer welding can also be affected. Models [70,79–81] predict that the development of oriented polymer chains results in a shear-induced disentanglement process that decreases entanglement densities. This could negatively impact welding energy for printing conditions where entanglement does not have sufficient time to recover during cooling, as the degree of chain stretching during shear is determined by the competition between shear deformation and chain relaxation in the tube. Printing at low temperatures and high velocities was found to decrease the weld strength in the prints of multiple semi-crystalline polymers, including PLA, PP, and PA [62]. However, the extrusion-induced orientation can also be relaxed after deposition with increasing build temperature or residence time because polymer chain mobility is

enhanced, and thus relaxation can occur more easily as orientation gets lost. For a PLA with low crystallinity [70], the weld strength decrease is observed at printing velocities above 60 mm/s at lower temperatures, when relaxation times are expected to increase considerably. On the other hand, a small effect of printing velocity on tearing energy is reported for PBSA and PBS [66] because larger velocities than applied are probably needed to observe significant effects. This seems to be the case of the printed samples of PHBH studied here, where the good adhesion, evaluated in terms of homogeneity of the interlayers observed by SEM [Figure 4.9, shown below in paragraph 3.3], is not deteriorated by the printing velocity. Then, it can be assumed that the entanglement density is slightly affected by the shear rate or that the chains have enough time to relax and re-entangle.

Certainly, the formation of welds during 3D printing is very complex. Although, as mentioned above, there is an apparent loss of entanglement with increasing alignment, the rate of chain reorientation would still be close to the equilibrium values given by the tube models of polymer dynamics, as discussed by Gunha et al. (2020) [85]. Thus, interfacial entanglement reformation should be relatively insensitive to alignment, and welds of oriented molecules should be as strong as bulk isotropic materials when the molecules have sufficient time to diffuse along their tube. This is certainly not the general behavior in 3D printing processes. With this concept in mind, Seppala et al. (2017) [86] analyzed the welding between ABS layers under rapidly changing mobility conditions. They discussed several factors that may contribute to the underperformance observed in 3D printing, including the necessity of longer effective welding times, degradation at higher temperatures, stress concentration due to the shape of the part, and the polymer alignment playing an important role.

In summary, the welding might not be limited to inter diffusion, and other arguments should be considered. Similarly, Constanzo et al. (2022) [87] discussed the effect of anisotropy on welding. They analyzed the behavior of copolyesters with different relaxation times but similar welding properties. The different chain stiffness of these copolyesters affected the non-equilibrium configuration of the entanglement network after printing in a way that the lower molecular extensibility of the stiffer chains was related to a decrease in anisotropy degree able to regulate the weld response. The results agreed with the findings from molecular simulations of 3D print samples, where the residual molecular anisotropy could affect the mechanical properties since the aligned material near the weld is weaker than the non-aligned material [85]. Therefore, the alignment effect at high printing rates could decrease mechanical properties, even though the reptation times indicate sufficient time to diffuse along the tube.

It should also be noted that molecular dynamics and processing conditions could affect the crystallization dynamics, as stated before. The development of the oriented shear-induced crystallinity precursors depends on the deformation rate that is experienced by the polymer melt. The flow strength can be quantified by dimensionless numbers, such as the Deborah number, De, and the Weissenberg number, Wi. Following the analysis proposed by McIlroy and Olmsted [81,82], the description of the 3D printing process can result in flow-induced crystallization under the following conditions: (1) The flow is sufficiently strong to stretch polymer chains, a condition that can be quantified by the Rouse Weisenberg number ($W_{iR} = \dot{\gamma}\tau_R$) that governs polymer stretching, greater than 1. (2) When the residual stretch persists at the onset of nucleation, a condition that can be quantified by the inverse of the Deborah number, D_e^{-1}, defined as the ratio of the time taken for the material to cool to the melting temperature, τ_m, to the stretch relaxation time, τ_R, $De^{-1} = \frac{\tau_m}{\tau_R}$, lower than 1. Under these conditions, $W_{iR} > 1 \wedge De^{-1} < 1$, the stretched

polymer chains would provide flow-enhanced crystallization. The apparent shear rates considered in this study (8 V/d, where V is the printing velocity and d=0,4 mm is the nozzle diameter) were of the order of $\dot{\gamma} = 400\, s^{-1}$ (V = 20 mm/s) to $\dot{\gamma} = 800 s^{-1}$ (V = 40 mm/s). According to the Rouse/stretch relaxation time of PHBH, estimated by fitting viscoelastic moduli to the Likhtman–McLeish theory (τ_R = 0.001 s, see Figure 4.5), the shear rate values are sufficiently low so that the applied flow does not stretch polymer chains. In addition, the condition of $De^{-1} < 1$ will be acquired only for $\tau_m < 10^{-3}$ s, a value which is not expected for the 3D printing procedure considered here (see temperature profile in Figure 4). The analysis is of proven utility in the discussion of flow-enhanced structures during extrusion printing of polylactic acid (PLA) and polycaprolactone (PCL) [82]. PC analysis shows that at high temperatures, the polymer stretch becomes fully relaxed before the temperature reaches the melting point, so there is no flow-enhanced crystallization. However, the analyzed PLA behaves quite different because it has a much higher glass transition temperature that will arrest crystallization during printing. The entanglement time calculated for PHBH ($\tau e = 3.5 \cdot 10^{-6}$s), which is even lower than the corresponding value for PCL ($\tau e = 1.9 \cdot 10^{-5}$s), allows expecting a similar behavior for both polymers. As explained above, the W_{iR} and De^{-1} calculations for PHBH predict that flow-induced crystallization is not favored under the printing conditions studied here.

4.3.1.3 Evaluation of the Effect of Pressure and Temperature on Specific Volume/Density

The pressure-volume-temperature (PVT) diagram is widely used in science and industry for polymer injection molding [83]. However, the exact change of the specific volume during the printing process is usually not considered. Only a few recent papers refer to density models that simulate the velocity profile inside the nozzle and study the effect of pressure on viscosity and flow inside the printer [84,85].

In this work, following the perspective of investigating the parameters that affect the strength and quality of the printed parts, for example, from the rheology and microstructure, as already discussed in the rheological characterization section, we will try to introduce a qualitative analysis of the observed shrinkage and warpage in terms of the pressure-volume-temperature data obtained for the PHBH polymer.

Figure 4.6 presents the PVT diagrams obtained under isobaric cooling for the PHBH polymer. The experimental data were fitted to the Tait equation, a two-domain empirical model to plot the specific volume as a function of the process variables: pressure and temperature (changes due to shear during extrusion are not considered). Fitting parameters are included in Table 4.2.

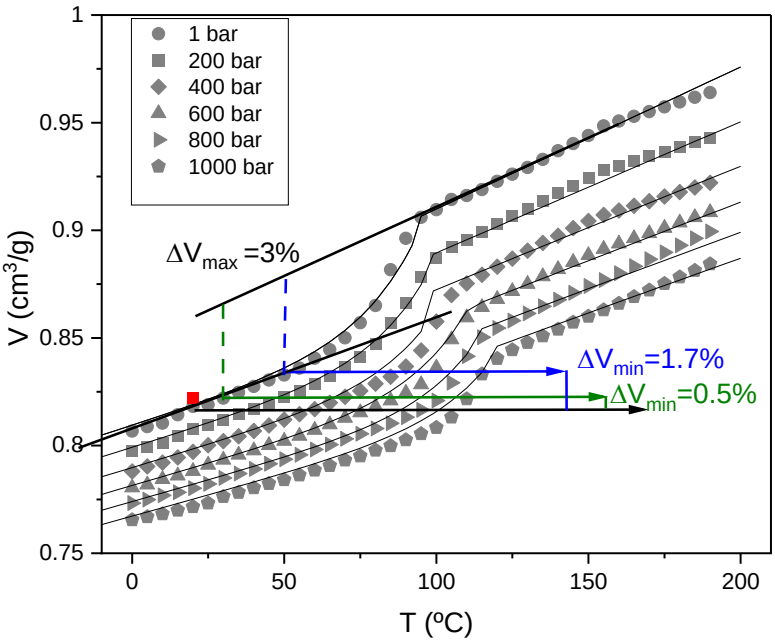

Figure 4.6 PVT diagram obtained under the isobaric cooling condition at 5 °C/min for PHBH polymer. Grey symbols are experimental-specific volumes at the pressures specified in the legend. Lines correspond to the Tait equation. The red symbol corresponds to the density of the printed part measured using an electronic densitometer (not PVT data). Changes in the specific volume are discussed in the text (lines in blue

correspond to changes when T_{bed} = 50 °C, and lines in green correspond to changes for T_{bed} = 30 °C).

Table 4.2 Two-domain Tait equation estimated parameters of the PHBH polymer PVT experimental data obtained in isobaric cooling at 5 °C/min.

Solid State		**Molten State**		**Liquid-Solid Transition**	
b_{1s} (cm^3/g)	0.8540	b_{1m} (cm^3/g)	0.9100	b_5 (°C)	98
b_{2s} (cm^3/g °C)	$4.5 \cdot 10^{-4}$	b_{2m} (cm^3/g °C)	$6.628 \cdot 10^{-4}$	b_6 (°C/Pa^2)	$2.32 \cdot 10^{-7}$
b_{3s} (Pa)	1.11910^8	b_{3m} (Pa)	$6.5970 \cdot 10^7$		
b_{4s} ($°C^{-1}$)	1.12310^{-3}	b_{4m} ($°C^{-1}$)	$1.75 \cdot 10^3$		
b_7 (cm^3/g)	$6.06 \cdot 10^{-2}$				
b_8 ($°C^{-1}$)	$5.4 \cdot 10^{-2}$				
b_9 (Pa^{-1})	$1.9 \cdot 10^{-8}$				

Most extrusion processes are carried out in a narrow range of pressures, generally not exceeding 1000 bar, and density changes inside the nozzle must be accounted for by taking the density of the melt at that pressure. However, it has been reported that the value of the specific volume at the start of the process does not affect the final shrinkage. Therefore, in 3D printing, since filament deposition is performed at atmospheric pressure (1 bar) with temperature changing very rapidly from the extrusion temperature to the bed temperature, set at T = 30 °C or T = 50 °C, the most important volume change will be due to the crystallization process taken at 1 bar. In fact, during cooling, three different regions are characteristic: molten, transition, and solid zone. It is expected that during the solidification of the filament, the rapid cooling will shift the crystallization transition, in the diagram at T_c = 100 °C, towards lower temperatures and that the main shrinkage taking place before the filament is deposited, as marked in Figure 4.6, would be due to crystallization (3.8%). Once the filament is deposited, the shrinkage is governed by the thermal expansion coefficient of the solid part, which accounts for the volume change calculated by taking the specific volume at bed temperature and the specific volume at

room temperature (this would be the minimum shrinkage expected in the final printed piece). In the case of PHBH, as the Tg = 0 °C, this coefficient is still large enough to give rise to some shrinkage that materializes as minimal distortions of the part dimensions, as seen in Figure 4.7.

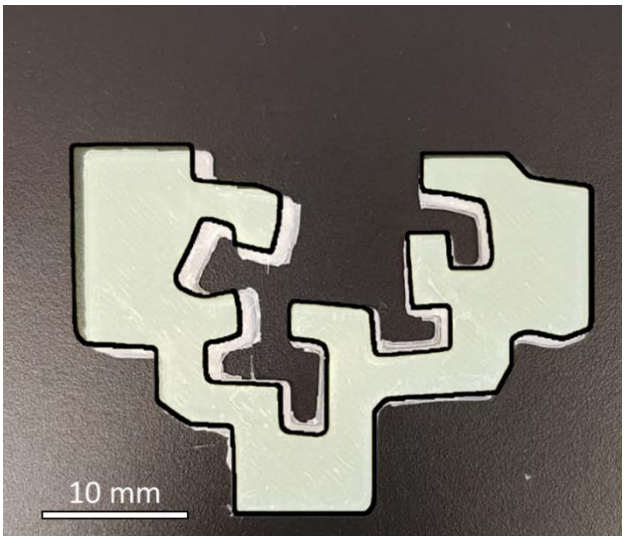

Figure 4.7. Image of the printed logo of the UPV/EHU with a dimensional comparison with the model.

In addition, Figure 4.6 shows the specific volume of a sample obtained in the 3D printing process. The fast solidification process does not prevent crystallization as the density value is very similar to that obtained under slow solidification conditions, in agreement with the crystallinity values determined by DSC included in Figure 4.2.

The PVT data at the exact temperature profile of the filament during deposition can give us information about the evolution of the shrinkage of the sample. The PVT diagram contains valuable information when the experimental procedure is designed correctly (hold temperature, cooling time) to investigate and optimize the reduction of dimensional distortions of 3D printed parts.

4.3.2 Mechanical Properties

4.3.2.1 Effect of the Bed and Nozzle Temperatures

To determine the best printing conditions of the PHBH, the discussion of the results obtained in the mechanical tests by varying the printing conditions is carried out in this section. Table 6 shows the mechanical parameters of Young's modulus, tensile strength, and strain at the break of the 3D-printed specimens at 180 °C, 190 °C, and 200 °C, keeping the printing velocity constant (30 mm/s) and varying the bed temper-ature (30 °C and 50 °C).

Table 4.3 Mechanical properties of the 3D pattern printed at different bed and nozzle temperatures.

Condition	Nozzle T (°C)	Bed T (°C)	Printing Velocity (mm/s)	Young Modulus, E (MPa)	Tensile Strength, σ_M (MPa)	Strain at Break, ε_B (%)
L12	180	30	30	1110 ± 27	14.9 ± 1.0	2.15 ± 0.02
L22	180	50	30	1150 ± 78	17.0 ± 1.3	2.67 ± 0.22
M12	190	30	30	1200 ± 66	16.5 ± 1.4	2.55 ± 0.25
M22	190	50	30	1260 ± 30	18.5 ± 1.4	2.89 ± 0.03
H12	200	30	30	1241 ± 85	16.3 ± 2.0	2.31 ± 0.05
H22	200	50	30	1210 ± 98	17.6 ± 2.6	2.60 ± 0.16

As can be seen, an increase in nozzle temperature leads to an improvement in mechanical parameters. Several authors reported similar results for other materials [92–96]. In all cases, this trend is attributable to the fact that high nozzle temperatures reduce the formation of voids because the viscosity of the resin and the air pressure decreases.

In the case of the material under consideration in this work, the PHBH, it is possible to note from Table 4.3 that the variation of the nozzle temperature from 180 °C to 190 °C results in an increase of 9.7% of the tensile strength and 15% of the tensile strain at break. Although the increase is not as high as for the other materials reported in the literature, this could be due to the particular isothermal crystallization of PHBH during

the printing process, confirmed by the simulation results, which leads to a printed pattern with few voids. This will be verified by the SEM analysis reported below.

By increasing the nozzle temperature to 200 °C, the tensile strength and tensile strain parameters remain constant within the errors reported in Table 4.3. This is probably attributable to the beginning of the degradation of the sample, as already mentioned previously and confirmed by thermogravimetric analysis.

Moreover, it is known that for semi-crystalline polymers, a higher print bed temperature leads to an improvement in the strength of the interfacial bond and the dimensional accuracy of printed patterns due to the longer time for molecular diffusion before the onset of crystallization [68,69,87–89] This behavior has been reported for PP [86], and PLA [90]. In these cases, parts printed with high temperatures in the print bed can achieve mechanical properties comparable with specimens obtained by injection molding. Furthermore, this trend is also confirmed by Xiaoyong et al. [91] for PEEK, in which higher bed temperatures can improve the interfacial strength between layers in the printing process.

In the case of PHBH, as can be seen from the values reported in Table 4.3, a slight improvement in the tensile strength and tensile strain values is observed using a bed temperature of 50 °C.

4.3.2.1 Effect of the Printing Velocity

Finally, Table 4.4 shows the mechanical parameter values obtained from printed specimens using 190 °C as the nozzle temperature and 50 °C as the bed temperature at different printing velocities. The values of the nozzle and bed temperatures were cho-sen based on the best results recorded in the specimens printed at velocities of 30 mm/s. As seen from Table 4.4, even the change in printing velocity determines a change in Young's modulus and ductility of the specimens.

Table 4.4 Mechanical properties of the 3D pattern printed at different printing velocities.

Condition	Nozzle T (°C)	Bed T (°C)	Printing Velocity (mm/s)	Young Modulus, E (MPa)	Tensile Strengh, σ_M (MPa)	Strain at Break, ε_B (%)
M21	190	50	20	970 ± 90	13.2 ± 3.0	2.53 ± 0.23
M22	190	50	30	1260 ± 30	18.5 ± 1.4	2.89 ± 0.03
M23	190	50	40	1090 ± 105	16.8 ± 1.5	2.91 ± 0.41

A printing velocity of 20 mm/s produces specimens with Young's modulus value of 23% lower than that found in specimens printed at velocities of 30 mm/s. A decrease in the toughness of the specimens is also observed: the values of tensile strength and strain at break decrease by 28% and 13%, respectively. This could be attributed to the fact that a slower print velocity allows the previous layers to crystallize before the next layer adheres to them because the heat dissipates rapidly [92]. This results in less compactness in the material and, therefore, poorer mechanical properties, as was also found in the case of PLA printed at low printing velocities [93] and PLA with wood fiber [94].

A lowering of mechanical performance is also found in specimens printed with a printing velocity of 40 mm/s, in which there is a decrease of 13% in the value of Young's modulus and 10% in the value of tensile strength compared to the samples printed at 30 mm/s. This behavior could be explained by Abeykoon et al. [93]. They found that for PLA, a printing velocity higher than 90 mm/s could influence the fusion of the filament as polymers have poor thermal conductivity, leading to adhesion problems between the layers and, therefore, inferior mechanical properties. Thus, as in the case of PLA, it has been found that the best printing velocity is 90 mm/s; while the recommended print

velocity is 30 mm/s for PHBH. This is also an advantage in terms of energy savings since higher printing velocity would lead to higher energy consumption and, because they do not result in an improvement in the mechanical properties, in this case, it is not worth using higher printing velocities. In terms of the final quality of the printed part, greater vibrations are generated with the highest printing velocity when the nozzle changes printing direction. Consequently, the printed polymer will have ringing or ghosting artifacts or even produce layer shifting during printing.

4.3.2.2 Effect of the Raster Angle

Table 4.5 compares the mechanical properties of the specimens obtained following the M12 conditions (190 °C as nozzle temperature, 30 °C as bed temperature, and 30 mm/s as printing velocity, but with different raster orientations) and the specimens obtained by compression molding. To mimic the compactness conditions obtained during compression molding, the raster orientation of the layers has been set in such a way that each layer is oriented in the same direction as the previous one, which is that of the longest axis of the specimen, corresponding to the direction at which the traction occurs.

Table 4.5 Mechanical properties of the 3D pattern printed at different raster angles compared with the patterns obtained from compression molding.

Condition	Nozzle T (°C)	Bed T (°C)	Printing Velocity (mm/s)	Young Modulus, E (MPa)	Tensile Strength, σ_M (MPa)	Strain at Break, ε_B (%)
M12 [45°, 45°]	190	30	30	1200 ± 66	16.5 ± 1.4	2.55 ± 0.25
M12 [90°, 90°]	190	30	30	1280 ± 51	20.1 ± 1.0	3.58 ± 0.12
Compression Molding	-	-	-	1320 ± 90	24.0 ± 1.9	6.78 ± 1.0

According to the results obtained in this study, 3D printed samples with the layers oriented in the same direction to each other, which is also the direction of stretching [M12

(90°, 90°)], exhibit better properties than samples where the layers are oriented at 45° to each other [M12 (45°, 45°)]. Indeed, there is a 6% increase in Young's modulus, 17% in tensile strength, and 30% in the strain at the break between the two types of printed samples. This behavior can be attributed to the fact that the layers are oriented in the same direction in which the stretching force is applied. Therefore, the sample could strengthen under stretching and oppose a higher resistance before breaking. Similar results were found in the case of materials based on ABS [95] and PP filled with short carbon fibers [96].

4.3.2.3 FFF vs. Compression Molding

The specimens obtained by compression molding have a higher toughness than the 3D-printed specimens [90°, 90°] (with a 47% higher strain at break value) but maintain similar parameters of Young's modulus and tensile strength. This is generally due to the presence of pores [108], anisotropy, and poor adhesive strength between the layers of the 3D printed pattern [109–112], which negatively affect the mechanical performance of the specimens.

Figure 4.8 shows the typical stress-strain curves of 3D-printed samples using the M22 condition listed in Table 2.1 in the Chapter II and compression molding specimens. Photographs of representative 3D-printed specimens at the beginning and end of the test are also shown in the figure, and it is possible to appreciate the high quality (i.e., resolution) of the specimens. Both specimens have a brittle behavior characterized by breaking before reaching the yielding point.

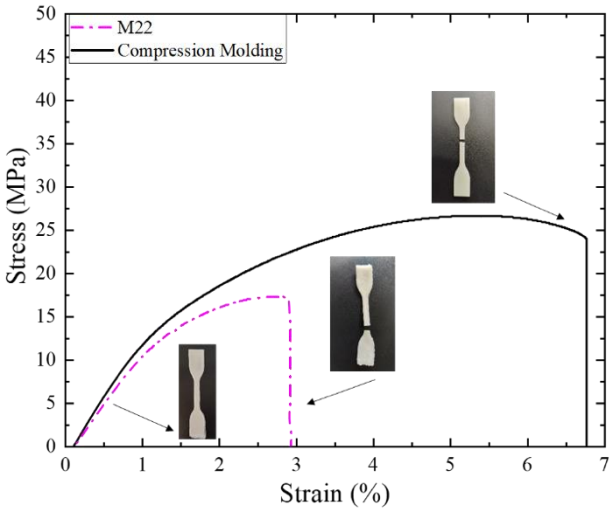

Figure 4.8 Tensile stress-strain curves of 3D printed using the M22 condition and compression molding PHBH.

4.3.3 SEM Analysis: Cross-Sectional Morphology

Figure 4.9 shows SEM micrographs of the cross-section of the 3D printed specimens obtained with different conditions (a, b, and c) and compression molding speci-men (d). No differences in the morphology are observed depending on the printing conditions; consequently, changes in the parameters of the printing process do not affect the morphology. The samples' morphology appears compact, indicating that during the printing process, the adhesion between the different layers took place effi-ciently, thus avoiding the formation of many air gaps. As expected, the only difference between the specimens manufactured by FFF and those manufactured by compression molding was that no trapped air nor any holes resulting from 3D printing were ob-served in the specimens obtained by compression molding.

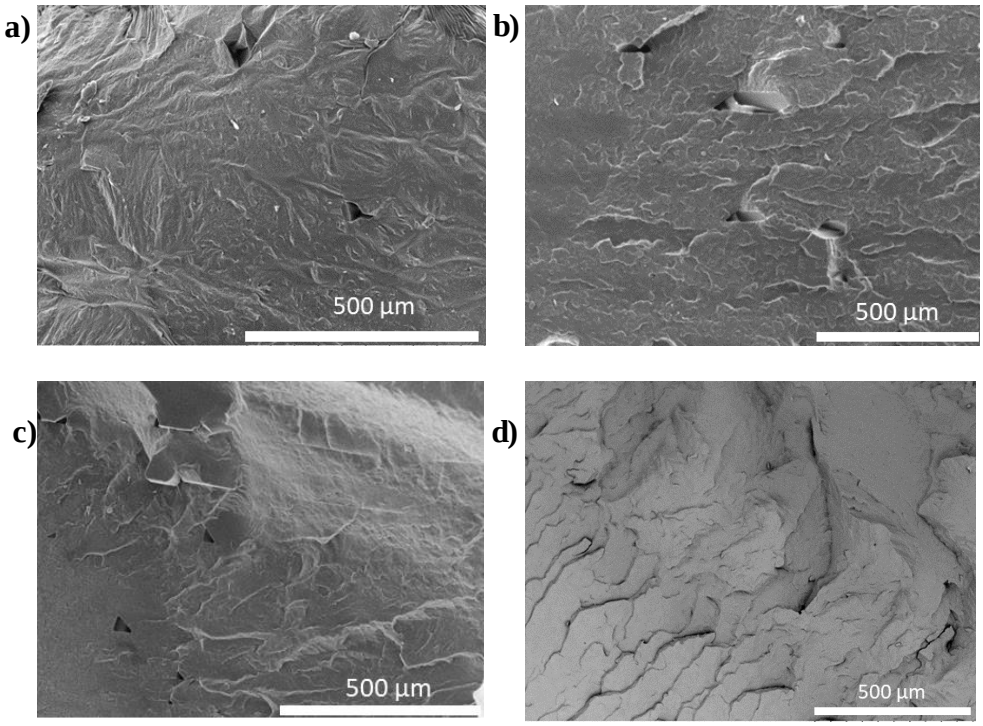

Figure 4.9 Micrograph of the cross-section of printed filaments obtained employing L22 (a), M22 (b), M12 [90°,90°] (c), and compression molding (d).

This behavior is different from that previously reported for PBSA by Candal et al. [66], in which it was possible to distinguish the various filaments in the layers of the printed pattern. In contrast, a similar behavior was reported by Abeykoon et al. [93] for PLA, for which 3D-printed patterns with 100% infill density have no air gaps. The behavior is consistent with the different entanglement densities calculated for these samples, as indicated in the rheological section. The entanglement density for the PBS (Z = 8) and PBSA (Z = 9), considerably lower than the density calculated for PHBH (Z = 18) and PLA (Z = 19), could explain the different welding between polymer layers.

4.4 Conclusions

In this work, a comprehensive study of the printing properties of PHBH was conducted. DSC results on 3D printed specimens showed that, in the case of PHBH, unlike what usually happens in the FFF field, the crystallization during the printing process

occurs in an isothermal manner after layer deposition and not during the non-isothermal cooling stage. This result was also confirmed by a computational sim-ulation of the temperature profile during printing.

Once the printability of PHBH was demonstrated via rheological analysis, differ-ent printing conditions were used to determine a correlation between the printing con-ditions and the mechanical and morphological properties. The analysis of the dynamic viscoelastic moduli leads to discuss the correlation between the chain entanglement modulus and the welding response of the prints.

Through this study, it was possible to propose that an increase in the temperature of the nozzle from 170 °C to 180 °C (i.e., a temperature below the degradation temper-ature of PHBH, i.e., 200 °C) and of the bed from 30 °C to 50 °C provokes an improve-ment of the mechanical properties. In fact, a 15% increase in the tensile strain at break was determined with these printing conditions. Such an improvement is due to the re-duction of void formation, as demonstrated by SEM.

The effect of printing velocity on printing properties was also determined. Printing velocities of 20, 30, and 40 mm/s were used, and intermediate printing velocities re-sulted in better mechanical properties. This is an advantage in terms of energy savings, as spending more energy printing at higher velocities is not desirable.

It was demonstrated that the mechanical properties are better in the specimens in which the layers are oriented in the same direction with respect to each other and with respect to the test direction. Indeed, there is a 6% increase in Young's modulus, 17% in tensile strength, and 30% in the strain at break in the samples printed with a raster an-gle of 90°. Furthermore, the mechanical properties obtained for the 3D-printed speci-mens are comparable with those obtained from compression molding in terms of stiffness.

4.5 References

1. European Bioplastics e.V., 2020b, "Bioplastics Market Data", Accessed 10 March 2020.
2. Lee, S.Y. Bacterial Polyhydroxyalkanoates. *Biotechnol. Bioeng.* **1996**, *49*, 1–14, doi:10.1002/(SICI)1097-0290(19960105)49:1<1::AID-BIT1>3.0.CO;2-P.
3. Lee, S.Y. Plastic Bacteria? Progress and Prospects for Polyhydroxyalkanoate Production in Bacteria. *Trends Biotechnol.* **1996**, *14*, 431–438, doi:https://doi.org/10.1016/0167-7799(96)10061-5.
4. Sudesh, K.; Abe, H.; Doi, Y. Synthesis, Structure and Properties of Polyhydroxyalkanoates: Biological Polyesters. *Prog. Polym. Sci.* 2000, *25*, 1503–1555.
5. Yan, S.; Tyagi, R.D.; Surampalli, R.Y. Polyhydroxyalkanoates (PHA) Production Using Wastewater as Carbon Source and Activated Sludge as Microorganisms. *Water Sci. Technol.* **2006**, *53*, 175–180, doi:10.2166/wst.2006.193.
6. Raza, Z.A.; Abid, S.; Banat, I.M. Polyhydroxyalkanoates: Characteristics, Production, Recent Developments and Applications. *Int. Biodeterior. Biodegrad.* 2018, *126*, 45–56.
7. Madison, L.L.; Huisman, G.W. Metabolic Engineering of Poly (3-Hydroxyalkanoates): From DNA to Plastic. *Microbiol. Mol. Biol. Rev.* **1999**, *63*, 21–53, doi:10.1128/MMBR.63.1.21-53.1999.
8. Reddy, C.S.K.; Ghai, R.; Kalia, V. Polyhydroxyalkanoates: An Overview. *Bioresour. Technol.* **2003**, *87*, 137–146, doi:https://doi.org/10.1016/S0960-8524(02)00212-2.
9. Serrano, J. Polyhydroxyalkanoates (PHAs) Polymers Produced by Microorganisms. A Solution to Environmental Pollution 2010. *Teoría Y Prax. Investig.* **2010**, *5*.
10. Gonzalez Garcia, Y.; Meza Contrera, J.C.; Gonzalez Reynoso, O.; Cordova Lopez, J.A. Synthesis and Biodegradation of Polyhydroxialkanoates: Bacterially Produced Plastics. *Rev. Int. Contam. Ambient.* **2013**, *29*, 77–115.
11. Sharma, V.; Sehgal, R.; Gupta, R. Polyhydroxyalkanoate (PHA): Properties and Modifications. *Polymer (Guildf).* **2021**, *212*, 123161, doi:10.1016/J.POLYMER.2020.123161.
12. Li, S.; Cai, L.; Wu, L.; Zeng, G.; Chen, J.; Wu, Q.; Chen, G.-Q. Microbial

Synthesis of Functional Homo-, Random, and Block Polyhydroxyalkanoates by β-Oxidation Deleted Pseudomonas Entomophila. *Biomacromolecules* **2014**, *15*, 2310–2319, doi:https://doi.org/10.1021/bm500669s.

13. Zheng, Y.; Chen, J.-C.; Ma, Y.-M.; Chen, G.-Q. Engineering Biosynthesis of Polyhydroxyalkanoates (PHA) for Diversity and Cost Reduction. *Metab. Eng.* **2020**, *58*, 82–93, doi:https://doi.org/10.1016/j.ymben.2019.07.004.
14. Sodian, R.; Sperling, J.S.; Martin, D.P.; Egozy, A.; Stock, U.; Mayer Jr, J.E.; Vacanti, J.P. Technical Report: Fabrication of a Trileaflet Heart Valve Scaffold from a Polyhydroxyalkanoate Biopolyester for Use in Tissue Engineering. *Tissue Eng.* **2000**, *6*, 183–188, doi:10.1089/107632700320793.
15. Wu, L.-P. Polyhydroxyalkanoates (PHA): Biosynthesis, Industrial Production and Applications in Medicine. *New York Nov. Sci.* **2014**.
16. Porter, M.M.; Lee, S.; Tanadchangsaeng, N.; Jaremko, M.J.; Yu, J.; Meyers, M.; McKittrick, J. Porous Hydroxyapatite-Polyhydroxybutyrate Composites Fabricated by a Novel Method via Centrifugation. In *Mechanics of Biological Systems and Materials, Volume 5*; Springer, 2013; pp. 63–71.
17. Hong, S.K.; Shirai, Y.; Nor, A.; Hassan, M.A. Semi-Continuous and Continuous Anaerobic Treatment of Palm Oil Mill Effluent for the Production of Organic Acids and Polyhydroxyalkanoates. *Res. J. Environ. Sci.* **2009**, *3*, 552–559, doi:10.3923/rjes.2009.552.559.
18. Hazari, A.; Wiberg, M.; Johansson-Ruden, G.; Green, C.; Terenghi, G. A Resorbable Nerve Conduit as an Alternative to Nerve Autograft in Nerve Gap Repair. *Br. J. Plast. Surg.* **1999**, *52*, 653–657, doi:10.1054/bjps.1999.3184.
19. Bugnicourt, E.; Cinelli, P.; Lazzeri, A.; Alvarez, V.A. Polyhydroxyalkanoate (PHA): Review of Synthesis, Characteristics, Processing and Potential Applications in Packaging. **2014**.
20. Lizarraga-Valderrama, L.R.; Nigmatullin, R.; Taylor, C.; Haycock, J.W.; Claeyssens, F.; Knowles, J.C.; Roy, I. Nerve Tissue Engineering Using Blends of Poly (3-hydroxyalkanoates) for Peripheral Nerve Regeneration. *Eng. Life Sci.* **2015**, *15*, 612–621, doi:https://doi.org/10.1002/elsc.201400151.
21. Chen, G.-Q.; Wu, Q. Microbial Production and Applications of Chiral Hydroxyalkanoates. *Appl. Microbiol. Biotechnol.* **2005**, *67*, 592–599, doi:DOI: 10.1007/s00253-005-1917-2.

22. Baptist, J.N.; Ziegler, J.B. Method of Making Absorbable Surgical Sutures from Poly Beta Hydroxy Acids 1965.
23. Шишацкая, Е.И.; Николаева, Е.Д.; Виноградова, О.Н.; Волова, Т.Г. Experimental Wound Dressings of Degradable PHA for Skin Defect Repair. **2016**, doi:10.1007/s10856-016-5776-4.
24. Dhania, S.; Rani, R.; Kumar, R.; Thakur, R. Fabricated Polyhydroxyalkanoates Blend Scaffolds Enhance Cell Viability and Cell Proliferation. *J. Biotechnol.* **2023**, *361*, 30–40, doi:https://doi.org/10.1016/j.jbiotec.2022.11.014.
25. Ni, J.; Wang, M. In Vitro Evaluation of Hydroxyapatite Reinforced Polyhydroxybutyrate Composite. *Mater. Sci. Eng. C* **2002**, *20*, 101–109, doi:https://doi.org/10.1016/S0928-4931(02)00019-X.
26. Reis, E.C.C.; Borges, A.P.B.; Fonseca, C.C.; Martinez, M.M.M.; Eleotério, R.B.; Morato, G.O.; Oliveira, P.M. Biocompatibility, Osteointegration, Osteoconduction, and Biodegradation of a Hydroxyapatite-Polyhydroxybutyrate Composite. *Brazilian Arch. Biol. Technol.* **2010**, *53*, 817–826, doi:https://doi.org/10.1590/S1516-89132010000400010.
27. Alves, M.I.; Macagnan, K.L.; Rodrigues, A.A.; de Assis, D.A.; Torres, M.M.; de Oliveira, P.D.; Furlan, L.; Vendruscolo, C.T.; Moreira, A. da S. Poly (3-Hydroxybutyrate)-P (3HB): Review of Production Process Technology. *Ind. Biotechnol.* **2017**, *13*, 192–208, doi:https://doi.org/10.1089/ind.2017.0013.
28. Karahaliloglu, Z.; Ercan, B.; Taylor, E.N.; Chung, S.; Denkbaş, E.B.; Webster, T.J. Antibacterial Nanostructured Polyhydroxybutyrate Membranes for Guided Bone Regeneration. *J. Biomed. Nanotechnol.* **2015**, *11*, 2253–2263, doi:10.1166/jbn.2015.2106.
29. Akaraonye, E.; Moreno, C.; Knowles, J.C.; Keshavarz, T.; Roy, I. Poly (3-hydroxybutyrate) Production by Bacillus Cereus SPV Using Sugarcane Molasses as the Main Carbon Source. *Biotechnol. J.* **2012**, *7*, 293–303, doi:10.1002/biot.201100122.
30. Yano T, Nomoto T, Kozaki S, Imamura T, Honma T, Canon KK 2006.
31. Pouton, C.W.; Akhtar, S. Biosynthetic Polyhydroxyalkanoates and Their Potential in Drug Delivery. *Adv. Drug Deliv. Rev.* **1996**, *18*, 133–162, doi:https://doi.org/10.1016/0169-409X(95)00092-L.
32. Yagmurlu, M.F.; Korkusuz, F.; Gürsel, I.; Korkusuz, P.; Örs, Ü.; Hasirci, V.

Sulbactam-cefoperazone Polyhydroxybutyrate-co-hydroxyvalerate (PHBV) Local Antibiotic Delivery System: In Vivo Effectiveness and Biocompatibility in the Treatment of Implant-related Experimental Osteomyelitis. *J. Biomed. Mater. Res. An Off. J. Soc. Biomater. Japanese Soc. Biomater. Aust. Soc. Biomater. Korean Soc. Biomater.* **1999**, *46*, 494–503, doi:10.1002/(sici)1097-4636(19990915)46:4<494::aid-jbm7>3.0.co;2-e.

33. Gursel, I.; Yagmurlu, F.; Korkusuz, F.; Hasirci, V. In Vitro Antibiotic Release from Poly (3-Hydroxybutyrate-Co-3-Hydroxyvalerate) Rods. *J. Microencapsul.* **2002**, *19*, 153–164, doi:10.1080/02652040110065413.
34. Valappil, S.P.; Peiris, D.; Langley, G.J.; Herniman, J.M.; Boccaccini, A.R.; Bucke, C.; Roy, I. Polyhydroxyalkanoate (PHA) Biosynthesis from Structurally Unrelated Carbon Sources by a Newly Characterized Bacillus Spp. *J. Biotechnol.* **2007**, *127*, 475–487, doi:DOI: 10.1016/j.jbiotec.2006.07.015.
35. Valappil, S.P.; Misra, S.K.; Boccaccini, A.R.; Roy, I. Biomedical Applications of Polyhydroxyalkanoates, an Overview of Animal Testing and in Vivo Responses. *Expert Rev. Med. Devices* **2006**, *3*, 853–868, doi:10.1586/17434440.3.6.853.
36. Yao YC, Zhan XY, Zhang J, Zou XH, Wang ZH, Xiong YC, Chen J, C.G. A Specific Drug Targeting System Based on Polyhydroxyalkanoate Granule Binding Protein PhaP Fused with Targeted Cell Ligands. *Biomaterials* **2008**, *36*, doi:10.1016/j.biomaterials.2008.09.008.
37. Avérous, L.; Pollet, E. Biorenewable Nanocomposites. *MRS Bull.* **2011**, *36*, 703–710, doi:https://doi.org/10.1557/mrs.2011.206.
38. Abid, S.; Raza, Z.A.; Rehman, A. Synthesis of Poly (3-Hydroxybutyrate) Nanospheres and Deposition Thereof into Porous Thin Film. *Mater. Res. Express* **2016**, *3*, 105042, doi:DOI 10.1088/2053-1591/3/10/105042.
39. Plackett, D.; Siró, I. Polyhydroxyalkanoates (PHAs) for Food Packaging. In *Multifunctional and nanoreinforced polymers for food packaging*; Elsevier, 2011; pp. 498–526.
40. Samaniego, K.; Matos, A.; Sánchez-Safont, E.; Candal, M. V; Lagaron, J.M.; Cabedo, L.; Gamez-Perez, J. Role of Plasticizers on PHB/Bio-TPE Blends Compatibilized by Reactive Extrusion. *Materials (Basel).* **2022**, *15*, 1226, doi:https://doi.org/10.3390/ma15031226.
41. Anderson, A.J.; Dawes, E. Occurrence, Metabolism, Metabolic Role, and

Industrial Uses of Bacterial Polyhydroxyalkanoates. *Microbiol. Rev.* **1990**, *54*, 450–472, doi:10.1128/mr.54.4.450-472.1990.

42. Vinet L, Z.A. A "Missing" Family of Classical Orthogonal Polynomials. *J. Phys. A Math. Theor.* **2010**, *54*, 450–472, doi:10.1088/1751-8113/44/8/085201.
43. Zhao, W.; Chen, G.-Q. Production and Characterization of Terpolyester Poly (3-Hydroxybutyrate-Co-3-Hydroxyvalerate-Co-3-Hydroxyhexanoate) by Recombinant Aeromonas Hydrophila 4AK4 Harboring Genes PhaAB. *Process Biochem.* **2007**, *42*, 1342–1347, doi:https://doi.org/10.1016/j.procbio.2007.07.006.
44. Tan, D.; Yin, J.; Chen, G.-Q. Production of Polyhydroxyalkanoates. In *Current developments in biotechnology and bioengineering*; Elsevier, 2017; pp. 655–692.
45. Eraslan, K.; Aversa, C.; Nofar, M.; Barletta, M.; Gisario, A.; Salehiyan, R.; Goksu, Y.A. Poly (3-Hydroxybutyrate-Co-3-Hydroxyhexanoate)(PHBH): Synthesis, Properties, and Applications-A Review. *Eur. Polym. J.* **2022**, 111044, doi:10.1016/j.eurpolymj.2022.111044.
46. Sato, H.; Nakamura, M.; Padermshoke, A.; Yamaguchi, H.; Terauchi, H.; Ekgasit, S.; Noda, I.; Ozaki, Y. Thermal Behavior and Molecular Interaction of Poly (3-Hydroxybutyrate-Co-3-Hydroxyhexanoate) Studied by Wide-Angle X-Ray Diffraction. *Macromolecules* **2004**, *37*, 3763–3769, doi:https://doi.org/10.1021/ma049863t.
47. Wu C-S, Liao H-T, C.Y.-X. Characterisation, Biodegrad-Ability and Application of Palm Fibre-Reinforced Polyhy-Droxyalkanoate Composites. *Polym Degrad Stabil* **2017**, *140*, 55–63, doi:https://doi.org/10.1016/j.polymdegradstab.2017.04.016.
48. Wu C, L.H. Interface Design of Environmentally Friendly Carbon Nanotube-Filled Polyester Composites: Fabrication, Characterisation, Functionality and Application. *Express Polym Lett* **2017**, *11*, doi:10.3144/expresspolymlett.2017.20.
49. C-S., W. Characterization, Functionality and Application of Siliceous Sponge Spicules Additive-Based Manufacturing Biopolymer Composites. *Addit Manuf* **2018**, *22*, 13–20, doi:https://doi.org/10.1016/j.addma.2018.04.034.
50. Tian, J.; Zheng, Y.; Ouyang, Q.; Xue, P.; Guo, B.; Xu, J. Structure and Properties of Biodegradable Polymer Materials for Fused Deposition Modeling 3D Printing. **2023**, doi:10.5772/intechopen.110175.

51. Kovalcik, A.; Sangroniz, L.; Kalina, M.; Skopalova, K.; Humpolíček, P.; Omastova, M.; Mundigler, N.; Müller, A.J. Properties of Scaffolds Prepared by Fused Deposition Modeling of Poly(Hydroxyalkanoates). *Int. J. Biol. Macromol.* **2020**, *161*, 364–376, doi:10.1016/j.ijbiomac.2020.06.022.

52. Kovalcik, A.; Smilek, J.; Machovsky, M.; Kalina, M.; Enev, V.; Dugova, H.; Cernekova, N.; Kovacova, M.; Spitalsky, Z. Properties and Structure of Poly (3-Hydroxybutyrate-Co-4-Hydroxybutyrate) Filaments for Fused Deposition Modelling. *Int. J. Biol. Macromol.* **2021**, *183*, 880–889, doi:https://doi.org/10.1016/j.ijbiomac.2021.04.183.

53. Stanzani, V.; Giubilini, A.; Checchi, M.; Messori, M.; Bondioli, F.; Palumbo, C. Eco-Friendly Biodegradable Materials as New Promising 3D-Printed Scaffold for Eco-Sustainable Regenerative Medicine. *Ital. J. Anat. Embryol.* **2021**, *125*, 159.

54. Giubilini, A.; Siqueira, G.; Clemens, F.J.; Sciancalepore, C.; Messori, M.; Nyström, G.; Bondioli, F. 3D-Printing Nanocellulose-Poly(3-Hydroxybutyrate-Co-3-Hydroxyhexanoate) Biodegradable Composites by Fused Deposition Modeling. *ACS Sustain. Chem. Eng.* **2020**, *8*, 10292–10302, doi:10.1021/acssuschemeng.0c03385.

55. Valentini, F.; Dorigato, A.; Rigotti, D.; Pegoretti, A. Polyhydroxyalkanoates/Fibrillated Nanocellulose Composites for Additive Manufacturing. *J. Polym. Environ.* **2019**, *27*, 1333–1341, doi:https://doi.org/10.1007/s10924-019-01429-8.

56. Caputo, M.R.; Tang, X.; Westlie, A.H.; Sardon, H.; Chen, E.Y.-X.; Müller, A.J. Effect of Chain Stereoconfiguration on Poly (3-Hydroxybutyrate) Crystallization Kinetics. *Biomacromolecules* **2022**, *23*, 3847–3859, doi:https://doi.org/10.1021/acs.biomac.2c00682.

57. Jiang, Z.; Liu, P.; Sue, H.-J.; Bremner, T. Effect of Annealing on the Viscoelastic Behavior of Poly (Ether-Ether-Ketone). *Polymer (Guildf).* **2019**, *160*, 231–237, doi:https://doi.org/10.1016/j.polymer.2018.11.052.

58. Yasuniwa, M.; Tsubakihara, S.; Sugimoto, Y.; Nakafuku, C. Thermal Analysis of the Double-melting Behavior of Poly (L-lactic Acid). *J. Polym. Sci. Part B Polym. Phys.* **2004**, *42*, 25–32.

59. Sangroniz, L.; Cavallo, D.; Müller, A.J. Self-Nucleation Effects on Polymer Crystallization. *Macromolecules* **2020**, *53*, 4581–4604,

doi:https://doi.org/10.1021/acs.macromol.0c00223.

60. Seppala, J.E.; Migler, K.D. Infrared Thermography of Welding Zones Produced by Polymer Extrusion Additive Manufacturing. *Addit. Manuf.* **2016**, *12*, 71–76, doi:https://doi.org/10.1016/j.addma.2016.06.007.
61. Candal, M.V.; Calafel, I.; Fernández, M.; Aranburu, N.; Aguirresarobe, R.H.; Gerrica-Echevarria, G.; Santamaría, A.; Müller, A.J. Study of the Interlayer Adhesion and Warping during Material Extrusion-Based Additive Manufacturing of a Carbon Nanotube/Biobased Thermoplastic Polyurethane Nanocomposite. *Polymer (Guildf).* **2021**, *224*, doi:10.1016/J.POLYMER.2021.123734.
62. Vaes, D.; Van Puyvelde, P. Semi-Crystalline Feedstock for Filament-Based 3D Printing of Polymers. *Prog. Polym. Sci.* **2021**, *118*, 101411.
63. Mackay, M.E. The Importance of Rheological Behavior in the Additive Manufacturing Technique Material Extrusion. *J. Rheol. (N. Y. N. Y).* **2018**, *62*, 1549–1561, doi:https://doi.org/10.1122/1.5037687.
64. Thumsorn, S.; Prasong, W.; Kurose, T.; Ishigami, A.; Kobayashi, Y.; Ito, H. Rheological Behavior and Dynamic Mechanical Properties for Interpretation of Layer Adhesion in FDM 3D Printing. *Polymers (Basel).* **2022**, *14*, 2721, doi:https://doi.org/10.3390/polym14132721.
65. Phan, D.D.; Swain, Z.R.; Mackay, M.E. Rheological and Heat Transfer Effects in Fused Filament Fabrication. *J. Rheol. (N. Y. N. Y).* **2018**, *62*, 1097–1107, doi:https://doi.org/10.1122/1.5022982.
66. Candal, M.V.; Calafel, I.; Aranburu, N.; Fernández, M.; Gerrica-Echevarria, G.; Santamaría, A.; Müller, A.J. Thermo-Rheological Effects on Successful 3D Printing of Biodegradable Polyesters. *Addit. Manuf.* **2020**, *36*, 101408, doi:10.1016/j.addma.2020.101408.
67. Cox, W, Mertz, E. Correlation of Dynamic and Steady Flow Viscosities. *J. Polym. Sci., 28*, 619–622, doi:http://dx.doi.org/10.1002/pol.1958.120281181253.
68. Cross, M.M. Rheology of Non-Newtonian Fluids: A New Flow Equation for Pseudoplastic Systems. *J. Colloid Sci.* **1965**, *20*, 417–437, doi:https://doi.org/10.1016/0095-8522(65)90022-X.
69. McIlroy, C.; Olmsted, P.D. Disentanglement Effects on Welding Behaviour of Polymer Melts during the Fused-Filament-Fabrication Method for Additive Manufacturing. *Polymer (Guildf).* **2017**, *123*, 376–391,

doi:https://doi.org/10.1016/j.polymer.2017.06.051.

70. Costanzo, A.; Spotorno, R.; Candal, M.V.; Fernández, M.M.; Müller, A.J.; Graham, R.S.; Cavallo, D.; McIlroy, C. Residual Alignment and Its Effect on Weld Strength in Material-Extrusion 3D-Printing of Polylactic Acid. *Addit. Manuf.* **2020**, *36*, 101415, doi:https://doi.org/10.1016/j.addma.2020.101415.
71. Likhtman, A.E.; McLeish, T.C.B. Quantitative Theory for Linear Dynamics of Linear Entangled Polymers. *Macromolecules* **2002**, *35*, 6332–6343, doi:https://doi.org/10.1021/ma0200219.
72. Likhtman, A. Reptate 2019.
73. Palade, L.-I.; Lehermeier, H.J.; Dorgan, J.R. Melt Rheology of High L-Content Poly (Lactic Acid). *Macromolecules* **2001**, *34*, 1384–1390, doi:https://doi.org/10.1021/ma001173b.
74. Shmueli, Y.; Jiang, J.; Zhou, Y.; Xue, Y.; Chang, C.-C.; Yuan, G.; Satija, S.K.; Lee, S.; Nam, C.-Y.; Kim, T. Simultaneous in Situ X-Ray Scattering and Infrared Imaging of Polymer Extrusion in Additive Manufacturing. *ACS Appl. Polym. Mater.* **2019**, *1*, 1559–1567.
75. Yang, F.; Pitchumani, R. Healing of Thermoplastic Polymers at an Interface under Nonisothermal Conditions. *Macromolecules* **2002**, *35*, 3213–3224.
76. Ausejo, J.G.; Rydz, J.; Musioł, M.; Sikorska, W.; Sobota, M.; Włodarczyk, J.; Adamus, G.; Janeczek, H.; Kwiecień, I.; Hercog, A. A Comparative Study of Three-Dimensional Printing Directions: The Degradation and Toxicological Profile of a PLA/PHA Blend. *Polym. Degrad. Stab.* **2018**, *152*, 191–207.
77. Liu, F.; Vyas, C.; Poologasundarampillai, G.; Pape, I.; Hinduja, S.; Mirihanage, W.; Bartolo, P. Structural Evolution of PCL during Melt Extrusion 3D Printing. *Macromol. Mater. Eng.* **2018**, *303*, 1700494.
78. de Jager, B.; Moxham, T.; Besnard, C.; Salvati, E.; Chen, J.; Dolbnya, I.P.; Korsunsky, A.M. Synchrotron X-Ray Scattering Analysis of Nylon-12 Crystallisation Variation Depending on 3D Printing Conditions. *Polymers (Basel).* **2020**, *12*, 1169.
79. Ianniruberto, G.; Marrucci, G. Convective Constraint Release (CCR) Revisited. *J. Rheol. (N. Y. N. Y).* **2014**, *58*, 89–102.
80. Graham, R.S.; Likhtman, A.E.; McLeish, T.C.B.; Milner, S.T. Microscopic Theory of Linear, Entangled Polymer Chains under Rapid Deformation Including Chain

Stretch and Convective Constraint Release. *J. Rheol. (N. Y. N. Y).* **2003**, *47*, 1171–1200.

81. Das, A.; Riet, J.A.; Bortner, M.J.; McIlroy, C. Rheology, Crystallization, and Process Conditions: The Effect on Interlayer Properties in Three-Dimensional Printing. *Phys. Fluids* **2022**, *34*, 123108, doi:https://doi.org/10.1063/5.0128660.
82. McIlroy, C. A Fundamental Rule: Determining the Importance of Flow Prior to Polymer Crystallization. *Phys. Fluids* **2019**, *31*, 113103, doi:https://doi.org/10.1063/1.5129119.
83. Wang, J.; Hopmann, C.; Kahve, C.; Hohlweck, T.; Alms, J. Measurement of Specific Volume of Polymers under Simulated Injection Molding Processes. *Mater. Des.* **2020**, *196*, 109136, doi:https://doi.org/10.1016/j.matdes.2020.109136.
84. Mishra, A.A.; Momin, A.; Strano, M.; Rane, K. Implementation of Viscosity and Density Models for Improved Numerical Analysis of Melt Flow Dynamics in the Nozzle during Extrusion-Based Additive Manufacturing. *Prog. Addit. Manuf.* **2022**, *7*, 41–54, doi:https://doi.org/10.1007/s40964-021-00208-z.
85. Kazmer, D.O.; Colon, A.R.; Peterson, A.M.; Kim, S.K. Concurrent Characterization of Compressibility and Viscosity in Extrusion-Based Additive Manufacturing of Acrylonitrile Butadiene Styrene with Fault Diagnoses. *Addit. Manuf.* **2021**, *46*, 102106, doi:https://doi.org/10.1016/j.addma.2021.102106.
86. Hertle, S.; Drexler, M.; Drummer, D. Additive Manufacturing of Poly (Propylene) by Means of Melt Extrusion. *Macromol. Mater. Eng.* **2016**, *301*, 1482–1493, doi:https://doi.org/10.1002/mame.201600259.
87. Gao, X.; Qi, S.; Kuang, X.; Su, Y.; Li, J.; Wang, D. Fused Filament Fabrication of Polymer Materials: A Review of Interlayer Bond. *Addit. Manuf.* **2021**, *37*, 101658, doi:https://doi.org/10.1016/j.addma.2020.101658.
88. Spoerk, M.; Arbeiter, F.; Raguž, I.; Weingrill, G.; Fischinger, T.; Traxler, G.; Schuschnigg, S.; Cardon, L.; Holzer, C. Polypropylene Filled with Glass Spheres in Extrusion-based Additive Manufacturing: Effect of Filler Size and Printing Chamber Temperature. *Macromol. Mater. Eng.* **2018**, *303*, 1800179, doi:https://doi.org/10.1002/mame.201800179.
89. Spoerk, M.; Holzer, C.; Gonzalez-Gutierrez, J. Material Extrusion-based Additive Manufacturing of Polypropylene: A Review on How to Improve Dimensional

Inaccuracy and Warpage. *J. Appl. Polym. Sci.* **2020**, *137*, 48545, doi:https://doi.org/10.1002/app.48545.

90. Benwood, C., Anstey, A., Andrzejewski, J., Misra, M., & Mohanty, A.K. Improving the Impact Strength and Heat Resistance of 3D Printed Models: Structure, Property, and Processing Correlationships during Fused Deposition Modeling (FDM) of Poly (Lactic Acid). *Acs Omega* **2018**, *3*, 4400–4411, doi:http://doi.org/ 10.1021/acsomega.8b00129.
91. Xiaoyong, S.; Liangcheng, C.; Honglin, M.; Peng, G.; Zhanwei, B.; Cheng, L. Experimental Analysis of High Temperature PEEK Materials on 3D Printing Test. In Proceedings of the 2017 9th International conference on measuring technology and mechatronics automation (ICMTMA); IEEE, 2017; pp. 13–16.
92. Hsueh, M.-H.; Lai, C.-J.; Wang, S.-H.; Zeng, Y.-S.; Hsieh, C.-H.; Pan, C.-Y.; Huang, W.-C. Effect of Printing Parameters on the Thermal and Mechanical Properties of 3d-Printed Pla and Petg, Using Fused Deposition Modeling. *Polymers (Basel)*. **2021**, *13*, 1758.
93. Abeykoon, C.; Sri-Amphorn, P.; Fernando, A. Optimization of Fused Deposition Modeling Parameters for Improved PLA and ABS 3D Printed Structures. *Int. J. Light. Mater. Manuf.* **2020**, *3*, 284–297.
94. Yang, T.-C.; Yeh, C.-H. Morphology and Mechanical Properties of 3D Printed Wood Fiber/Polylactic Acid Composite Parts Using Fused Deposition Modeling (FDM): The Effects of Printing Speed. *Polymers (Basel)*. **2020**, *12*, 1334, doi:https://doi.org/10.3390/polym12061334.
95. Ziemian, C.; Sharma, M.; Ziemian, S. Anisotropic Mechanical Properties of ABS Parts Fabricated by Fused Deposition Modelling. *Mech. Eng.* **2012**, *23*, 159–180.
96. Spoerk, M.; Savandaiah, C.; Arbeiter, F.; Traxler, G.; Cardon, L.; Holzer, C.; Sapkota, J. Anisotropic Properties of Oriented Short Carbon Fibre Filled Polypropylene Parts Fabricated by Extrusion-Based Additive Manufacturing. *Compos. Part A Appl. Sci. Manuf.* **2018**, *113*, 95–104, doi:https://doi.org/10.1016/j.compositesa.2018.06.018.

Chapter V

5. Tailoring the nucleation and crystallization of Polyhydroxybutyrate by copolymerization

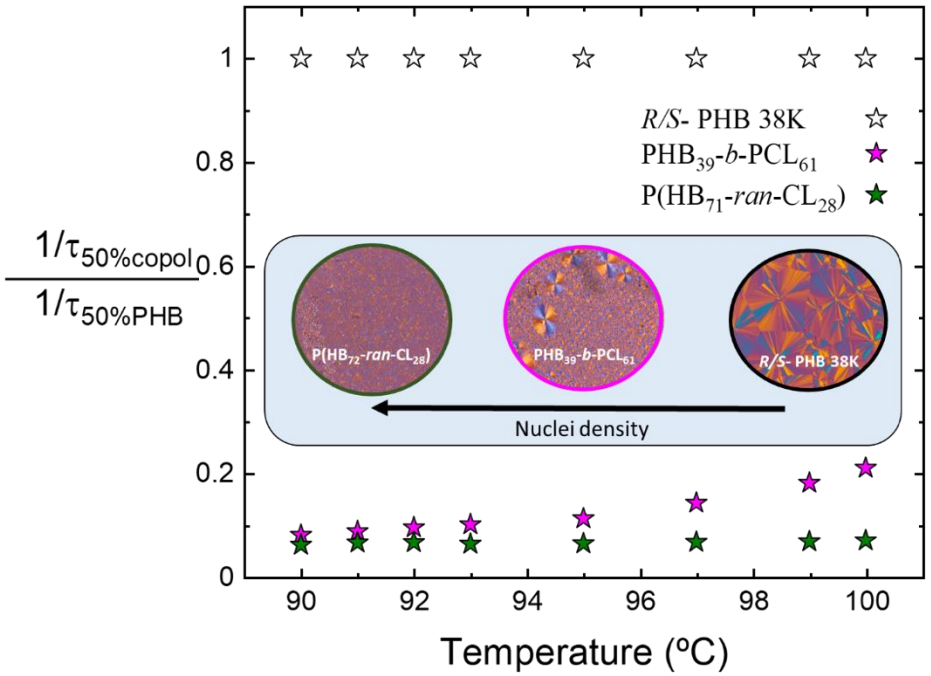

5.1 Abstract

In the polyester family, the biopolymer with the greatest industrial potential could be poly(3-hydroxybutyrate) (PHB), which can nowadays be produced biologically or chemically. The scarce commercial use of PHB is because of its poor mechanical properties, which can be improved by incorporating a flexible aliphatic polyester with good mechanical performance, such as poly(ε-caprolactone) (PCL), while retaining its biodegradability. This work studies the structural, thermal, and morphological properties of block and random copolymers of PHB and PCL. The presence of a comonomer influences the thermal parameters following non-isothermal crystallization and the kinetics of isothermal crystallization. Specifically, the copolymers exhibit lower melting and crystallization temperatures and present lower overall crystallization kinetics than neat homopolymers. The nucleation rates of the PHB components are greatly enhanced in the copolymers, reducing spherulitic sizes and promoting transparency with respect to neat PHB. However, their spherulitic growth rates are depressed so much, that superstructural growth becomes the dominating factor that reduces the overall crystallization kinetics of the PHB component in the copolymers. The block and random copolymers analyzed here also display important differences in structure, morphology, and crystallization that were examined in detail. Our results show that copolymerization can tailor the thermal properties, morphology (spherulitic size), and crystallization kinetics of PHB, potentially improving the processing, optical, and mechanical properties of PHB.

Caputo, M. R., Shi, C., Tang, X., Sardon, H., Chen, E. Y.-X., Müller, A. J. Tailoring the nucleation and crystallization of Polyhydroxybutyrate by copolymerization. ***Submitted***

5.2 Introduction

One of the most critical challenges for contemporary society is the need to decrease the use of plastics derived from petroleum sources and promote the production and use of biobased materials. In this context, packaging materials defined as 'sustainable' have been identified as priorities by manufacturing industries and consumers.[1,2] Aliphatic polyesters are a priority, given their biodegradability and biocompatibility.[3–6] A class of polyesters much studied in the last decade is that of polyhydroxyalkanoates, PHAs,[7–9] of bacterial origin[10] and produced in bacterial cytoplasm as a source of carbon and energy storage.[11,12] Research has demonstrated that PHAs undergo complete degradation in a time span ranging from 6 months to 2 years.[13] On the other hand, the PHB biodegradation process does not foresee the formation of toxic products and, specifically, it has the capability to occur in both aerobic and anaerobic environments: the products of the aerobic process are carbon dioxide and water, while the products of the anaerobic process are carbon dioxide and methane.[14,15] The biodegradation of PHB and its copolymers can occur by bacteria and fungi (microorganisms) found in the soil or industrial waste. Microorganisms are able to release enzymes (i. e. PHB depolymerase[16]) which are used to degrade polymers up to hydroxyacids, constituent elements of polydiroxyalkanoates.

Given its thermal properties resembling those of isotactic polypropylene, [17–19] among the PHAs family, PHB is the most extensively researched polymer. PHB has many advantages: it is resistant to humidity and ultraviolet rays, has excellent barrier properties, and is water insoluble.[20,21] However, it also has some disadvantages as well: it is highly brittle[22–24] and thermally decomposes immediately after melting, [25,26] thus severely limiting its industrial use. Another disadvantage of PHB is that its bacterial

synthesis is slow and with little control over the molecular weights and, therefore, a synthetic route has recently been developed to produce PHB chemically.[27,28]

Purely isotactic PHB produced from chemical synthesis is not enantiomerically pure *R* as the bacterial one, but it is a racemic mixture (*R/S*); its structural and thermal properties have been studied and found to be very similar to those of bacterial PHB.[29] The isotactic PHB from chemical synthesis also has similarly poor mechanical properties as the PHB of bacterial origin and, therefore, investigations for their improvement have been conducted. Recently it has been made possible to obtain an interesting and important result: the controlled introduction of stereodefects in semi-crystalline PHB chains led to a PHB material with optical and mechanical capabilities alike to isotactic polypropylene.[30]

Furthermore, a standard approach to enhance the the mechanical properties of PHB is through copolymerization with monomers of other PHAs to obtain copolymers such as poly(3-hydroxybutyrate-co-3-hydroxyhexanoate) (PHBH) and poly(3-hydroxybutyrate-co-3-hydroxyvalerate) (PHBV). These copolymers are softer and more flexible, have a reduced melting point than neat PHB, and have higher impact resistance. The advantage of such materials is that their properties can be tuned according to their composition, however their disadvantage is that, up to now, their bacterial synthesis does not allow complete control of their composition and steroregularity.[11,31] Thus, further steps have been taken to make the production and use of PHB-based materials easier: the path taken in recent years has been to produce blends with PLA[22,32,33] and PCL,[34–36] for example. However, in this case, the problems due to degradation or the uncontrolled nature of biologically produced PHB remained.

A synthetic route has recently been reported to produce copolymers based on PHB and poly(ε-caprolactone) (PCL).[37] PCL is a semi-crystalline polyester with low

glass transition (T_g = -60 ºC) and melting (T_m = 50-70 ºC) temperatures and excellent mechanical properties, as it is ductile even with a high degree of crystallinity.[38] It is one of the most used polyesters in biomedical and packaging applications, given its biocompatibility and biodegradability.[39–41] Its biocompatibility is due to the fact that PCL, under physiological conditions, degrades by hydrolysis of its ester bonds.[42,43] But it can also be biodegraded by microorganisms present in the soil and by fungi.[44,45] The intuition in choosing PCL, due to its excellent mechanical properties, was successful as the resulting materials were ductile and tough, as they synergistically combine the best properties of the starting materials: the high Young's modulus of PHB[46] and the ductility of PCL.[47]

The result of the work carried out by Tang *et al.*,[37] are two types of new copolymers: a PHB-*b*-PCL block copolymer and a P(HB-*ran*-CL) random copolymer. As both PHB and PCL are semi-crystalline materials, it is of utmost importance to study how their structure, nucleation, and crystallization are affected by the incorporation of a second crystallizable comonomer. Regulating the crystallization rate and degree of crystallinity is a determining factor for applications, as biodegradation rate, permeation, and mechanical properties critically depend on crystallinity degree and morphology (spherulitic size). Therefore, this work aims to study the structure, morphology, nucleation, and overall crystallization rate of two representative PHB/PCL random and block copolymers compared with their homopolymers.

5.3 Results and Discussion

5.3.1 Melt-segregation by in Situ SAXS Real-Time Synchrotron

In general, diblock copolymers tend to have phase separation, and this can be anticipated by evaluating the segregation strenght, denoted by the product χN, where χ is the Flory-Huggins interaction parameter, and N is the degree of polymerization.

The equation[48] 5.1 can be used to calculate an approximate value of the Flory-Huggins interaction parameter (χ):

$$\chi_{12} = 0.34 + \frac{V_1}{RT}(\delta_1 - \delta_2)^2 \quad (5.1)$$

where V_1 refers to the the molar volume of component 1, T (K) represents the temperature at which both polymers are in the molten state (468 K or 195 °C), R is the gas constant with the value of 1.987 cal/K and δ_1 and δ_2 are the solubility parameters of each block expressed in $(cal/cm^3)^{1/2}$.

In this case, to calculate the sample interaction parameter χ, a reference molar volume of 100 cm^3/mol was employed, and the solubility parameters for each block were obtained from existing literature sources: [δ_{PHB} = 9.14 $(cal/cm^3)^{1/2}$; δ_{PCL} = 9.39$(cal/cm^3)^{1/2}$][48,49]. Subsequently, the value of the product χN was calculated and turned out to be approximately 33. For block copolymers, there are different degrees of miscibility in the melt based on the value that the product χN assumes: when χN is $\leq$10, the blocks in the copolymer are miscible in the melt, when χN is between 10 and 30, the blocks are weakly segregated, when χN is between 30 and 50 the blocks are intermediately segregated and, finally, when χN is >50 the two blocks are strongly segregated in the melt. Consequently, in the case of the system under examination, the separation that occurs is intermediate, as demonstrated also by the presence of the spherulites analyzed below (a fact that indicates that the phase segregation was overcome by the crystallization that was able to break out of the constrains of the phase segregated domains).

To better understand this phase separation in the melt, SAXS experiments were performed in the block copolymer, whose spectrum was compared with that of the random copolymer.

Figure 5.1 riports the plot of the intensity as a function of the scattering vector (q) for PHB_{39}-*b*-PCL_{61} (a) and P(HB_{72}-*ran*-CL_{28}) (b) samples in the melt. For the block copolymer, the presence of a diffraction peak at low q values is observed. This indicates that the blocks are segregated in the melt, as indicated by the calculation performed above, unlike the random copolymer, which obviously does not show phase separation, as the distribution of comonomers is random and hence it forms a single phase in the melt.

PHB and PCL have been reported to be immiscible in the melt in the case of blends.[35,50,51] Furthermore, phase segregation in PHB-based materials has also been reported in the case of PHBV blends with high hydroxyvalerate (HV) content.[52–55]

In the case of the block copolymer, it is possible to calculate the value of D from the value of q_{max} according to the following equation:

$$D = \frac{2\pi}{q_{max}} \tag{5.2}$$

The resulting value is about 45 nm and can be attributed to the distance between lamellae in a phase-segregated melt.

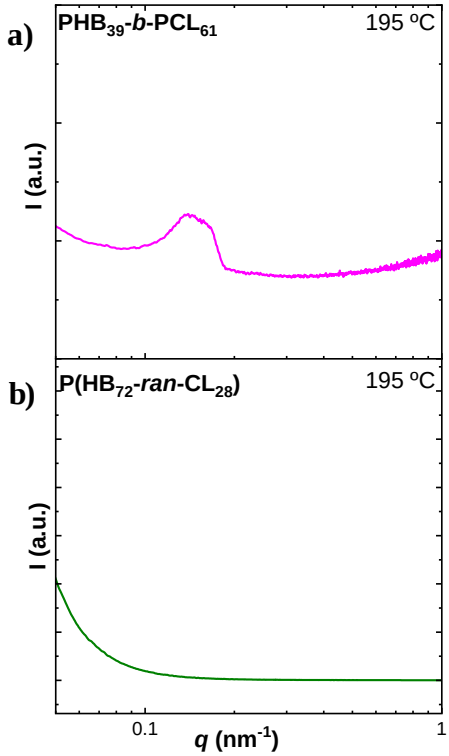

Figure 5.1. SAXS diffractograms acquired at 195 ºC for PHB_{39}-*b*-PCL_{61} (a) and P(HB_{72}-*ran*-CL_{28}) (b).

5.3.2 TGA and Non-isothermal DSC Results

Figure 5.2 shows the thermogravimetric curves of PHB and PCL neat samples reported in previous works[29,56] and those of the PHB_{39}-*b*-PCL_{61} and P(HB_{72}-*ran*-CL_{28}) copolymers. The homopolymers have a TGA curve consisting of a single degradation step, lower for PHB (about 280 ºC) and higher for PCL (about 380 ºC). The two copolymers exhibit two steps of degradation, as expected. Both in the block copolymer and in the random copolymer, the step at lower T can be attributed to the PHB component and the one at higher T to the PCL component. It is noted that the presence of PCL slightly increases the stability of PHB.

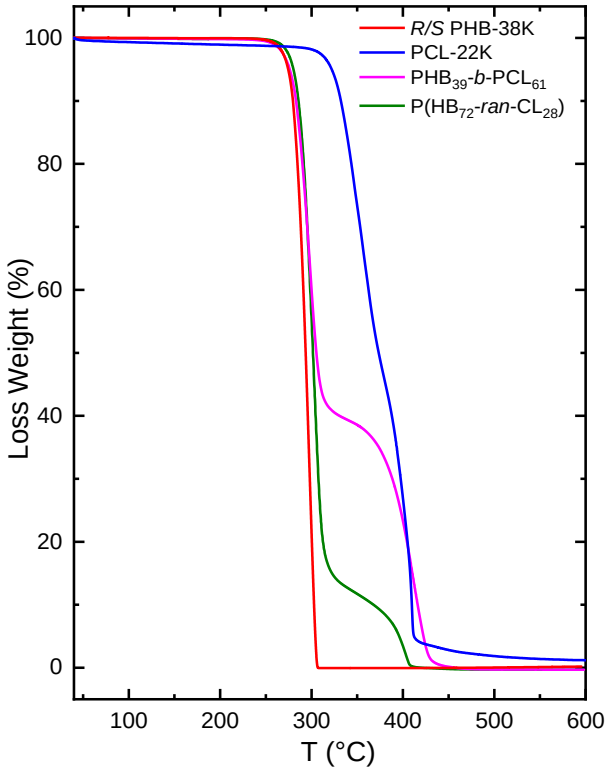

Figure 5.2. Weight loss (%)as a function of the temperature (°C) for PHB_{39}-*b*-PCL_{61}, P(HB_{72}-*ran*-CL_{28}), *R/S* PHB-38K and PCL-22K.

Figure 5.3 reports the DSC cooling curves from the melt (a) and the successive heating (b) of the samples involved in this study. The PHB_{39}-*b*-PCL_{61} block copolymer exhibits a crystallization exotherm due to the crystallization of the PCL block, which, in the copolymer, crystallizes at lower temperatures than the previously studied homopolymer (blue curve,[56]). It should be noted that the PHB block cannot crystallize during cooling at 20 °C/min. In the heating scan (Figure 5.3b), the first melting endotherm that appears at lower temperatures (at approximately 51.1 °C) corresponds to the melting of PCL block crystals, which melt at lower temperatures than in the PCL homopolymer.

Immediately after the melting of the PCL block in Figure 5.3b, a cold crystallization exotherm corresponding to the PHB block is observed at about 72 °C. Despite being absent in the reference neat PHB polymer (red curve in Figure 5.4b), this

phenomenon has been reported for higher molecular weight PHB samples[29]. This behavior can be attributed in part to the slightly higher molecular weight of the block copolymer's PHB chains but primarily to the presence of the covalently bonded PCL block chains, which apparently reduces the crystallization capacity of the PHB block. During cooling from the melt at 20 ºC/min the PHB block was not able to crystallize, as opposed to the neat PBH employed here for comparison purposes. However, the PHB block can crystallize upon heating from the glassy state in the observed cold-crystallization exotherm. At higher temperatures (i.e., 164 ºC), the melting peak of the PHB block is observed. The melting process is complex and at higher magnification a small cold-crystallization process is observed as well as bimodal melting. The behavior somewhat resembles that of neat PHB and it is typical of reorganization and recrystallization during the scan, as observed previously by us in this neat chemically synthesized PBH material. [29]

During the cooling process, the P(HB_{72}-*ran*-CL_{28}) random copolymer does not crystallize according to Figure 5.3a. In the successive heating process, a phenomenon of cold crystallization followed by melting is observed. Given the temperatures at which these phenomena occur, they can be atributed to the PHB block chains, which cold crystallize and then melt. The amount of PCL within the random copolymer is too low to allow it to crystallize. But, precisely, the presence of randomly distributed PCL units in the copolymer lowers the melting point of PHB (and its crystallinity), as the PCL units interrupt the linear crystallizable sequences of PHB. The PHB phase in the PHB-*ran*-PCL copolymer has a melting peak at about 145 ºC, lower than that of the block copolymer or neat PHB. As already observed in the case of the block copolymer and the neat polymer, the melting peak of PHB has a typical shape of crystal reorganization during heating.

Table 5.1 lists the thermal parameters obtained from the non-isothermal crystallization experiments, including the degree of crystallinity calculated as reported in Section 2.1.1. Considering the occurrence of the colf crystallization phenomenon described above, two degrees of crystallinity are distinguished, one calculated at 25 ºC and one calculated at 100 ºC, during the melting process.

It should be noted that, at 25 ºC, unlike the PHB homopolymer, the PHB component in the two copolymers has a degree of crystallinity equal to 0, since in the cooling process the chains did not crystallize. On the contrary, the PCL block is semi-crystalline, for both homopolymer and block copolymer cases.

At 100 ºC, the degree of crystallinity of the PHB remains constant in the case of the homopolymer (i.e., 41%), while it reaches a value of 46% in the case of the block copolymer (similar to the neat PHB homopolymer considering the error of the measurement, i.e., typically between 10 to 15%) and only 22% in the case of the random copolymer, as the PHB component cold crystallizes in the two copolymers during heating. The degree of crystallinity of the PCL component at 100 ºC is equal to zero, as it is molten.

Summarizing, incorporating 28% PCL units randomly distributed within the PHB chains depresses its melting temperature by approximately 22 ºC and reduces the non-isothermal crystallization substantially, as the material is not able to crystallize during cooling from the melt at 20 ºC/min. Nevertheless, the PHB segments (72%) within the random copolymer can cold crystallize during heating (at 20 ºC/min) to achieve a maximum degree of crystallinity that is only 22%, or about half the degree of crystallinity that neat PHB can developed during cooling from the melt. These results reveal the strong effects caused by random copolymerization with PCL. The PCL segments (28%) in the random copolymer are unable to crystallize (lowering even more the total crystallinity degree of the sample).

On the other hand, in the case of the block copolymer with 39% PHB, both blocks are able to crystallize, but the 61% PCL content also reduces the non-isothermal crystallization kinetics of the PHB block and this component is not able to crystallize during cooling from the melt at 20 ºC/min. The PHB blocks can only crystallize during heating from the glassy state at (at 20 ºC/min), but the crystals formed melt at slightly lower temperatures than those of neat PHB (i.e., 4.5 ºC lower), while the degree of crystallinity of the PHB blocks is comparable within error to that of neat PHB.

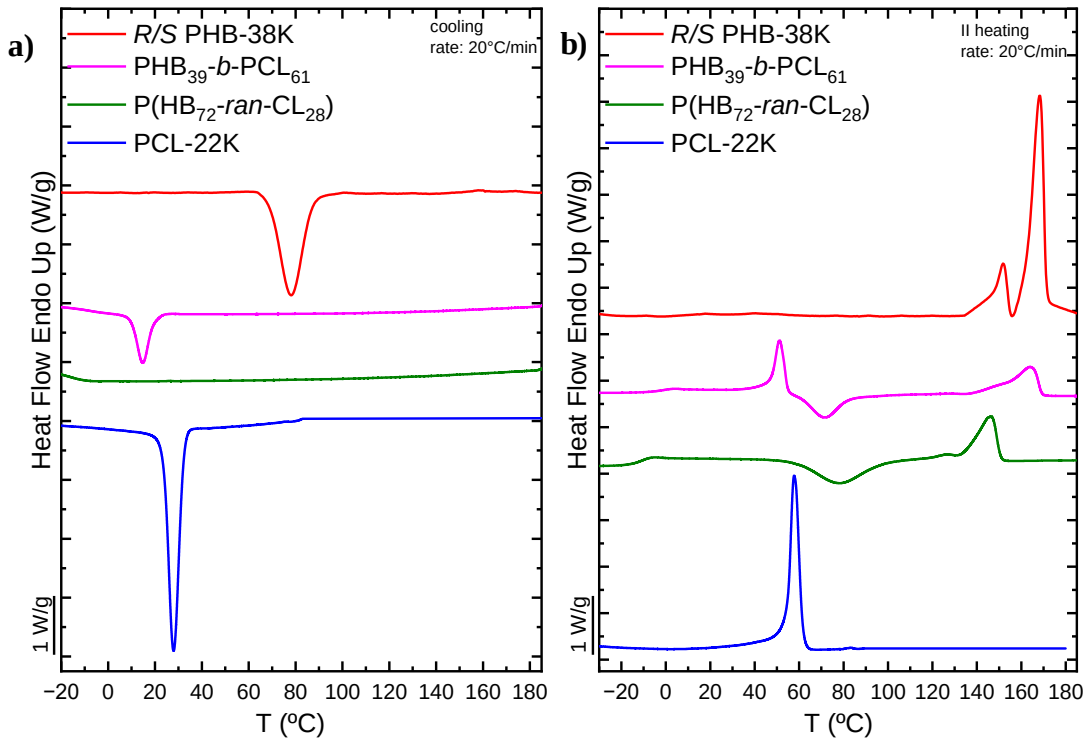

Figure 5.3. a) DSC cooling scans at 20 ºC/min and b) subsequent DSC heating scans at 20 ºC/min for PHB_{39}-*b*-PCL_{61}, P(HB_{72}-*ran*-CL_{28}), *R/S* PHB-38K and PCL-22K.

Table 5.1. Calorimetric data extracted from Figure 5.4 for *R/S*-PHB 38K, PCL-22K PHB_{39}-*b*-PCL_{61} and P(HB_{72}-*ran*-CL_{28}).

	***R/S*-PHB 38K**	**PCL 22K**	**PHB_{39}-*b*-PCL_{61}**	**P(HB_{72}-*ran*-CL_{28})**
$T_{c/cc}$ **(°C)**	78.0	28.0	14.8 (PCL block) 71.4 (PHB block)	78.3
$\Delta H_{c/cc}$ **(J/g)**	60	60	22 (PCL block) 22(PHB block)	37
T_m **(°C)**	151.8/168.5	58.9	51.2 (PCL block) 164.0 (PHB block)	126.2/146.5
ΔH_m **(J/g)**	14/87	60	21 (PCL block) 27 (PHB block)	32
$x_{c,25\ ^oC}$ **(%)**	41	43	25 (PCL) 0 (PHB)	0 (PHB) 0 (PCL)
$x_{c,100\ ^oC}$ **(%)**	41	0	0 (PCL) 46 (PHB)	0 (PCL) 22 (PHB)
T_g **(°C)**	1.4	-50.6	-3.9	-14.0
% PCL	0	100	61	28
M_n **(kDa)**	38	22	36 (Total) 14 (PHB) 22 (PCL)	75

5.3.3 Non-isothermal PLOM Results

The morphology of the samples was studied by PLOM to understand better the effect of phase segregation in the block copolymer and any differences between the block and random copolymer.

Figure 5.4 reports PLOM micrographs of the PHB_{39}-*b*-PCL_{61} block and P(HB_{72}-*ran*-CL_{28} random copolymers compared to the PHB homopolymer. The micrograph in

Figure 5.4a belongs to the homopolymer of PHB at room temperature taken after cooling from the melt at 20 ºC/min. Instead, in the case of the block and random copolymers, the micrographs shown in Figure 5.4b and Figure 5.4c were obtained during the second heating process (immediately after cooling from the melt at 20 ºC/min) at 100 ºC for the block copolymer and at 107 ºC for the random copolymer (both temperatures exceed the cold crystallization temperature for the PHB component according to Figure 5.3b), since, as already observed previously by DSC (Figure 5.3a), no crystallization of the PHB component was detected in the copolymers during the cooling process from the melt.

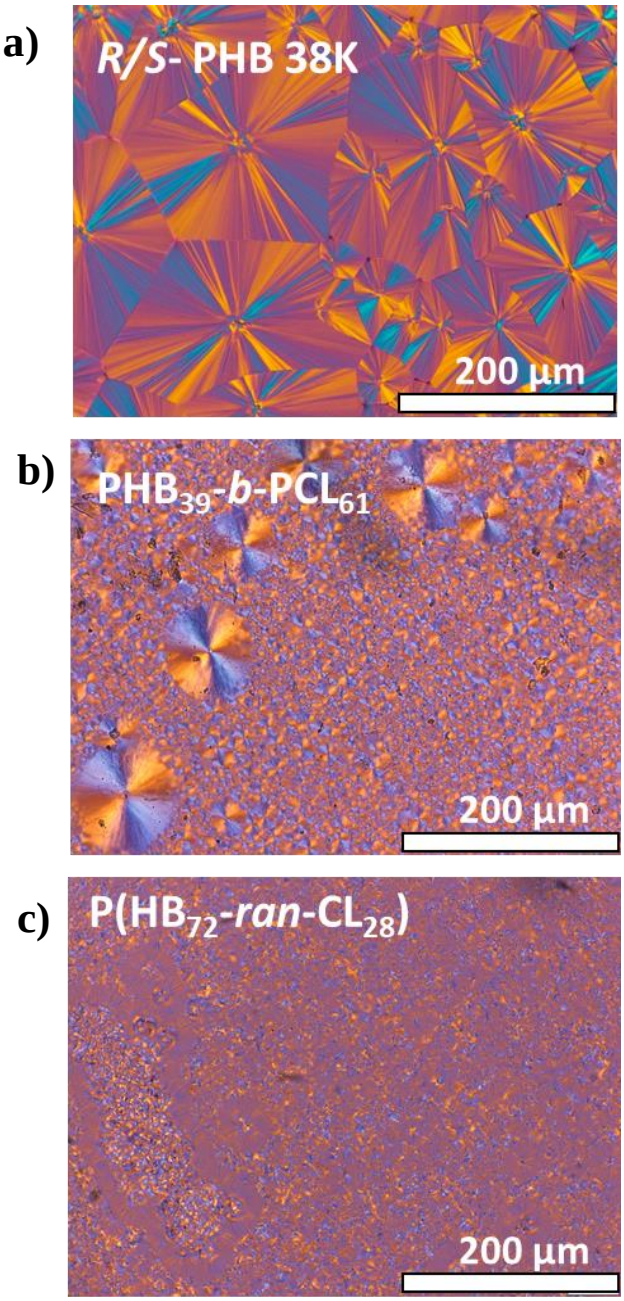

Figure 5.4. PLOM micrographs corresponding to PHB superstructural morphology. For the neat *R/S*-PHB 38K (a), the micrograph was taken after cooling it from the melt at 20 ºC/min at 25 ºC. In the case of the copolymer samples, the micrographs were taken during the second heating run at 100 ºC for the PHB_{39}-*b*-PCL_{61} sample (b) and at 107 ºC for the P(HB_{72}-*ran*-CL_{28}) sample.

The first aspect that can be noticed is the disparity in the nucleation density of PHB in the copolymer samples, compared to neat PHB, which is characterized by a low nucleation density and, thus, large spherulitic sizes (Figure 5.4a). The nucleation density of the PHB component, as deduced by the large number of spherulites per unit area, is very high for the block copolymer PHB_{39}-*b*-PCL_{61} (Figure 5.4b) and even higher in the random copolymer P(HB_{72}-*ran*-CL_{28}) (Figure 5.4c), compared with the PHB homopolymer (Figure 5.4a). In the case of the P(HB_{72}-*ran*-CL_{28}) random copolymer, Figure 5.4c is characterized by a very fine PHB microspherulitic morphology. In this copolymer, the PCL block does not crystallize, and even if it did, the micrograph was taken at temperatures well above the melting of PCL crystals.

The formation of well-defined PHB spherulites in the PHB_{39}-*b*-PCL_{61} block copolymer indicates that crystallization take precedence over the phase segregation observed in the molten stat detected by SAXS. This phenomenon occurs due toa break-out process during the heating DSC scan, triggered by the cold crystallizzation of PHB block chains. As can be seen from the micrograph shown in Figure 5.4b, in the PHB_{39}-*b*-PCL_{61} block copolymer, the PHB block crystallizes forming negative spherulites. This is clearly indicated by the first and third quadrant yellow extinction colors that can be seen when using a lambda red tint plate at 45 º with respect to the polarizer direction (as we have done in this work[57]). This is a peculiar aspect since, previous literature reports that PHB tends to form positive spherulites both in enantiomerically pure *R*-PHB of bacterial origin [58,59] and in the case of synthetic origin PHB in the form of a racemic mixture *R/S* [29].

This inversion in the sign of the spherulites has already been reported in the literature for PHB, when it is blended with miscible polymers, and, more specifically, in the case of blends with polymethylacrylate (PMA) [60], and polybutylene adipate (PBA).

[61] In the first case, a critical composition is reported at which the inversion occurs, i.e., 60% PHB and 40% PMA[60], and in the second case, the inversion is governed by the crystallization temperature, as low crystallization temperatures lead to the formation of negative spherulites in the PHB/PBA blend (50/50)[61]. In both cases, the inversion is due to the rotation of the lamellae with respect to the classical direction, which would make the spherulite positive. This optical sign switch is only observable when the PHB is in fully miscible systems with no phase separations or segregations. This could also be an explanation for the system studied in this paper, given the intermediate phase segregation that characterizes the PHB_{39}-*b*-PCL_{61} sample (see Section 5.3.1).

5.3.4 Isothermal PLOM Results

As spherulites were detected in the PHB_{39}-*b*-PCL_{61} block copolymer during the non-isothermal crystallization, isothermal crystallization experiments were contucted to evaluete6 spherulitic growth rates by PLOM. The sample was cooled rapidly from the melt (at a rate of 50 ºC/min) to various isothermal crystallization temperatures ranging from 90 to 110 ºC. The growth rate *G* (μm/s) of the spherulites was then determined by calculating the slope of the linear graph graphing the spherulitic radius over time for each crystallization temperature. Employing this approach, it was possible to follow the isothermal spherulitic growth from the melt specifically for the PHB block in the PHB_{39}-*b*-PCL_{61} copolymer, as the crystallization temperatures for the PCL block are much lower. Unfortunately, attempts to follow the PCL block spherulitic growth failed, as the sample crystallized with a very high number of very small spherulites.

Typically, two phenomena [62,63] compete in the trend of spherulitic growth rate as a function of temperature which yield a bell-shaped curve. On the right side of the bell-shaped curve, as temperature decreases, the growth rate increases. In this elevated

temperature range (near the melting point), the growth rate is primarly influenced by secondary nucleation kinetics, wich intesifies with supercooling until it reaches its peak level.. At this maximum point, the melt viscosity has increased so much, as temperature is reduced, that diffusion takes over. The rate at which crystalas grow is controlled by gradual movement of polymer chains towards the crystallization front. As a result, the growth rate decreases with a decrease in temperature.. When a temperature value close to T_g is reached, the growth rate decreases gradually until reaches zero as long-range chain mobility stops below T_g.

In Figure 5.5a, the results of the spherulitic growth rate as a function of T_c are reported. For the PHB_{39}-*b*-PCL_{61} block copolymer, it was possible to measure the growth rate of the PHB block only on the right side of the typical bell shaped-curve (magenta squares in the graph) as after rapid cooling to crystallization temperatures below 90 ºC, the sample isothermally crystallized into many small spherulites (due to a high nucleation density) which saturated the observation area. The spherulitic growth rates for the reference PHB sample have been reported in a previous work[29] and are included in Figure 5.5a for comparison purposes (red dots in the graph).

In both samples, secondary nucleation dominates the superstructural growth and determines the trend of the graph in Figure 5.5a. The T_c range is similar for both samples and it is evident that the PHB block in the copolymer crystallizes more slowly than the reference pure PHB. Notice that the number average molecular weight of the reference material is 38.000 g/mol while that of the PHB block is only 14.000 g/mol. One would expect lower molecular weight PHB homopolymer chains to crystallize faster[25]. However, in this case, the 14.000 g/mol PHB chains are covalently bonded to PCL chains and this seems to be the determining factor in the observed behaviour. In fact, the *G* values corresponding to the PHB block within the PHB-*b*-PCL copolymer are always lower than

those of the reference neat PHB. The reason is probably due to the presence of the covalently bonded PCL block chains which are molten at the crystallization temperature of the PHB block, and their high mobility interferes with the spherulitic growth of the PHB block chains at the growth front, slowing down the crystal growth of the PHB block. This has also been reported for samples of PLLA-*b*-PCL block copolymer in which the molten PCL block chains slow down the crystallization of the PLLA block [64] in view of their weakly/intermediate segregated strength in the melt, such as the system under study.

Figure 5.5b shows the *G* value of PHB_{39}-*b*-PCL_{61} copolymer divided by the *G* value of neat PHB as a function of temperature: it can be noticed that in the entire T_c range, the normalized *G* value is, on average, 0.35 and this indicates that the PHB_{39}-*b*-PCL_{61} block copolymer has a 65% slower spherulitic growth rate than the PHB homopolymer sample employed here for comparison purposes.

Figure 5.6 shows two PLOM images taken at the indicated T_c values for PHB_{39}-*b*-PCL_{61} (a) and *R/S* PHB-38K [29] (b). The difference in morphology is evident, as the presence of negative spherulites is observed in the PHB block spherulites, contrary to what is observed in the reference PHB which has an average positive sign. Furthermore, the reference PHB is characterized by banded spherulites (Figure 5.6b) unlike the PHB block within the copolymer, which forms very clear Maltese crosses without any banding.

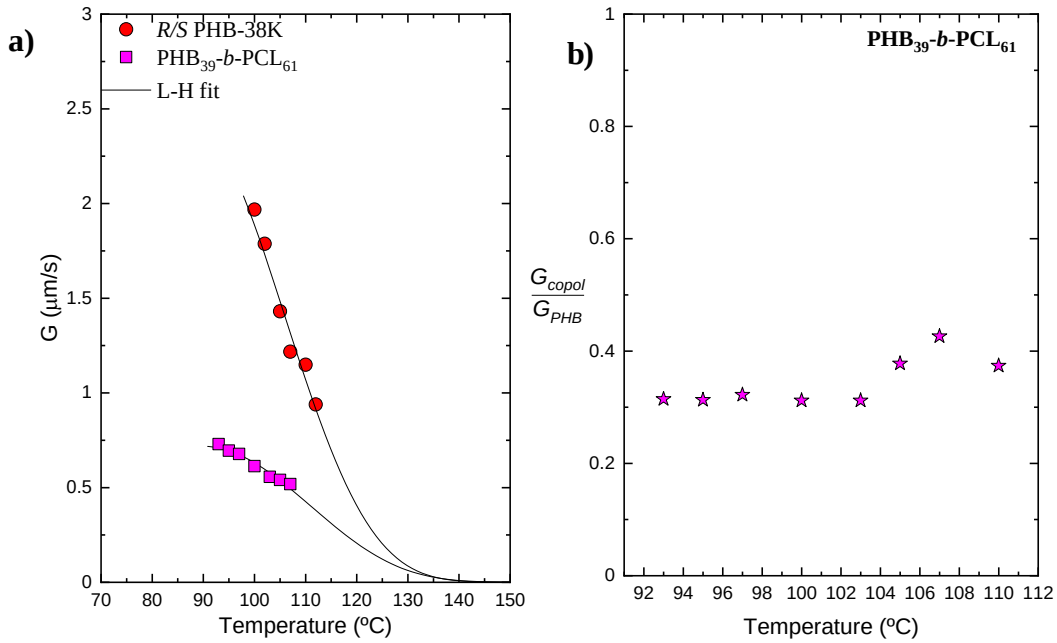

Figure 5.5 Spherulitic growth rate (*G*) as a function crystallization temperature (a) for PHB_{39}-*b*-PCL_{61} sample compared with *R/S* PHB-38K [29], and normalized spherulitic growth rate ($\frac{G_{copol}}{G_{PHB}}$) over crystallization temperature (b). The solid lines in the graph on the left are fits to the Lauritzen and Hoffman equation.

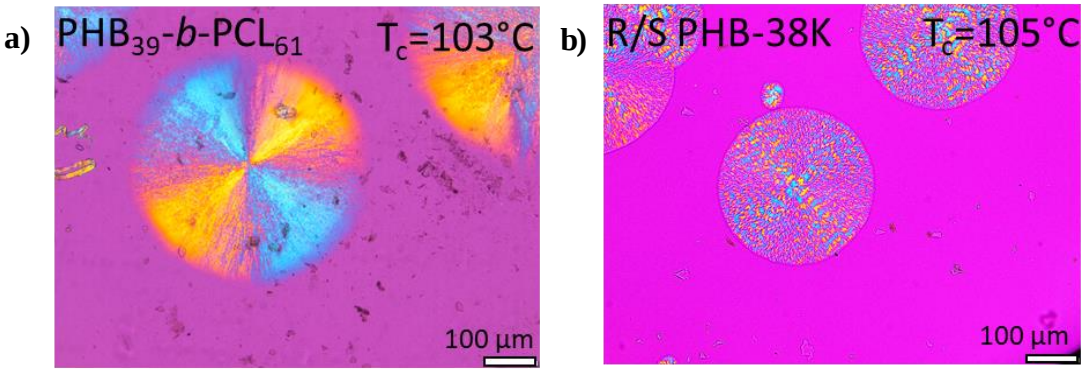

Figure 5.6 PLOM micrographs taken at the indicated T_c for *R/S* PHB_{39}-*b*-PCL_{61} (a) and PHB-38K [29] (b).

The theory of Lauritzen-Hoffman [65] was used to fit the experimental data and the solid lines in Figure 5.5a are the result of this fit.

The used Lauritzen-Hoffman equation was the following:

$$G = G_o \, exp\left[\frac{-U^*}{R(T_c - T_0)}\right]\left[\frac{-K_g^G}{fT(T_m^0 - T_c)}\right] \quad (5.3)$$

In this equation G_o is a constant that includes all terms that are not temperature dependent, U^* is an energy that in this study, assumes the value of 1550 cal/mol. More specifically it is a transport activation energy for the diffusion of polymer chains; R is the universal gas constant, T_c is the crystallization temperature, T_0 is 30ºC degrees lower than the T_g and is the temperature that corresponds to the frozen movement of the chains, T_m^0 is the equilibrium melting temperature and f is a temperature correction factor represented by the following expression $2T_c/(T_m^0 + T_c)$. Furthermore, K_g^G is a constant proportional to the energy barrier for the spherulitic growth or secondary nucleation, given by the expression:

$$K_g^G = \frac{j\, b_0\, \sigma\sigma_e T_m^0}{k\, \Delta H_m^0} \quad (5.4)$$

j assumes the value of 2 for the Regime II crystallization, a regime where the secondary nucleation and the spread of the nucleus on the growth front are equivalent[66], b_0 is the chain's width, σ represents the lateral surface free energy, σ_e is the fold surface energy, k is the Boltzmann constant and is the equilibrium latent heat of fusion. If $\ln G + \frac{-U}{R\,(T_c - T_0)}$ is plotted versus $\frac{1}{T_c(\Delta T)f}$, it is possible to obtain a straight line where K_g^G is the slope and G_o the intercept. Through K_g^G, it could be possible to calculate the $\sigma\sigma_e$ value, and by the expression $\sigma = 0.1\Delta H_m^0\sqrt{a_0 b_0}$, where $a_0 b_0$ is the chain cross-sectional area, it is possible to obtain the values of σ and σ_e. Furthermore, it is also possible to calculate q, the work that macromolecules do to fold as $2a_0 b_0 \sigma_e$.[67]

The parameters obtained from the fits are shown in Table 5.2. Even though the theory fits the data points, as shown in Figure 5.5a, the fitting parameters have values that are very close and probably within the errors involved in the fits. For the random P(HB_{72}-*ran*-CL_{28}) copolymer it was not possible to follow the spherulite growth of the PHB component, as the spherulites are too small (even at high T_c values) and saturate the observation area very quickly as a result of a nucleation density higher than that observed for the spherulites of the PHB block within the block copolymer.

Table 5.2. Isothermal kinetics data parameters derived from experimental results obtained by PLOM. The data for *R/S* PHB-38K are present in the literature. [29]

Sample	G^0 (cm/s)	K^G_g (K^2)	σ (erg/cm^2)	σ_e (erg/cm^2)	q (erg)	R^2
PHB_{39}-*b*-PCL_{61}	3.85	3.67×10^5	8.39	228.2	8.42×10^{-13}	0.995
R/S PHB-38K [29]	136	3.33×10^5	8.39	284.2	1.05×10^{-12}	0.986

5.3.5 Study of the Overall Crystallization Kinetics by DSC

DSC was used to conduct isothermal crystallization experiments, aimed at investigating the overall crystallization kinetics resulting from the combined effects of primary nucleation and the growth of supestructural aggregates. The discussion below is divided into two sections for ease of understanding. Indeed, in section 5.3.5.1, the crystallization of the PHB block in the PHB_{39}-*b*-PCL_{61} and P(HB_{72}-*ran*-CL_{28}) copolymers is discussed in comparison with the neat PHB. In section 5.3.5.2, the crystallization of the PCL block in the PHB-*b*-PCL block copolymer is presented, for the case in which the PHB block was quenched to the amorphous state and also for the different case in which it was allowed to crystallize first.

One of the ways to analyse the overall crystallization kinetics results is to fit them with the Avrami theory[68–70] represented by the following equation:

$$1 - V_c(t - t_0) = \exp(-k(t - t_0)^n) \quad (5.5)$$

in which V_c is the relative volumetric transformed fraction into semi-crystalline state, *t is* the experimental time, t_0 is the induction time, *k* represents the overall crystallization rate constant, and *n* is the Avrami index, whichis connected to the nucleation rate and the growth dimensionality of the crystals.

5.3.5.1 PHB block crystallization within PHB_{39}-b-PCL_{61} and crystallization of the PHB component within P(HB_{72}-ran-CL_{28})

As previously mentioned, the results of the global isothermal crystallization of the PHB component in the PHB_{39}-*b*-PCL_{61} and P(HB_{72}-*ran*-CL_{28}) samples are reported in this section. Figure 5.7a reports the inverse half-crystallization time, $1/\tau_{50\%}$, over the crystallization temperature for the PHB component in the PHB_{39}-*b*-PCL_{61} and P(HB_{72}-*ran*-CL_{28}) copolymers in contrast with the reference PHB. The value of $1/\tau_{50\%}$ is the inverse of the time that the polymeric materials need, during an isotherm, to crystallize to 50% of their relative crystallinity. Experimentally, this parameter contains two contributions, namely nucleation and superstructural growth, in fact, it is an experimental measure of the overall crystallization rate.As can be seen in Figure 5.7a. As depicted in Figure 5.7a, the PHB component in the PHB_{39}-*b*-PCL_{61} and P(HB_{72}-*ran*-CL_{28}) samples crystallize more slowly than in the reference neat PHB. The reason for this beavior may be attributed to the presence of PCL, which, at the crystallization temperatures of PHB, is in the molten state and interferes with the crystal growth, as argued above for the block copolymer case, resulting in a decrease of the overall crystallization as well. For the random copolymer, a plasticization effect could be expected, as the T_g of the copolymer is lower than the T_g of neat PHB, as predicted for a random copolymer, see Table 5.1.

This behavior was also found in the case of random copolymers composed of PBS and PCL, in which it was also observed that a solvent-type effect increased as the amount of PCL increased, slowing down the crystallization rate of PBS. [71]

The reduction of the overall crystallization rate of the copolymers compared to the neat reference polymers has been extensively thoroughly investigated in existing literature and has also been recorded by Arandia *et al*.[72], in the case of random copolymers based on polybutylene succinate and polybutylene azelate: the incorporation of units of BAz results in an increase in the density of nuclei but a decrease in the overall crystallization rate of PBS. A similar situation arises for many random copolyesters, as reported in ref. [73]

The solid lines in Figure 5.7a symbolize the Lauritzen and Hoffman equation used to fit the experimental data.

The Lauritzen and Hoffman theory described previously can be used to fit the overall isothermal crystallization data obtained from the DSC. In this case, the equation to be applied changes with the introduction of a new parameter, i.e., the inverse of the half-crystallization time, $\tau_{50\%}$, and becomes as follows:

$$\frac{1}{\tau_{50\%}} = \frac{1}{\tau_{50\%}} exp\left[\frac{U}{R(T_c - T_0)}\right]\left[\frac{-K_g^{\tau}}{fT(T_m^0 - T_c)}\right] \quad (5.6)$$

All terms have already been described in the main text (Paragraph 3.4), except for K_g^{τ} which now becomes a constant that is proportional to the energy barrier for both primary nucleation and spherulitic growth. Thus, it encompasses more information than K_g^G which only refers to secondary nucleation or growth.

As can be seen, in the case of PHB_{39}-*b*-PCL_{61}, the fit was performed with two crystallization Regimens: for low T_c the fit was performed with Regime III, and for high T_c with Regime II. According to the L-H theory, three Regimes are distinguished for the

description of two competing phenomena which are the creation of fresh nuclei and the deposition of chains on the lateral surface of the nuclei to complete their growth. In Regime I, the secondary nucleation rate is extremely reduced, in Regime II the secondary nucleation rate and lateral growth rates are comparable, and in Regime III the secondary nucleation rate is the fastest. This behavior was not found in the reference neat PHB not inthe P(HB_{72}-*ran*-CL_{28}), in which the fits were performed with only one Regime (i.e. Regime II). The presence of these two Regimes is, in the block copolymer, due once again to the molten PCL, which interferes with the crystallization of the PHB block and is also found in the case of polypropylene/ethylene-octene[74] blends and polyethylene(butylene/diethylene succinate) block copolymers[75]. Regarding the P(HB_{72}-*ran*-CL_{28}) random copolymer, the PCL is present in very small quantities compared to the PHB, and this probably does not interfere with the Regime of crystallization of the PHB, which takes place in Regime III only. The results of the Lauritzen and Hoffman fit are listed in Table 5.3, where the correct relationship between K^{τ}_{g} (II) and K^{τ}_{g} (III) is observed, which is around 2 for the block copolymer PHB_{39}-*b*-PCL_{61}.

Figure 5.7b shows the value of $1/\tau_{50\%}$ of PHB_{39}-*b*-PCL_{61} and P(HB_{72}-*ran*-CL_{28}) copolymers divided by the value of $1/\tau_{50\%}$ of neat PHB with respect to the crystallization temperature. It is observedIt can be noticed that in the case of the random copolymer, this value is almost constant and always less than 0.1. In the case of the block copolymer there is an increase in the normalized value of $1/\tau_{50\%}$, which assumes the value of 0.2 in the case of high T_c. If we compare Figure 5.7b with Figure 5.7b, it can be observed that the reduction in spherulitic growth rate leads to a normalized ratio of growth rate of 0.3, which increases to 0.4 at high temperatures. These values are higher than the ratios of normalized overall crystallization rates (0.1 to 0.2), and this indicate that the decrease in

the overall crystallization rate of the PHB component within the copolymers is influenced significantly by both nucleation and spherulitic growth rate.

Both the PHB components in the block copolymer and the random copolymer crystallize more slowly than the reference PHB homopolymer (90% slower in the random copolymer and 80% slower for the block copolymer). Considering Figure 5.6a, where it was not possible to measure the spherulitic growth of the random copolymer due to its high nucleation density (see Figure 5.4c), it can be considered that the slow and determining step for the overall crystallization rate is the spherulitic growth rate. In spite of the fact that nucleation is enhanced in the PHB component of the copolymers, their overall crystallization is much smaller than in neat PHB because of the slow spherulitic growth.

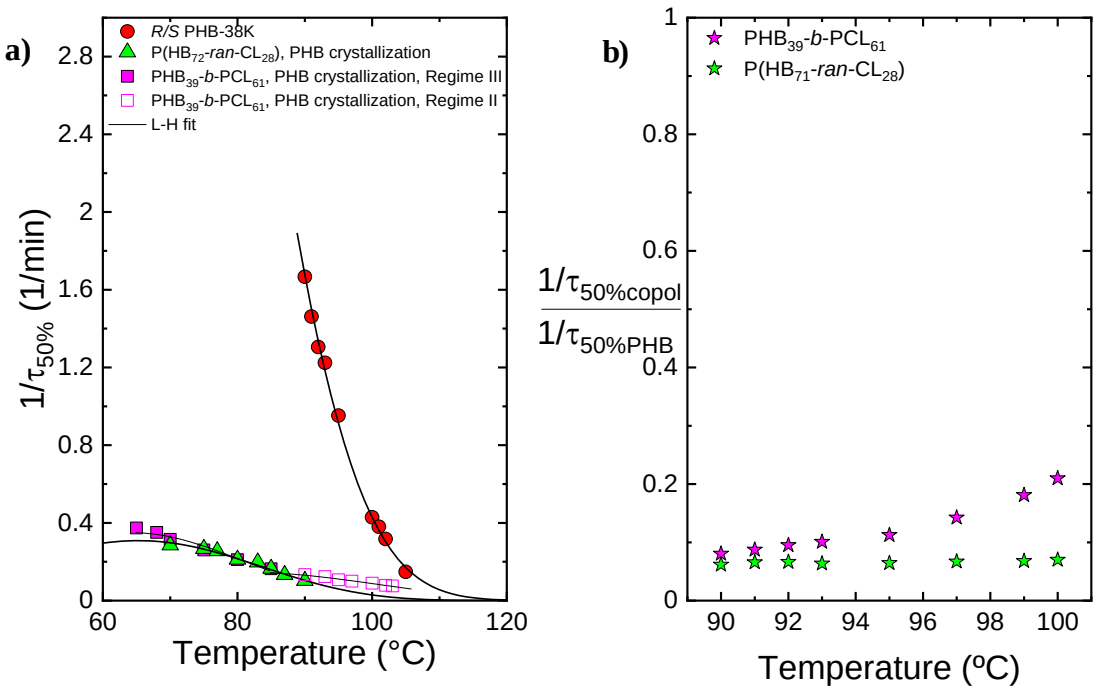

Figure 5.7. Inverse of half-crystallization time ($1/\tau_{50\%}$) (a) and normalized inverse of half-crystallization time ($1/\tau_{50\%}$) (b) as a function of T_c for PHB block crystallization

in PHB_{39}-*b*-PCL_{61} and P(HB_{72}-*ran*-CL_{28}) samples in comparation with *R/S* PHB-38K.[29] The solid lines in (a) represent the fits to the Lauritzen and Hoffman theory.

Table 5.3. Overall isothermal kinetics data parameters derived from experimental results obtained by DSC.

Sample	$1/\tau_0$(1/s)	K^{τ}_{g} (K^2)	σ (erg/cm^2)	σ_e (erg/cm^2)	q (erg)	R^2
PHB_{39}-*b*-PCL_{61} Regime III (PHB crystallization)	7.40×10^{10}	7.79×10^{5}	8.39	332.5	1.23×10^{-12}	0.994
PHB_{39}-*b*-PCL_{61} Regime II (PHB crystallization)	1.90×10^{5}	3.74×10^{5}	8.39	318.9	1.18×10^{-12}	0.996
P(HB_{72}-*ran*-CL_{28})	1.83×10^{5}	2.77×10^{5}	8.39	253.4	9.35×10^{-13}	0.997
R/S PHB-38K[29]	7.22×10^{12}	6.20×10^{5}	8.39	699.9	2.58×10^{-12}	0.990

Figure 5.8a reports the degree of crystallinity (x_c) obtained at the end of the isothermal crystallization process for the two copolymers and for the reference PHB as a function of crystallization temperature. The value of the degree of crystallinity increases with the increase of the crystallization temperature for all the samples; and in the case of the block copolymer, it reaches values that are very similar to those of the reference PHB, while in the case of the random copolymer the values are significantly lower as expected. In the random copolymer, the PHB chains are interrupted by randomly placed units of PCL which limit the maximum degree of crystallinity achieved. It is important to realize that even though the crystallinity degree achieved at the end of the crystallization period is the same for the PHB block and neat PHB, their crystallization kinetics is very different

(as indicated in Figure 5.7). Therefore, the achievement of this similar degree of crystallization upon saturation can only be achieved at extremely different times at the same crystallization temperatures.

Figure 5.8b shows the progression of the crystallization enthalpy obtained during the isothermal crystallization process at T_c=90 ºC for the *R/S* PHB-38K, PHB_{39}-*b*-PCL_{61} and P(HB_{72}-*ran*-CL_{28}) samples as a function of time. It is observed that the time required for the material to crystallize completely is very small (less than 0.5 min) in the case of the reference PHB homopolymer than in the block and random copolymer. This corroborates the findings obtained from the comprehensive isothermal crystallization experiments shown in Figure 5.7. It should also be noted that the crystallization enthalpy in Figure 5.8b is normalized by dividing it by the maximum enthalpy achieved after crystallization has saturated, but if Figure 5.7a is observed, it can be realized that in the case of the random copolymer, not only the PHB component crystallizes much slower than neat PHB, but also achieves a final degree of crystallinity which is substantially lower.

Copolymerizing PHB with PCL provokes higher nucleation, which is normally related to better optical properties (higher transparency) and also lower degree of crystallinity, at least in the random copolymer case (or in the block copolymer case, depending on the cooling rate or crystallization time). Lower degrees of crystallinity in PHB with smaller spherulites can produce much tougher materials from a mechanical point of view than brittle neat PHB.[30]

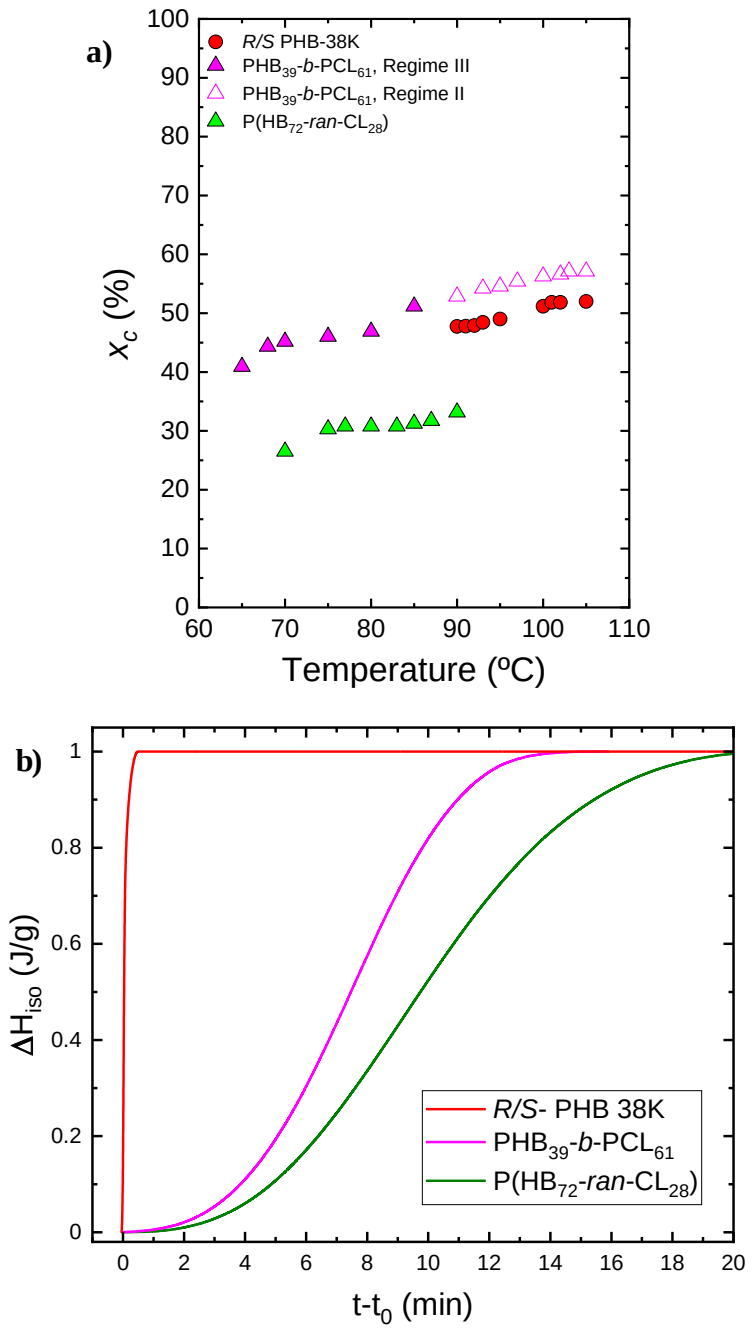

Figure 5.8. Degree of crystallinity (x_c) obtained during isothermal crystallization as a function of T_c (a) and enthalpy obtained during the isothermal crystallization process (ΔH_{iso}) at T_c=90 ºC as a function of time (b).

The experimental data of isothermal crystallization have been fitted, as described previously, with the Avrami theory. Figures 5.9 through 5.10 present examples of

comparisons between the DSC experimental isotherms and the prediction of the Avrami fit (a) and the typical Avrami plot in the conversion range used to make the fit (b), obtained using the free App developed by Pérez-Camargo *et al.*[76] The detailed results are shown in Tables 5.4 and 5.5. The fitting obtained is very for the whole range of T_c in the primary crystallization range (employing a conversion range between 3 and 20% where the free growth approximation is usually valid), and the correlation coefficient was always greater than 0.999. Also for the value of $\tau_{50\%}$, the values predicted by Avrami's theory are in good agreement with the experimental ones, indicating that the fits are a good representation of the experimental data until 50% conversion. Tables 5.4 and 5.5 also shows the Avrami index which assumes, on average, the value of 3, and this indicates the presence of instantaneously nucleated spherulites on average for the entire crystallization temperature range, as previously demonstrated by PLOM analysis.

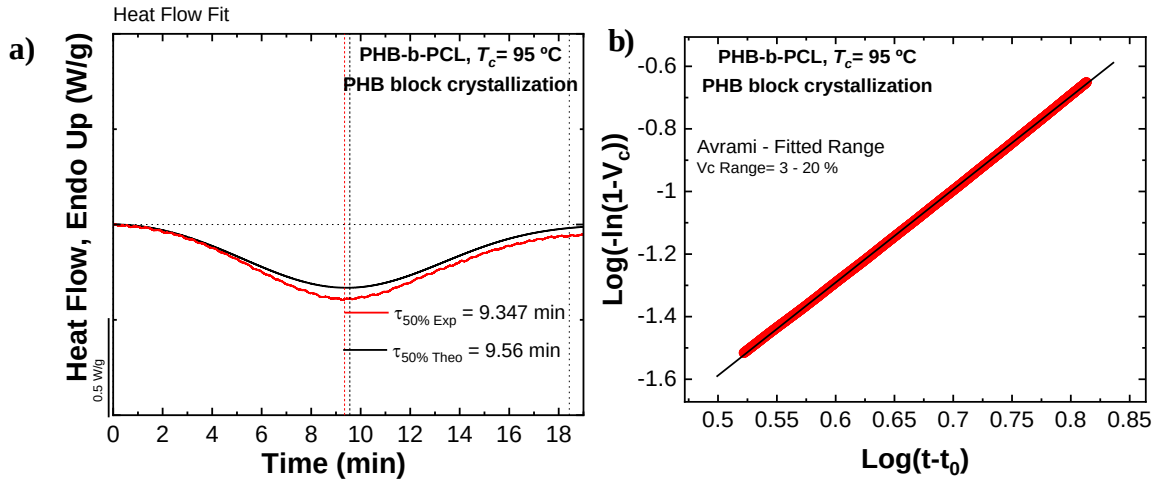

Figure 5.9. The Avrami fit equation using the free Origin plug-in developed by Pérez-Camargo *et al.* [76] for PHB block crystallization in PHB_{39}-*b*-PCL_{61} sample at T_c= 95 °C.

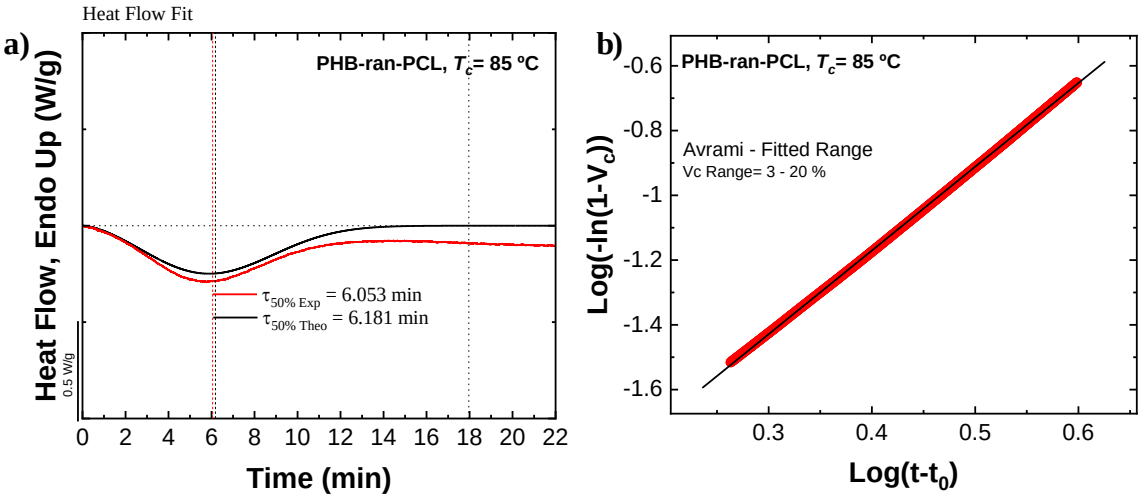

Figure 5.10 The Avrami fit equation using the free Origin plug-in developed by Pérez-Camargo *et al.* [76] for P(HB_{72}-*ran*-CL_{28}) at T_c= 85 ºC.

Table 5.4 Avrami fitting parameters obtained from by the free App [76] for PHB crystallization in PHB_{39}-*b*-PCL_{61} sample.

T_c(°C)	t_0(min)	$\tau_{50\% Exp}$ (min)	$\tau_{50\% Theo}$ (min)	n	$K^{\frac{1}{n}}(min^{-1})$	$K\ (min^{-n})$	R^2
65	0.56	2.674	2.772	2.84	0.316	$3.82x10^{-2}$	0.999
68	0.581	2.767	2.892	2.71	0.301	$3.88x10^{-2}$	0.999
70	0.653	3.172	3.214	2.96	0.274	$2.18x10^{-2}$	0.999
75	0.653	3.84	3.74	2.75	0.233	$1.84x10^{-2}$	0.999
80	0.66	4.753	4.703	2.97	0.408	$7.00x10^{-2}$	0.999
85	0.68	6.502	6.664	2.894	0.137	$3.20x10^{-3}$	0.999
90	0.685	7.47	7.884	2.62	0.266	$3.13x10^{-2}$	0.999
93	0.735	8.117	8.127	2.76	0.107	$2.14x10^{-3}$	0.999
95	0.755	9.347	9.56	2.97	0.092	$8.41x10^{-4}$	0.999
97	0.772	8.882	8.837	2.68	0.098	$2.01x10^{-3}$	0.999
100	0.78	9.097	9.143	2.58	0.094	$2.30x10^{-3}$	0.999

102	0.803	12.678	12.543	2.94	0.070	4.10×10^{-4}	0.999
103	0.872	13.3	13.478	3.07	0.065	2.33×10^{-4}	0.999

Table 5.5. Avrami fitting parameters obtained from by the free App [76] for P(HB_{72}-*ran*-CL_{28}) sample.

T_c(°C)	t_0(min)	$\tau_{50\% Exp}$ (min)	$\tau_{50\% Theo}$ (min)	n	$K^{\frac{1}{n}}(min^{-1})$	$K\ (min^{-n})$	R^2
70	0.428	3.502	3.513	2.86	0.251	1.92×10^{-2}	0.999
75	0.448	3.74	3.793	2.63	0.229	2.09×10^{-2}	0.999
77	0.507	3.918	3.843	2.86	0.213	5.65×10^{-2}	0.999
80	0.613	4.712	4.787	2.62	0.181	1.14×10^{-2}	0.999
83	0.613	5.06	5.164	2.69	0.168	8.37×10^{-3}	0.999
85	0.738	6.053	6.181	2.59	0.140	6.24×10^{-3}	0.999
87	0.785	7.507	7.446	2.98	0.118	1.74×10^{-3}	0.999
90	0.95	9.749	9.708	2.71	0.088	1.42×10^{-3}	0.999

5.3.5.2 PCL block crystallization in PHB_{39}-b-PCL_{61} from crystalline and amorphous PHB.

This section reports the results of the isothermal crystallization of the PCL block in the PHB_{39}-*b*-PCL_{61} sample, compared with the results obtained for a reference neat PCL.[56] It should be observed that the isothermal crystallization of PCL was performed using two different pathways. In the first, the sample rapidly cooled from the molten state at rate of 60 °C/min directly to the crystallization temperature of PCL and under these

conditions the PHB block was not capable ofcrystallize, as was demonstrated by subsequent heating runs after the PCL block crystallization (where the PHB cold crystallized and melted with identical enthalpies). Therefore the block of PCL was crystallized isothermally as the PHB block was kept amorphous. In the second thermal protocol, the PHB_{39}-*b*-PCL_{61} sample was first cooled from the melt as in Figure 5.3 (at 20 ºC/min), then heated until 100 ºC to allow for the PHB cold crystallization at 20 ºC/min. Then, the samples was quenchedat 60 ºC/min to the isothermal crystallization temperature to measure the heat evolved as a function of time in the DSC corresponding to the PCL block in the presence of the PHB block crystals. After the isothermal step was completed, the sample was heated up to 100 ºC (at 20 ºC/min) to melt only the PCL crystals and then quenched again at 60 ºC/min to the nextchosen T_c value.

In Figure 5.11a, the inverse of the half-crystallization rate ($1/\tau_{50\%}$) is reported over T_c. Both in the case of amorphous and semi-crystalline PHB block, the crystallization of the PCL block is always slower than neat PCL, but a nucleating effect of the PHB block crystals on the PCL block can be observed when the PHB block is in the semi-crystalline state. Thus, the PCL block crystallizatin is always faster when the PHB block is semi-crystalline, for the same T_c value. This is likely because of the fact that the PHB crystals act as a nucleating agent for the PCL chains, which, in this way, crystallize more rapidly than when the PHB block is in an amorphous state which could hamper the crystallization process of the PCL chains.

Figure 5.11b shows the degree of crystallinity (x_c) calculated at the completion of the isothermal crystallization process for the PCL block, in the case of amorphous and semi-crystalline PHB block, and for the reference PCL. For neat PCL, the degree of crystallinity is constant with temperature. However, in the case of the PCL block, there is a small increase in the crystallinity degree with T_c. It should be noticed that the

crystallinity degree of the PCL block is between 10 and 15% while neat PCL reaches 45%. In the case where the PHB block is semi-crystalline the degree of crystallinity is even smaller than of the amorphous PHB block. The effect of the PHB block, therefore, decreases the crystallization rate of the PCL but also the amount of crystallinity it can achieve. It should be observed that when the PHB block is allowed to crystallize first, at high temperatures, the spherulites formed are templates for the crystallization of the PCL block. As the PCL block is covalently bonded, when the PHB block chains crystallize, the PCL block chains are segregated to the interlamellar amorphous regions in between crystalline PHB lamellae. Subsequently, when the material is further cooled from its molten state, the PCL can solely crystallize within the limited spaces present between the crystalline PHB lamellae. A similar situation happens in many double crystalline block copolymers, as reviewed elsewhere. So, it is not surprising that the PCL block crystallizes at the slowest rate when it is doing so inside the previously crystallized PHB spherulites, generating double crystalline spherulites. It is more surprising, that quenching the sample to prevent the PHB block chains from crystallizing also causes such an important retardation in the PCL crystallization. This behaviour maybe due to the intermediate segregation strength present in this block copolymer.

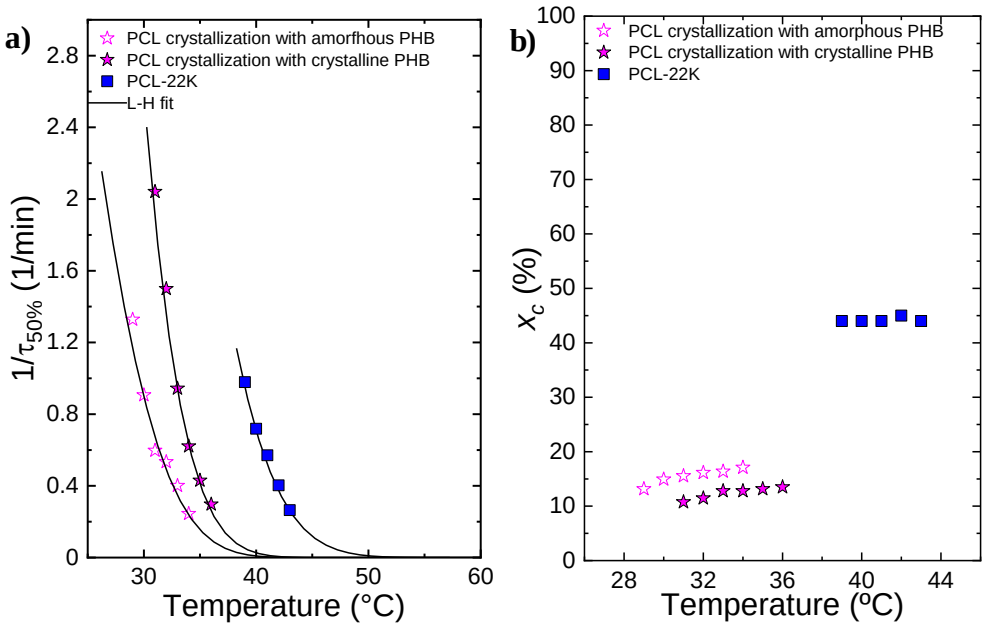

Figure 5.11. Inverse of half-crystallization time ($1/\tau_{50\%}$) (a) and degree of crystallinity (x_c) calculated during isothermal crystallization as a function of T_c for PCL block crystallization from crystalline PHB, full stars, and amorphous PHB, empty stars, in PHB_{39}-*b*-PCL_{61} sample in comparation with PCL 22K.[56] The solid lines in (a) represent the fits to the Lauritzen and Hoffman theory.

The results of fitting the LH theoriy to the crystallization kinetics of the PCL block are presented in Table 5.6.

Table 5.6. Overall isothermal kinetics data parameters described in the Paragraph 3.5 derived from experimental results obtained by DSC.

Sample	$1/\tau_0$(1/s)	K^{τ}_g (K^2)	σ (erg/cm^2)	σ_e (erg/cm^2)	q (erg)	R^2
PHB_{39}-*b*-PCL_{61} (PCL crystallization from amorphous PHB)	1.25×10^{6}	9.57×10^{4}	7.70	112.9	4.17×10^{-13}	0.994

PHB_{39}-*b*-PCL_{61} (PCL crystallization from crystalline PHB)	$1.67x10^{7}$	$1.18x10^{5}$	5.80	137.0	$5.10x10^{-13}$	0.996
PCL-22K[56]	$3.14x10^{8}$	$2.10x10^{5}$	7.07	230.9	$8.60x10^{-13}$	0.996

The overall isothermal crystallization experimental data was also fitted with Avrami's theory using the free app developed by Pérez-Camargo *et al*.[76] In Figure 5.11 and 5.12a the Avrami fits are presented and in Figure 5.11b and 5.12b the typical Avrami plots are shown in the conversion range to make the fit for the PCL block with the crystalline (5.11) and amorphous (5.12) PHB, respectively. The detailed results are shown in Table 5.7 (crystalline PHB) and 5.8 (amorphous PHB). The fit was performed in the primary crystallization regime and the correlation factor is always high (>0.999). The agreement is also high between the experimental and theoretical data of $\tau_{50\%}$. Tables 5.7 and 5.8 also report the Avrami indices: it can be observed that, in the case of crystallization of PCL from amorphous and crystalline PHB, the value of *n* assumes, on average, the value of 3, indicative of the presence of instantaneous spherulites for all T_c.

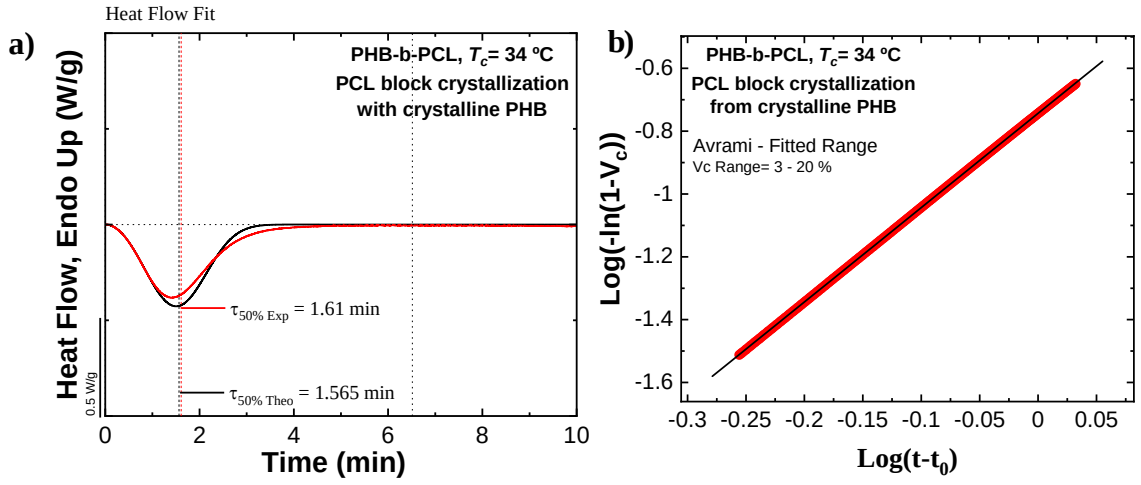

Figure 5.11. The Avrami fit equation using the free Origin plug-in developed by Pérez-Camargo *et al.* [76] for PCL block crystallization in PHB_{39}-*b*-PCL_{61} sample with crystalline PHB at T_c= 34 ºC.

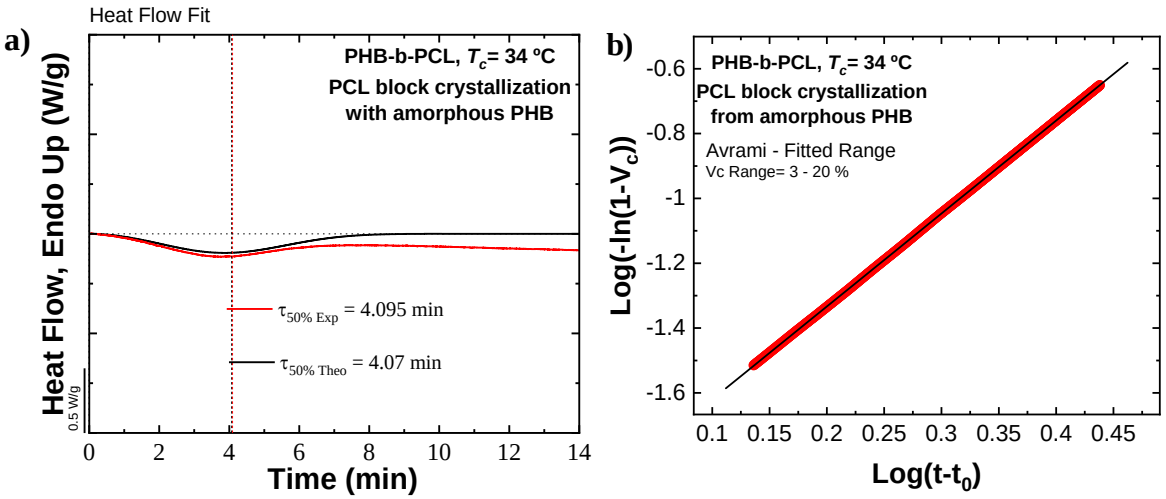

Figure 5.12. The Avrami fit equation using the free Origin plug-in developed by Pérez-Camargo *et al.* [76] for PCL block crystallization in PHB_{39}-*b*-PCL_{61} sample with amorphous PHB at T_c= 34 ºC.

Table 5.7. Avrami fitting parameters obtained from by the free App [76] for PCL crystallization from crystalline PHB in PHB_{39}-*b*-PCL_{61} sample.

T_c(ºC)	t_0(min)	$\tau_{50\% Exp}$ (min)	$\tau_{50\% Theo}$ (min)	*n*	$K^{\frac{1}{n}}(min^{-1})$	$K\ (min^{-n})$	R^2
31	0.387	0.49	0.489	2.44	1.757	3.96	0.999
32	0.448	0.667	0.671	2.49	1.285	1.87	0.999
33	0.482	1.06	1.046	2.67	0.833	$6.15x10^{-1}$	0.999
34	0.495	1.61	1.565	3	0.565	$1.81x10^{-1}$	0.999
35	0.628	2.324	2.251	3.06	0.394	$5.79x10^{-2}$	0.999
36	0.872	3.365	3.309	2.9	0.266	$2.16x10^{-2}$	0.999

Table 5.8 Avrami fitting parameters obtained from by the free App [76] for PCL crystallization from amorphous PHB in PHB_{39}-*b*-PCL_{61} sample.

T_c(°C)	t_0(min)	$\tau_{50\% Exp}$ (min)	$\tau_{50\% Theo}$ (min)	*n*	$K^{\frac{1}{n}}(min^{-1})$	$K\ (min^{-n})$	R^2
29	0.355	0.753	0.779	2.71	1.483	1.36	0.999
30	0.51	1.103	1.112	2.86	0.547	$5.12x10^{-1}$	0.999
31	0.525	1.675	1.651	3.20	0.302	$1.39x10^{-1}$	0.999
32	0.542	1.875	1.969	3.0	0.358	$1.33x10^{-1}$	0.999
33	0.577	2.495	2.277	3.1	0.283	$5.69x10^{-2}$	0.999
34	0.722	4.095	4.07	2.87	0.340	$1.24x10^{-2}$	0.999

5.4 Conclusion

In this chapter it has been studied how the inclusion of PCL units in a random or blocky arrangement influences the morphology, thermal properties, and crystallization kinetics of PHB. The PHB_{39}-*b*-PCL_{61} block copolymer exhibited an intermediate segregation strength in the melt, while the P(HB_{72}-*ran*-CL_{28}) random copolymer showed the expected single-phase melt. Nevertheless, the crystallization of the PHB block was capable to break out the phase-segregated structure of the melt to form well-developed negative spherulites. This is a novel finding, as PHB normally forms positive spherulites; therefore, the covalently bonded PCL block can alter the optical properties of the PHB block spherulites.

Neat PHB exhibits a low nucleation density, resulting in the formation of large spherulites that concentrate stresses and are mostly responsible for its characteristic brittleness, together with its high degree of crystallinity. The block copolymer sample

exhibits a higher nucleation density and smaller spherulites on average. However, the random copolymer displayed an extremely fine micro spherulitic texture that would be highly beneficial for both mechanical properties and transparency. In addition, both block and random copolymer samples examined here presented a much lower spherulitic growth rate and overall crystallization rate. In the case of the block copolymer, the PHB block is capable of developing a degree of crystallinity comparable to that of neat PHB but at much higher crystallization times, while being covalently bonded to a softer PCL block with reduced crystallinity degree. The PHB component of the random copolymer displays a much lower T_m value and crystallinity degree than neat PHB, and the PCL component does not crystallize as it is a minor component randomly distributed along the chains. Therefore, this random copolymer is an attractive biodegradable material with improved processing (due to its lower melting temperature), and potentially much better mechanical and optical properties than neat PHB in view of its lower degree of crystallinity and microspherulitic morphology.

In the special scenario of the PHB_{39}-*b*-PCL_{61} diblock copolymer, both blocks can crystallize, and we demonstrated that if the PHB is crystallized first at higher temperatures, it can nucleate the PCL block. However, if the PHB block is quenched so that it remains amorphous during the crystallization of PCL block, the isothermal crystallization kinetics is faster than when the PHB block is semi-crystalline but still much lower than neat PCL. In both cases, the degree of crystallinity attained during isothermal crystallization by the PCL block is much lower (between 10-20%) than in the case of neat PCL with comparable chain length (which can reach approximately 40% crystallinity during isothermal crystallization).

5.5 References

1. Stark, N.M.; Matuana, L.M. Trends in Sustainable Biobased Packaging Materials: A Mini Review. *Mater. Today Sustain.* **2021**, *15*, 100084.
2. Zinoviadou, K.G.; Kastanas, P.; Gougouli, M.; Biliaderis, C.G. Innovative Bio-Based Materials for Packaging Sustainability. In *Innovation Strategies in the Food Industry*; Elsevier, 2022; pp. 173–192.
3. Manavitehrani, I.; Fathi, A.; Badr, H.; Daly, S.; Negahi Shirazi, A.; Dehghani, F. Biomedical Applications of Biodegradable Polyesters. *Polymers (Basel).* **2016**, *8*, 20.
4. Vert, M.; Li, S.M.; Spenlehauer, G.; Guérin, P. Bioresorbability and Biocompatibility of Aliphatic Polyesters. *J. Mater. Sci. Mater. Med.* **1992**, *3*, 432–446.
5. Albertsson, A.-C.; Varma, I.K. Aliphatic Polyesters: Synthesis, Properties and Applications. *Degrad. aliphatic polyesters* **2002**, 1–40.
6. Li, S.; Vert, M. Biodegradable Polymers: Polyesters 1999.
7. Koller, M.; Mukherjee, A. A New Wave of Industrialization of PHA Biopolyesters. *Bioengineering* **2022**, *9*, 74.
8. Amaro, T.M.M.M.; Rosa, D.; Comi, G.; Iacumin, L. Prospects for the Use of Whey for Polyhydroxyalkanoate (PHA) Production. *Front. Microbiol.* **2019**, *10*, 992.
9. Kourmentza, K.; Kachrimanidou, V.; Psaki, O.; Pateraki, C.; Ladakis, D.; Koutinas, A. Competitive Advantage and Market Introduction of PHA Polymers and Potential Use of PHA Monomers. In *The Handbook of Polyhydroxyalkanoates*; CRC Press, 2020; pp. 167–202 ISBN 1003087663.
10. LEMOIGNE; M. Produits de Deshydration et de Polymerisation de L'acide B=Oxybutyrique. *Bull. Soc. Chim. Biol.* **1926**, *8*, 770–782.
11. Raza, Z.A.; Abid, S.; Banat, I.M. Polyhydroxyalkanoates: Characteristics, Production, Recent Developments and Applications. *Int. Biodeterior. Biodegrad.* 2018, *126*, 45–56.
12. Sharma, V.; Sehgal, R.; Gupta, R. Polyhydroxyalkanoate (PHA): Properties and Modifications. *Polymer (Guildf).* **2021**, *212*, 123161, doi:10.1016/J.POLYMER.2020.123161.
13. Nishida, H.; Tokiwa, Y. Effects of Higher-order Structure of Poly (3-hydroxybutyrate) on Its Biodegradation. I. Effects of Heat Treatment on Microbial

Degradation. *J. Appl. Polym. Sci.* **1992**, *46*, 1467–1476.

14. Tokiwa, Y.; Calabia, B.P. Review Degradation of Microbial Polyesters. *Biotechnol. Lett.* **2004**, *26*, 1181–1189.
15. Brandl, H.; Gross, R.A.; Lenz, R.W.; Fuller, R.C. Plastics from Bacteria and for Bacteria: Poly (β-Hydroxyalkanoates) as Natural, Biocompatible, and Biodegradable Polyesters. *Microb. Bioprod.* **1990**, 77–93.
16. Reddy, C.S.K.; Ghai, R.; Kalia, V. Polyhydroxyalkanoates: An Overview. *Bioresour. Technol.* **2003**, *87*, 137–146, doi:https://doi.org/10.1016/S0960-8524(02)00212-2.
17. Bucci, D.Z.; Tavares, L.B.B.; Sell, I. PHB Packaging for the Storage of Food Products. *Polym. Test.* **2005**, *24*, 564–571.
18. Markl, E.; Grünbichler, H.; Lackner, M. PHB-Bio Based and Biodegradable Replacement for PP: A Review. *Nov. Tech. Nutr. Food Sci* **2018**, *2*, 206–209.
19. Shah, K. Original Research Article Optimization and Production of Polyhydroxybutarate (PHB) by Bacillus Subtilis G1S1from Soil. *Int J Curr Microbiol App Sci* **2014**, *3*, 377–387.
20. Israni, N.; Shivakumar, S. Polyhydroxyalkanoates in Packaging. *Biotechnol. Appl. polyhydroxyalkanoates* **2019**, 363–388.
21. Bugnicourt, E.; Cinelli, P.; Lazzeri, A.; Alvarez, V.A. Polyhydroxyalkanoate (PHA): Review of Synthesis, Characteristics, Processing and Potential Applications in Packaging. **2014**.
22. Arrieta, M.P.; Samper, M.D.; Aldas, M.; López, J. On the Use of PLA-PHB Blends for Sustainable Food Packaging Applications. *Materials (Basel).* **2017**, *10*, 1008.
23. Turco, R.; Santagata, G.; Corrado, I.; Pezzella, C.; Di Serio, M. In Vivo and Post-Synthesis Strategies to Enhance the Properties of PHB-Based Materials: A Review. *Front. Bioeng. Biotechnol.* **2021**, *8*, 619266.
24. Smith, M.K.M.; Paleri, D.M.; Abdelwahab, M.; Mielewski, D.F.; Misra, M.; Mohanty, A.K. Sustainable Composites from Poly (3-Hydroxybutyrate)(PHB) Bioplastic and Agave Natural Fibre. *Green Chem.* **2020**, *22*, 3906–3916.
25. Ariffin, H.; Nishida, H.; Shirai, Y.; Hassan, M.A. Determination of Multiple Thermal Degradation Mechanisms of Poly (3-Hydroxybutyrate). *Polym. Degrad. Stab.* **2008**, *93*, 1433–1439.
26. Pachekoski, W.M.; Dalmolin, C.; Agnelli, J.A.M. The Influence of the Industrial

Processing on the Degradation of Poly (Hidroxybutyrate)-PHB. *Mater. Res.* **2013**, *16*, 237–332.

27. Tang, X.; Chen, E.Y.X. Chemical Synthesis of Perfectly Isotactic and High Melting Bacterial Poly(3-Hydroxybutyrate) from Bio-Sourced Racemic Cyclic Diolide. *Nat. Commun. 2018 91* **2018**, *9*, 1–11, doi:10.1038/s41467-018-04734-3.
28. Tang, X.; Westlie, A.H.; Watson, E.M.; Chen, E.Y.X. Stereosequenced Crystalline Polyhydroxyalkanoates from Diastereomeric Monomer Mixtures. *Science (80-.).* **2019**, *366*, 754–758, doi:10.1126/science.aax8466.
29. Caputo, M.R.; Tang, X.; Westlie, A.H.; Sardon, H.; Chen, E.Y.-X.; Müller, A.J. Effect of Chain Stereoconfiguration on Poly (3-Hydroxybutyrate) Crystallization Kinetics. *Biomacromolecules* **2022**, *23*, 3847–3859, doi:https://doi.org/10.1021/acs.biomac.2c00682.
30. Quinn, E.C.; Westlie, A.H.; Sangroniz, A.; Caputo, M.R.; Xu, S.; Zhang, Z.; Urgun-Demirtas, M.; Müller, A.J.; Chen, E.Y.-X. Installing Controlled Stereo-Defects Yields Semicrystalline and Biodegradable Poly (3-Hydroxybutyrate) with High Toughness and Optical Clarity. *J. Am. Chem. Soc.* **2023**.
31. Sudesh, K.; Abe, H.; Doi, Y. Synthesis, Structure and Properties of Polyhydroxyalkanoates: Biological Polyesters. *Prog. Polym. Sci.* 2000, *25*, 1503–1555.
32. Abdelwahab, M.A.; Flynn, A.; Chiou, B.-S.; Imam, S.; Orts, W.; Chiellini, E. Thermal, Mechanical and Morphological Characterization of Plasticized PLA–PHB Blends. *Polym. Degrad. Stab.* **2012**, *97*, 1822–1828.
33. Kervran, M.; Vagner, C.; Cochez, M.; Poncot, M.; Saeb, M.R.; Vahabi, H. A Review on Thermal Degradation of Polylactic Acid (PLA)/Polyhydroxybutyrate (PHB) Blends. *Polym. Degrad. Stab.* **2022**, 109995.
34. Przybysz, M.; Marć, M.; Klein, M.; Saeb, M.R.; Formela, K. Structural, Mechanical and Thermal Behavior Assessments of PCL/PHB Blends Reactively Compatibilized with Organic Peroxides. *Polym. Test.* **2018**, *67*, 513–521.
35. Lovera, D.; Márquez, L.; Balsamo, V.; Taddei, A.; Castelli, C.; Müller, A.J. Crystallization, Morphology, and Enzymatic Degradation of Polyhydroxybutyrate/Polycaprolactone (PHB/PCL) Blends. *Macromol. Chem. Phys.* **2007**, *208*, 924–937, doi:10.1002/macp.200700011.
36. Garcia-Garcia, D.; Ferri, J.M.; Boronat, T.; López-Martínez, J.; Balart, R.

Processing and Characterization of Binary Poly (Hydroxybutyrate)(PHB) and Poly (Caprolactone)(PCL) Blends with Improved Impact Properties. *Polym. Bull.* **2016**, *73*, 3333–3350.

37. Tang, X.; Shi, C.; Zhang, Z.; Chen, E.Y.X. Toughening Biodegradable Isotactic Poly(3-Hydroxybutyrate) via Stereoselective Copolymerization of a Diolide and Lactones. *Macromolecules* **2021**, *54*, 9401–9409, doi:10.1021/acs.macromol.1c01199.
38. Chynoweth, K.R.; Stachurski, Z.H. Crystallization of Poly (ε-Caprolactone). *Polymer (Guildf).* **1986**, *27*, 1912–1916.
39. Jenkins, M.J.; Harrison, K.L. The Effect of Molecular Weight on the Crystallization Kinetics of Polycaprolactone. *Polym. Adv. Technol.* **2006**, *17*, 474–478.
40. Nofar, M.; Sacligil, D.; Carreau, P.J.; Kamal, M.R.; Heuzey, M.-C. Poly (Lactic Acid) Blends: Processing, Properties and Applications. *Int. J. Biol. Macromol.* **2019**, *125*, 307–360.
41. Kfoury, G.; Raquez, J.-M.; Hassouna, F.; Odent, J.; Toniazzo, V.; Ruch, D.; Dubois, P. Recent Advances in High Performance Poly (Lactide): From "Green" Plasticization to Super-Tough Materials via (Reactive) Compounding. *Front. Chem.* **2013**, *1*, 32.
42. Sun, H.; Mei, L.; Song, C.; Cui, X.; Wang, P. The in Vivo Degradation, Absorption and Excretion of PCL-Based Implant. *Biomaterials* **2006**, *27*, 1735–1740.
43. Malikmammadov, E.; Tanir, T.E.; Kiziltay, A.; Hasirci, V.; Hasirci, N. PCL and PCL-Based Materials in Biomedical Applications. *J. Biomater. Sci. Polym. Ed.* **2018**, *29*, 863–893.
44. Nishida, H.; Tokiwa, Y. Distribution of Poly (β-Hydroxybutyrate) and Poly (ε-Caprolactone) Aerobic Degrading Microorganisms in Different Environments. *J. Environ. Polym. Degrad.* **1993**, *1*, 227–233.
45. Gonçalves, S.P.C.; Martins-Franchetti, S.M. Action of Soil Microorganisms on PCL and PHBV Blend and Films. *J. Polym. Environ.* **2010**, *18*, 714–719.
46. Yeo, J.C.C.; Muiruri, J.K.; Thitsartarn, W.; Li, Z.; He, C. Recent Advances in the Development of Biodegradable PHB-Based Toughening Materials: Approaches, Advantages and Applications. *Mater. Sci. Eng. C* **2018**, *92*, 1092–1116.
47. Nair, L.S.; Laurencin, C.T. Biodegradable Polymers as Biomaterials. *Prog. Polym.*

Sci. **2007**, *32*, 762–798.

48. Hiemenz, P.C.; Lodge, T.P. *Polymer Chemistry*; CRC press, 2007; ISBN 1420018272.
49. Terada, M.; Marchessault, R.H. Determination of Solubility Parameters for Poly (3-Hydroxyalkanoates). *Int. J. Biol. Macromol.* **1999**, *25*, 207–215.
50. Lisuardi, A.; Schoenberg, A.; Gada, M.; Gross, R.A.; McCarthy, S. Biodegradation of Blends of Poly (b-Hydroxybutyrate) and Poly (e-Caprolactone). *Polym Mater Sci Eng* **1992**, *67*, 298–300.
51. Kumagai, Y.; Doi, Y. Enzymatic Degradation and Morphologies of Binary Blends of Microbial Poly (3-Hydroxy Butyrate) with Poly (ε-Caprolactone), Poly (1, 4-Butylene Adipate and Poly (Vinyl Acetate). *Polym. Degrad. Stab.* **1992**, *36*, 241–248.
52. Saito, M.; Inoue, Y.; Yoshie, N. Cocrystallization and Phase Segregation of Blends of Poly (3-Hydroxybutyrate) and Poly (3-Hydroxybutyrate-Co-3-Hydroxyvalerate). *Polymer (Guildf).* **2001**, *42*, 5573–5580.
53. Yoshie, N.; Fujiwara, M.; Ohmori, M.; Inoue, Y. Temperature Dependence of Cocrystallization and Phase Segregation in Blends of Poly (3-Hydroxybutyrate) and Poly (3-Hydroxybutyrate-Co-3-Hydroxyvalerate). *Polymer (Guildf).* **2001**, *42*, 8557–8563.
54. Yoshie, N.; Asaka, A.; Inoue, Y. Cocrystallization and Phase Segregation in Crystalline/Crystalline Polymer Blends of Bacterial Copolyesters. *Macromolecules* **2004**, *37*, 3770–3779.
55. Yoshie, N.; Inoue, Y. Cocrystallization and Phase Segregation in Blends of Two Bacterial Polyesters. In Proceedings of the Macromolecular Symposia; Wiley Online Library, 2005; Vol. 224, pp. 59–70.
56. Fernández-Tena, A.; Pérez-Camargo, R.A.; Coulembier, O.; Sangroniz, L.; Aranburu, N.; Guerrica-Echevarria, G.; Liu, G.; Wang, D.; Cavallo, D.; Müller, A.J. Effect of Molecular Weight on the Crystallization and Melt Memory of Poly (ε-Caprolactone)(PCL). *Macromolecules* **2023**.
57. Wunderlich, B. Macromolecular Physics. Vol. 1, Crystal Structure, Morphology, Defects (1973).
58. Barham, P.J.; Keller, A.; Otun, E.L.; Holmes, P.A. Crystallization and Morphology of a Bacterial Thermoplastic: Poly-3-Hydroxybutyrate. *J. Mater. Sci. 1984 199*

1984, *19*, 2781–2794, doi:10.1007/BF01026954.

59. Crist, B.; Schultz, J.M. Polymer Spherulites: A Critical Review. *Prog. Polym. Sci.* 2016, *56*, 1–63.
60. Lugito, G.; Yang, C.-Y.; Woo, E.M. Phase-Separation Induced Lamellar Re-Assembly and Spherulite Optical Birefringence Reversion. *Macromolecules* **2014**, *47*, 5624–5632.
61. Woo, E.M.; Tsai, W.-T.; Lugito, G. Interior Dissection on Domain-Dependent Birefringence Types of Poly (3-Hydroxybutyrate) Spherulites in Blends. *Macromolecules* **2017**, *50*, 283–295.
62. Müller, A.J.; Michell, R.M.; Lorenzo, A.T. Isothermal Crystallization Kinetics of Polymers. *Polym. Morphol. Princ. Charact. Process.* **2016**, *714*, 181–203.
63. Michell, R.M.; Mueller, A.J. Confined Crystallization of Polymeric Materials. *Prog. Polym. Sci.* **2016**, *54*, 183–213, doi:https://doi.org/10.1016/j.progpolymsci.2015.10.007.
64. Castillo, R.V.; Muller, A.J.; Raquez, J.-M.; Dubois, P. Crystallization Kinetics and Morphology of Biodegradable Double Crystalline PLLA-b-PCL Diblock Copolymers. *Macromolecules* **2010**, *43*, 4149–4160.
65. Hoffman, J.D.; Lauritzen, J.I.; Jr. Crystallization of Bulk Polymers With Chain Folding: Theory of Growth of Lamellar Spherulites. *J. Res. Natl. Bur. Stand. Sect. A, Phys. Chem.* **1961**, *65A*, 297, doi:10.6028/JRES.065A.035.
66. Pitt, C.G.; Chasalow, F.I.; Hibionada, Y.M.; Klimas, D.M.; Schindler, A. Aliphatic Polyesters. I. The Degradation of Poly (E-caprolactone) in Vivo. *J. Appl. Polym. Sci.* **1981**, *26*, 3779–3787, doi:https://doi.org/10.1002/app.1981.070261124.
67. Mark, J.E. *Physical Properties of Polymers Handbook*; Springer, 2007; Vol. 1076;.
68. Reiter, G.; Strobl, G.R. *Progress in Understanding of Polymer Crystallization*; Springer, 2007; Vol. 714; ISBN 3540473076.
69. Avrami, M. Granulation, Phase Change, and Microstructure Kinetics of Phase Change. III. *J. Chem. Phys.* **1941**, *9*, 177–184.
70. Avrami, M. Kinetics of Phase Change. II Transformation-time Relations for Random Distribution of Nuclei. *J. Chem. Phys.* **1940**, *8*, 212–224, doi:https://doi.org/10.1063/1.1750631.
71. Safari, M.; Mugica, A.; Zubitur, M.; Martínez de Ilarduya, A.; Muñoz-Guerra, S.; Müller, A.J. Controlling the Isothermal Crystallization of Isodimorphic PBS-Ran-

PCL Random Copolymers by Varying Composition and Supercooling. *Polymers (Basel)*. **2019**, *12*, 17.

72. Arandia, I.; Zaldua, N.; Maiz, J.; Pérez-Camargo, R.A.; Mugica, A.; Zubitur, M.; Mincheva, R.; Dubois, P.; Müller, A.J. Tailoring the Isothermal Crystallization Kinetics of Isodimorphic Poly (Butylene Succinate-Ran-Butylene Azelate) Random Copolymers by Changing Composition. *Polymer (Guildf)*. **2019**, *183*, 121863.
73. Pérez-Camargo, R.A.; Arandia, I.; Safari, M.; Cavallo, D.; Lotti, N.; Soccio, M.; Müller, A.J. Crystallization of Isodimorphic Aliphatic Random Copolyesters: Pseudo-Eutectic Behavior and Double-Crystalline Materials. *Eur. Polym. J.* **2018**, *101*, 233–247.
74. Svoboda, P.; Trivedi, K.; Svobodova, D.; Mokrejs, P.; Vasek, V.; Mori, K.; Ougizawa, T.; Inoue, T. Isothermal Crystallization in Polypropylene/Ethylene–Octene Copolymer Blends. *Mater. Chem. Phys.* **2011**, *131*, 84–93.
75. Soccio, M.; Lotti, N.; Finelli, L.; Munari, A. Effect of Transesterification Reactions on the Crystallization Behaviour and Morphology of Poly (Butylene/Diethylene Succinate) Block Copolymers. *Eur. Polym. J.* **2009**, *45*, 171–181.
76. Pérez-Camargo, R.A.; Liu, G.; Wang, D.; Müller, A.J. Experimental and Data Fitting Guidelines for the Determination of Polymer Crystallization Kinetics. *Chinese J. Polym. Sci* **2022**, *40*, 1–34, doi:https://doi.org/10.1007/s10118-022-2724-2.

Chapter VI

6. Experimental Part Synthesis, morphology and crystallization kinetics of Polyheptalactone (PHL)

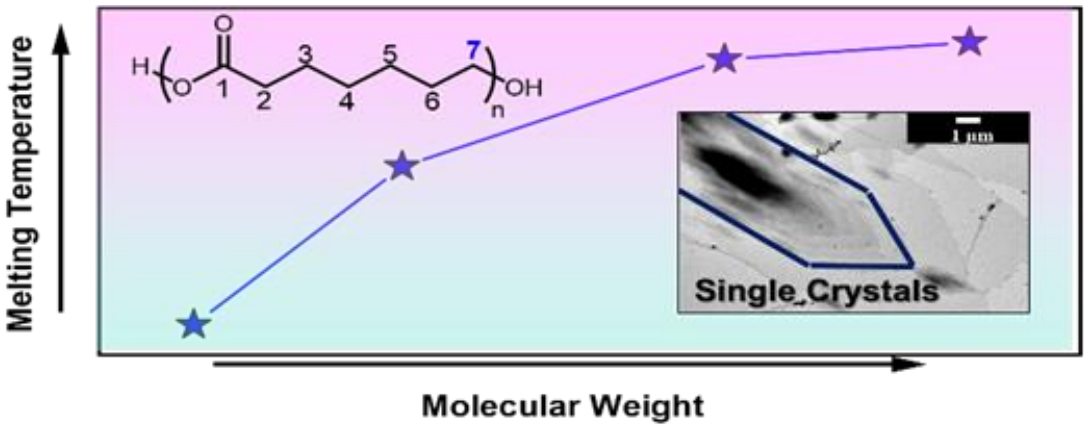

6.1 Abstract

Aliphatic polyesters are widely studied due to their excellent properties, low-cost production, and also because, in many cases, they are biodegradable and/or recyclable. Therefore, expanding the range of available aliphatic polyesters is highly desirable. This paper reports the synthesis, morphology, and crystallization kinetics of a scarcely studied polyester, polyheptalactone (PHL). First, we synthesized the η-heptalactone monomer by the Baeyer-Villiger oxidation of cycloheptanone before several polyheptalactones of different molecular weights (in the range between 2 and 12 kDa), and low dispersities were prepared by Ring-Opening Polymerization (ROP). The influence of molecular weight on primary nucleation rate, spherulitic growth rate, and overall crystallization rate was studied for the first time. All these rates increased with PHL molecular weight, and they approached a plateau for the highest molecular weight samples employed here. Single crystals of PHLs were prepared for the first time, and hexagonal-shaped flat single crystals were obtained. The study of the crystallization and morphology of PHL revealed strong similarities with PCL, making PHLs very promising materials, considering their potential biodegradable character.

Caputo, M. R., Olmos, A., Li, B., Olmedo-Martínez, J. L., Malafronte, A., De Rosa, C., Haritz Sardon, Rachel K. O'Reilly, Andrew P. Dove, Müller, A. J. (2023). Synthesis, Morphology, and Crystallization Kinetics of Polyheptalactone (PHL). *Biomacromolecules*.

6.2 Introduction

Plastic materials are widely used for their versatility, low production cost, and easy manufacturing. Furthermore, plastic materials possess a wide range of properties, so it is possible to find them in almost all production sectors, such as packaging, clothing, medicine, or electronics[1–3]. On the other hand, the massive production and use of plastics have led to one of the main problems of the last decades: plastic waste and its disposal[4-7]. Another negative aspect is that these plastic materials are petroleum derivatives, which increases the emission of CO_2 into the atmosphere and affects climate change [8]. To overcome this problem, recycling these plastic materials to obtain value-added products has been used to manage issues associated with their disposal [9–14]. Additionally, producing and using materials with lower environmental impact is an alternative[15-18]

Polyesters are conventionally processed in various forms, such as fibers, filaments, resins, etc., and have broad applications across packaging, textiles, automotive, medical, electronic, and construction fields. Some polyesters can be recycled through physical (mechanical) and chemical (hydrolysis, methanolysis, and glycolysis reaction) methods, and their recycled parts can also be used in the packaging and construction fields. The ability for efficient and effective recycling of polyesters could lead to the reduction of CO_2 emissions and, consequently, of global warming [17,18]

A versatile aliphatic polyester that is also biodegradable is polycaprolactone (PCL), which is usually obtained by ring-opening polymerization (ROP) of ε-caprolactone or by polycondensation of hydroxycaproic acid[19]. PCL is a biocompatible and biodegradable polymer; it is miscible with several other polymers[20],[21],[22], and the costs associated with its production are very low. These advantageous properties make

PCL one of the most used polyesters and suitable for different fields of application, such as tissue engineering, drug delivery systems, or as an additive for polyurethanes. [23–26]

Similar alternative polymeric materials are being investigated, considering the advantages of aliphatic polyesters. Poly(η-heptalactone), a polyester derived from η-heptalactone (lactone that contains one more carbon atom than ε-caprolactone), has been largely understudied thus far, as it is not commercially available. Given the similarity in structure to ε-caprolactone (PCL), PHL could be expected to exhibit comparable properties in processability, melting, and crystallization temperatures. Another potentially interesting aspect could be the presence of one more carbon atom than polycaprolactone, which could affect the crystallization. For example, in a recently published study[26], it was reported that PEB (poly-(ethylene brassylate)), a short-long aliphatic polyester (with 13 methylene groups in its repeat unit), exhibits a peculiar crystallization behavior due to a similar self-poisoning effect to that observed previously in long-chain alkanes[26–29]. The self-poisoning effect consists on the display of a crystallization rate minima upon decreasing the isothermal crystallization temperature. In the case of long-chain alkanes, extended-chain lamellae form first at high crystallization temperature, then segments with the folded chain conformation attach, upon decreasing T_c values, to the growth front, preventing further growth until they detach, and growth can again proceed in the extended form[26–29]. The higher ratio of methylene groups versus ester groups in PEB along the aliphatic chain leads to properties that come closer to that of polyethylene (PE), as the polar group is "diluted" along the non-polar rest of the chain. In this sense, PEB is closer to PE, while PHL is closer to PCL.

Only a few reports have shown the ability to synthesize PHL, all have resulted in polymers with large dispersity values (2.8) [30]. The synthesis and characterization of low polydispersity poly(η-heptalactone) (PHL) with predictable molecular weights and a

study of the crystallization of these interesting materials have not been reported previously in the literature. Therefore, in this work, we report the synthesis, thermal, and structural characterization of polyheptalactone (PHL). The effect of the PHL molecular weight on its thermal properties, nucleation, and crystallization kinetics is studied for the first time. Additionally, we report, also for the first time, the preparation of single crystals of this scarcely studied semicrystalline polymer. Studying crystallization, morphology, and crystallization kinetics is very important as these aspects influence properties such as thermal properties, mechanical behavior, and biodegradation potential.

6.3 Results and Discussion

As η-heptalactone (HL) is not commercially available, it was first synthesized and characterized. The first aim was to obtain poly(η-heptalactone) (PHL) with predictable molecular weight and low dispersity. Therefore ROP kinetics of the HL polymerization was studied as catalyzed by an organocatalyst, namely diphenyl phosphate. A range of different DPs of PHL homopolymers were targeted for further investigation of crystallization kinetics.

6.3.2 Synthesis of poly(η-heptalactone)

η-Heptalactone was synthesized by Baeyer-Villiger oxidation following a literature procedure. The pure product was confirmed with ^{1}H NMR spectroscopy and was consistent with previous literature data (Figure 6.1) [31]. After the successful preparation of the monomer, the homopolymerization of η-heptalactone was carried out. Diphenyl phosphate (DPP) was selected as the catalyst as a result of the superior ability of this catalyst to provide polylactones with narrow dispersities and end group

fidelity[32]. The polymerization was initiated by a dual-head initiator and chain transfer agent to be consistent with our previously reported PCL work[33] (Figure 6.2).

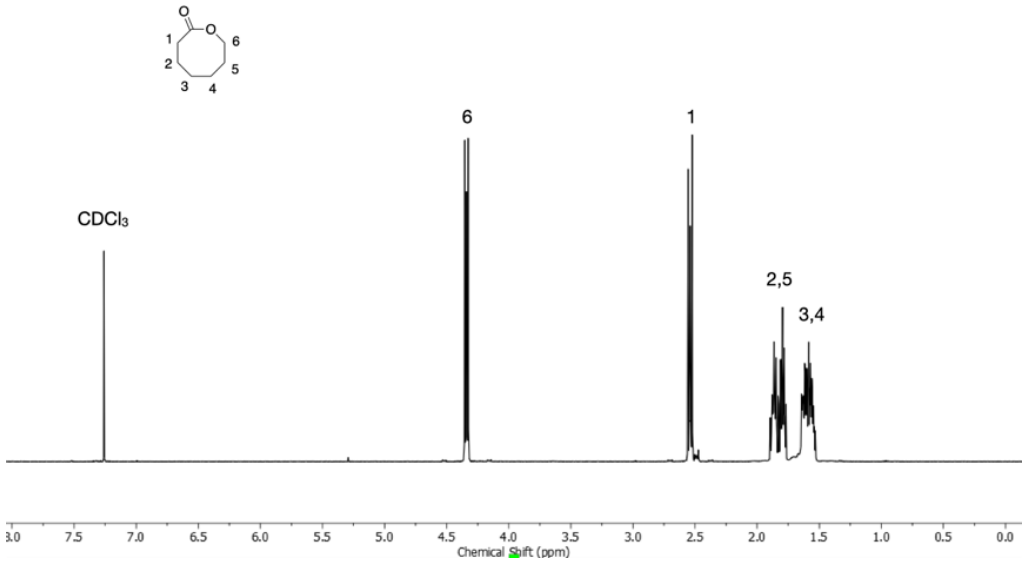

Figure 6.1. ^{1}H NMR spectroscopy in $CDCl_3$ of η-heptalactone monomer.

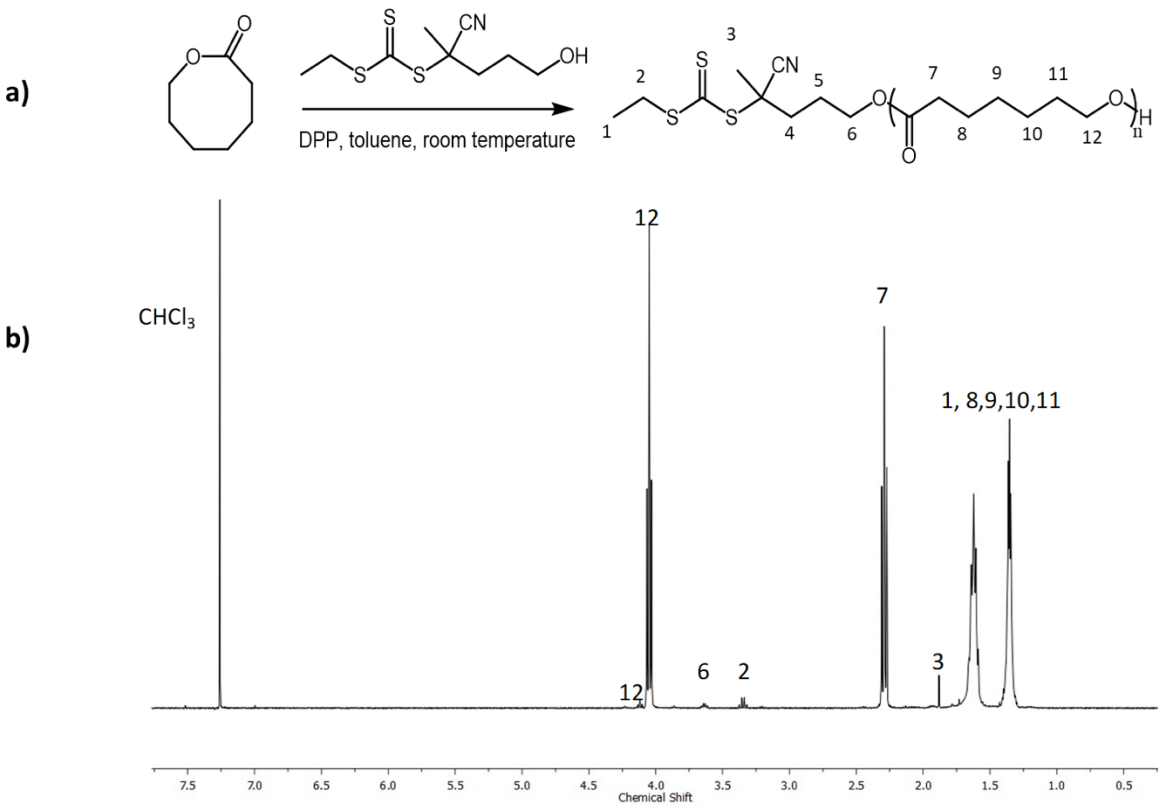

Figure 6.2. (a) Synthesis of the PHL polymers by ROP of η-heptalactone catalyzed by DPP and (b) ^{1}H NMR spectrum of PHL 35 ($CDCl_3$, 400MHz).

The ROP of η-heptalactone was attempted at a monomer concentration of 4 M in toluene as solvent at room temperature in an N_2-filled glovebox, with dual-head RAFT initiator (DP_{tot}= 100) and 1 mol % DPP catalyst. ^{1}H NMR spectroscopic analysis was employed to monitor the reactions and characterize the resulting polymers (Figure 6.2b). The disappearance of the characteristic signals of the methylene protons of the HL monomer at δ = 4.28 ppm and the concomitant appearance of these methylene protons in the polymer chain at δ = 4.05 ppm permit to calculate the conversion. The polymerization reached 70% conversation after 4 h while still exhibiting first-order kinetics (Figure 6.3). Using these conditions, different DPs of PHL were targeted for further crystallization study. Different conversion degrees were obtained depending on the reaction time, and

therefore four different samples of PHL with different molecular masses were synthesized (Table 6.1).

Table 6.1. Polymerization time, degree of conversion, average molecular masses, and polydispersity of the synthesized samples of PHL.

Time (h)	Sample	Conversion (%)	M_n[a](GPC) (kDa)	M_w[a](GPC) (kDa)	$Đ_M$	M_n [^{1}H (NMR)][b] (kDa)
1	PHL 15	15	6.2	7.0	1.11	2.2
2	PHL 35	35	9.9	11.4	1.11	4.7
4	PHL 66	70	16.6	19.6	1.15	9.2
5	PHL 90	90	20.8	22.7	1.17	11.8

[a]) measured by SEC, [b]) measured by ^{1}H NMR spectroscopy.

The average molecular weight was measured by ^{1}H NMR spectroscopy, and SEC The polymer molecular weights were determined by end-group analysis by ^{1}H NMR spectroscopy, comparing the ratio between the polymer $CH_2OC{=}O$ resonances of (δ = 4.05) and the chain transfer reagent $SCH_2CCN(CH_3)$ resonance (δ =3.69). Size exclusion chromatography (SEC) analysis is reported in SI and revealed low dispersity ($Đ_M$ < 1.2) and good overlap of the refractive index (RI) and ultraviolet (UV) (λ = 309 nm, corresponding to the π-π^* electronic transition of the thiocarbonyl moiety) peak in the SEC traces, which signifies the retention of the RAFT end group (Figure 6.4).

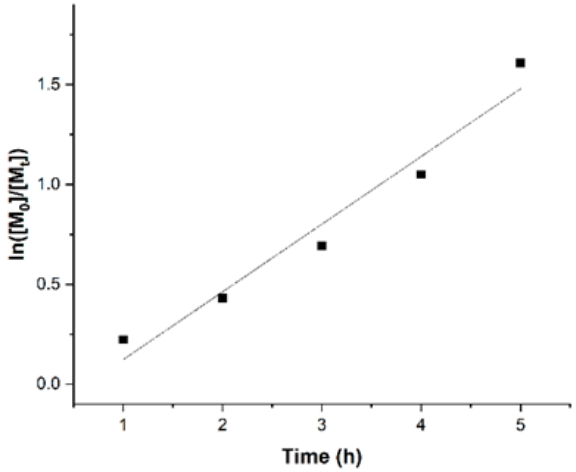

Figure 6.3. Kinetic plot for the polymerization of η-heptalactone using DPP as a catalyst at room temperature in toluene with $[HL]_0$:$[CTA]_0$:$[cat.]_0$ = 100:1:1 and initial monomer concentration = 4 M.

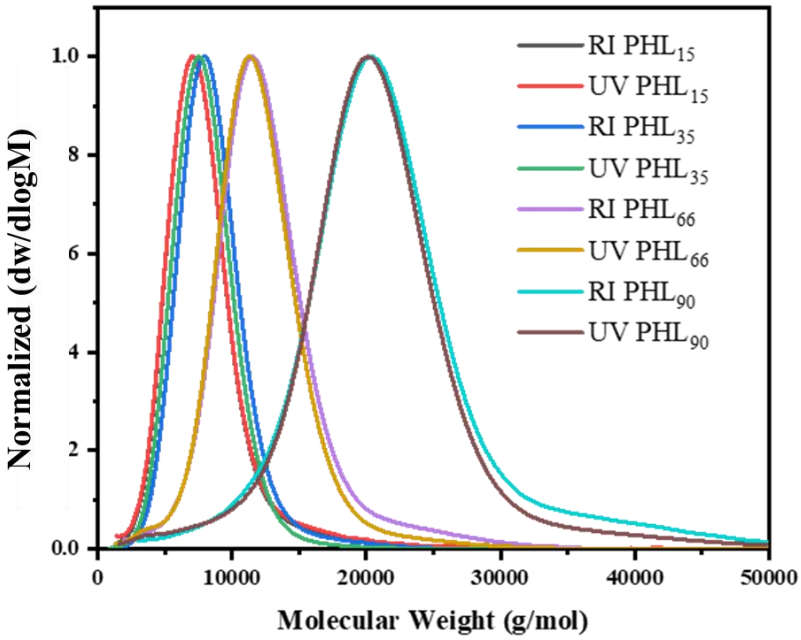

Figure 6.4. Overlaid RI and UV (λ = 309 nm) SEC chromatograms of PHL using $CHCl_3$ with 0.1% TFE as an eluent with polystyrene (PS) standards.

6.3.3 X-ray powder diffraction

The X-ray powder diffraction profiles of the as-prepared and melt-crystallized samples of PHL of higher molecular mass (samples PHL 66 and PHL 90), acquired in the 2θ region comprised between 5° and 40°, are shown in Figure 6.5a and Figure 6.5b, respectively.

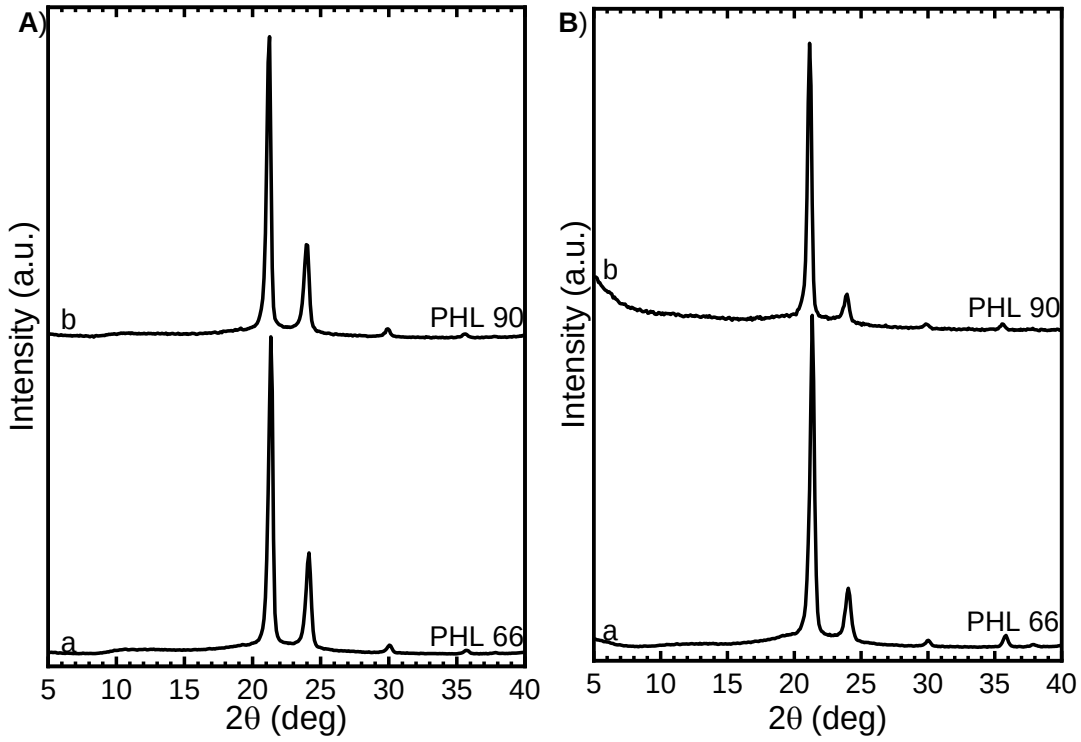

Figure 6.5. X-ray powder diffraction profiles of the as-prepared (A) and melt-crystallized (B) specimens of samples PHL 66 (a) and PHL 90 (b).

The diffraction profiles of both as-prepared and melt-crystallized samples (Figure 6.5a and Figure 6.5b) are characterized by two strong and sharp reflections at 2θ ≈ 21° and 24° and other minor diffraction peaks of lower intensity in the 2θ region comprised between 25° and 40°. Similar diffraction profiles have been obtained for the different samples in Table 1. The X-ray diffraction profiles of PHL (Figure 6.5) appear similar to that of polyethylene (PE)[34] and other linear aliphatic polyesters, —(—O—$(CH_2)_m$—CO—)$_n$—, such as poly(11-undecalactone) (PUDL, m = 10) [35].,

poly(δ-valerolactone) (PVL, *m* = 4)[36], poly(β-propiolactone) (PPL, *m* = 2) [37], poly(16-hexadecalactone) (PHDL, *m* = 15)[38],poly(12-dodecalactone) (PDDL, *m* = 11) [39], poly(15-pentadecalactone) (PPDL, *m* = 14) [40], and poly(*ε*-caprolactone) (PCL, *m* = 5) [41],[42].

6.3.4 TGA Results

Figure 6.6 shows the weight loss profiles of the four PHL samples revealed by TGA. In the case of the two samples with the lowest molecular weight (PHL 15 and PHL 35), the TGA curves are characterized by a two-step weight loss at about 210 ºC and 380 ºC. This phenomenon disappears in the two samples with the highest molecular weight (PHL 66 and PHL 90), with only one weight loss step at about 400 ºC. This particular behavior has already been observed previously in the case of PCL samples with different molecular weights,[43] in which the reason for the first step of weight loss for low molecular weight samples was initially attributed to the development of ε-caprolactone in the thermal decomposition process and FT-IR spectroscopic analyses subsequently confirmed this. Since PCL is chemically similar to PHL, it is possible that the behavior detected by the TGA could be attributed to the same cause, i.e., the production of η-heptalactone during the thermal degradation process.

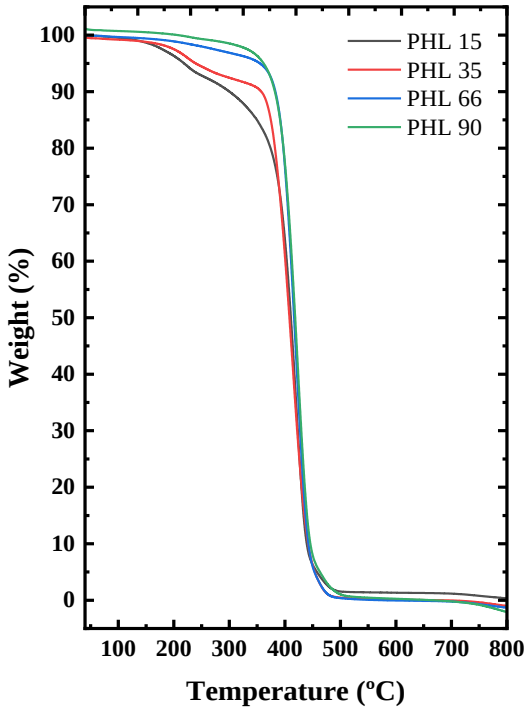

Figure 6.6. Weight loss (%) as a function of the temperature (°C) for PHL samples.

6.3.5 Non-isothermal DSC

Figure 6.7 shows DSC results obtained during cooling from the melt and subsequent heating scans of the different molecular weight PHL samples. It is observed that the crystallization temperature increases as a function of molecular weight, from 36 ºC for the lowest molecular weight to 42.5 ºC for the highest molecular weight. The melting temperature has a similar behavior, increasing as a function of molecular weight from 55 ºC to 61.5 ºC. Figure 6.8a shows the change in T_m as a function of molecular weight. As expected, the melting temperature increases with molecular weight but does not reach saturation in the range of molecular weights explored here. The same trend is observed for $T_{c,}$ as reported in Figure 6.8b.

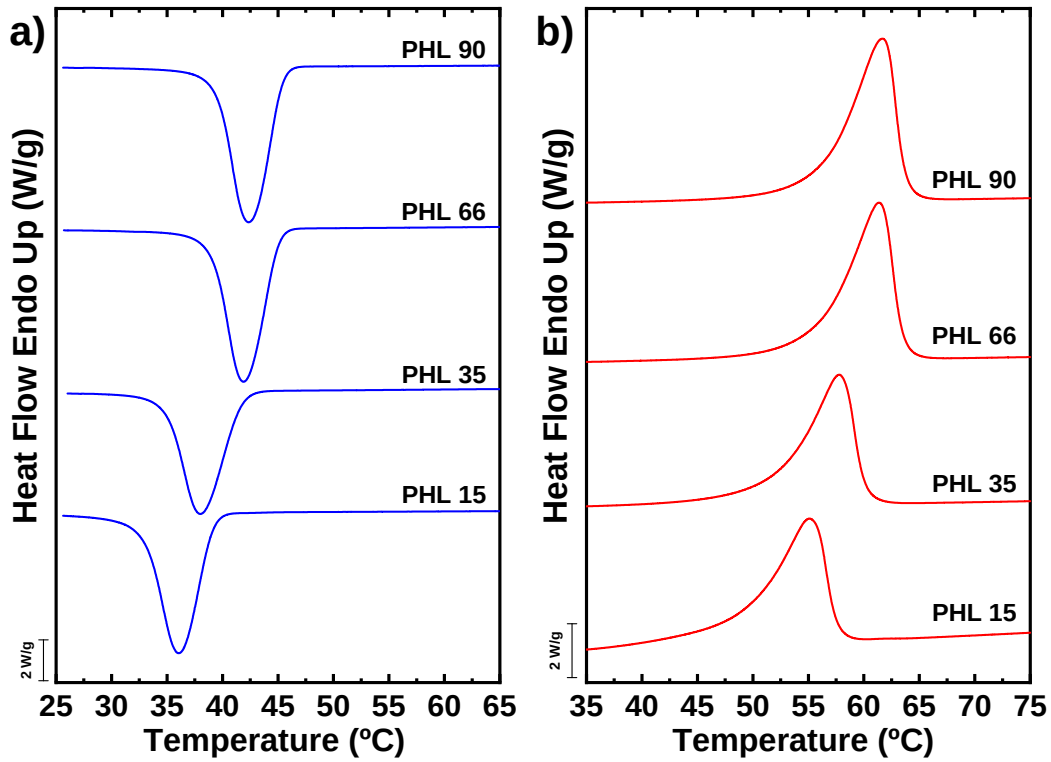

Figure 6.7. a) DSC thermograms (cooling scans) at 20 ºC/min and b) subsequent DSC thermograms (heating scans) at 20 ºC/min for PHL samples.

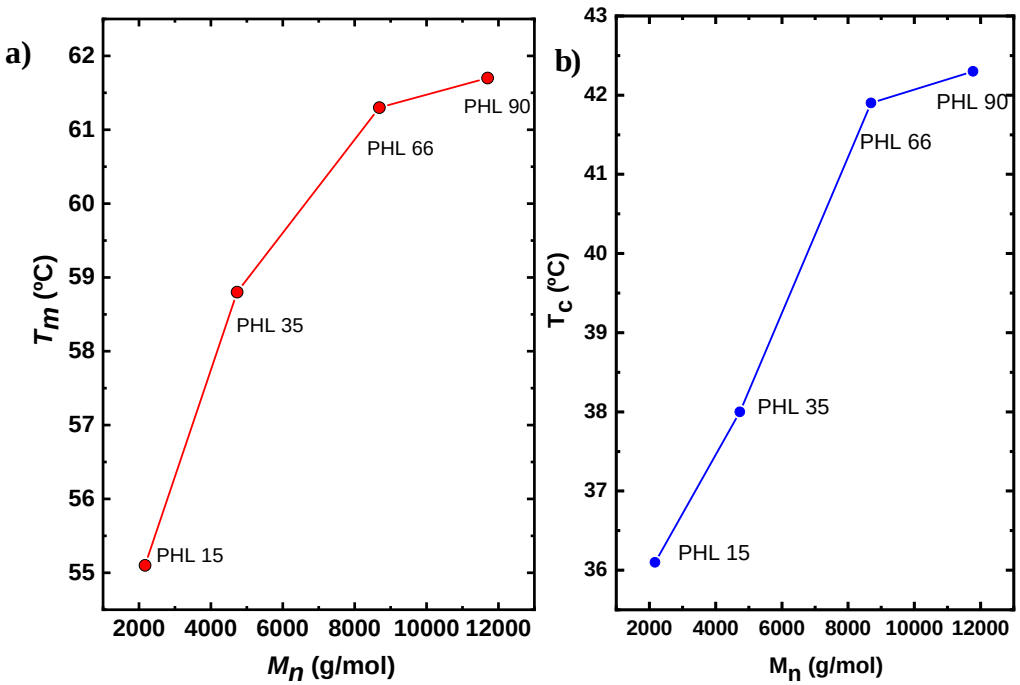

Figure 6.8. Melting (a) and crystallization (b) temperatures as a function of molecular weight of PHL samples; the solid red line in the bottom plot is a line to guide the eye.

The values of the melting and crystallization temperatures with the relative enthalpies are shown in Table 6.2. The same table also shows the glass transition temperature (T_g), and degree of crystallinity (x_c) values obtained in the second heating scan. Figure 6.9 reports an enlargement of the second heating scans to appreciate the glass transition better.

Table 6.2. Thermal parameters obtained from non-isothermal crystallization

	T_g (°C)	T_c (°C)	T_m (°C)	ΔH_c (J/g)	ΔH_m (J/g)	X_c (%)
PHL 15	-39.3	36.1	55.1	86	84	43
PHL 35	-42.5	38.0	58.8	77	79	41
PHL 66	-41.1	41.9	61.3	91	90	46
PHL 90	-39.7	42.3	61.7	91	93	48

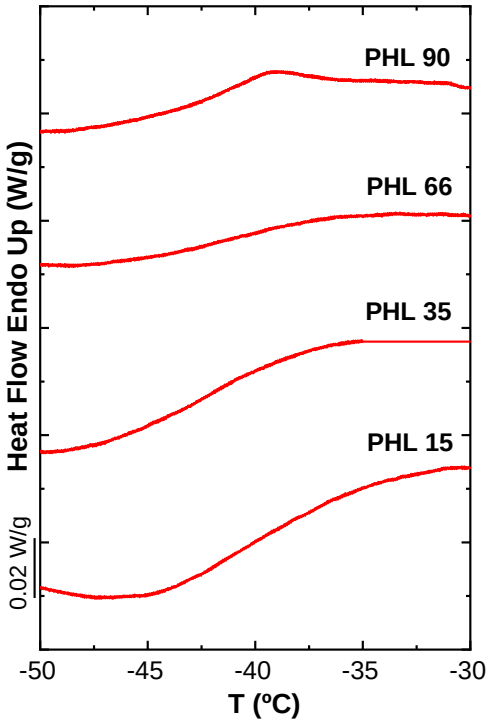

Figure 6.9. Glass transition for the four PHL samples.

6.3.6 Morphology and Spherulitic Growth

The samples were analyzed by PLOM to study their superstructural morphology. Figure 6.10 shows the PLOM micrographs using the same magnification scale bar (500 µm) collected at 25 ºC after non-isothermal crystallization from the melt at 20 ºC/min. The micrographs of the samples with the lowest and highest molecular weight (PHL 15 and PHL 90) are reported since the morphology does not show significant differences for the other samples. Samples crystallize, forming microspherulites, regardless of their molecular weight. The results imply that the samples possess a very high nucleation density, probably coming from catalytic debris, which can act as very active nucleating heterogeneities.

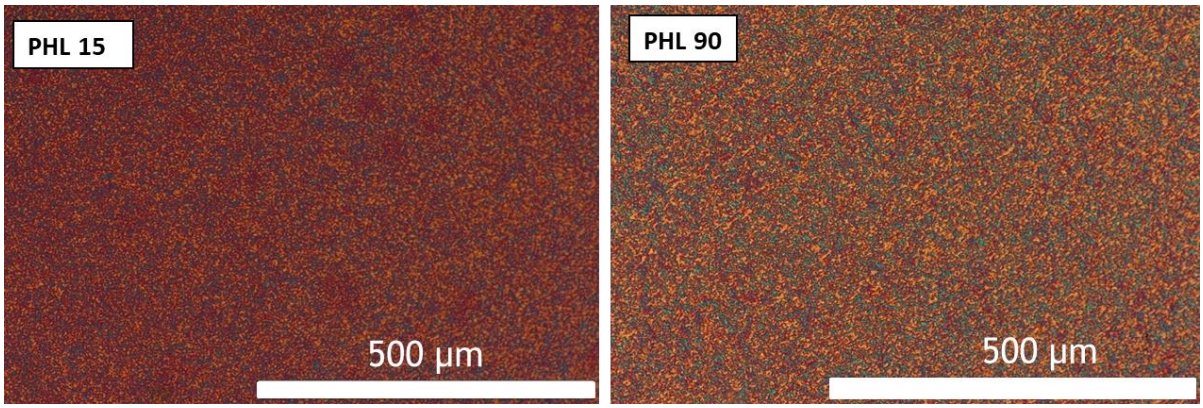

Figure 6.10. PLOM micrographs for PHL samples. Micrographs were taken at 25 ºC after melting for 1 minute at 90 ºC and cooling at 20 ºC/min.

When the samples are isothermally crystallized, the morphology can be better appreciated, as heterogeneous nuclei activation is known to decrease when the isothermal crystallization temperature increases. Figure 6.11 shows the PLOM micrographs acquired during isothermal crystallization experiments at the indicated T_c and with the same supercooling value (the equilibrium melting temperature needed to calculate the supercooling was also obtained in this work, see below). The samples were cooled from

the melt (at 50 ºC/min) to a chosen crystallization temperature in the range of 45 to 60 ºC. Although the crystals appear larger, they do not have the classic circular shape typical of spherulites: they resemble more axialites or lamellar aggregates with two-dimensional symmetry. As their average sizes are close to one another, the nucleation is probably instantaneous, as was later confirmed by the overall crystallization kinetics measurements (see below).

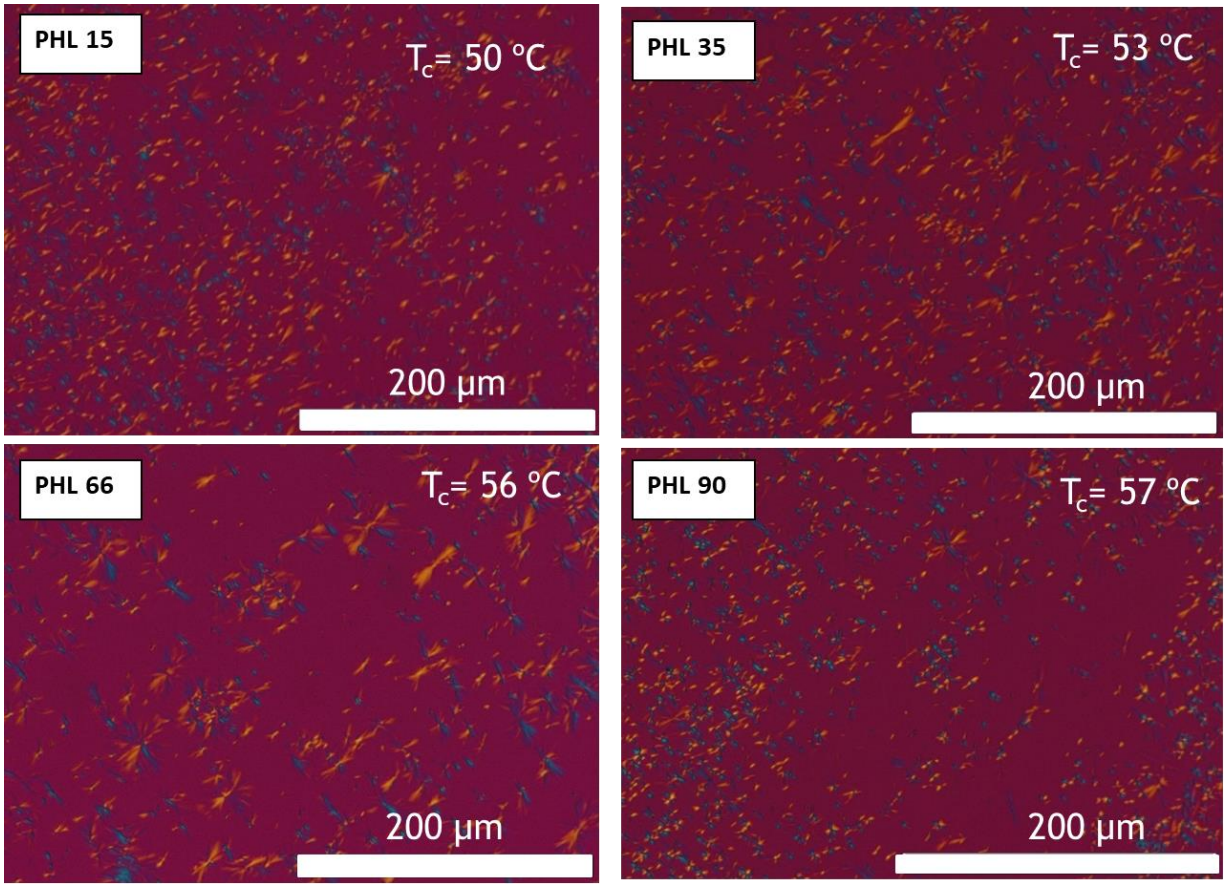

Figure 6.11. PLOM micrographs taken at the indicated T_c values and at the same supercooling (ΔT=5 ºC). The rate of cooling from the melt was 20 ºC/min.

Given the shape of the crystals, to measure the growth rate, *G* (µm/s), the length variation from one extreme to the other was measured as a function of time for different crystallization temperatures (the plots were always linear).

The typical growth rate (G) trend as a function of temperature is represented by a bell-shaped curve, given by the competition of two opposite phenomena[44],[45]. On the right-hand side of the plot, the growth rate increases as T_c decreases because the secondary nucleation increases with the supercooling until a maximum (i.e., G is controlled by secondary nucleation in this high-temperature range). This maximum corresponds to the point at which the viscosity of the melt is so high that the growth of the crystals is dominated by the slow diffusion of the chains to the crystallization front. Subsequently, the growth rate decreases and becomes zero at T_g.

In the case of the PHL samples involved in this study, it was possible to measure growth rates only on the right side of the G versus T_c curve at high crystallization temperatures. Any attempt to do growth measurements at lower temperatures failed, as the material crystallized during the fast cooling to T_c.

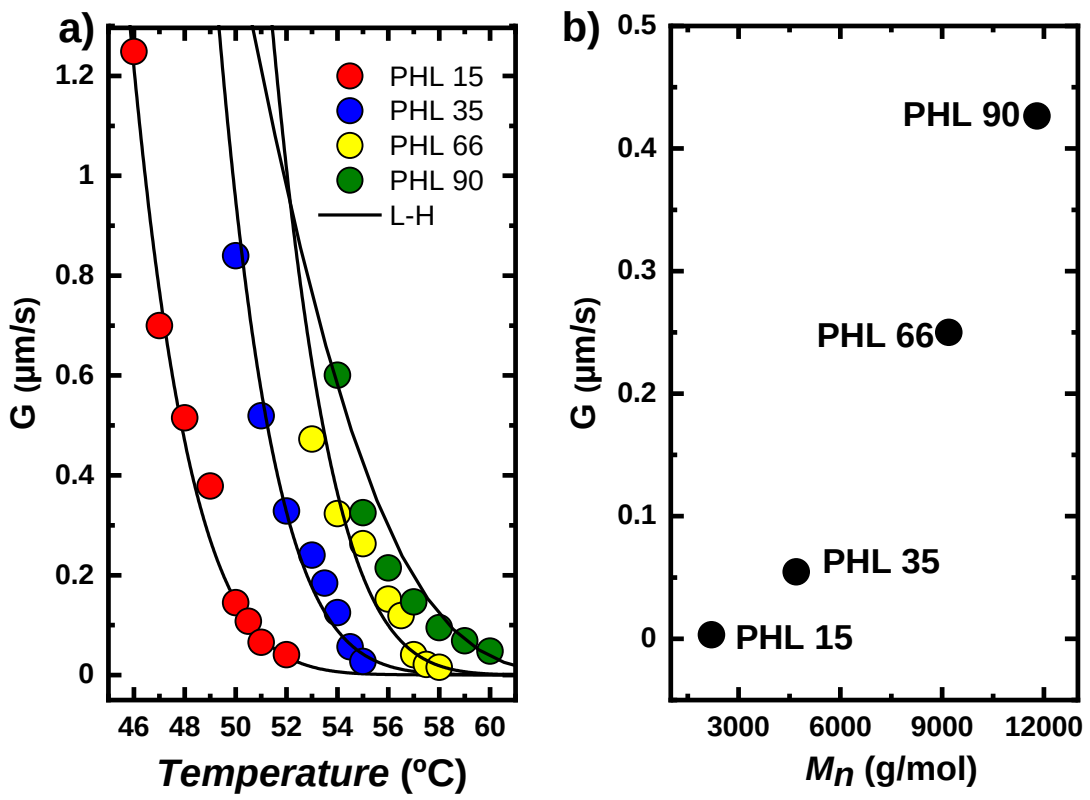

Figure 6.12. Spherulitic growth rate (G) as a function of: (a) crystallization temperature and (b) molecular weight at T_c =54.5 ºC for samples PHL 15, PHL 35, PHL 66, and PHL 90. The solid lines in the left graph are fits to the Lauritzen and Hoffman equation.

Figure 6.12a shows the results of the spherulitic growth rate as a function of T_c for the four samples involved in this work, determined by PLOM experiments. The trend is similar for all samples and is the typical trend where secondary nucleation dominates the superstructural growth. It is possible to notice that the molecular weight of each sample influences the growth rate values. Indeed, the growth rate is faster as the molecular weight increases, and the spherulites of the higher molecular weight samples grow faster at the same crystallization temperature in the molecular weight range studied in this work. This behavior is evident from the graph shown in Figure 6.12b, in which the growth rate is represented as a function of M_n at the same crystallization temperature. This result is consistent with the control of secondary nucleation. It has already been reported in the

case of other low molecular weight polyesters, such as PCL [46],[47],[48], PEO [49] and PDEO [50]. If higher molecular weight samples could be obtained, eventually, diffusion factors will take over, and the growth rate would eventually decrease as the molecular weight increases.

The solid lines reported in Figure 6.12a are fits to the Lauritzen and Hoffman theory.

The Lauritzen-Hoffman equation is given by[51]:

$$G = G_o \, exp\left[\frac{-U^*}{R(T_c - T_0)}\right]\left[\frac{-K_g^G}{fT(T_m^0 - T_c)}\right] \tag{6.1}$$

where: G_o is a constant that includes all terms that do not depend on temperature, U^* is the transport activation energy for the polymer chains diffusion (in this study, a value of 1500 cal/mol was employed), R is the universal gas constant, T_c is the crystallization temperature, T_0 is the temperature at which the movement of the chains is frozen, and it is 30ºC degrees lower than the T_g, T_m^0 is the equilibrium melting temperature, f is a temperature correction factor, given by the expression $2T_c/(T_m^0 + T_c)$. K_g^G is a constant proportional to the energy barrier for the spherulitic growth or secondary nucleation:

$$K_g^G = \frac{j\, b_0\, \sigma\sigma_e T_m^0}{k\, \Delta H_m^0} \tag{6.2}$$

j assumes the value of 2 for the Regime II crystallization, a regime where the secondary nucleation and the spread of the nucleus on the growth front are equivalent[52], b_0 is the chain's width, σ the lateral surface free energy, σ_e is the fold surface energy, k is the Boltzman constant and, finally, ΔH_m^0 is the equilibrium latent heat of fusion. When $\ln G + \frac{-U}{R\,(T_c - T_0)}$ is plotted versus$\frac{1}{T_c(\Delta T)f}$, it is possible to obtain a straight line in which K_g^G is the slope and G_o the intercept. From the K_g^G value, the $\sigma\sigma_e$ value can be obtained, and,

using the expression $\sigma = 0.1\Delta H_m^0\sqrt{a_0 b_0}$, where $a_0 b_0$ is the chain cross-sectional area, it is possible to calculate the values of σ and σ_e. Moreover, it is also possible to calculate the work that the macromolecule does to fold as $q = 2a_0 b_0 \sigma_e$[53].

The detailed analysis of the parameters can be found in the Table 6.3 where differences in the K_g^G, σ_e and q values are noted: these parameters decrease with increasing molecular weight. This indicates that the energy barrier for the PHL spherulites to grow decreases as M_n increases, in the molecular weight range explore in this work. A similar behavior has already been observed previously for PCL samples in a low to medium molecular weight range[46,48].

Table 6.3. Isothermal kinetics data parameters described in the Paragraph 3.4 derived from experimental results obtained by PLOM.

Sample	G^0(cm/s)	K^G_g (K^2)	σ (erg/cm^2)	σ_e (erg/cm^2)	q (erg)	R^2
PHL 15	753	$3.55\text{x}10^5$	11.16	136.19	$5.03\text{x}10^{-13}$	0.987
PHL 35	808	$1.18\text{x}10^5$	11.16	133.44	$4.92\text{x}10^{-13}$	0.946
PHL 66	854	$6.12\text{x}10^4$	11.16	69.74	$2.57\text{x}10^{-13}$	0.939
PHL 90	902	$2.92\text{x}10^4$	11.16	33.27	$1.34\text{x}10^{-13}$	0.932

6.3.7 Overall crystallization kinetics obtained by DSC

The overall crystallization process is the transformation from the melt to the semicrystalline state, including both primary nucleation and superstructural growth. DSC is a convenient and precise technique to determine the overall isothermal crystallizatio n

kinetics. Representative DSC isotherms are reported in Figures 6.13 (a, b) and 6.14 (a, b, c, d). The experimental data can be fitted with the Avrami and the Lauritzen and Hoffman theory[54,55].

The inverse of the induction time (t_0) is reported as a function of T_c in Figure 6.15. The induction time is the time that elapses before the DSC detects any crystallization process. Therefore, the inverse of the induction or incubation time is proportional to the primary nucleation rate (before crystal growth starts from the created primary nuclei). The primary nucleation rate increases (if compared at a constant temperature) as the PHL molecular weight increases. Still, the difference between PHL 66 and PHL 90 is very small, indicating a saturation effect, which was not observed for the spherulitic growth rates.

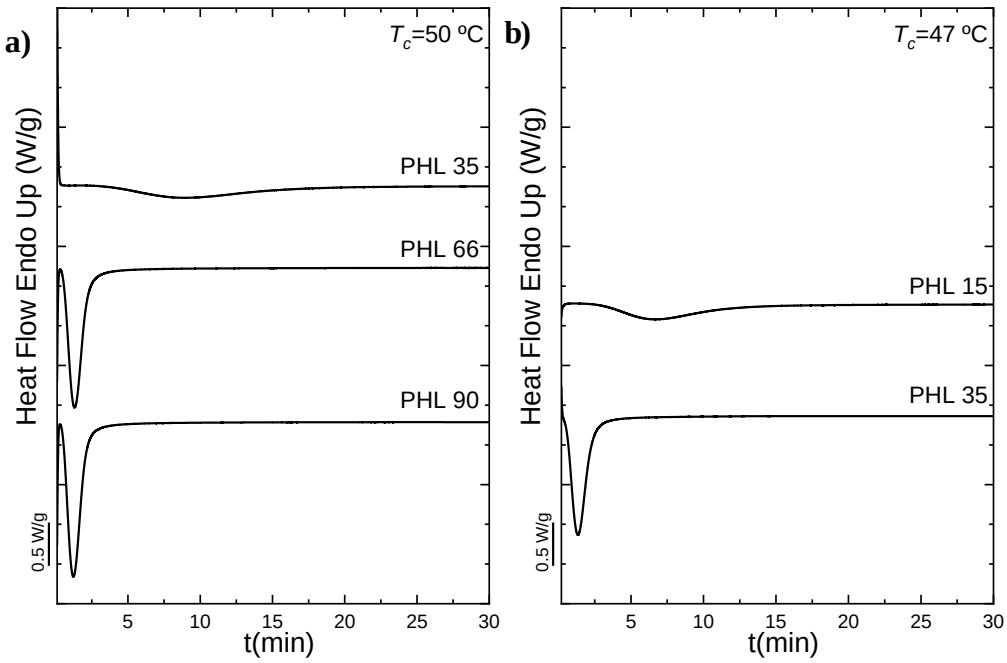

Figure 6.13. DSC scans recorded during isotherms at (a) T_c=50 ºC for PHL 35, PHL 66, PHL 90 and at (b) T_c= 47 ºC for PHL 15 and PHL 35.

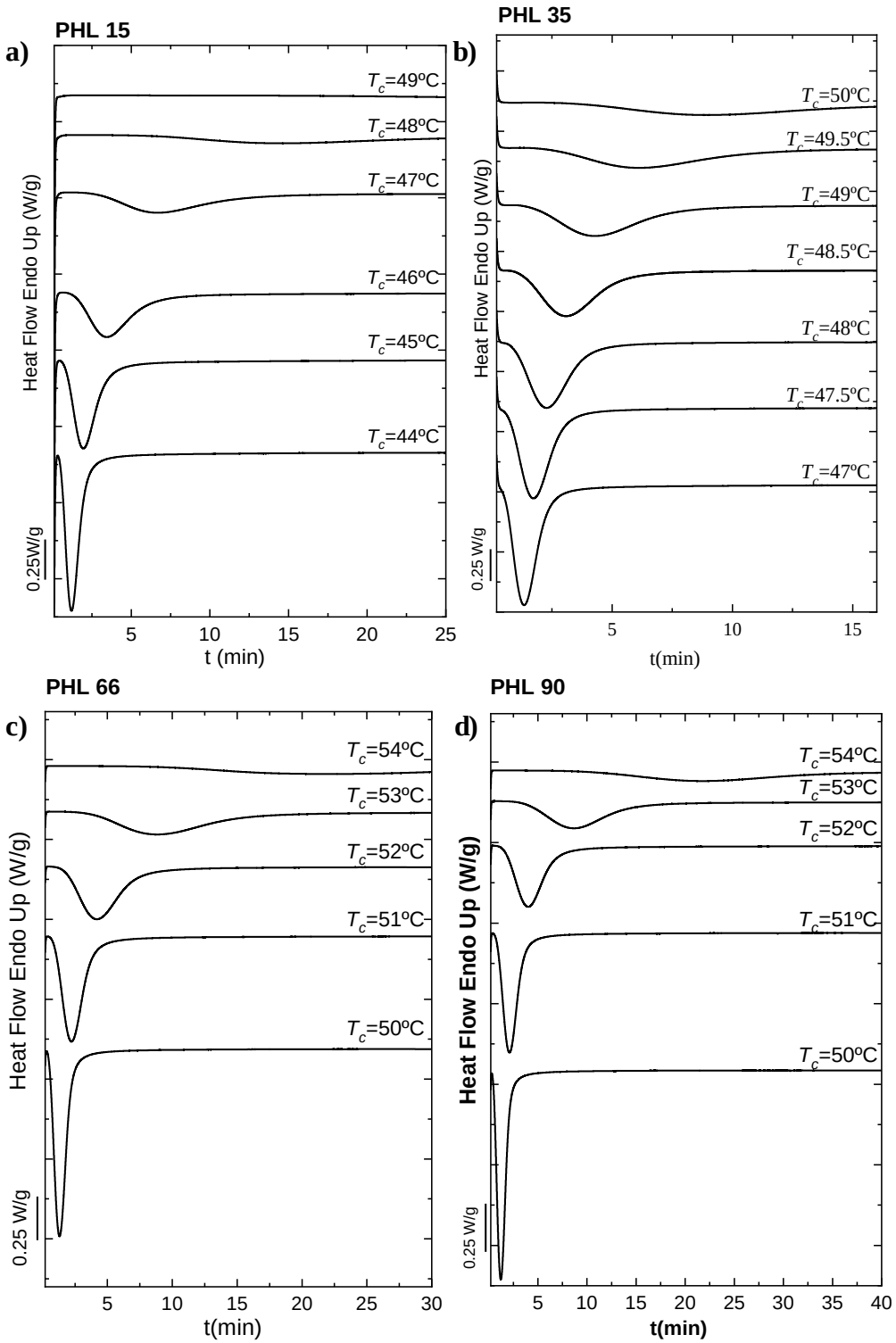

Figure 6.14. DSC scans recorded during isotherms for PHL 15 (a) PHL 35 (b), PHL 66 (c) and PHL 90 (d).

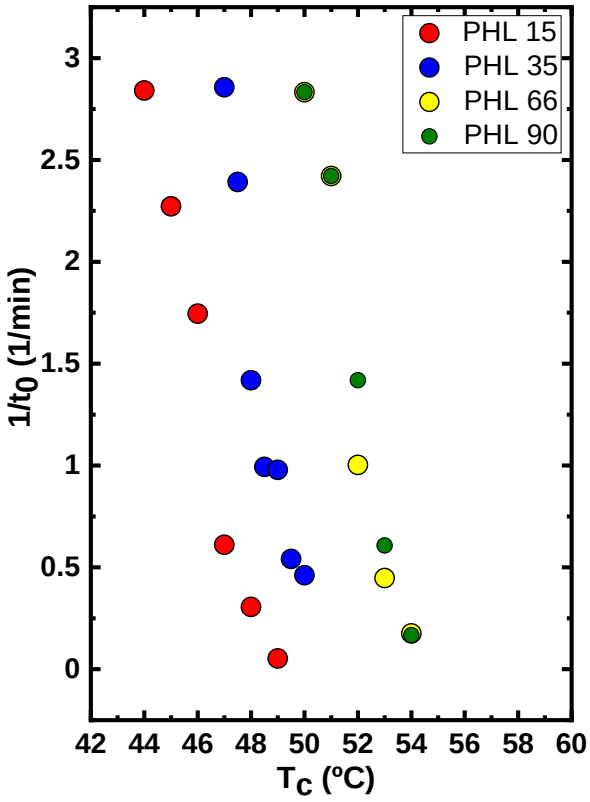

Figure 6.15. The inverse of induction time ($1/t_0$) as a function of T_c

The inverse of the half crystallization rate ($1/\tau_{50\%}$) is plotted in Figure 6.16 as a function of T_c (a) and molecular weight at a constant T_c (b). This value is the inverse of the time polymers need to achieve 50% of their relative crystallinity during an isothermal process. It represents an experimental value of the overall crystallization rate. The trend is similar to that seen for the inverse of the induction time: i.e., samples with higher molecular weight crystallize faster and at lower supercooling than samples with lower molecular weight. However, the difference between PHL 66 and PHL 90 is minimal in the temperature range where the experimental data was gathered. Figure 6.16b plots $1/\tau_{50\%}$ values as a function of the molecular weight at the same value as the crystallization temperature.

It should be noted that for the PHL 60 and PHL 90 cases, the values were extrapolated with the Lauritzen and Hoffman fits, as no experimental data for these samples could be measured at T_c=47 ºC. In any case, we have obtained a similar trend for

primary nucleation rate, spherulitic growth, and overall crystallization rate; as in all cases, these rates increase with PHL molecular weight, but they are close to starting to saturate at the highest molecular weight values employed here. Similar behavior has already been observed in the case of PCL[46,47], PLLA[56], and PHB [57] in the low to medium molecular weight range.

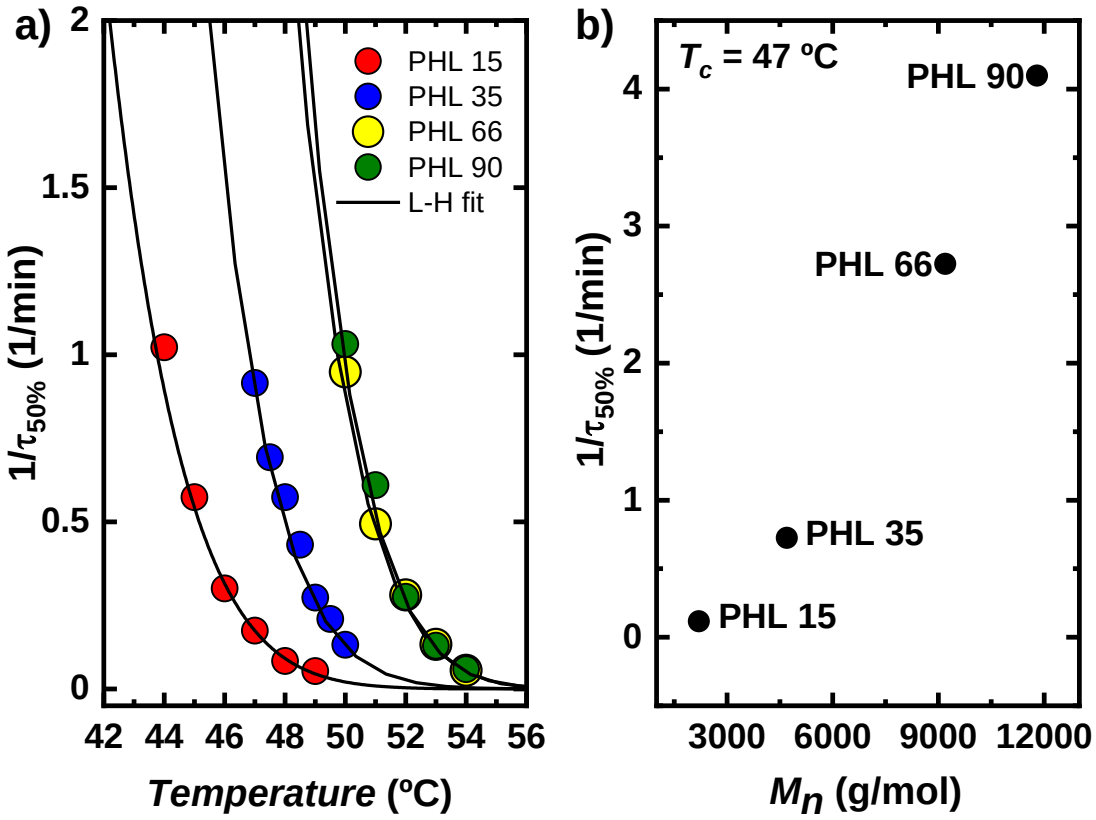

Figure 6.16. Overall crystallization rate ($1/\tau_{50\%}$) as a function of: (a) crystallization temperature and (b) molecular weight at T_c = 47 ºC, for PHL 15, PHL 35, PHL 66, and PHL 90. The solid lines in the left graph are fits to the Lauritzen and Hoffman equation.

The experimental data of the overall DSC crystallization rate was fitted by the Avrami equation[58–60], which can be expressed as:

$$1 - V_c(t - t_0) = \exp(-k(t - t_0)^n) \quad (6.3)$$

In this equation, V_c represents the relative volumetric transformed fraction, t the experimental time, t_0 is the induction time, k the overall crystallization rate constant, and n the Avrami index, related to the nucleation rate and the growth dimensionality of the crystals; the value of n can fluctuate between 2 and 4 in the case of bulk polymers. Avrami index values close to 2 are correlated with instantaneously nucleated axialites. If n=3, two possibilities exist, either sporadically nucleated axialites or instantaneously nucleated spherulites, and finally, n=4 indicates the generation of sporadically nucleated spherulites. If the nucleation is between instantaneous and sporadic, fractional values of the Avrami index can be obtained[61].

Figure 6.17a shows an example of the PHL 35 sample where the experimental data of the isothermal DSC is plotted together with its Avrami fit, and Figure 6.17b shows the typical Avrami plot in the conversion range used to perform the fit. The agreement between the experimental data and the Avrami fit is excellent, as in this case, the Arami equation describes not only the primary crystallization range (which is typical) but also the secondary crystallization range, after the superstructural entities (i.e., axialites most likely in this case) have impinged on one another, at experimental times beyond the peak value.

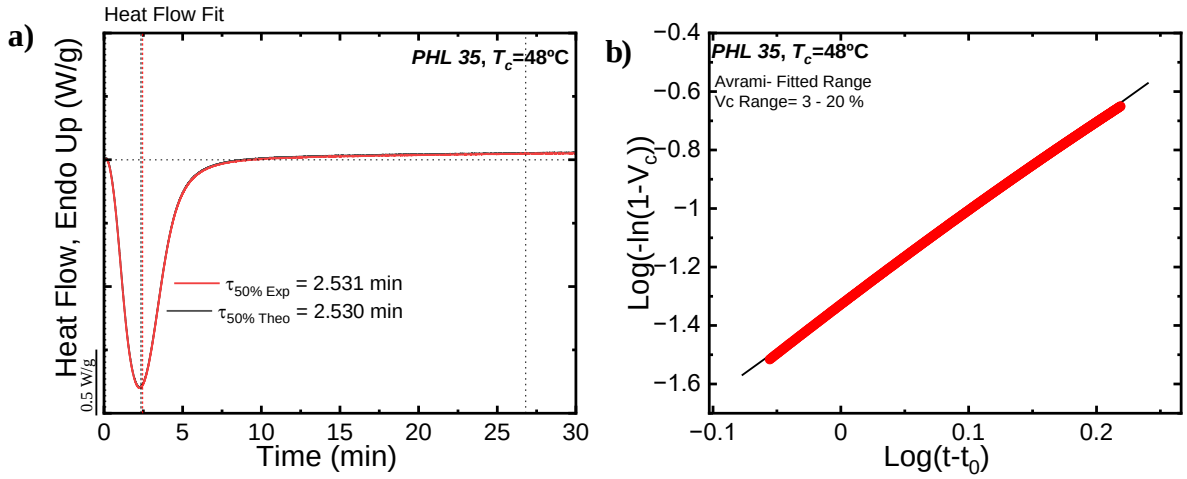

Figure 6.17. The Avrami fit equation using the free Origin plug-in developed by Pérez-Camargo *et al.*[61] for PHL 35 at T_c= 48 °C.

Tables 6.4-6.7 list the fitting parameters for all the samples employed here; it is possible to notice that the fittings obtained are always excellent with correlation coefficients larger than 0.999. The experimental values of $\tau_{50\%}$ are also in excellent agreement, as expected by the quality of the fit, with those predicted by the Avrami theory. Tables 6.4-6.7 also report the Avrami index, and it is noted that values between 2.2 and 3 were obtained. These values can be interpreted as representing axialites whose nucleation varies from close to instantaneous (n=2) to sporadic (n=3). In the cases where n=3, the values could also represent spherulites instantaneously nucleated; however, according to the PLOM observations presented in Figure 6.11, they were not observed.

Table 6.4. Avrami fitting parameters obtained by the free App [61] for PHL 15.

T_c (°C)	t_0 (min)	n	K (min^{-n})	$K^{1/n}$ (min^{-1})	R	$\tau_{50\% exp}$(min)	$\tau_{50\% Theo}$ (min)
44	0.352	2.85	8.00×10^{-01}	5.30×10^{-01}	1.000	0.951	0.978
45	0.440	3.14	1.37×10^{-01}	1.94×10^{-03}	1.000	1.674	1.742
46	0.573	3.50	1.26×10^{-02}	2.25×10^{-07}	0.999	3.140	3.327
47	1.638	3.04	3.80×10^{-03}	4.39×10^{-08}	1.000	5.535	5.730
48	3.272	3.44	1.58×10^{-04}	8.38×10^{-14}	0.999	11.425	11.933
49	19.102	2.17	$1,23 \times 10^{-03}$	4.84×10^{-07}	1.000	18.504	18.646

Table 6.5. Avrami fitting parameters obtained by the free App [61] for PHL 35.

T_c (°C)	t_0 (min)	n	K (min^{-n})	$K^{1/n}$ (min^{-1})	R	$\tau_{50\% exp}$(min)	$\tau_{50\% Theo}$ (min)
47	0.350	2.85	5.59×10^{-01}	1.91×10^{-01}	1.000	1.079	1.092
47.5	0.418	2.95	2.47×10^{-01}	1.61×10^{-02}	1.000	1.418	1.442
48	0.705	2.6	1.63×10^{-01}	8.95×10^{-03}	0.999	1.745	1.743
48.5	1.007	2.52	8.24×10^{-02}	1.85×10^{-03}	0.999	2.327	2.316
49	1.022	2.85	1.80×10^{-02}	1.07×10^{-05}	1.000	3.599	3.656
49.5	1.848	2.58	1.23×10^{-02}	1.18×10^{-05}	1.000	4.751	4.772
50	2.167	2.83	2.39×10^{-03}	3.81×10^{-08}	1.000	7.394	7.563

Table 6.6. Avrami fitting parameters obtained by the free App [61] for PHL 66.

T_c (°C)	t_0 (min)	n	K (min^{-n})	$K^{1/n}$ (min^{-1})	R	$\tau_{50\% exp}$(min)	$\tau_{50\% Theo}$ (min)
50	0.353	2.86	6.37×10^{-01}	2.75×10^{-01}	1.000	1.036	1.054
51	0.413	3.31	7.56×10^{-02}	1.94×10^{-04}	1.000	1.955	2.024
52	0.997	3.03	1.59×10^{-02}	3.55×10^{-06}	1.000	3.471	3.555
53	2.237	2.96	1.97×10^{-03}	$9,81 \times 10^{-09}$	1.000	7.242	7.493
54	5.693	2.91	1.81×10^{-04}	1.29×10^{-11}	1.000	17.042	17.995

Table 6.7. Avrami fitting parameters obtained by the free App [61] for PHL 90.

T_c (°C)	t_0 (min)	n	K (min^{-n})	$K^{1/n}$ (min^{-1})	R	$\tau_{50\%\,exp}$(min)	$\tau_{50\%\,Theo}$ (min)
50	0.353	2.75	7.94×10^{-01}	5.30×10^{-01}	1.000	0.952	0.969
51	0.413	3.23	1.02×10^{-01}	6.28×10^{-04}	1.000	1.810	1.640
52	0.705	3.37	9.98×10^{-03}	1.70×10^{-07}	1.000	3.519	3.627
53	1.647	3.37	7.70×10^{-04}	3.22×10^{-11}	1.000	7.507	7.736
54	5.985	3.01	1.40×10^{-04}	2.51×10^{-12}	0.999	16.901	16.922

Moreover, in this work, during the isothermal crystallization process, the equilibrium melting temperature of the four PHL samples was calculated, and for this purpose, the Hoffman-Weeks extrapolation was used. Figure 6.18 shows the extrapolations obtained. No monotonic change with the molecular weight was obtained, and the equilibrium melting temperatures are in the range of 71-75 ºC, which considering the error of the extrapolations performed, could be regarded as similar to one another. The average T_m^0 value obtained is close to 73 ºC, similar to some of the values reported for PCL (i.e., 78 ºC)[62].

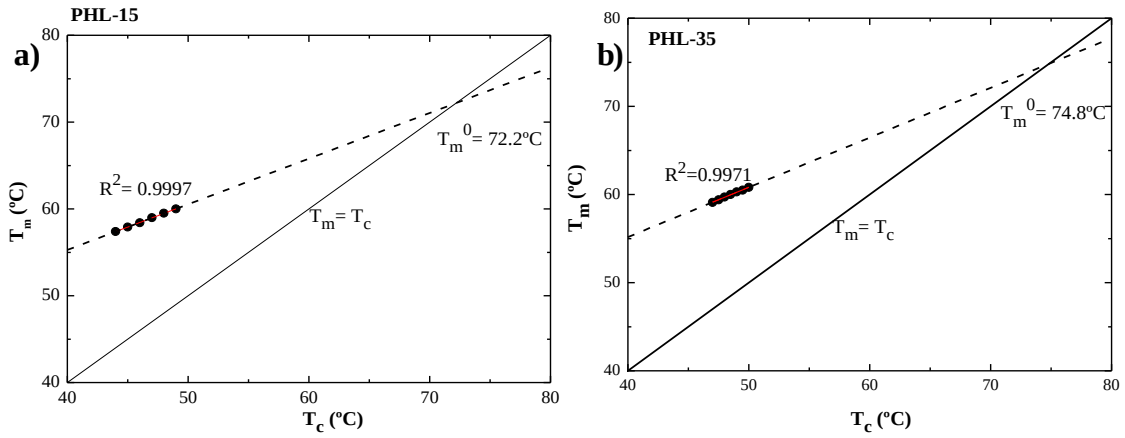

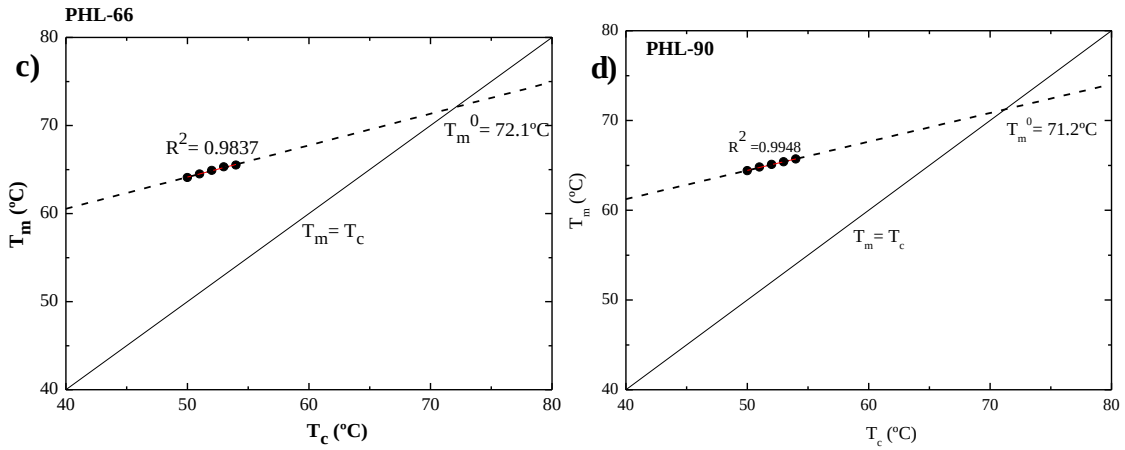

Figure 6.18. Hoffman-Weeks plots for PHL 15 (a), PHL 35 (b), PHL 66 (c), and PHL 90K (d).

6.3.8 Transmission Electron Microscopy (TEM)

TEM analysis was performed on the PHL 15 and PHL 35 samples; the corresponding results are shown in Figure 6.19(a, b). In the present study, the TEM analysis was conducted after staining, so the dark areas are the amorphous areas, and the brighter areas are the crystalline areas. The presence of straight and long lamellae (white lines in Figures a and b) is observed, and their thickness was measured manually using the ImageJ software. Figure 6.20 shows the thickness distribution histograms. For both samples, the lamellar thickness is very similar, with an average thickness of 8 nm, a value comparable to that obtained for PCL[63].

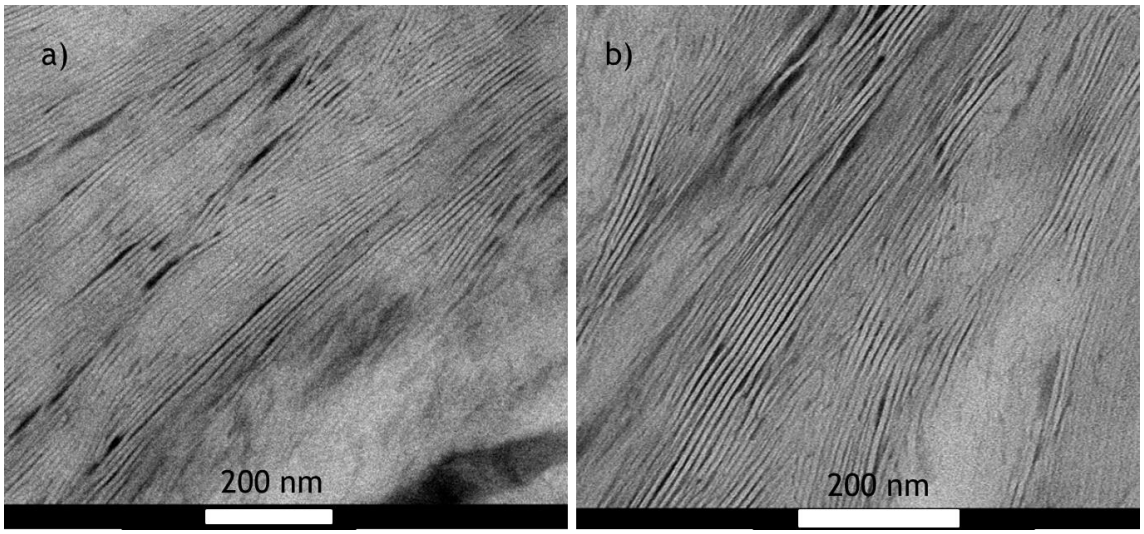

Figure 6.19. TEM micrographs taken at room temperature. Before cryo-cutting at -90ºC, the samples were crystallized by cooling from the melt at 20ºC/min.

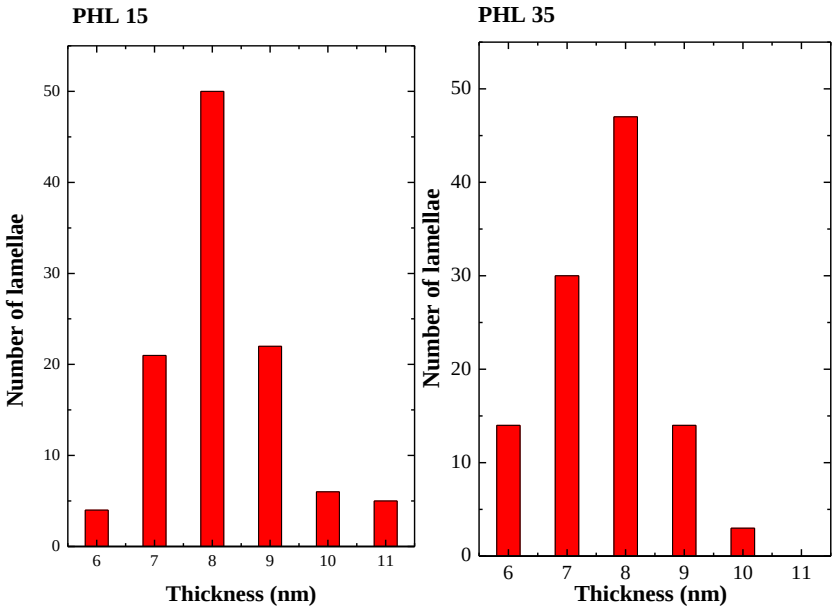

Figure 6.20. Distribution of the measured lamellae thickness of PHL 15 and PHL 35.

Single crystals of the sample PHL 66 were prepared from a dilute solution in 1-hexanol. A bright-field TEM image of the obtained crystals is reported in Figure 6.20.

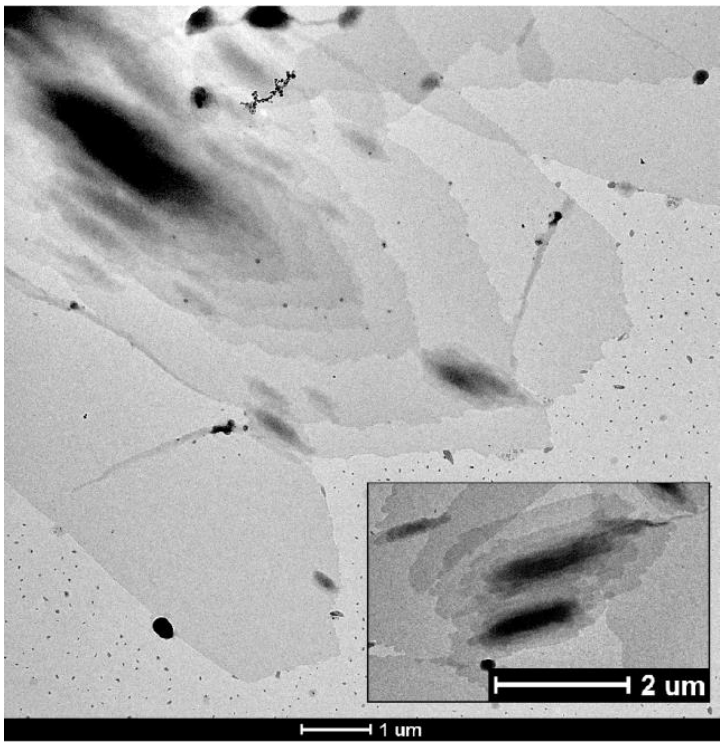

Figure 6.21. Bright-field TEM image of PHL 66 single crystals.

Hexagonal-shaped flat single crystals were observed. Most crystals are multilayered. This single crystal morphology has been reported for other aliphatic polyesters, such as PUDL[35] and PCL[64]·[46,65]. Single crystals with various thicknesses were observed (Figure 6.21). Some crystals are transparent to the electron beam, whereas others are completely opaque. Preliminary experiments have shown that single-layered crystals, and each monolamellar part at the edge of all multilayered crystals, yield well-resolved electron diffraction (ED) patterns. The interpretation of the ED patterns and the full resolution of the crystal structure of PHL is in progress.

6.4 Conclusions

This study reports the synthesis and comprehensive crystallization study of a new polyester with seven carbon atoms in its repeating unit, i.e., polyheptalactone, PHL. The WAXS diffraction pattern of this material was collected and found to be very similar to PE and linear aliphatic polyesters. The effect of molecular weight was studied in both non-isothermal and isothermal experiments. It was found that high molecular weights correspond to materials with higher melting temperatures and faster nucleation and crystallization kinetics.

TEM analysis confirmed the presence of a lamellar morphology whose thickness is similar to that reported for PCL (8 nm). Finally, single crystals of this polymer were prepared, and they displayed flat hexagonal shapes. Studies for determining the exact crystalline structure and unit cell parameters of PHL are in progress.

Polyheptalactones are very promising materials to increase the palette of commercially available polyesters with a potential biodegradable character, given the similarities found between their structure and properties and the various aliphatic polyesters already in use, such as PCL.

6.5 References

1. Cooper, T.A. Developments in Plastic Materials and Recycling Systems for Packaging Food, Beverages and Other Fast-Moving Consumer Goods. *Trends Packag. Food, Beverages Other Fast-Moving Consum. Goods* **2013**, 58–107.
2. Cuadros-Rodríguez, L.; Lazúen-Muros, M.; Ruiz-Samblás, C.; Navas-Iglesias, N. Leachables from Plastic Materials in Contact with Drugs. State of the Art and Review of Current Analytical Approaches. *Int. J. Pharm.* **2020**, *583*, 119332.
3. Arif, Z.U.; Khalid, M.Y.; Sheikh, M.F.; Zolfagharian, A.; Bodaghi, M. Biopolymeric Sustainable Materials and Their Emerging Applications. *J. Environ. Chem. Eng.* **2022**, 108159.
4. Siddique, R.; Khatib, J.; Kaur, I. Use of Recycled Plastic in Concrete: A Review. *Waste Manag.* **2008**, *28*, 1835–1852.
5. Rao, V. V; Sonashree, R.; Halbavi, R.R. Review on Plastic Waste Disposal and Role of Microorganisms in Bioremediation of Plastics. *Res. Anthol. Emerg. Tech. Environ. Remediat.* **2022**, 481–492.
6. Chen, H.L.; Nath, T.K.; Chong, S.; Foo, V.; Gibbins, C.; Lechner, A.M. The Plastic Waste Problem in Malaysia: Management, Recycling and Disposal of Local and Global Plastic Waste. *SN Appl. Sci.* **2021**, *3*, 1–15.
7. Gangwar, P.; Tiwari, S. Stabilization of Soil with Waste Plastic Bottles. *Mater. Today Proc.* **2021**, *47*, 3802–3806.
8. Altalhi, T.A. *Handbook of Bioplastics and Biocomposites Engineering Applications*; John Wiley & Sons, 2022; ISBN 1119160138.
9. Frounchi, M. Studies on Degradation of PET in Mechanical Recycling. *Macromol. Symp.* **1999**, *144*, 465–469, doi:10.1002/masy.19991440142.
10. Ávila, A.F.; Duarte, M. V. A Mechanical Analysis on Recycled PET/HDPE Composites. *Polym. Degrad. Stab.* **2003**, *80*, 373–382, doi:10.1016/S0141-3910(03)00025-9.
11. Achilias, D.S.; Roupakias, C.; Megalokonomos, P.; Lappas, A.A.; Antonakou, V. Chemical Recycling of Plastic Wastes Made from Polyethylene (LDPE and HDPE) and Polypropylene (PP). *J. Hazard. Mater.* **2007**, *149*, 536–542, doi:10.1016/j.jhazmat.2007.06.076.
12. Rorrer, N.A.; Nicholson, S.; Carpenter, A.; Biddy, M.J.; Grundl, N.J.; Beckham, G.T. Combining Reclaimed PET with Bio-Based Monomers Enables Plastics

Upcycling. *Joule* **2019**, *3*, 1006–1027, doi:10.1016/j.joule.2019.01.018.

13. Vollmer, I.; Jenks, M.J.F.; Roelands, M.C.P.; White, R.J.; van Harmelen, T.; de Wild, P.; van Der Laan, G.P.; Meirer, F.; Keurentjes, J.T.F.; Weckhuysen, B.M. Beyond Mechanical Recycling: Giving New Life to Plastic Waste. *Angew. Chemie Int. Ed.* **2020**, *59*, 15402–15423.
14. Jehanno, C.; Alty, J.W.; Roosen, M.; De Meester, S.; Dove, A.P.; Y-X Chen, E.; Leibfarth, F.A.; Sardon, H. Critical Advances and Future Opportunities in Upcycling Commodity Polymers. *Nature* **2022**, *603*, 803, doi:10.1038/s41586-021-04350-0.
15. Ganewatta, M.S.; Wang, Z.; Tang, C. Chemical Syntheses of Bioinspired and Biomimetic Polymers toward Biobased Materials. *Nat. Rev. Chem.* **2021**, *5*, 753–772.
16. Rosenboom, J.G.; Langer, R.; Traverso, G. Bioplastics for a Circular Economy. *Nat. Rev. Mater. 2022 72* **2022**, *7*, 117–137, doi:10.1038/s41578-021-00407-8.
17. Deopura, B.L.; Alagirusamy, R.; Joshi, M.; Gupta, B. *Polyesters and Polyamides*; Elsevier, 2008; ISBN 1845694600.
18. Yamashita, H.; Nakano, Y. *Polyester: Properties, Preparation and Applications*; Nova Science Publishers, Incorporated, 2008; ISBN 1604567538.
19. Guarino, V.; Gentile, G.; Sorrentino, L.; Ambrosio, L. Polycaprolactone: Synthesis, Properties, and Applications. *Encycl. Polym. Sci. Technol.* **2002**, 1–36.
20. Mamun, A. Retardation of the Growth Rate of the Basal and Overgrown Lamellar Crystals of PCL/PVME Miscible Binary Blends with Thickness Confinement. *Polym. J.* **2022**, *54*, 653–665.
21. Wei, Q.; Sun, D.; Yang, R.; Wang, Y.; Zhang, J.; Li, X.; Wang, Y. Influence of Fused Deposition Molding Printing Process on the Toughness and Miscibility of Polylactic Acid/Polycaprolactone Blends. *J. Mater. Eng. Perform.* **2022**, *31*, 1338–1345.
22. Mareau, V.H.; Prud'Homme, R.E. Growth Rates and Morphologies of Miscible PCL/PVC Blend Thin and Thick Films. *Macromolecules* **2003**, *36*, 675–684.
23. Mohamed, R.M.; Yusoh, K. A Review on the Recent Research of Polycaprolactone (PCL). *Adv. Mater. Res.* **2016**, *1134*, 249–255.
24. Schmitt, P.R.; Dwyer, K.D.; Coulombe, K.L.K. Current Applications of Polycaprolactone as a Scaffold Material for Heart Regeneration. *ACS Appl. Bio*

Mater. **2022**.

25. Backes, E.H.; Harb, S.V.; Beatrice, C.A.G.; Shimomura, K.M.B.; Passador, F.R.; Costa, L.C.; Pessan, L.A. Polycaprolactone Usage in Additive Manufacturing Strategies for Tissue Engineering Applications: A Review. *J. Biomed. Mater. Res. Part B Appl. Biomater.* **2022**, *110*, 1479–1503.
26. Marxsen, S.F.; Song, D.; Zhang, X.; Flores, I.; Fernández, J.; Sarasua, J.R.; Müller, A.J.; Alamo, R.G. Crystallization Rate Minima of Poly (Ethylene Brassylate) at Temperatures Transitioning between Quantized Crystal Thicknesses. *Macromolecules* **2022**, *55*, 3958–3973.
27. Organ, S.J.; Ungar, G.; Keller, A. Rate Minimum in Solution Crystallization of Long Paraffins. *Macromolecules* **1989**, *22*, 1995–2000.
28. Ungar, G.; Putra, E.G.R.; De Silva, D.S.M.; Shcherbina, M.A.; Waddon, A.J. The Effect of Self-Poisoning on Crystal Morphology and Growth Rates. *Interphases Mesophases Polym. Cryst. I* **2005**, 45–87.
29. Ungar, G. "Self-Poisoning" of Crystal Growth Faces in Long Alkanes and Poly (Ethylene Oxide) Fractions. *Cryst. Polym.* **1993**, 63–72.
30. RameshKumar, S.; Shaiju, P.; O'Connor, K.E. Bio-Based and Biodegradable Polymers-State-of-the-Art, Challenges and Emerging Trends. *Curr. Opin. Green Sustain. Chem.* **2020**, *21*, 75–81.
31. Van Der Mee, L.; Helmich, F.; De Bruijn, R.; Vekemans, J.A.J.M.; Palmans, A.R.A.; Meijer, E.W. Investigation of Lipase-Catalyzed Ring-Opening Polymerizations of Lactones with Various Ring Sizes: Kinetic Evaluation. *Macromolecules* **2006**, *39*, 5021–5027, doi:10.1021/ma060668j.
32. Ottou, W.N.; Sardon, H.; Mecerreyes, D.; Vignolle, J.; Taton, D. Update and Challenges in Organo-Mediated Polymerization Reactions. *Prog. Polym. Sci.* **2016**, *56*, 64–115.
33. Arno, M.C.; Inam, M.; Coe, Z.; Cambridge, G.; Macdougall, L.J.; Keogh, R.; Dove, A.P.; O'Reilly, R.K. Precision Epitaxy for Aqueous 1D and 2D Poly (ε-Caprolactone) Assemblies. *J. Am. Chem. Soc.* **2017**, *139*, 16980–16985.
34. Bunn, C.W. The Crystal Structure of Long-Chain Normal Paraffin Hydrocarbons. The "Shape" of The< CH2 Group. *Trans. Faraday Soc.* **1939**, *35*, 482–491.
35. Kim, E.; Uyama, H.; Doi, Y.; Ha, C.-S.; Iwata, T. Crystal Structure and Morphology of Poly (11-Undecalactone) Solution-Grown Single Crystals.

Macromolecules **2004**, *37*, 7258–7264.

36. Furuhashi, Y.; Sikorski, P.; Atkins, E.; Iwata, T.; Doi, Y. Structure and Morphology of the Aliphatic Polyester Poly (Δ-valerolactone) in Solution-grown, Chain-folded Lamellar Crystals. *J. Polym. Sci. Part B Polym. Phys.* **2001**, *39*, 2622–2634.
37. Furuhashi, Y.; Iwata, T.; Sikorski, P.; Atkins, E.; Doi, Y. Structure and Morphology of the Aliphatic Polyester Poly-β-Propiolactone in Solution-Grown Chain-Folded Lamellar Crystals. *Macromolecules* **2000**, *33*, 9423–9431.
38. Kim, E.; Uyama, H.; Doi, Y.; Ha, C.; Iwata, T. Crystal Structure and Morphology of Poly (16-hexadecalactone) Chain-folded Lamellar Crystals. *Macromol. Biosci.* **2005**, *5*, 734–742.
39. Kim, E.; Uyama, H.; Doi, Y.; Ha, C.-S.; Iwata, T. Crystal Structure and Morphology of Poly (12-Dodecalactone). *Biomacromolecules* **2005**, *6*, 572–579.
40. Gazzano, M.; Malta, V.; Focarete, M.L.; Scandola, M.; Gross, R.A. Crystal Structure of Poly (Ω-pentadecalactone). *J. Polym. Sci. Part B Polym. Phys.* **2003**, *41*, 1009–1013.
41. Bittiger, H.; Marchessault, R.H.; Niegisch, W.D. Crystal Structure of Poly-ε-Caprolactone. *Acta Crystallogr. Sect. B Struct. Crystallogr. Cryst. Chem.* **1970**, *26*, 1923–1927.
42. Chatani, Y.; Okita, Y.; Tadokoro, H.; Yamashita, Y. Structural Studies of Polyesters. III. Crystal Structure of Poly-ε-Caprolactone. *Polym. J.* **1970**, *1*, 555–562.
43. Unger, M.; Vogel, C.; Siesler, H.W. Molecular Weight Dependence of the Thermal Degradation of Poly (ε-Caprolactone): A Thermogravimetric Differential Thermal Fourier Transform Infrared Spectroscopy Study. *Appl. Spectrosc.* **2010**, *64*, 805–809.
44. Müller, A.J.; Michell, R.M.; Lorenzo, A.T. Isothermal Crystallization Kinetics of Polymers. *Polym. Morphol. Princ. Charact. Process.* **2016**, *714*, 181–203.
45. Michell, R.M.; Mueller, A.J. Confined Crystallization of Polymeric Materials. *Prog. Polym. Sci.* **2016**, *54*, 183–213, doi:https://doi.org/10.1016/j.progpolymsci.2015.10.007.
46. Su, H.-H.; Chen, H.-L.; Díaz, A.; Casas, M.T.; Puiggalí, J.; Hoskins, J.N.; Grayson, S.M.; Pérez, R.A.; Müller, A.J. New Insights on the Crystallization and Melting of

Cyclic PCL Chains on the Basis of a Modified Thomson–Gibbs Equation. *Polymer (Guildf)*. **2013**, *54*, 846–859.

47. Pérez, R.A.; Córdova, M.E.; López, J. V; Hoskins, J.N.; Zhang, B.; Grayson, S.M.; Müller, A.J. Nucleation, Crystallization, Self-Nucleation and Thermal Fractionation of Cyclic and Linear Poly (ε-Caprolactone) S. *React. Funct. Polym.* **2014**, *80*, 71–82.
48. Du, Z.; Yang, Y.; Xu, J.; Fan, Z. Effect of Molecular Weight on Spherulitic Growth Rate of Poly (E-caprolactone) and Poly (E-caprolactone)-b-poly (Ethylene Glycol). *J. Appl. Polym. Sci.* **2007**, *104*, 2986–2991.
49. Ding, N.; Amis, E.J. Kinetics of Poly (Ethylene Oxide) Crystallization from Solution: Temperature and Molecular Weight Dependence. *Macromolecules* **1991**, *24*, 3906–3914.
50. Gomez, M.A.; Fatou, J.G.; Bello, A. Spherulitic Growth Rates of Poly (3, 3-Diethyl Oxetane). *Eur. Polym. J.* **1986**, *22*, 661–664.
51. Hoffman, J.D.; Davis, G.T.; Lauritzen, J.I. The Rate of Crystallization of Linear Polymers with Chain Folding. In *Treatise on solid state chemistry*; Springer, 1976; pp. 497–614.
52. Pitt, C.G.; Chasalow, F.I.; Hibionada, Y.M.; Klimas, D.M.; Schindler, A. Aliphatic Polyesters. I. The Degradation of Poly (E-caprolactone) in Vivo. *J. Appl. Polym. Sci.* **1981**, *26*, 3779–3787, doi:https://doi.org/10.1002/app.1981.070261124.
53. Mark, J.E. *Physical Properties of Polymers Handbook*; Springer, 2007; Vol. 1076;.
54. Lorenzo, A.T.; Müller, A.J. Estimation of the Nucleation and Crystal Growth Contributions to the Overall Crystallization Energy Barrier. *J. Polym. Sci. Part B Polym. Phys.* **2008**, *46*, 1478–1487, doi:10.1002/POLB.21483.
55. Hoffman, J.D.; Lauritzen, J.I.; Jr. Crystallization of Bulk Polymers With Chain Folding: Theory of Growth of Lamellar Spherulites. *J. Res. Natl. Bur. Stand. Sect. A, Phys. Chem.* **1961**, *65A*, 297, doi:10.6028/JRES.065A.035.
56. Xiang, S.; Jun, S.; Li, G.; Bian, X.; Feng, L.; Chen, X.; Liu, F.; Huang, S. Effects of Molecular Weight on the Crystallization and Melting Behaviors of Poly (L-Lactide). *Chinese J. Polym. Sci.* **2016**, *34*, 69–76.
57. Caputo, M.R.; Tang, X.; Westlie, A.H.; Sardon, H.; Chen, E.Y.-X.; Müller, A.J. Effect of Chain Stereoconfiguration on Poly (3-Hydroxybutyrate) Crystallization Kinetics. *Biomacromolecules* **2022**, *23*, 3847–3859,

doi:https://doi.org/10.1021/acs.biomac.2c00682.

58. Reiter, G.; Strobl, G.R. *Progress in Understanding of Polymer Crystallization*; Springer, 2007; Vol. 714; ISBN 3540473076.
59. Avrami, M. Kinetics of Phase Change. II Transformation-time Relations for Random Distribution of Nuclei. *J. Chem. Phys.* **1940**, *8*, 212–224, doi:https://doi.org/10.1063/1.1750631.
60. Avrami, M. Granulation, Phase Change, and Microstructure Kinetics of Phase Change. III. *J. Chem. Phys.* **1941**, *9*, 177–184.
61. Pérez-Camargo, R.A.; Liu, G.; Wang, D.; Müller, A.J. Experimental and Data Fitting Guidelines for the Determination of Polymer Crystallization Kinetics. *Chinese J. Polym. Sci* **2022**, *40*, 1–34, doi:https://doi.org/10.1007/s10118-022-2724-2.
62. Chen, H. L., Li, L. J., Ou-Yang, W. C., Hwang, J. C., & Wong, W.Y. Chen, Hsin-Lung, et Al. "Spherulitic Crystallization Behavior of Poly (ε-Caprolactone) with a Wide Range of Molecular Weight. *Macromolecules* **1997**, *30*, 1718–1722, doi:https://doi.org/10.1021/ma960673v.
63. X Yu, N Wang, S.L. Crystal and Multiple Melting Behaviors of PCL Lamellae in Ultrathin Films. *J. Cryst. Growth* **2016**, doi:https://doi.org/10.1016/j.jcrysgro.2015.12.021.
64. Iwata, T.; Doi, Y. Morphology and Enzymatic Degradation of Poly (E-caprolactone) Single Crystals: Does a Polymer Single Crystal Consist of Micro-crystals? *Polym. Int.* **2002**, *51*, 852–858.
65. Casas, M.T.; Puiggalí, J.; Raquez, J.-M.; Dubois, P.; Córdova, M.E.; Müller, A.J. Single Crystals Morphology of Biodegradable Double Crystalline PLLA-b-PCL Diblock Copolymers. *Polymer (Guildf).* **2011**, *52*, 5166–5177.

Chapter VII

7. Conclusions

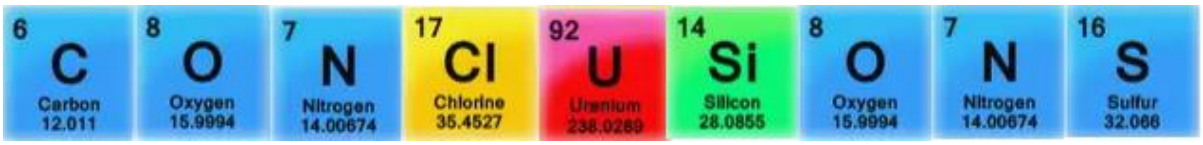

7.1 General Conclusions

This thesis aimed to study new systems based on polyesters, specifically polyhydroxybutyrate, to increase their use, given their excellent barrier and thermal properties. Calorimetry, morphology, and mechanical properties measurements were carried out for all the studied systems, and the changes in properties between the new and the reference systems were evaluated.

The primary objective of the first part of the thesis was to uncover the potential impact of PHB stereochemistry on its crystallization behavior. To achieve this, an analysis involving the enantiomerically pure bacterial PHB R and PHB samples with a 50% racemic R/S chain mixture was conducted. A significant effect that has been noticed is that there is a change in the crystallization behavior: in fact, a higher spherulite growth rate and an overall crystallization rate are found in the case of the R-PHB sample of bacterial origin, given its enantiomeric purity, despite the higher molecular weight.

The presence of the mixture of R and S configuration chains can slow down both the primary nucleation and the growth of the spherulites. The implications of these findings are substantial: the use of synthetic racemic PHB has the potential to expand the utility of PHB-based materials. Its incorporation in the formulation of copolymers and blends with other polyesters could yield novel materials featuring slower crystallization kinetics and an extended processability window.

The investigation then continues with an extensive exploration of the printability characteristics of PHBH. Through an in-depth examination of 3D printed samples using Differential Scanning Calorimetry (DSC), a noteworthy observation emerged in contrast to typical trends in the Fused Filament Fabrication (FFF) field. Unlike the conventional non-isothermal cooling stage, the crystallization process in PHBH occurred isothermally after each layer deposition during printing. This insight was corroborated by

computational simulations of the temperature profile throughout the printing process. Having established the printability of PHBH through rheological analysis, diverse printing conditions were employed to establish a link between these conditions and the resulting mechanical and morphological properties. The study indicated that elevating the nozzle temperature from 170°C to 180°C, while still below PHBH's degradation temperature of 200°C, along with increasing the bed temperature from 30°C to 50°C, resulted in enhanced mechanical properties. This improvement can be attributed to the reduction in void formation, as substantiated by scanning electron microscopy (SEM) images. Furthermore, the influence of printing velocity on print quality was investigated. Among printing velocities of 20, 30, and 40 mm/s, intermediate velocities demonstrated superior mechanical properties. The study also demonstrated that optimal mechanical properties are achieved when the layers are oriented consistently in relation to one another and in line with the test direction. Finally, it was demonstrated that the mechanical properties attained through 3D printing were comparable to those achieved via compression molding, particularly in terms of stiffness.

To deepen the study of PHB copolymers, it has been investigated how the incorporation of PCL units in either a random or blocky manner influences PHB's morphology, thermal characteristics, and crystallization kinetics. The block copolymer, PHB_{39}-*b*-PCL_{61}, displayed a moderate level of segregation within the molten state, while the random copolymer, P(HB_{72}-*ran*-CL_{28}), exhibited the anticipated single-phase melt behavior. Nevertheless, the crystallization of the PHB block within the block copolymer managed to disrupt the phase-separated structure of the melt, leading to the formation of distinct negative spherulites. This discovery holds novelty, given that PHB typically forms positive spherulites. The neat PHB has a limited nucleation density, resulting in the creation of large spherulites that accumulate stress and contribute significantly to its

inherent brittleness, alongside its notably high crystallinity. The block copolymer sample, however, demonstrated a heightened nucleation density, resulting in smaller spherulites on average. Conversely, the random copolymer exhibited an exceptionally fine micro-spherulitic structure, which offers potential mechanical properties and transparency advantages. Moreover, both block and random copolymer samples displayed markedly slower spherulitic growth rates and overall crystallization rates; in the block polymer, PHB block could attain a level of crystallinity comparable to that of pure PHB, even if at significantly extended crystallization times, and this is due to the covalent bonding with the softer PCL block. In contrast, the PHB component within the random copolymer exhibited a lower melting temperature and degree of crystallinity than neat PHB. The PCL component, being a minor constituent distributed randomly along the chains, did not undergo crystallization. Consequently, this random copolymer presents an appealing biodegradable material option with improved processability (owing to its reduced melting temperature) and the potential for enhanced mechanical and optical properties compared to pure PHB, attributable to its decreased crystallinity and micro-spherulitic structure.

Finally, the research presents a comprehensive exploration involving the synthesis and detailed investigation of the crystallization behavior of a novel polyester containing seven carbon atoms within each repeating unit, denoted as polyheptalactone (PHL) that, through WAXS diffraction pattern, it was observed to closely resemble polyethylene (PE) and linear aliphatic polyesters in terms of its crystalline arrangement. The impact of molecular weight on the crystallization characteristics was examined using both non-isothermal and isothermal experiments, and a direct correlation between higher molecular weights and elevated melting temperatures was found, alongside more rapid nucleation and crystallization kinetics. TEM analysis confirmed the presence of a lamellar morphology, with a thickness akin to that reported for poly(ε-caprolactone) (PCL),

approximately 8 nanometers. Moreover, the preparation of single crystals from this polymer unveiled hexagonal structures with flat surfaces. This potential is underscored by the structural and property similarities observed between polyheptalactones and various existing aliphatic polyesters, such as PCL, which are already established in practical applications.

7.2 List of Publications

In this section, all the publications related to this thesis and those resulting from collaborations unrelated to this topic are listed.

1. **Caputo, M. R.,** Shi, C., Tang, X., Sardon, H., Chen, E. Y.-X., Müller, A. J. Tailoring the nucleation and crystallization of Polyhydroxybutyrate by copolymerization. ***Submitted***

2. **Caputo, M. R.,** Olmos, A., Li, B., Olmedo-Martínez, J. L., Malafronte, A., De Rosa, C., Haritz Sardon, Rachel K. O'Reilly, Andrew P. Dove, Müller, A. J. (2023). Synthesis, Morphology, and Crystallization Kinetics of Polyheptalactone (PHL). *Biomacromolecules*, 24, 7, 3256-3267.

3. Malafronte, A., Scoti, M., **Caputo, M. R.,** Li, B., O'Reilly, R. K., Dove, A. P., Müller, A. J., De Rosa, C. (2023). Crystal Structure of Poly (7-heptalactone). *Macromolecules*, 2023, 56, 11, 4153-4162.

4. **Caputo, M. R**., Fernández, M., Aguirresarobe, R., Kovalcik, A., Sardon, H., Candal, M. V., & Müller, A. J. (2023). Influence of FFF Process Conditions on the Thermal, Mechanical, and Rheological Properties of Poly (hydroxybutyrate-co-hydroxy Hexanoate). *Polymers*, *15*(8), 1817.

5. Quinn, E. C., Westlie, A. H., Sangroniz, A., **Caputo, M. R.,** Xu, S., Zhang, Z., ... & Chen, E. Y. X. (2023). Installing Controlled Stereo-Defects Yields Semicrystalline and Biodegradable Poly (3-Hydroxybutyrate) with High Toughness and Optical Clarity. *Journal of the American Chemical Society*, *145*(10), 5795-5802.

6. **Caputo, M. R**., Tang, X., Westlie, A. H., Sardon, H., Chen, E. Y. X., & Müller, A. J. (2022). Effect of chain stereoconfiguration on poly (3-hydroxybutyrate) crystallization kinetics. *Biomacromolecules*, *23*(9), 3847-3859.

7. Damonte, G., Maddalena, L., Fina, A., Cavallo, D., M üller, A. J., **Caputo, M. R**., Mariani, A., Monticelli, O. (2022). On novel hydrogels based on poly (2-hydroxyethyl acrylate) and polycaprolactone with improved mechanical properties prepared by frontal polymerization. *European Polymer Journal*, *171*, 111226.

8. Fenni, S. E., **Caputo, M. R**., Müller, A. J., & Cavallo, D. (2022). Surface roughness enhances self-nucleation of high-density polyethylene droplets dispersed within immiscible blends. *Macromolecules*, *55*(4), 1412-1423.

9. Flores, I., Pérez-Camargo, R. A., Gabirondo, E., **Caputo, M. R**., Liu, G., Wang, D., Sardon, H., Müller, A. J. (2022). Unexpected structural properties in the saturation region of the odd–even effects in aliphatic polyethers: Influence of crystallization conditions. *Macromolecules*, *55*(2), 584-594.

10. Carmeli, E., Fenni, S. E., **Caputo, M. R.**, Müller, A. J., Tranchida, D., & Cavallo, D. (2021). Surface nucleation of dispersed polyethylene droplets in immiscible blends revealed by polypropylene matrix self-nucleation. *Macromolecules*, *54*(19), 9100-9112.

7.3 Conference Presentations

i. Participation in the 'Noche Europea de los Investigatores' in October 2020;

ii. Participation in the 'ZientiaAstea/Semana de La Ciencia' in November 2020;

iii. Virtual 10th EPF Summer School 2021- Polymers and Circular Economy-17/19 May 2021;

iv. Participation with a Poster in the 'GEP/SLAP 2022' Congress in May 2022 (Donostia, Spain);
Poster: ''Cristallization, morphology, thermal and barrier properties of synthetic poly8hydroxybutyrate)'';

v. Participation with a Poster in the 'Course in Macromolecular Science for Advanced and Suistainable Materials' in July 2022 (Erice, Italy);

Poster: ‘‘Determination of Crystal Lattice and influence of Molecualar weight on the crystallization of Polyheptalactone (PHL)’’.

7.4 Collaborations

This thesis has been carried oun in collaboration with various universities.

The samples studied in Chapters III and V were synthesized in the research group of Prof. Eugene Chen at the University of Colorado.

COLORADO STATE UNIVERSITY

The samples studied in Chapter VI were synthesized by Prof. Andrew Dove's research group at the University of Birmingham.

UNIVERSITY OF BIRMINGHAM

The preparation of the single crystal of PHL in Chapter VI was carried out by the research group of Prof. Claudio De Rosa at the University of Naples Federico II.

UNIVERSITÀ DEGLI STUDI
DI NAPOLI FEDERICO II

Resumen y Conclusiones

En este trabajo se han estudiado varios sistemas basados en poliésteres con el objetivo de entender las relaciones entre sus estructuras-propiedades y diseñar estrategias para mejorarlos.

La familia de poliésteres más investigada en esta tesis es la de los polihidroxialcanoatos (PHAs), poliésteres biodegradables de origen bacteriano con excelentes propiedades térmicas y de barrera, ideales para aplicaciones en embalaje y en la industria biomédica pero con dos grandes defectos que limitan su uso en aplicaciones prácticas: alta cristalinidad lo que implica malas propiedades mecánicas y puntos de fusión muy cercanos a la temperatura de degradación de estos materiales, lo cual limita su ventana de procesamiento. El homopolímero más estudiado, perteneciente a esta familia, es el polihidroxibutirato (PHB), con propiedades muy similares al polipropileno, pero con los defectos anteriormente mencionados: fragilidad y degradabilidad durante el procesado. Para limitar estos problemas, es posible producir, por medio de bacterias,copolímeros con otros PHA que tienen propiedades ligeramente mejores. Sin embargo, estos copolímeros son difíciles de obtener con pesos moleculares controlados y, por lo tanto, con propiedades específicas.

Este trabajo explora como reemplazar el clásico PHB obtenido por bacterias por nuevos sistemas sintéticos basados en PHB. La estructura, morfología y propiedades de estos nuevos materiales sintéticos es estudiada por: : calorimetría diferencial de barrido (DSC), microscopio de luz óptica polarizada (PLOM), propiedades mecánicas, difracción de rayos X de ángulo ancho y pequeño (WAXS y SAXS), barrido electrónico y transmisión. (SEM y TEM) e impresión 3D.

La primera parte de esta tesis presenta, por primera vez, un estudio térmico y morfológico completo de nuevas muestras de PHB sintético con diferentes pesos

moleculares y su comparación con un PHB bacteriano. Las muestras de PHB sintético son una mezcla racémica de macromoléculas con configuración 50% R y 50% S, mientras que el PHB bacteriano es enantioméricamente puro con cadenas 100% R. Se llevaron a cabo experimentos de cristalización isotérmica y no isotérmicalos cuales revelaron que las cadenas R y S del PHB pueden cocristalizar en la misma celda unitaria que el R-PHB. En particular, la presencia de cadenas S tiene un efecto retardante en la velocidad de cristalización global, lo que potencialmente ofrece beneficios en términos de capacidad de fabricación y aplicaciones industriales del material. Además, se realiza una investigación preliminar sobre una muestra de PHB en la que se introducen de forma controlada imperfecciones en la estereoquímica, con el objetivo de evaluar posibles alteraciones en sus propiedades térmicas, mecánicas, ópticas y de barrera. A pesar de lo que suele ocurrir, en este caso la presencia de estereodefectos mejora las propiedades mecánicas y ópticas. Además, las propiedades de barrera siguen siendo similares a las de los materiales normalmente utilizados en los envases.

Esta investigación continúa reportando un estudio innovador para la familia de PHAs ya que, hasta ahora, nunca se había intentado imprimir en 3D un PHA sin el uso de aditivos para ayudar a la impresión. Esta investigación examina la influencia de los parámetros de impresión específicos utilizados en la fabricación de filamentos fusibles (FFF) sobre las características del poli(hidroxibutirato-co-hidroxihexanoato) o PHBH. Se realizó un estudio reológico preliminar para verificar la imprimibilidad de PHBH. Un estudio reológico preliminar fue realizado para verificar la printabilidad del PHBH. Además, se ha observado que, a diferencia de lo que ocurre normalmente en FFF, la cristalización del PHBH se produce de forma isotérmica, de acuerdo con mediciones calorimétricas y con un estudio computacional realizado para simular el perfil de temperatura durante el proceso de impresión. Adicionalmente, se ha demostrado que las

propiedades mecánicas mejoran con temperaturas más altas de la boquilla y de la cama de impresión.

Con el objetivo de incrementar la difusión de materiales basados en PHAs, una parte de esta investigación se dedica al estudio de dos nuevos copolímeros de origen sintético basados en PHB y policaprolactona (PCL). El trabajo reporta el estudio térmico y morfológico de un copolímero en bloque y un copolímero aleatorio y se han obtenido diversos resultados: la presencia del comonómero influye en la cristalización no isotérmica, disminuyendo las temperaturas de cristalización y fusión. El análisis SAXS revela una diferencia estructural importante entre el copolímero en bloque y el copolímero aleatorio: el copolímero en bloque exhibe una segregación de fases débil en el fundido, que está ausente en el copolímero aleatorio.

En ambos copolímeros se produce una reducción del tamaño de las esferulitas lo que, en consecuencia, influye, en la transparencia, mejorándola, de los copolímeros respecto a los PHB puros. Además, el crecimiento de las esferulitas también se ralentiza, lo que reduce la cinética de cristalización global del PHB en los copolímeros. Estos resultados son prometedores porque sugieren que las propiedades de los productos basados en PHB pueden adaptarse, por medio de copolimerización, para mejorar su procesabilidad y sus propiedades finales.

Finalmente, este trabajo reportala síntesis de un nuevo poliésterde base biológica que tiene un átomo de carbono más que el PCL, y la poliheptalactona (PHL).

Este trabajo también investiga la influencia del peso molecular en la velocidad de nucleación primaria, el crecimiento esferulítico y la velocidad de cristalización global.Se ha observado que los pesos moleculares elevados aumentan estos valores de velocidad hasta alcanzar un plateau. Además,monocristales de PHL fueron preparados a partir de solución por primera vez, observándose, por TEM, una morfología hexagonal plana . Este

estudio revela grandes similitudes entre PHL y PCL y esto es importante para la difusión del uso de materiales sostenibles.